Distribution Agreement

In presenting this thesis or dissertation as a partial fulfillment of the requirements for an advanced degree from Emory University, I hereby grant to Emory University and its agents the non-exclusive license to archive, make accessible, and display my thesis or dissertation in whole or in part in all forms of media, now or hereafter known, including display on the world wide web. I understand that I may select some access restrictions as part of the online submission of this thesis or dissertation. I retain all ownership rights to the copyright of the thesis or dissertation. I also retain the right to use in future works (such as articles or books) all or part of this thesis or dissertation.

Signature:

_____ _____

Sheri Lense Date

The Effect of Methylene Spacers on the Spectral, Electrochemical, Structural, and Photophysical Properties and Electron Injection Dynamics of Bis(4,4'-disubstituted-2,2'-bipyridyl) Ruthenium(II) Dye Analogues and
The Effect of Alkali Metal Ions on the Structure and Spectroscopy of a Tripodal Co(II) Complex

By

Sheri Lense
Doctor of Philosophy

Chemistry

Cora E. MacBeth, Ph.D.
Advisor

Craig L. Hill, Ph.D.
Committee Member

Tianquan Lian, Ph.D.
Committee Member

Accepted:

Lisa A. Tedesco, Ph.D.
Dean of the James T. Laney School of Graduate Studies

Date

The Effect of Methylene Spacers on the Spectral, Electrochemical, Structural, and Photophysical Properties and Electron Injection Dynamics of Bis(4,4'-disubstituted-2,2'-bipyridyl) Ruthenium(II) Dye Analogues and The Effect of Alkali Metal Ions on the Structure and Spectroscopy of a Tripodal Co(II) Complex

By

Sheri Lense
B.A. Princeton University, 2003

Advisor: Cora E. MacBeth, Ph.D.

An abstract of
A dissertation submitted to the Faculty of the
James T. Laney School of Graduate Studies of Emory University
in partial fulfillment of the requirements for the degree of
Doctor of Philosophy
in Chemistry
2010

Abstract

The Effect of Methylene Spacers on the Spectral, Electrochemical, Structural, and Photophysical Properties and Electron Injection Dynamics of Bis(4,4'-disubstituted-2,2'-bipyridyl) Ruthenium(II) Dye Analogues and
The Effect of Alkali Metal Ions on the Structure and Spectroscopy of a Tripodal Co(II) Complex

By Sheri Lense

Variations of *cis*-dithiocyanatobis(2,2'-bipyridyl-4,4'-dicarboxylate)ruthenium(II) (N3), in which methylene spacers were inserted between the bipyridyl and carboxylic acid or methyl ester groups, were synthesized and characterized to study the effects of methylene spacers on the spectral, electrochemical, and structural properties and electron injection dynamics. The complexes exhibit very similar electronic absorption spectra that are blue-shifted with respect to the N3 dye. For all complexes, the reversibility of the Ru(II/III) couple increases with increasing linker length. The complexes with one methylene spacer are significantly less stable under reducing conditions than the complexes with two or three methylene spacers. Electron transfer from the modified dyes to TiO_2 was also investigated. The injection yields are smaller for the modified dyes than for the N3 dye, likely because electron injection is slower, allowing for competing decay processes to become more competitive.

Part II of this thesis describes the coordination of alkali metal ions by tripodal Co(II) complexes. The alkali metal ions influence both the local and extended geometry of these complexes. Upon alkali metal ion coordination the ligand geometry around the transition metal ion changes from trigonal monopyramidal to trigonal bipyramidal and the solid-state structure takes on an extended form, with the transition metal complexes linked through shared alkali metal ions to form one-dimensional chains.

The Effect of Methylene Spacers on the Spectral, Electrochemical, Structural, and Photophysical Properties and Electron Injection Dynamics of Bis(4,4'-disubstituted-2,2'-bipyridyl) Ruthenium(II) Dye Analogues and The Effect of Alkali Metal Ions on the Structure and Spectroscopy of a Tripodal Co(II) Complex

By

Sheri Lense
B.A. Princeton University, 2003

Advisor: Cora E. MacBeth, Ph.D.

A dissertation submitted to the Faculty of the
James T. Laney School of Graduate Studies of Emory University
in partial fulfillment of the requirements for the degree of
Doctor of Philosophy
in Chemistry
2010

Acknowledgements

I would like to thank my advisor, Dr. Cora E. MacBeth, for all her help and support in preparing this dissertation, which I greatly appreciate. I would also like to thank my committee, Dr. Craig L. Hill and Dr. Tianquan Lian, for their helpful suggestions. The MacBeth group, Lei Chu, Matthew Jones, Kelly Kluge, Savita Sharma and Omar Villanueva, gave many helpful suggestions for my thesis defense. I would also like to acknowledge Dr. Dave Stockwell for his help in collecting the electron injection data and Chantelle Anfuso and HaiMing Zhu for their helpful advice for calculating the electron injection parameters. Additionally, I would like to thank my wonderful family, Lloyd, Susan, Miriam and Sara Lense, as well as John Bowers, for always being loving and supportive.

Table of Contents

List of Figures, Tables and Schemes

List of Figures

List of Tables

List of Schemes

Part I. The Effect of Methylene Spacers on the Spectral, Electrochemical, Structural, and Photophysical Properties and Electron Injection Dynamics of Bis(4,4'-disubstituted-2,2'-bipyridyl) Ruthenium(II) Dye Analogues

Chapter I. Introduction

I. Solar Cells

Solar cells, also known as photovoltaic (PV) cells, convert sunlight to electricity via the photoelectric effect. Dwindling supplies of fossil fuels and concerns about the environmental effects of burning them have resulted in a great deal of interest in technologies capable of exploiting clean renewable energy resources such as sunlight. While solar cells are produced commercially, a challenge to widespread utilization of photovoltaic electricity is cost compared to the cost of electricity produced by conventional technologies; The former runs approximately 0.25–0.45 euro/kWh ($0.31-$0.55/kWh), whereas the latter costs only 0.1-0.2 euro/kWh.[1] Therefore, it is necessary to develop low-cost and efficient solar cells.

Currently, 'first generation' silicon wafer PV cells, made from monocrystalline silicon wafers, make up ~ 90% of the solar cell market.[1] Silicon wafer PV cells are currently the most efficient, with efficiencies of up to 25.0%.[2] However, they are costly since the silicon crystals are expensive and slow to grow and require greater thickness to absorb a given amount of sunlight compared to other semiconductors.[1] Thus, a significant amount of research in the development of second and third generations of PV cells is focused on developing cost-effective alternatives to silicon wafer PV cells.

II. Thin Film Solar Cells (TFSCs)

Second and third generations of PV cells utilize thin film technologies to create thin film solar cells (TFSCs). They employ semiconductors that are better at absorbing sunlight

than monocrystalline silicon, allowing thinner layers of these semiconductors to be used. Thin films of these semiconductors are deposited directly onto a substrate.[3] TFSCs can be divided into four main categories: Silicon-based TFSCs, chalcogenide-based TFSCs, organic or polymer TFSCs, and dye-sensitized solar cells (DSSCs). DSSCs are the subject of this thesis, and will be discussed in more depth after a brief overview of the other types of TFSCs.

Silicon-based TFSCs utilize amorphous, nanocrystalline or polycrystalline silicon. While amorphous silicon is easy to prepare and benign, it is susceptible to degradation, and after 1-2 months of field exposure the efficiency is only 4-6%. Additionally, the amorphous silicon is a poor conductor, necessitating the use of a transparent tin oxide conductive layer between the glass and silicon. Multiple junction amorphous silicon cells have higher efficiencies of 8-10%, but are still susceptible to degradation and require a conducting tin oxide layer.[3] Polycrystalline silicon has been shown to be more conductive and durable than amorphous silicon, and modules utilizing polycrystalline silicon have shown energy conversion efficiencies of 7-8%.[3]

A second category of TFSCs utilizes chalcogenide-based semiconductors such as cadmium telluride (CdTe) and copper indium diselenide or copper indium gallium diselenide (CI(G)S). These cells have among the highest conversion efficiencies of TFSCs (16.7% for a CdTe-based cell and 19.4% for a CI(G)S-based cell).[2] However, concerns over cadmium's environmental toxicity have limited commercial interest in CdTe-based cells.[3] CI(G)S-based cells have proven difficult to commercialize. Moreover, they currently require a CdS layer, raising concern over Cd toxicity, and the supply of indium is limited, which would prevent large-scale manufacture.[3]

Organic TFSCs, the third category, feature a thin layer of semiconducting organic

molecules or polymers, often one electron-conductor and one hole-conductor to facilitate charge separation, sandwiched between two electrodes.[4] Organic semiconductors require only inexpensive and naturally abundant elements, and are often easy to synthesize and to modify, but the efficiencies are still low compared to cells utilizing inorganic semiconductors (5.15% for an organic polymer cell in 2009).[2]

The last category of TFSCs, DSSCs, is the subject of Part I of this thesis. DSSCs are unique in that photon absorption and charge transport are divided between two different species: A dye absorbs the photon, exciting an electron that is subsequently injected into the conduction band of a wide band gap semiconductor. The electron is then transported through the semiconductor to the electrode. The dye is reduced by an electrolyte in solution, and the electrolyte is then reduced at the counter electrode. A schematic of a DSSC is shown in Figure 1-1. The most commonly used semiconductor for DSSCs is TiO_2. With a band gap of 3.2 eV (anatase),[5] TiO_2 is not sensitive to visible light on its own. There has been a great deal of research into the dye, electrolyte and semiconductor components of DSSCs since O'Regan and Graetzel's seminal paper in 1991.[6] The following sections will describe the development of the DSSC and the most commonly used photosensitizer, the N3 dye, and then attempts to improve on the N3 dye as a means of increasing the efficiencies of DSSCs.

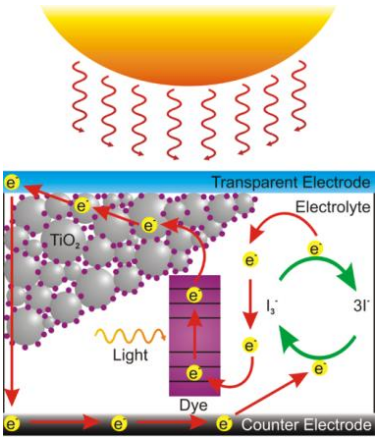

Figure 1-1. Schematic of DSSC, used with permission of the artist.[7]

III. DSSCs

In 1991, O'Regan and Graetzel published an article in *Nature* describing DSSCs capable of converting 7.1 to 7.9% of simulated solar light to electrical current.[6] These cells were based on the same principle as previous DSSCs, but used semiconducting TiO_2 nanoparticles rather than a smooth semiconductor surface. This greatly increased the semiconductor surface area available for dye absorption: A cubic close packing of 15 nm-sized spheres to a 10 μm thick layer is calculated to produce a 2,000-fold increase in surface area over the geometric surface.[6]

O'Regan and Graetzel's cell consisted of a monolayer of the dye $[Ru(bpy)_2(CN)_2]_2Ru(dcbpy)_2^{2-}$ (bpy = bipyridine, dcbpy = 4,4'-dicarboxy-2,2'-bipyridine) adsorbed to a 10 μm thick optically transparent film of TiO_2 nanoparticles. The TiO_2 films had previously been deposited on a conducting glass sheet from a colloidal solution, and then briefly sintered at 450 °C to achieve electronic contact between particles. The trimeric $[Ru(bpy)_2(CN)_2]_2Ru(dcbpy)_2^{2-}$ dye was then deposited on the bare film, changing it from colorless to a deep brownish-red as the absorption onset shifted from the ultraviolet to 750 nm. The DSSCs were found to harvest a high proportion of the incident solar energy flux

(46%), convert more than 80% of incident photons to electrical current, and produce current densities greater than 12 mA cm^{-2}. Additionally, the cells could be made with low-to-medium purity materials using low-cost processes and were stable over at least five million turnovers, making them feasible for practical applications.[6]

Graetzel and co-workers had previously found that the dye *cis*-diaquabis(2,2'-bipyridyl-4,4'-dicarboxylate)ruthenium(II) ($Ru(dcbpy)_2(H_2O)_2$) sensitized wide band-gap semiconductors such as TiO_2 over a broad visible spectral range.[8] This discovery came as somewhat of a surprise, since the excited states of bis(2,2'-bipyridyl)ruthenium(II) and its analogues were generally found to be shorter lived than tris(2,2'-bipyridyl)ruthenium(II) and its analogues. However, when $Ru(dcbpy)_2(H_2O)_2$ was bound to TiO_2 via the carboxylic acid moiety, electron transfer from the excited state of the complex to the semiconductor occurred fast enough ($\tau < 7$ ps, where τ = the lifetime of the excited state) to give a quantum yield near 100%.[9]

In addition to fast electron transfer to wide band gap semiconductors, bis(2,2'-bipyridyl)ruthenium(II)-type semiconductors are chemically stable and able to harvest a larger portion of the visible-light spectrum than tris(2,2'-bipyridyl)ruthenium(II)-type sensitizers, making them attractive candidates for use in solar energy conversion. Nazeeruddin *et al.* performed a systematic investigation of *cis*-$Ru(dcbpy)_2(X)_2$ complexes (X = Cl^-, Br^-, I^-, CN^- and SCN^-) on nanocrystalline TiO_2 electrodes. $Ru(dcbpy)_2(NCS)_2$ (N3) (Figure 1-2) was found to be the most promising charge-transfer sensitizer. It absorbs a broad range of visible light and possesses a relatively long-lived excited state. A DSSC employing the N3 dye was found to convert 10% of AM 1.5 solar radiation into electricity.[9]

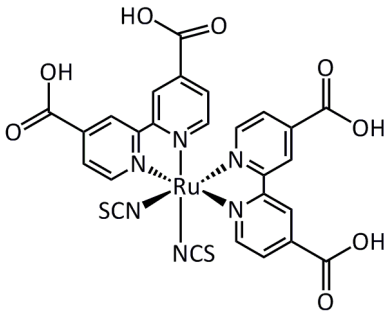

Figure 1-2. *cis*-$Ru(dcbpy)_2(NCS)_2$ (N3).[9]

The N3 dye, along with the related $(Bu_4N)_2[Ru(dcbpyH)_2(NCS)_2]$ (N719) dye,[10] remain standard dyes for DSSCs. However, there is room for improvement for the dye component of DSSCs. The N3 dye lacks in absorption in the red region of the visible spectrum (650-900 nm) and has a relatively low molar excitinction coefficient.[11] Increased absorption in the red region of the visible spectrum will improve photocurrent and therefore overall efficiency. Additionally, an increase in molar extinction coefficient allows for thinner DSSCs, which increases the open current voltage due to less transport loss in the TiO_2 nanostructure, also improving cell efficiency.[11]

The creation of dyes that improve in these areas proves a considerable challenge due to other constraints placed on the photosensitizers. Red-shifting the visible absorption spectrum requires either stabilization of the ligand-centered excited state or destabilization of the Ru(II) t_{2g} orbitals. However, the HOMO of the dye must be maintained at a potential above the semiconductor conduction band to create a driving force for forward electron transfer, and the LUMO of dye must be at a potential more negative than that of iodide (or other reducing electrolyte) to permit regeneration of the photosensitizer from the oxidized state.[11] To improve on the N3 dye, it is valuable both to study ways to red shift the visible absorption spectrum and increase the molar extinction coefficient of the N3 dye, and to probe the interfacial electron transfer between dyes such as the N3 dye and wide band-gap

semiconductors such as TiO_2. The following sections will look at attempted improvements on the N3 dye and will review previous studies probing interfacial electron transfer from dyes to semiconductors.

IV. Improvements on the N3 Dye

To address the absorption in the red region of the spectrum and the molar extinction coefficient, Klein, Nazeeruddin and co-workers designed a 4,4'-bis(carboxyvinyl)-2,2'-bipyridine ligand (L^2), in which a vinyl moiety is inserted between the bipyridyl and carboxylic acid groups.[11,12] They metallated these dyes in either a homoleptic manner, (K8) $(Ru(II)L^2_2(NCS)_2)$,[12] or heteroleptic manner, (K9) $(Ru(II)L^2L^9(NCS)_2$, with L^9 = 4,4'-dinonyl-2,2'-bipyridine).[11] K8 is shown in Figure 1-3. The effect of increased conjugation on the bipyridyl ligand can be seen in the UV-visible absorption spectrum of K8 compared to N3 in DMF: The lower energy metal-to-ligand charge transfer (MLCT) band is red-shifted (555 nm compared to 535 nm), and the extinction coefficient increases from 13,600 $M^{-1}cm^{-1}$ to 18,000 $M^{-1}cm^{-1}$.[12]

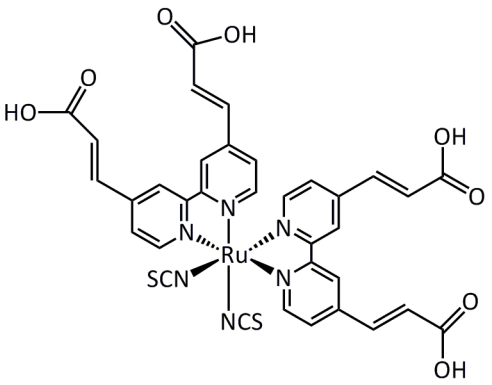

Figure 1-3. *cis*- $Ru(II)L^2_2(NCS)_2$ (K8).[12]

With regard to electron transfer to TiO_2, the recombination dynamics for the K8 dye were indistinguishable to those observed for the N3 dye, indicating insertion of the vinyl groups does not significantly decrease electronic coupling between dye and TiO_2, as might

be expected given that the vinyl groups do not decrease the conjugation between the bipyridyl ligand and semiconductor.[12] However, the electron injection yield is 10-20% lower for K8 to TiO_2 compared to N3 to TiO_2.[12] One possible explanation for the decrease in injection yield is that increasing the conjugation of the bipyridyl ligands decreases the potential of the ligand-based LUMO, which in turn decreases the driving force and hence electron transfer rate from the dye to the TiO_2 conduction band. A decreased rate of electron transfer could allow competing processes, such as transfer to surface states on the TiO_2 and quenching between dyes, to play a larger role, resulting in a lower injection yield to the TiO_2 conduction band. While the results from the complexes utilizing the 4,4'-bis(carboxyvinyl)-2,2'-bipyridine ligand are promising, the decreased injection yield illustrates the challenge in designing more efficient dyes.

Other attempts to improve on the N3 dye by red-shifting the visible absorption spectrum and increasing molar extinction coefficient include the 'black dye', $(C_2H_5)_3NH)[Ru(H3tcterpy)(NCS)3]$, where H3tcterpy = 4,4',4''-tricarboxy-2,2':6',2''-terpyridine,[13] which also has a lower energy MLCT band than the N3 dye and hence enhanced light absorption in the red and near-IR region; a solar cell conversion efficiency of η = 11.1% (where $\eta = P_m/(E*A_c)$ and P_m is the maximum power point, E is the input light irradiance and A_c is the surface area of the cell) was measured for the black dye in 2006.[14]

Graetzel and co-workers have also looked at heteroleptic Ru dyes with an 'antenna function': thiophene groups attached to the bipyridyl ligand that increase the extinction coefficient and red-shift the absorption spectrum. The heteroleptic antenna dye Z991 (Figure 1-4) has an extinction coefficient almost 3 times higher than the black dye (N749). Conversion efficiencies of 12% have been reached with these dyes, and they appear to be very robust and stable.[14]

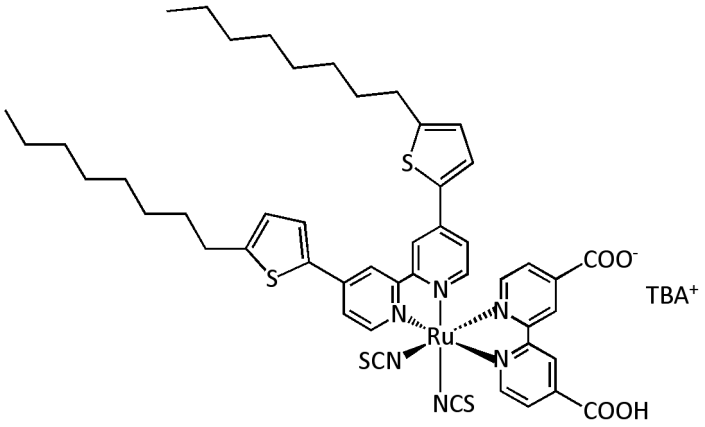

Figure 1-4. Z991 dye.[14]

Another potential problem with the N3 dye is the cost and rarity of ruthenium. Consequently, there have also been efforts to find dyes that circumvent the use of ruthenium. Organic photosensitizers are inexpensive, tend to be easy to synthesize and modify, many have higher molar absorption coefficients than Ru dyes, and they do not contain rare or semi-rare metals. Dyes investigated thus far include coumarin dyes, polyene dyes, hemicyanine dyes, thiophene-based dyes, indoline dyes, heteropolycyclic dyes, xanthene dyes, perylene dyes, porphyrin dyes, merocyanine dyes, catechol dyes, polymeric dyes, squaraine dyes, cyanine dyes and phthalocyanine dyes.[15,16] Many organic photosensitizers, such as coumarin dyes, polyene dyes, hemicyanine dyes, thiophene-based dyes, indoline dyes and heteropolycyclic dyes, are based on a donor-acceptor π-conjugated (D-π-A) system. Electron-donating (D) and electron-accepting (A) groups are linked by π-conjugated bridges, allowing for intramolecular charge transfer from the donor to acceptor parts of the dye, followed by electron transfer from the acceptor of the excited dye to the semiconductor.[15] However, organic dyes also have several disadvantages: they often have relatively narrow absorption bands in the visible region, tend to form π-stacked aggregations of TiO_2 surface, and are generally less stable than Ru dyes under irradiation.[15] Indoline-based dyes are

currently the most efficient organic sensitizers. They possess rhodanine rings as electron acceptors and indoline groups as electron donors, connected by an aromatic ring, and have conversion efficiencies of η = 5.1-6.5%. Graetzel's group synthesized the D205 dye, in which they added a bulky alkyl group to prevent dye aggregation and charge recombination. This modification brings the efficiency to η = 9.5%.[15]

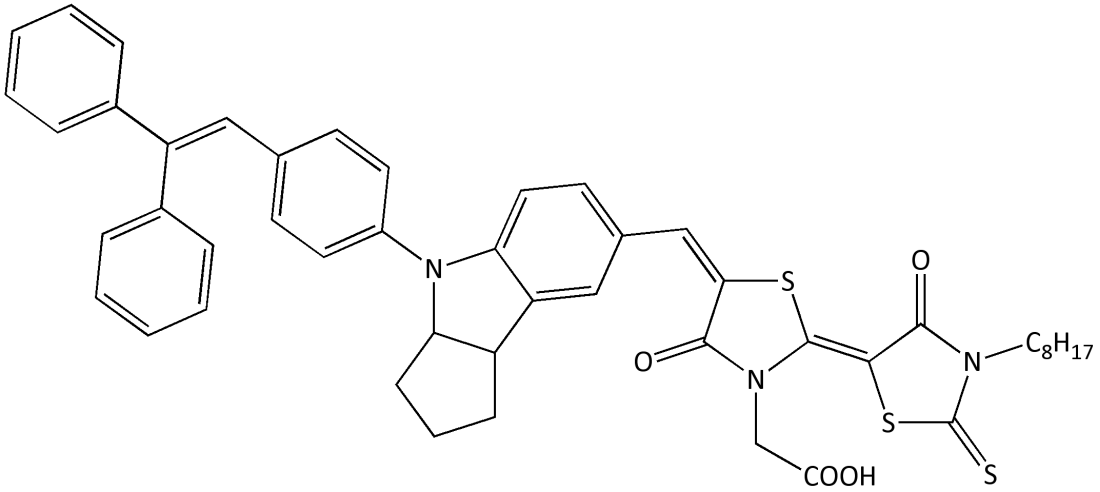

Figure 1-5. Indoline dye D205.[15]

Another interesting area of research is in Cu(I) polypyridyl dyes. Copper is less expensive and more abundant than ruthenium. Unlike other first-row transition metal analogues, Cu(I) bipyridyl complexes possess long-lived MLCT excited states that are often emissive. For other first-row transition metal (TM) analogues, metal-centered excited states are at a similar energy to the MLCT excited state, leading to rapid non-radiative quenching of the MLCT excited state by the metal-centered excited states. Since Cu(I) is d^{10}, metal-centered excited states do not easily quench the MLCT excited state. However, sterically-bulky ligands used to prevent a change in geometry from tetrahedral to square planar upon oxidation or excitation of the Cu(I) dye must be used. To date, Cu(I) dyes with conversion efficiencies of 1.9 and 2.3% have been synthesized.[17]

V. Interfacial Electron Transfer from the Dye to TiO_2

Generally, electron injection from the excited dye to the TiO_2 conduction band has not been considered a limiting factor in DSSC efficiency, since kinetic studies utilizing dye-sensitized TiO_2 nano-structured thin films have shown electron injection from dye to semiconductor to occur on a sub-picosecond time scale, much faster than the lifetime of the excited state of the dye.[18] However, recent studies by James R. Durrant's group using the N719 dye in a complete nanocrystalline TiO_2 DSSC found electron injection from the dye to TiO_2 to have a half-time of 150 ps[19] or 200±60 ps, with a quantum yield of 84±5%.[18] The slower electron injection rate measured in the complete DSSC (~20 times slower than that measured in a control that utilized dye-sensitized films covered in inert organic liquids[18]) is ascribed to an upward shift in the TiO_2 conduction band potential due to *tert*-butylpyridine and Li^+ used in the electrolyte.[18] With this slower electron injection rate, competition between electron injection and excited state decay can potentially play a role in limiting efficiency of the DSSC.

Electron injection dynamics from the excited dye to TiO_2 conduction band is also an important factor in attempts to improve on the N3 and N719 dye. For example, engineering a dye to have a red-shifted visible absorption spectrum with respect to the N3 dye may also result in a lower potential bipyridyl-based π^* orbital. This will result in a decreased driving force for electron transfer from the π^* orbital to TiO_2 conduction band, and therefore a decreased electron injection rate, which may allow competing relaxation processes to play a larger role and decrease electron injection yield. Such may be the case for the K8 dye, which features a more conjugated bipyridyl ligand than the N3 dye, and which exhibits a 10-20% lower electron injection yield than the N3 dye.[12] Modifying dyes may also influence the electron coupling between the dye and semiconductor and the potential of the

semiconductor band itself. Thus, enhanced understanding of interfacial electron injection dynamics may prove integral to the design of improved dyes.

The efficient conversion of an absorbed photon to electrical power requires (1) efficient injection from the dye to the semiconductor ($k_{inj} > k_o$, where k_o is the rate constant for decay of the excited state to the ground state), (2) efficient reduction of the oxidized dye by the redox electrolyte ($k_{red} > k_{cr}$, where k_{red} is the rate constant for reduction of the dye by the redox-active electrolyte, and k_{cr} is the rate of recombination between the injected electron and photogenerated dye cation), and (3) efficient charge collection (transport of the injected electrons and oxidized redox species to the working and counter electrodes, respectively, must be faster than charge combination between these species). Thus, the efficiency of DSSCs is improved by developing dye and semiconductor systems that create an optical compromise between fast electron injection from the excited dye to the semiconductor and slow charge recombination between the reduced semiconductor and oxidized dye.[20,21]

Many of the theoretical models used to describe interfacial electron transfer between a molecular dye and a semiconductor are based on Marcus theory. In traditional Marcus theory, the rate constant for electron transfer is given by the equation

$$k_{ET} = \nu_n \varkappa_e e^{-\Delta G^*/RT} \quad (1).$$

Here, ν_n is the nuclear frequency factor, $\varkappa_e$ is the electron transmission coefficient, and $\Delta G^* = \lambda(1 + \Delta G/\lambda)$. In this last equation ΔG is the driving force of the reaction and λ is the reorganization energy. In non-adiabatic systems, a semi-classical adaptation of Marcus Theory is often employed to account for the electronic coupling between reactants and products using the matrix element H_{ab}. In the high temperature limit $\nu_n \varkappa_e = (2\pi/\text{hbar})H_{ab}^2(4\pi RT)^{-1/2}$, giving the rate constant

$$k_{ET} = (2\pi/hbar)H_{ab}^{2}(4\pi RT)^{-1/2}*e^{-\Delta G^{*}/RT} (2).^{20,21}$$

When electron transfer is to a semiconductor there is not a single product state but rather a continuum of product states corresponding to different k states in the semiconductor, as shown in Figure 1-6. Electron transfer can be described as the sum of electron transfer to all possible acceptor states in the semiconductor:

$$k_{ET} = \frac{2\pi}{\hbar}\int dE\rho(E)(1-f(E,E_f)|avgH|^2 \frac{1}{4\pi\lambda k_B T} e^{\frac{-(\lambda+\Delta G^{o}+E)^2}{4\lambda k_B T}} \quad (3)\ ^{20,21}$$

Here, ΔG_o is the energy difference between the conduction band edge and the oxidation potential of the adsorbate excited state ($E_{cb} - E_{ox}$), $\varrho(E)$ is the density of excited states at energy E relative to the conduction band edge, avgH(E) is the average electronic coupling between different k states at the same energy R and the adsorbate excited state, and λ is the total reorganization energy.[20,21] Thus, the rate of electron transfer is dependent on the degree of electronic coupling between the dye excited state and the states in the semiconductor conduction band, the density of states in the semiconductor conduction band and their Fermi occupancy factor, the reorganization energy, and the driving force, the potential difference between the adsorbate excited state and conduction band states.

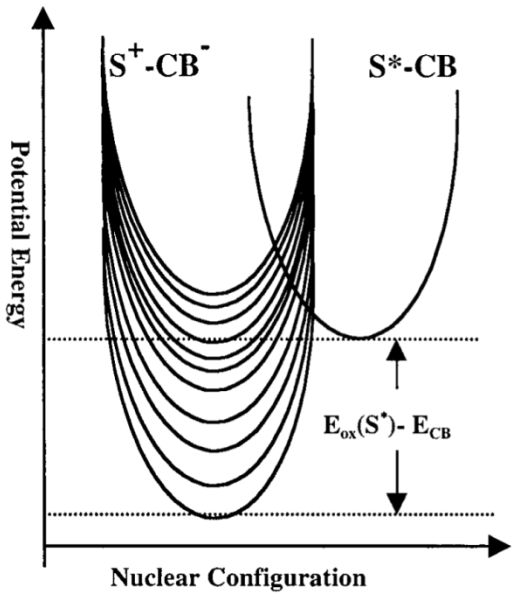

Figure 1-6. This schematic diagram, which illustrates the potential energy surface as a function of nuclear configuration for electron transfer from an excited dye molecule (S*) to the conduction band (CB) of a semiconductor, is taken from a paper by Lian *et al.*[20]

Several systematic studies have been conducted to probe each of these factors. Surface processes in nanostructured materials can be studied by ultrafast transient absorption techniques because of their large surface area and small size. Tim Lian's group and other groups have used transient mid-infrared (mid-IR) spectroscopy to study electron transfer in dye-semiconductor systems. Mid-IR spectroscopy can simultaneously probe vibrational transitions of the adsorbate in the ground, excited and oxidized states, and injected electrons in the semiconductor, which have strong absorption in this region due to free carrier absorption, intraband transitions, and trap absorption.[20,21]

To probe the effect of short bridge lengths on interfacial electron coupling, Anderson *et al.* examined the electron transfer kinetics of SnO_2 of a series of homologues of $Re(CO)_3Cl(dcbpy)$ (ReC*n*A) with methylene units $(CH_2)_n$ (n = 1-5) inserted between the bipyridyl rings and carboxylic acid groups (Figure 1-7). There had previously been several

studies on the effect of alkyl chain length on interfacial electron transfer through alkanethiol monolayers on gold. For $n \geq 8$ k_{ET} was found to vary exponentially with n: $k_{ET} = k_{ET,n=0}e^{-\beta(n)m}$, where $\beta(n)$ is the exponential decay coefficient and $k_{ET,n=0}$ is the extrapolated rate constant for $n = 0$. The dependence of coupling on the number of spacers for shorter alkyl chains is less well understood. Theoretical studies predict it to deviate from the exponential and oscillate between even and odd n.[22]

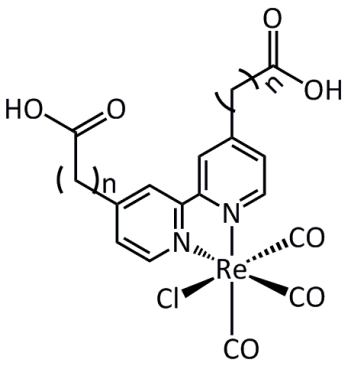

Figure 1-7. Homologues of $Re(CO)_3Cl(dcbpy)$ (ReC*n*A) with methylene unites $(CH_2)_n$ (n = 1-5) inserted between the bipyridyl rings and carboxylic acid groups.[22]

Insertion of methylene spacers would be expected to affect both the electronic coupling between the adsorbate and semiconductor and the oxidation potential of the adsorbate excited state. When the data was analyzed using a time-scaling approach the rate was found to decrease exponentially with bridge length for ReC3A, ReC4A and ReC5A, with $\beta(n) = 1.0$. ReC1A and ReC2A deviated from this trend, exhibiting nearly identical electron transfer rates. Anderson *et al.* suggest two explanations for this observation: At small bridge lengths, the exponential dependence of electronic coupling on spacer length may break down, as predicted by theoretical models that establish anion coupling as a function of bridge length. Electron transfer kinetics may also be fast enough at these short bridge lengths for electron transfer to fall into the adiabatic regime, so that solvent relaxation time

dictates electron transfer rates. However, kinetics are still slow (~ 10 ps) here compared to H_2O relaxation time, which has a substantial sub-picosecond component.[22]

The electronic and photophysical properties of $Re(CO)_3X$(bipyidyl) complexes differ significantly from those exhibited by other d^6 bipyidyl complexes (M^{II}(bipyridyl)$_2X_2$), where X = anionic ligand and M^{II} = Ru^{II} and Os^{II}. This is due in large part to the larger energy gap between the dπ Re orbitals and the π* orbitals of the bipyridyl ligand caused by the strong field CO ligands.[23] Given the differences between $Re(CO)_3X$(bipyidyl) complexes and Ru(bipyridyl)$_2X_2$ complexes and the widespread use of the latter in DSSCs, the first part of this thesis aims to explore the effect of methylene linking units on the spectroscopy and electrochemical properties of Ru(bipyridyl)$_2$(NCS)$_2$ complexes (Figure 1-8). Additionally, the electron transfer dynamics between the modified dyes and TiO_2 are investigated.

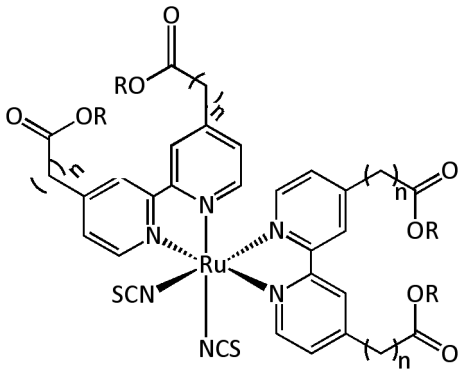

Figure 1-8. [Ru(L_n^{OR})$_2$(NCS)$_2$], modifications of the N3 dye, with methylene unites $(CH_2)_n$ (n = 1-3) inserted between the bipyridyl rings and carbonyl. R = H or Me.

VI. Outline for Part I of Thesis

I. Synthesis

II. Spectroscopy

III. Electrochemistry

IV. Structural Characterization

V. TiO_2 Film Sensitization and Electron Injection Dynamics

VI. Conclusion

VII. Experimental Section and Supplementary Material

Chapter II. The Effect of Methylene Spacers on the Spectral, Electrochemical, Structural, and Photophysical Properties and Electron Injection Dynamics of Bis(4,4'-disubstituted-2,2'-bipyridyl) Ruthenium(II) Dye Analogues

I. Synthesis

The ligands 2,2'-bipyridine-4,4'-di(methyl ethanoate) (L_1^{OMe}), 2,2'-bipyridine-4,4'-di(methyl propionate) (L_2^{OMe}), 2,2'-bipyridine-4,4'-di(propionic acid) (L_2^{OH}) and 2,2'-bipyridine-4,4'-di(butanoic acid) (L_3^{OH}) and their precursors were synthesized using modified literature procedures.[24] (See Experimental Section for details.)

Several experimental procedures were attempted to synthesize the corresponding $[Ru(L_n^{OMe})_2(NCS)_2]$ (n=1-2) and $[Ru(L_n^{OH})_2(NCS)_2]$ (n = 1-3) dyes. The N3 dye is traditionally synthesized by converting the corresponding chloride complex *cis*-$Ru(dcbpy)_2Cl_2$ to the thiocyanate complex by refluxing with several equivalents of NaNCS in darkness.[9] *cis*-$Ru(dcbpy)_2Cl_2$ is synthesized by refluxing $RuCl_3 \bullet 3H_2O$ and two equivalents of the ligand dcbpy in dimethylformamide in darkness under an inert atmosphere to afford *cis*-$Ru(dcbpy)_2Cl_2$, using a solvent-mediated reduction to reduce Ru(III) to Ru(II).[8] Since several other *cis*-$Ru(bipyridyl)_2$ complexes are synthesized using similar procedures involving solvent-mediated reduction of $RuCl_3 \bullet 3H_2O$ in DMF[25,26] it was attempted to use this procedure to synthesize $[Ru(L_1^{OH})_2Cl_2]$. However, the ^1H NMR spectrum of the result of the product showed only three main peaks in the aromatic region, indicating that while metallation had occurred, the desired *cis*-coordinated product, which would be expected to show six aromatic peaks due to the differing chemical environments of the pyridyl rings, had not formed. An additional concern was that the ligand could potentially coordinate to Ru(III) via the carboxylic acid groups, given the added flexibility from the methylene spacers, so it was decided to pursue $[Ru(L_1^{OMe})_2Cl_2]$, which might later be hydrolyzed following conversion to

the thiocyanate complex.

Metallation utilizing solvent-mediated reduction was attempted by refluxing the ligand L_1^{OMe}, $RuCl_3 \bullet 3H_2O$ and LiCl in DMF. While the ^1H NMR spectra in DMSO-d_6 of the resulting product showed six peaks of equal integration in the aromatic region, indicating metallation had occurred with two bipyridyl ligands in a *cis*-configuration, in the alkyl region the only peaks were at δ (ppm) =3.36 (H_2O), 3.11, 2.87 (DMF), 2.73 (DMF), 2.61, 2.50 (solvent peak) and 2.33, all more upfield than would be expected for the methylene and methyl ester protons.[27] The ^{13}C NMR spectrum in DMSO-d_6 shows alkyl peaks at 20.8 and 20.4 ppm, also must more upfield than would be expected for the methylene and methyl ester protons.[27]

This product was converted to the thiocyanate complex from the chloride complex by refluxing with an excess of KNCS in MeOH, since the lability of the chloride ligands made characterization difficult. In the region 1600-1800 cm^{-1}, the IR spectrum of the thiocyanate complex has only a weak band at 1638 cm^{-1} and moderate band at 1618 cm^{-1}, which can likely be assigned to pyridyl C-N and C-C stretching (see spectral data for the actual $[Ru(L_1^{OMe})_2(NCS)_2]$ complex below).

A reasonable explanation for these spectroscopic anomalies is that decarboxylation of the ligand occurred during metallation, to give the complex *cis*-$Ru(mebpy)_2Cl_2$, where mebpy = 4,4'-dimethyl-2,2'-bipyridine. The reported ^1H NMR spectrum for *cis*-$Ru(mebpy)_2Cl_2$ has peaks with δ (ppm) = 9.73 (1 H, d), 8.44 (1 H, s), 8.30 (1 H, s), 7.53 (1 H, d), 7.25 (1 H, d), 6.92 (1 H, d), 2.63 (3H, s, methyl), and 2.53 (3 H, s, methyl),[28] and the mystery complex has peaks with δ (ppm) = 9.75 (1H, d), 8.48 (1H, s), 8.32 (1H, s), 7.58 (1H, d), 7.30 (1H, d), 6.92 (1H, d), 2.61 (~2.5H, s), and 2.32 (~1.8H, s). Thus, the peaks in the aryl region for the product found here match the reported ^1H NMR spectrum for *cis*-

$Ru(mebpy)_2Cl_2$ fairly well, and the lowest field alkyl proton could be under the residual DMSO peak, in which case the peaks in the alkyl region match as well.

A similar finding was reported by Anderson *et al.* for the ethyl ester analogue of the N3 dye: In their attempt to synthesize $Ru(debpy)_3^{2+}$ (debpy = 2,2'-bipyridinyl-4,4'-dicarboxylic acid diethyl ester) via a microwave reaction of $RuCl_3$ with debpy in ethylene glycol, they synthesized instead $Ru(bpy)_3^{2+}$ (bpy = bipyridine), and detected CO_2 in the headspace of the reaction, indicating the ligand had been decarboxylated.[29] Mechanistic studies indicate that decarboxylation occurs from the acid form of the ligand.[29] Graetzel *et al.* also observed decarboxylation of the N3 dye at elevated temperatures.[30] In L_1^{OMe}, the methylene spacer is sandwiched between the bipyridyl and ester (or carboxylic acid, if hydrolysis occurs) groups, which would stabilize either an anionic charge or radical at the site in an intermediate or transition state, potentially making the site vulnerable to reaction with Ru(II) or Ru(III) and DMF's decomposition products. One possible decarboxylation mechanism would involve hydrolysis of the ester to form the carboxylic acid, followed by a hydrogen rearrangement to form the 4-methylpyridyl group and release CO_2.

Due to the ligand decomposition problem, procedures employing milder conditions were attempted. The Ru(II) precursor *cis*-$Ru(DMSO)_4Cl_2$, was used following a similar procedure to that used to synthesize $Ru(3,3'\text{-dcbpy})_2Cl_2$, $Ru(4,4'\text{-dcbpy})_2Cl_2$ and $Ru(5,5'\text{-dcbpy})_2Cl_2$ (dcpby = dicarboxy-2,2'-bipyridine).[31] However, formation of the tris-substituted product could not be avoided even upon addition of great excesses (30 equivalents) of LiCl.

Thus, a procedure Meyer *et al.*[32] used in the synthesis of Ru complexes containing vinyl-substituted bipyridyl ligands was adapted and used in the synthesis of precursors of both $[Ru(L_1^{OMe})_2(NCS)_2]$ and $[Ru(L_2^{OMe})_2(NCS)_2]$. Two equivalents of L_1^{OMe} were refluxed with one equivalent $RuCl_3 \bullet 3H_2O$, an excess (20 equivalents) of hydroquinone, to reduce the

Ru(III) to Ru(II), and an excess (30 equivalents) of LiCl, to prevent formation of the tris-substituted product, in a 2:1 dimethoxyethane-methanol solution. After refluxing, the solvent was removed and the resulting purple solid extracted into CH_2Cl_2 and washed with water and ether to remove the excess LiCl and hydroquinone, and a dark purple solid was isolated. The product was treated immediately with excess potassium thiocyanate in refluxing methanol (Scheme 1). It is assumed, based on similar synthetic protocols,[9,31,33] that the dark red products isolated after the first step are the corresponding dichloride complexes, $[Ru(L_n^{OMe})_2Cl_2]$ (where n = 1 or 2). These intermediates were unstable and were, therefore, converted directly to the corresponding bis(isothiocyanto) complexes, $[Ru(L_n^{OMe})_2(NCS)_2]$ (Scheme 2-1). Complete experimental procedures can be found in the Experimental Section. Once synthesized, the complexes were stored as solids in the dark. Solutions (CH_3CN) of the complexes were photochemically unstable and exhibited a decrease in their absorbance maxima after prolonged exposure (ca. 5 h) to sunlight.

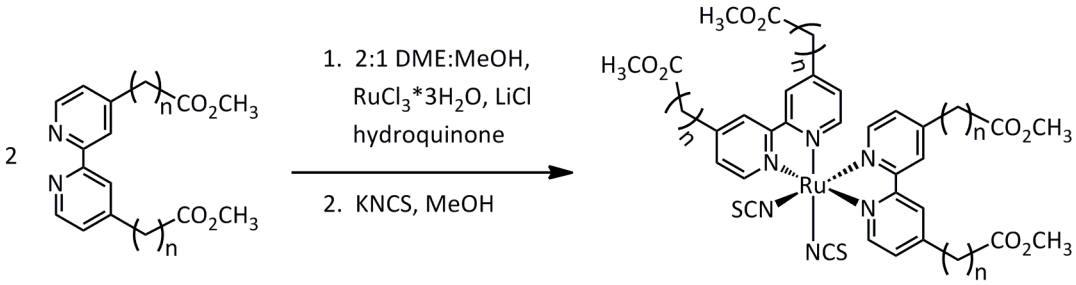

Scheme 2-1. Synthesis of $[Ru(L_n^{OMe})_2(NCS)_2]$, n = 1 or 2.

$[Ru(L_1^{OMe})_2(NCS)_2]$ and $[Ru(L_2^{OMe})_2(NCS)_2]$ were hydrolyzed to form the carboxylic acid derivatives by refluxing with excess triethylamine and KNCS in deionized H_2O under argon in the dark for 14 hours. 1M HCl was added until the product precipitated. ^1H NMR revealed that the product contained ~10 – 20% impurity (depending on whether or not the impurity contains a second set of pyridyl peaks that overlap with the product peaks and thus

cannot be seen), which were not separable by crystallography or chromatographic techniques. Please see the Experimental Section for more details.

$[Ru(L_2^{OH})_2(NCS)_2]$ and $[Ru(L_3^{OH})_2(NCS)_2]$ could also be directly synthesized from L_2^{OH} and L_3^{OH}, respectively, di-μ-chlorobis[(p-cymene)chloro-ruthenium(II)] (Ru p-cymene) and NH_4NCS using a procedure adapted from Graetzel *et al.*'s synthesis of the K8 complex (Scheme 2-2).[12] Conducting the reaction at 150 °C, as described in the literature,[12] led to a complex mixture of products, whereas conducting the reaction at 140 °C led to clean product save for a 10-20% impurity I was unable to remove, which is described further in the next section. Conducting the reaction at 130 °C instead of 140 °C did not decrease the relative amount of impurity. Graetzel *et al.* have since used this procedure to synthesize a variety of Ru(II) bearing potentially fragile bipyridyl ligands at temperatures ranging from 80 °C - 145 °C).[16,34,35] Complete experimental procedures can be found in the Experimental Section.

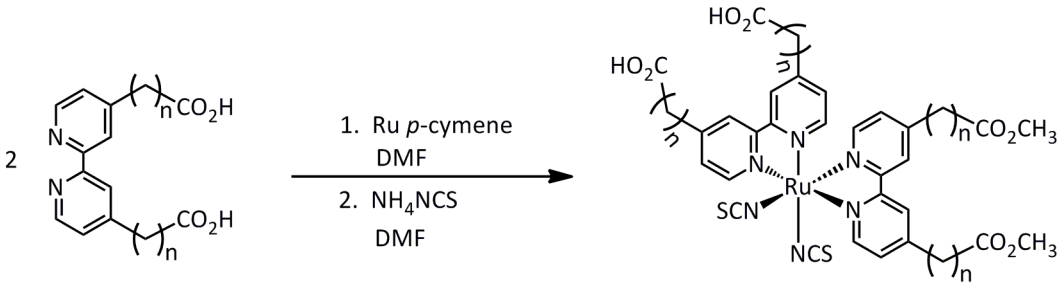

Scheme 2-2. Synthesis of $[Ru(L_n^{OH})_2(NCS)_2]$, n = 2 or 3.

It is worthy to note that the carboxylic acid derivative of the complex with one spacer could not be synthesized via an analogous reaction with Ru p-cymene, or upon lowering the reaction temperature to 130 °C; rather, a complex reaction mixture formed. The instability of this particular ligand derivative is also apparent in the electrochemical studies of $[Ru(L_1^{OMe})_2(NCS)_2]$ and $Ru(L_1^{OMe})_2(NCS)_2]$ (*vide infra*).

II. Spectroscopy

The methyl ester metal complexes were characterized by ^{1}H NMR, ^{13}C NMR, UV-visible absorption and infrared (IR) absorption spectroscopy, as well as mass spectrometry and elemental analysis. The ^{1}H NMR spectra of the complexes each show six peaks in the aromatic region, indicative of *cis*-bipyridyl coordination, as well as four and six peaks in the alkyl region for $[Ru(L_1^{OMe})_2(NCS)_2]$ and $[Ru(L_2^{OMe})_2(NCS)_2]$, respectively, that correspond to the protons of the methylene spacers and the methyl ester protons. The aromatic peaks are shifted more downfield for $[Ru(L_1^{OMe})_2(NCS)_2]$ than for $[Ru(L_2^{OMe})_2(NCS)_2]$ due to the closer proximity of the electron withdrawing ester group. This downfield shift is even more pronounced for the methylene spacer protons. This trend is expected, as the methylene spacers in $[Ru(L_2^{OMe})_2(NCS)_2]$ are further from both the deshielding ester and pyridyl groups than the single methylene spacer in $[Ru(L_1^{OMe})_2(NCS)_2]$. In the ^{13}C NMR spectra, the thiocyanate carbon peak appears at approximately 134 ppm for both $[Ru(L_1^{OMe})_2(NCS)_2]$ and $[Ru(L_2^{OMe})_2(NCS)_2]$, consistent with an N-bound isothiocyanate.[33] The IR spectra are also consistent with the proposed structures of $[Ru(L_1^{OMe})_2(NCS)_2]$ and $[Ru(L_2^{OMe})_2(NCS)_2]$, as the complexes exhibit diagnostic ν(CN) stretches at 2103 cm^{-1} and ν(CO) stretches at 1736 and 1731 cm^{-1}, respectively.

The UV-visible absorption spectra for $[Ru(L_1^{OMe})_2(NCS)_2]$, $[Ru(L_2^{OMe})_2(NCS)_2]$, and N3 recorded in DMSO are shown in Fig. 2-1 and the electronic spectral data are summarized in Table 1. Each complex displays one bipyridine centered π–π^* transition and two metal-to-ligand charge transfer (MLCT) bands characteristic of *cis*-coordinated ruthenium bipyridyl complexes.[36] Both $[Ru(L_1^{OMe})_2(NCS)_2]$ and $[Ru(L_2^{OMe})_2(NCS)_2]$ absorb at similar wavelengths with similar extinction coefficients. The absorptions of $[Ru(L_1^{OMe})_2(NCS)_2]$ and $[Ru(L_2^{OMe})_2(NCS)_2]$ are significantly blue shifted with respect to that

of the previously reported [Ru(L_0^{OEt})$_2$(NCS)$_2$] and N3 dyes (Table 2-1).[33,37] This shift arises due to the disruption in the conjugation between the carbonyl and pyridyl groups. The extinction coefficients of the MLCT bands of the modified dyes are smaller than those of the N3 dye due to decreased orbital overlap between the metal-based d orbitals and ligand-based π* orbitals. This decrease in orbital overlap can be explained by a decrease in π backbonding from the Ru(II) center to the π* orbital of the modified ligands, due to the disruption in conjugation of the ligands with the insertion of methylene spacers. Conversely, the extinction coefficient of the ligand-based π to π* transition is larger for the modified dyes than for the N3 dye, which can also be explained be decreased d orbital-π* orbital mixing.

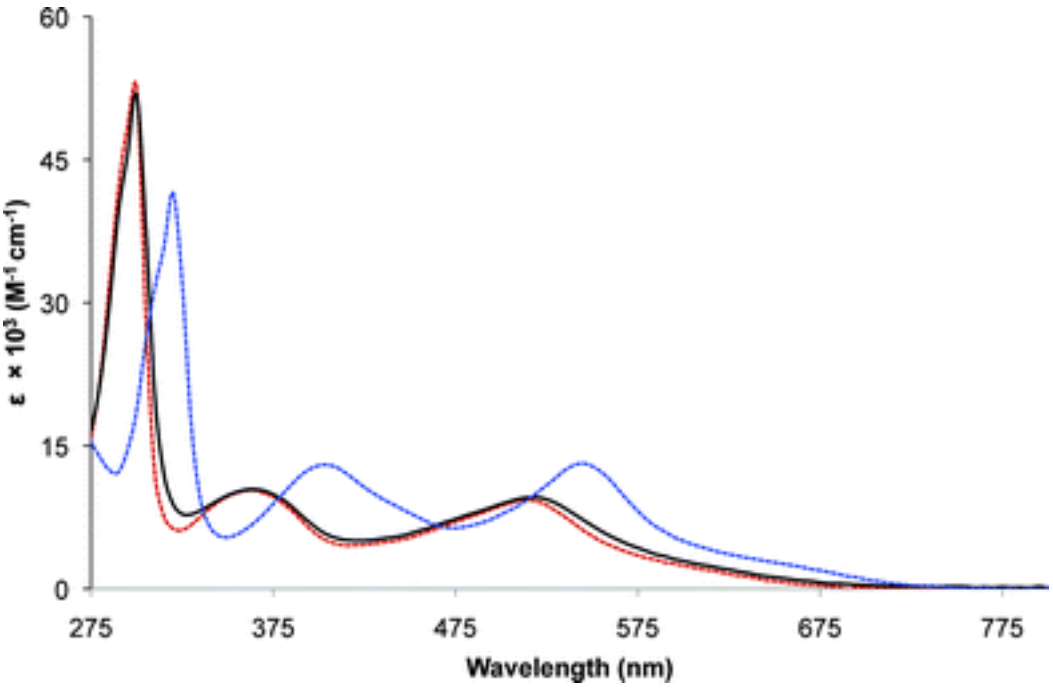

Figure 2-1. UV-visible absorption spectra of the N3 dye (---), Ru(L_1^{OMe})$_2$(NCS)$_2$] (---) and [Ru(L_2^{OMe})$_2$(NCS)$_2$] (---) recorded in DMSO. Data and graph from Lense *et al.*[23]

Complex	Solvent	MLCT	MLCT	π-π*	Emission Maximum
$[Ru(L_0^{OEt})_2(NCS)_2]$[a]	DMSO CH_3CN	550 (9.0) —	414 (9.5) —	320 (27.8) —	— 875
$[Ru(L_1^{OMe})_2(NCS)_2]$	DMSO CH_3CN	520 (9.6) 515 (10.0)	365 (10.5) 365 (11.0)	300 (52.3) 295 (54.0)	— 722[b]
$[Ru(L_2^{OMe})_2(NCS)_2]$	DMSO CH_3CN	515 (9.3) 515 (8.8)	365 (10.0) 360 (9.6)	300 (52.0) 300 (52.0)	— 715[b]
N3[a]	DMSO	542 (13.2)	400 (13.0)	318 (45.7)	—

Table 2-1. UV-visible absorption and luminescence data for *cis*-$[Ru(L_2)(NCS)_2]$ complexes, where L = 4,4'-substituted bipyridine. Wavelengths are reported in nm and the values in parentheses are molar extinction coefficients ($\varepsilon * 10^3$ M^{-1} cm^{-1}). [a]Data from Shklover *et al.*[33] [b]Emission spectra of $3*10^{-5}$ M^{-1} cm^{-1} solutions were recorded at 25 °C. Table from Lense *et al.*[23]

The ^1H NMR spectra of $[Ru(L_1^{OH})_2(NCS)_2]$, $[Ru(L_2^{OH})_2(NCS)_2]$ and $[Ru(L_3^{OH})_2(NCS)_2]$ similarly display six peaks in the aromatic region, indicative of *cis*-bipyridyl coordination, as well as two, four and six peaks in the alkyl region for $[Ru(L_1^{OH})_2(NCS)_2]$, $[Ru(L_2^{OH})_2(NCS)_2]$ and $[Ru(L_3^{OH})_2(NCS)_2]$, respectively, that correspond to the protons of the methylene spacers protons and a broad peak above 12 ppm due to the carboxylic acid proton. However, the ^1H NMR spectra of these complexes also show a second set of six peaks in the aromatic region that integrate ~10% compared to the main set of aromatic peaks. These indicate a ~10-20% impurity depending on whether the peaks are part of a set of 12 impurity peaks, with the remaining impurity peaks under the main aromatic peaks. This impurity was not separable using chromatography or recrystallization procedures. A likely explanation for this impurity is the NCS linkage isomer, which has been observed in the N3 dye and other analogues.[11,38] However, since the elemental analysis obtained did not match the calculated values (though this could be due to a decarboxylation reaction during

the elemental analysis measurements), this hypothesis could not be proved. In the ^{13}C NMR spectra of these complexes the thiocyanate carbon appears at 133.96, 133.15 and 133.06 ppm for $[Ru(L_1^{OH})_2(NCS)_2]$, $[Ru(L_2^{OH})_2(NCS)_2]$ and $[Ru(L_3^{OH})_2(NCS)_2]$, respectively, consistent with an N-bound isothiocyanate for the major component.[33] The impurity peaks were not large enough to be detected by ^{13}C NMR spectroscopy.

The IR spectra of these complexes contain ν(CN) stretches at 2102.1, 2107.3 and 2107.8 cm^{-1} for $[Ru(L_1^{OH})_2(NCS)_2]$, $[Ru(L_2^{OH})_2(NCS)_2]$ and $[Ru(L_3^{OH})_2(NCS)_2]$, respectively, compared with 2125.6 cm^{-1} for the N3 dye,[9] which can be explained by the more electron rich RuL_2 fragment in the modified dyes participating in less π backbonding than in the more charge-delocalized N3 RuL_2 fragment. ν(CO) stretching appears at 1725.3, 1712.4 and 1707.2 cm^{-1} for $[Ru(L_1^{OH})_2(NCS)_2]$, $[Ru(L_2^{OH})_2(NCS)_2]$ and $[Ru(L_3^{OH})_2(NCS)_2]$, compared with 1720.1 cm^{-1} for the N3 dye.[9]

The UV-visible absorption spectra of the modified carboxylic acid derivatives are all blue-shifted with respect to the N3 dye[33] but very similar with respect to each other and to those of the methyl ester derivatives. Interestingly, the extincition coefficients for the modified dyes are all smaller for the MLCT transitions and larger for the π-π^* transitions, indicating decreased metal-ligand overlap for the modified dyes compared to the N3 dye.[33] As for the methyl ester derivatives, this may be ascribed to decreased π backbonding from the Ru(II) d orbitals to the ligand-based π^* orbital due to the decreased electron delocalization in the modified ligands. The λ_{max} and extinction coefficient values are listed in Table 2-2.

Complex	MLCT	MLCT	π-π*
N3[1]	542 (1.32)	400 (1.30)	318 (4.57)
$[Ru(L_1^{OH})_2(NCS)_2]$	515 (0.94)	360 (1.07)	300 (4.99)
$[Ru(L_2^{OH})_2(NCS)_2]$	515 (0.92)	360 (1.1)	300 (5.3)
$[Ru(L_3^{OH})_2(NCS)_2]$	515 (1.03)	360 (1.21)	300 (5.67)

Table 2-2. UV-visible absorption data for *cis*-$[Ru(L_2)(NCS)_2]$ complexes, where L = 4,4'-substituted bipyridine. Wavelengths are reported in nm and the values in parentheses are molar extinction coefficients ($\varepsilon * 10^4$ M^{-1} cm^{-1}). Spectra were recorded in DMSO. [1]Data from Shklover *et al.*[33]

III. Electrochemistry

Cyclic voltammetry of $[Ru(L_1^{OMe})_2(NCS)_2]$ and $[Ru(L_2^{OMe})_2(NCS)_2]$, performed in DMF and reported vs. Fc/Fc^+, show quasi-reversible events centered at 0.18 V and 0.23 V for $[Ru(L_2^{OMe})_2(NCS)_2]$ and $[Ru(L_1^{OMe})_2(NCS)_2]$, respectively, which are assigned to the Ru(II/III) couple (Fig. 2-2). Neither the one electron oxidation of $[Ru(L_1^{OMe})_2(NCS)_2]$ nor of $[Ru(L_2^{OMe})_2(NCS)_2]$ is completely reversible at scan rates ranging from 50 mV s^{-1} - 250 mV s^{-1}. However, the oxidation of $[Ru(L_2^{OMe})_2(NCS)_2]$ appears to be more reversible than that of $[Ru(L_1^{OMe})_2(NCS)_2]$; that is, the ΔE_p value (0.077 V) and the i_{pr}/i_{pf} ratio (0.95) recorded for $[Ru(L_2^{OMe})_2(NCS)_2]$ are closer to the ideal values of ΔE_p (0.059 V) and i_{pr}/i_{pf} (1.0) expected for a reversible process.[39] Additionally, the ratio of $i_{pf}/\nu^{1/2}$ for $[Ru(L_2^{OMe})_2(NCS)_2]$ varies only slightly with increasing scan rate. These results differ from the Ru(II/III) oxidation reported for $[Ru(L_0^{OEt})_2(NCS)_2]$ (E_p^{ox} = 0.56 mV vs. Fc/Fc^+ at 100 mV s^{-1}) in DMF, which was found to be chemically irreversible at all scan rates up to 10,000 mV s^{-1}.[40] The greater reversibility observed for $[Ru(L_2^{OMe})_2(NCS)_2]$ and $[Ru(L_1^{OMe})_2(NCS)_2]$ may be due to the fact that these complexes are oxidized at a lower potential than $[Ru(L_0^{OEt})_2(NCS)_2]$, making it less thermodynamically favorable for the oxidized Ru(III)

centers to oxidize the coordinated isothiocyanate ligands.

Two quasi-reversible ligand reduction events centered at -1.985 and -2.236 V (vs. Fc/Fc^{+}) were observed for $[Ru(L_2^{OMe})_2(NCS)_2]$ and three irreversible ligand reduction events were observed for $[Ru(L_1^{OMe})_2(NCS)_2]$ at -2.065, -2.128, and -2.529 V. The cyclic voltammograms of $[Ru(L_1^{OMe})_2(NCS)_2]$ and $[Ru(L_2^{OMe})_2(NCS)_2]$ are displayed in Fig. 2-2. Wolfbauer *et al.* reported observing four reduction processes for $[Ru(L_0^{OEt})_2(NCS)_2]$,[41] the first two of which, at -1.480 mV and -1.697 mV (vs. Fc/Fc^{+}), were chemically and electrochemically reversible.[41] It is possible that additional ligand reduction events occur for $[Ru(L_1^{OMe})_2(NCS)_2]$ and $[Ru(L_2^{OMe})_2(NCS)_2]$, but that they occur at potentials too negative to be observed in the DMF solvent window.

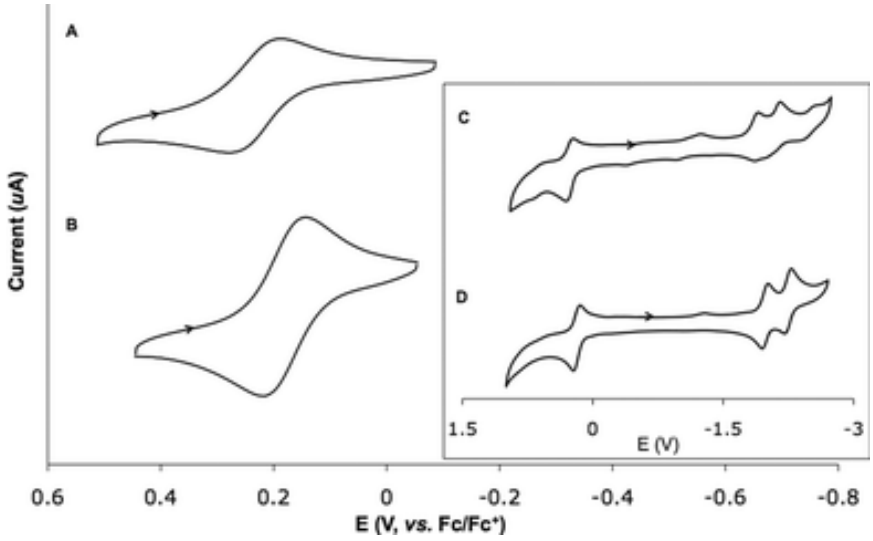

Figure 2-2. Cyclic voltammograms (vs. Fc/Fc^{+}) of the one electron oxidation of (A) $[Ru(L_1^{OMe})_2(NCS)_2]$ and (B) $[Ru(L_2^{OMe})_2(NCS)_2]$ and (inset) complete voltammograms of (C) $[Ru(L_1^{OMe})_2(NCS)_2]$ and (D) $[Ru(L_2^{OMe})_2(NCS)_2]$. Scans recorded in DMF (0.2 M n-Bu_4NPF_6) at 100 mV s^{-1} and reported vs. Fc/Fc^{+}. Figure from Lense *et al.*[23]

The degree of reversibility exhibited by complexes of this type is associated with the stability of the reduced form. The decreased stability of the reduced forms of

$[Ru(L_1^{OMe})_2(NCS)_2]$ may result from the presence of the vulnerable methylene group flanked by both the pyridyl and ester groups, which could stabilize either a radical or negative charge at the site, facilitating hydrogen or proton transfer within or between the reduced ligands.

Cyclic voltammetry was also performed on the carboxylic acid derivatives in DMF with 0.1 M $TBAPF_6$ and reported vs. Fc/Fc^+. The $E_{1/2}$ potentials for the Ru(II/III) oxidation (Table 2-3) decrease with linker length, with the largest drop between $[Ru(L_1^{OH})_2(NCS)_2]$ and N3, as would be expected from moving the electron withdrawing carboxylic acid group further from the Ru center. There was little differences between the Ru(II/III) oxidation potentials for $[Ru(L_1^{OH})_2(NCS)_2]$ and $[Ru(L_1^{OMe})_2(NCS)_2]$, and $[Ru(L_2^{OH})_2(NCS)_2]$ and $[Ru(L_2^{OMe})_2(NCS)_2]$, indicating the presence of a carboxylic acid versus a methyl ester functional group has little effect.

Complex	Ru(II/III) $E_{1/2}$ (V)
N3[1]	0.39
$[Ru(L_1^{OH})_2(NCS)_2]$	0.23
$[Ru(L_2^{OH})_2(NCS)_2]$	0.17
$[Ru(L_3^{OH})_2(NCS)_2]$	0.15
$[Ru(L_1^{OMe})_2(NCS)_2]$	0.23
$[Ru(L_2^{OMe})_2(NCS)_2]$	0.18

Table 2-3. Ru(II/III) oxidation potentials of $[Ru(L_n^{OR})_2(NCS)_2]$ (n =1-3, R = H, Me) and the N3 dye. Scans recorded in DMF (0.2 M n-Bu_4NPF_6) at 100 mV s^{-1} and reported vs. Fc/Fc^+.

The Ru(II/III) couple of the N3 dye is irreversible at scan speeds of 50, 100 and 250 mVs^{-1}, with a second event at +0.74V appearing next to the Ru(II/III) event at +0.39 V.[42] Bond *et al.* assign this higher potential peak to a second oxidation event corresponding to the oxidation of dye adsorbed to the electrode.[42] None of the dyes with methylene spacers show this discrete second oxidation event, possibly because the dye adsorbs to the electrode via the carboxylate acid groups,[42] and in the modified dyes the carboxylic acid

groups are further removed from and less strongly electronically coupled to the metal center. Consequently, the oxidation potential of the adsorbed and free dye molecules would not be expected to differ as much for the modified dye as it does for the N3 dye.

The reversibility of the Ru(II/III) couple in the modified dyes also increases with linker length. $[Ru(L_3^{OH})_2(NCS)_2]$'s Ru(II/III) couple fits the reversibility criteria well, with ΔE_p values close to the ideal 0.059 V for a one electron process (0.077 for a scan speed of 0.1 Vs^{-1}), I_c/I_a close to 1.0 (0.99 for a scan speed of 0.1 Vs^{-1}), and $i_p \propto \nu^{1/2}$, where ν = scan speed. The dyes with shorter linker lengths appear progressively less reversible, with the N3 dye being the least reversible (Table 2-4). However, the modified dyes may be adsorbed to the surface via the carboxylic acid groups, with the amount of dye adsorbed to the surface remaining constant throughout the duration of the scan, giving an I_c/I_a very close to 1.0 in the case of $[Ru(L_3^{OH})_2(NCS)_2]$, and a small ΔE_p since the oxidation is no longer diffusion limited.

Complex	ν (mVs^{-1})	ΔE (V)	I_c ($*10^{-5}A$)	I_p ($*10^{-5}A$)	I_c/I_a
N3[1]	50	0.161			
	100	0.170			
	250	0.160			
$[Ru(L_1^{OH})_2(NCS)_2]$	50	0.145	2.64	2.07	1.28
	100	0.126	3.05	2.72	1.12
	250	0.119	4.50	4.41	1.02
$[Ru(L_2^{OH})_2(NCS)_2]$	50	0.073	5.85	5.43	1.08
	100	0.073	8.16	7.59	1.07
	250	0.075	1.27	1.18	1.08
$[Ru(L_3^{OH})_2(NCS)_2]$	50	0.074	1.08	1.08	1.00
	100	0.077	1.50	1.51	0.99
	250	0.082	2.34	2.32	1.01

Table 2-4. Reversibility criteria for the Ru(II/III) oxidation events of $[Ru(L_n^{OH})_2(NCS)_2]$ (n=1-3) and the N3 dye. Scans recorded in DMF (0.2 M n-Bu_4NPF_6) at 100 mV s^{-1} and reported vs. Fc/Fc^+. [1]Data from Bond *et al.*[42]

The ligand-based reduction events were also studied for the carboxylic acid derivatives. Wolfbauer *et al.* had previously examined the ligand-base reduction of the N3 dye, since the carboxylic acid groups that anchor N3 to TiO_2 can participate in acid-base reactions that can significantly alter the electronic properties of the dcbpy ligand.[43] The reduction of $[Ru(bpy)_3]^{2+}$ (bpy = 2,2'-bipyridine) and related complexes usually involves a series of reversible one-electron ligand-based charge transfer processes. The ethyl ester analogue of N3, $[Ru(L_0^{OEt})_2(NCS)_2]$, exhibits two chemically and electrochemically reversible reduction events in DMF with half-wave potentials ($E^r_{1/2}$) of -1.48 and -1.70 V vs. Fc/Fc^+ at room temperature at platinum and glassy carbon electrodes.[41] In contrast, only the first of the N3 dye's two ligand reduction events is chemically reversible; the second is only partially reversible. Wolfbauer *et al.* suggest that this is because in the first step, one of the bipyridyl ligands is reduced, whereas in the second step, the second pyridyl ligand is reduced, followed by loss of the protons as H_2 gas.[43]

The $E_{1/2}$ potentials for ligand reduction of the modified dies is more negative than that of the N3 dye, as would be expected. Interestingly, the $E_{1/2}$ potential then becomes less negative as the linker length increases (Table 2-5). $[Ru(L_3^{OH})_2(NCS)_2]$ exhibits two ligand reduction events that appear pseudo-reversible at slower scan speeds (50 and 100 mV/s), and less so at a faster scan speed (250 mV/s). As with the Ru(II/III) couple, the redox events become progressively less reversible as the linker length decreases (Table 2-5). The greater degree of irreversibility for the $[Ru(L_1^{OH})_2(NCS)_2]$ ligand reduction events may be because of instability due to the vulnerable single methylene spacer, similar to $[Ru(L_1^{OMe})_2(NCS)_2]$.

Complexes	Ligand Reduction Potentials (V)	ΔE (V) (1st event, 2nd event)	I_c/I_a (1st event, 2nd event)
N3[1]	-1.525, -1.742	0.062, 0.07	1.08, 1.6
$[Ru(L_1^{OH})_2(NCS)_2]$	-2.266, -2.5595	0.155, 0.112	N/C
$[Ru(L_2^{OH})_2(NCS)_2]$	-2.1474, -2.3958	0.096, 0.11	N/C
$[Ru(L_3^{OH})_2(NCS)_2]$	-2.1245, -2.387	0.082, 0.09	0.96, N/C
$[Ru(L_1^{OMe})_2(NCS)_2]$	-2.065, -2.128, -2.529	0.161, 0.176, 0.174	N/C
$[Ru(L_2^{OMe})_2(NCS)_2]$	-1.985, -2.236	0.068, 0.079	0.87, 0.88

Table 2-5. Ligand reduction potentials of $[Ru(L_n^{OR})_2(NCS)_2]$ (n =1-3, R = H, Me) complexes and the N3 dye. Scans recorded in DMF (0.2 M n-Bu_4NPF_6) at 100 mV s^{-1} and reported vs. Fc/Fc^+. [1]Data from Wolfbauer *et al.*[43] N/C = not calculable.

IV. Structural Characterization

X-ray quality crystals of $[Ru(L_2^{OMe})_2(NCS)_2]$ were obtained by diffusing ether into an acetonitrile solution of the complex. The structure of $[Ru(L_2^{OMe})_2(NCS)_2]$ is shown in Fig. 2-3 and is one of the few examples of a structurally characterized *cis*-$[Ru(L)_2(X)_2]$ (where L = 4,4'-disubstitued-2,2'-bipyridyl and X = monodentate, anionic ligands) type complex.[33,44-48] As can be seen in Fig. 2-3, there is a large amount of static disorder amongst the bipyridyl substituents, particularly the methyl ester atoms. Consequently, the higher angle data collection was limited, and the reflection count was only 83.7% complete. Attempts to model the disorder did not improve the structure.

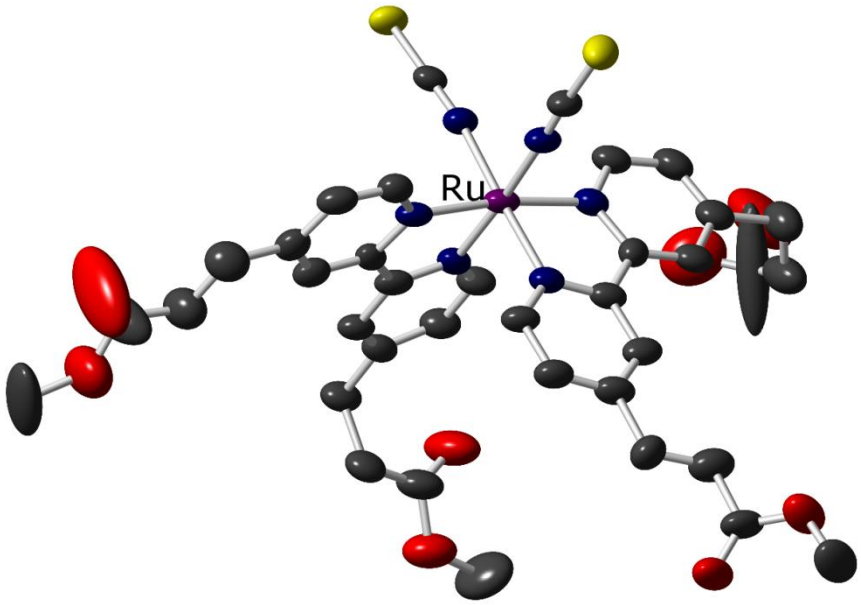

Figure 2-3. Thermal ellipsoid diagram of $[Ru(L_2^{OMe})_2(NCS)_2]$. Ellipsoids are drawn at 25 % probability and hydrogen atoms have been omitted for clarity. Oxygen is shown in red, carbon in gray, nitrogen in blue and sulfur in yellow.

The structure of $[Ru(L_2^{OMe})_2(NCS)_2]$ displays a distorted octahedral coordination environment about the Ru(II) center, which is similar to the previously reported ethyl ester analogue of the N3 dye, $[Ru(L_0^{OEt})_2(NCS)_2]$,[33] and the homologous complex containing unsubstituted 2,2'-bipyridyl ligands, $[Ru(2,2'\text{-bpy})_2(NCS)_2]$.[33,49] Both $Ru(2,2'\text{-bpy})_2(NCS)_2]\bullet CH_3CN$ and $[Ru(L_0^{OEt})_2(NCS)_2]\bullet CH_3CN$ display crystallographic C_2-symmetry. Each structure in this series displays a distorted octahedral coordination environment around the ruthenium center. The bond lengths and angles observed in the structure of $[Ru(L_2^{OMe})_2(NCS)_2]$ are quite similar to those found in both $Ru(2,2'\text{-bpy})_2(NCS)_2$ and $[Ru(L_0^{OEt})_2(NCS)_2]$ (Table 2-2). The small structural differences displayed by this series of compounds suggest that the basic ligand set enforces a rather rigid coordination geometry that is not strongly influenced by the 4,4'-bipyridyl substituents.

	1	**2**	**3**	**4**
Bond lengths/ Å				
Ru-N(NCS)	2.07(2)	2.049(6) 2.045(6)	2.053 2.059	2.054
Ru-N(L)$_{cis}$ [a]	2.01(1)	2.027(7) 2.062(6)	2.055 2.059	2.051
Ru-N(L)$_{trans}$ [a]	2.04(2)	2.042(6) 2.026(6)	2.025 2.038	2.041
N(NCS)-C(NCS)	1.13(3)	1.164(8) 1.156(8)	1.140 1.151	1.124
C(NCS)-S(NCS)	1.62(2)	1.617(7) 1.643(8)	1.631 1.626	1.655
Bond angles/°				
N(NCS)-Ru-N(NCS)'	86(1)	90.2(2)	91.30	88.71
N(L)$_{trans}$-Ru-N(L)$_{cis}$ [a] (same ligand)	78.353	79.0(3) 78.6(3)	79.27 79.14	78.68
N(L)$_{trans}$-Ru-N(L)$_{cis}$ [a] (different ligand)	96.372	95.5 95.3	97.93 96.76	96.35
N(L)$_{trans}$-Ru-N(L)$_{trans}$ [a]	95(1)	91.2(2)	91.91	90.71
N(L)$_{cis}$-Ru-N(L)$_{cis}$ [a]	172(1)	171.8(2)	175.04	173.01

Table 2-6. Selected bond lengths (Å) and angles (°) for [Ru(L_0^{OEt})$_2$(NCS)$_2$]•CH_3CN (1),[33] [Ru(L_2^{OMe})$_2$(NCS)$_2$] (2),[23] Ru(2,2'-bpy)$_2$(NCS)$_2$]•DMSO (3),[49] and Ru(2,2'-bpy)$_2$(NCS)$_2$]•CH_3CN (4).[49] [a]The N(L)*cis* and N(L)*trans* notation is used to refer to the nitrogen ligands of the bipyridyl ligands that are *cis* and *trans* to the coordinated NCS ligands.

V. TiO_2 Film Sensitization and Electron Injection Dynamics

The electron injection dynamics and yields for nanostructured TiO_2 films sensitized with the N3 dye, [Ru(L_1^{OH})$_2$(NCS)$_2$], [Ru(L_2^{OH})$_2$(NCS)$_2$] and [Ru(L_3^{OH})$_2$(NCS)$_2$] were also investigated. The TiO_2 films were sensitized by placing them in ethanol solutions of the dyes (~ 1 mg dye/mL EtOH) overnight. The amount of dye adsorbed to the TiO_2 was quantified using UV-visible absorption spectroscopy.

The TiO_2 film sensitized with [Ru(L_1^{OH})$_2$(NCS)$_2$] was also investigated by ATR-FTIR

spectroscopy. ATR-FTIR spectroscopy is a useful technique for probing the binding of photosensitizers to nanostructured thin films since the ν(CO) stretching frequency will shift upon deprotonation and upon adsorption to TiO_2.[50,51] For the $[Ru(L_1^{OH})_2(NCS)_2]$ film, ν(NCS) can be seen clearly, and there are two bands of greater intensity that can be assigned to ν(CO) stretches, possibly one bound and one not bound to the TiO_2, but the poor signal to noise ratio does not make a definitive assignment possible (Figure 2-4).

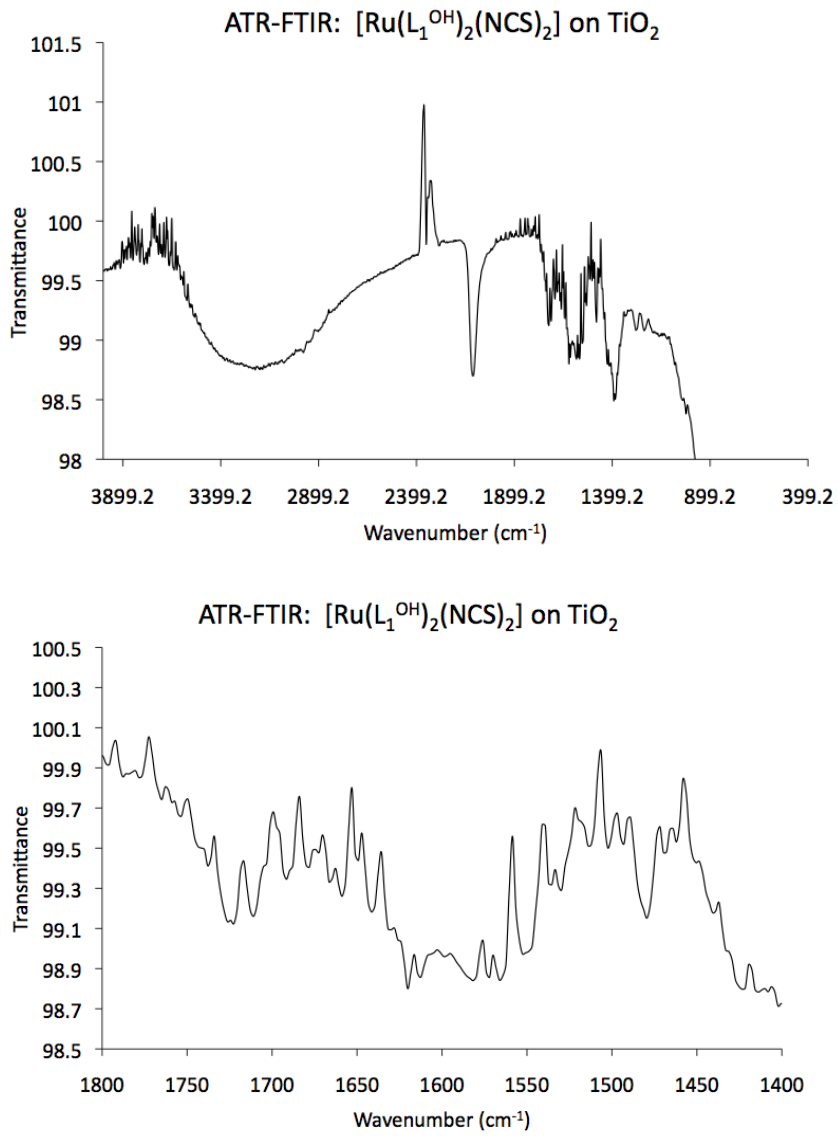

Figure 2-4. ATR-FTIR spectrum of nanostructured TiO_2 thin films sensitized with $[Ru(L_1^{OH})_2(NCS)_2]$. The top figure is the full spectrum, and the bottom is the region from 1800-1400 cm^{-1}.

Transient absorption spectroscopy was utilized to probe the electron transfer dynamics and quantum yields to TiO_2. The samples were pumped with pulses of 400 nm or 500 nm radiation and probed in the mid-IR region. The signals were all adjusted with

respect to the O.D. of the sensitized films at the wavelength at which measurements were performed, so that the signals from different films could be compared.

Interestingly, the dyes with the methylene spacers all have smaller injection yields (and hence signals) for electron injection to the TiO_2 (Figure 2-5). This may be due to several factors: Firstly, the methylene spacers likely decrease the electronic coupling between the excited photosensitizers and TiO_2, which would decrease the rate of forward electron injection and allow other processes, such as excited state decay, to become competitive. Secondly, the methylene spacers will allow for increased flexibility, particularly at longer chain lengths, which could allow for the bipyridyl groups to directly contact the TiO_2 surface and increase the rate of back electron transfer from the TiO_2 to the oxidized dye. If the dye sits perpendicular to the TiO_2 surface, back electron transfer requires transfer from the TiO_2 conduction band to the d orbital localized on the Ru(III), which overlap poorly.[52] However, if the dye can lie against the semiconductor, the electronic overlap between the TiO_2 conduction band and Ru(III) d orbital may be increased. Thirdly, modifications to the dyes may result in instabilities that can lead to decomposition of the dyes. Decomposition of the dye may also provide another pathway for excited state decay. Fourthly, modifications to the dyes may influence the potential of the TiO_2 conduction band, decreasing the driving force for electron injection and allowing other excited state decay mechanisms to become more competitive. The first and fourth factors may explain the trend N3 > $[Ru(L_2^{OH})_2(NCS)_2]$ > $[Ru(L_3^{OH})_2(NCS)_2]$ with respect to quantum yield. The quantum yield of $[Ru(L_1^{OH})_2(NCS)_2]$ is higher than that of $[Ru(L_2^{OH})_2(NCS)_2]$ in data measured at 400 nm but lower in data measured at 500 nm. A lower quantum yield for $[Ru(L_1^{OH})_2(NCS)_2]$ may be due to the instability of this particular dye discussed earlier, but more electron injection measurements would need to be run to meaningfully compare the quantum yields for $[Ru(L_1^{OH})_2(NCS)_2]$

and $[Ru(L_2^{OH})_2(NCS)_2]$.

The factors leading to the decreased quantum yields may be better understood by looking at the kinetics for electron injection to the TiO_2. For example, if poorer electronic overlap between the ligand-based excited state and TiO_2 conduction band due to the insulating methylene spacers is the case, the rate constants would be expected to be smaller, and transfer from the relaxed ^{3}MLCT excited state may dominate that from the high-energy excited ^{1}MLCT excited state, since intersystem crossing would be expected to be faster with respect to electron injection to the conduction band. Alternatively, if the flexible methylene spacers allow the dye to flop onto the semiconductor surface, the rate constants observed may be fast, but the quantum yield still small due to back electron transfer.

Asbury *et al.* previously measured electron injection from N3 to TiO_2 in samples pumped at 400 nm by measuring the transient mid-IR signal (1700-2400 cm^{-1}), and fit the rise time of the mid-IR signal using a biexponential rise function with rates 50±25 fs (>84%) and 1.7±0.5 ps (<16%), after deconvolution of the instrument response function, which they determined in a thin silicon wafer to be a Gaussian function with a full width at half maximum (FWHM) to be 0.19 ps. The data in this thesis was fit using Global fitting software.[53] The instrument response function was not determined independently for the experiments performed in this thesis so the FWHM was set at 0.2 ps. The data was fit using the equation

$$y = A_1(1-e^{-k1x}) + A_2(1-e^{-k2x}) \quad (1)$$

Additionally, the data was truncated at 200 ps, since the signal in some films began to decay at later times. The parameters obtained are listed in Table 2-4.

These results indicate the rates of both injection components progressively decrease as the linker length increases in $[Ru(L_0^{OH})_2(NCS)_2]$ (N3), $[Ru(L_1^{OH})_2(NCS)_2]$ and $[Ru(L_2^{OH})_2(NCS)_2]$. Thus, the lower quantum yields may be due to decreased electron injection rates, likely due to decreased electronic coupling between the between the photoexcited dyes and semiconductor, which allow competing exciting state decay processes to become more competitive. Interestingly, the electron injection rates for the $[Ru(L_1^{OH})_2(NCS)_2]$-sensitized film is calculated to be faster than the rates for the $[Ru(L_2^{OH})_2(NCS)_2]$-sensitized film, even though the injection yields are similar (400 nm) or greater (500 nm) for the $[Ru(L_2^{OH})_2(NCS)_2]$-sensitized film. This may be due to the particular instability of the for the $[Ru(L_1^{OH})_2(NCS)_2]$ dye, which could lead to decomposition of the TiO_2-adsorbed due upon irradiation, and which could also lead to additional excited state decay mechanisms involving chemical decomposition of the dye. $[Ru(L_3^{OH})_2(NCS)_2]$ was calculated to have a very fast injection component (k_1) though it had the lowest injection yield. This may be because at longer linker lengths the dye can flop over onto the TiO_2 surface, resulting in both fast forward electron transfer and recombination, or because of error due to the low signal measured for the $[Ru(L_3^{OH})_2(NCS)_2]$-sensitized film. Normalized electron injection data, which facilitates a visual comparison of the rates, is shown in Fig. 2-6.

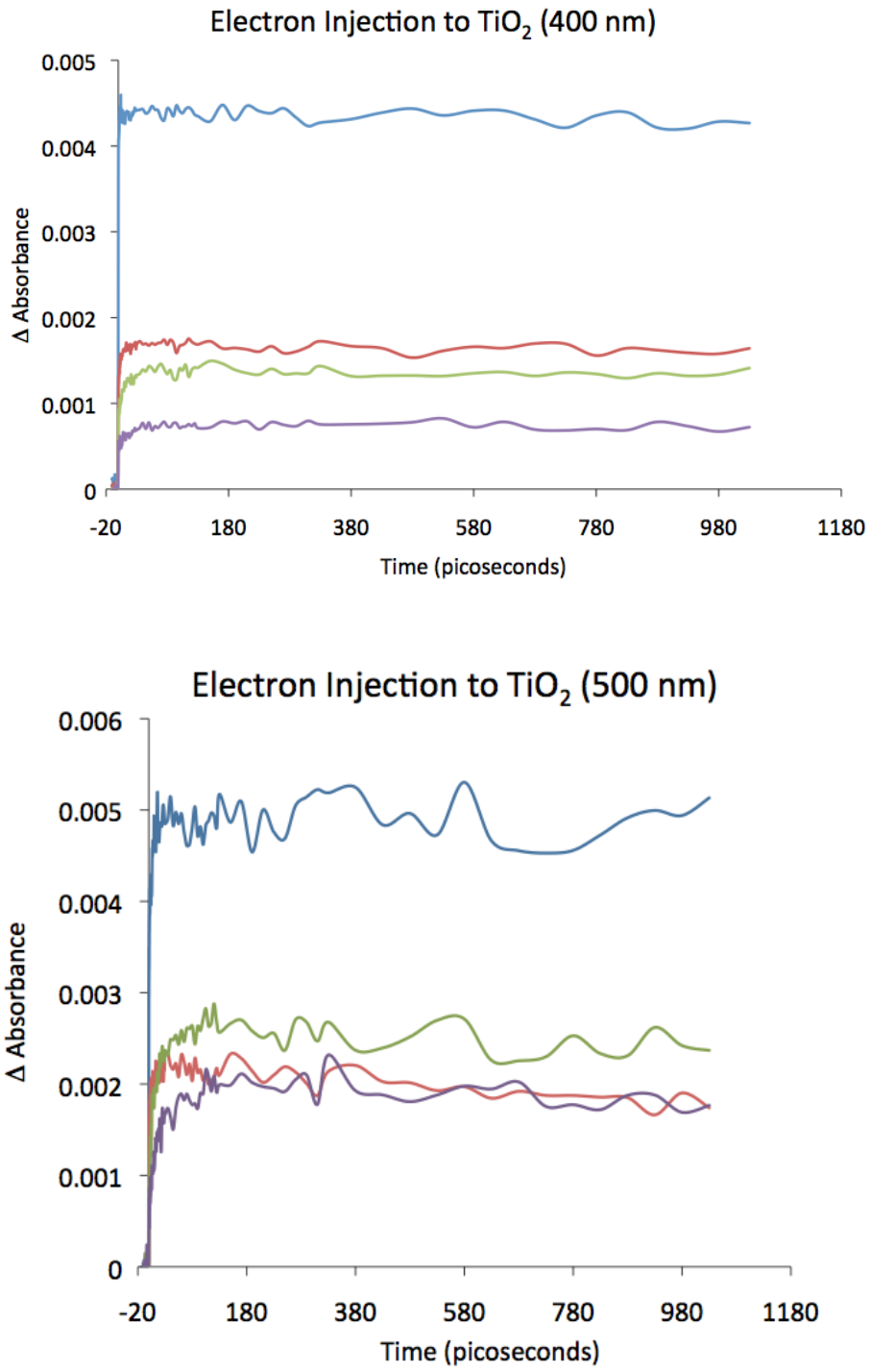

Figure 2-5. Electron injection to TiO_2 for the N3 dye (—), $[Ru(L_1^{OH})_2(NCS)_2]$ (—), $[Ru(L_2^{OH})_2(NCS)_2]$ (—) and $[Ru(L_3^{OH})_2(NCS)_2]$ (—) for dye-sensitized TiO_2 films pumped at 400 nm (top) and 500 nm (bottom).

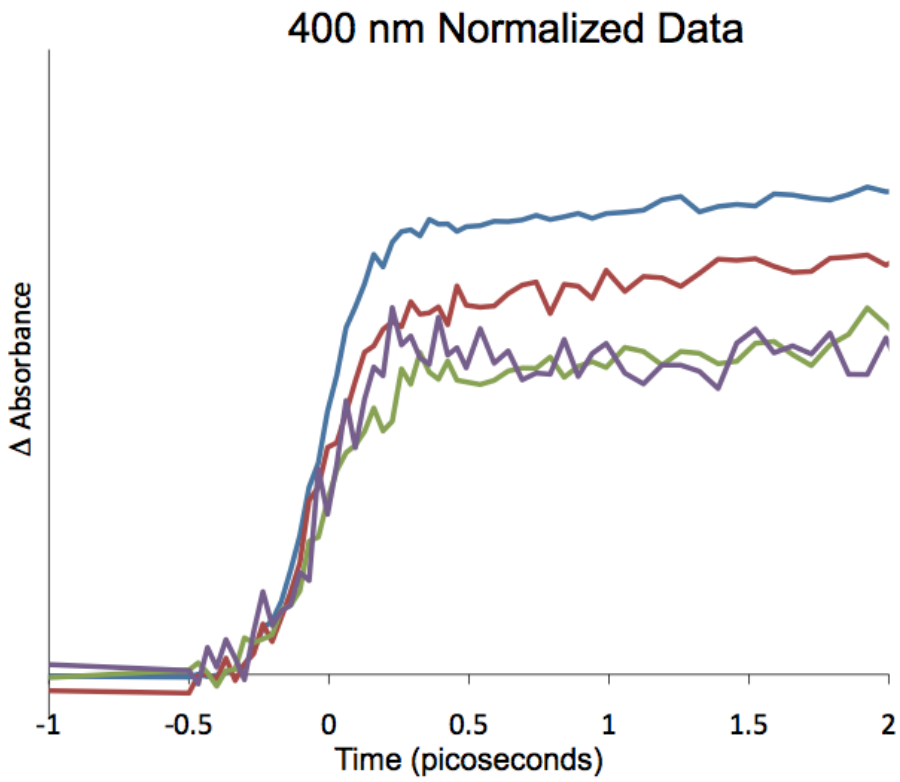

Figure 2-6. Normalized electron injection to TiO_2 for the N3 dye (—), $[Ru(L_1^{OH})_2(NCS)_2]$ (—), $[Ru(L_2^{OH})_2(NCS)_2]$ (—) and $[Ru(L_3^{OH})_2(NCS)_2]$ (—) for dye-sensitized TiO_2 films pumped at 400 nm.

	Complex	N3	N3_1	N3_2	N3_3
400 nm	k_1 (%)	7.95 (88)	6.96 (68)	5.50 (62)	8.43 (66)
	k_2 (%)	0.94 (12)	0.29 (32)	0.09 (38)	0.05 (34)
	$\Delta A(*10^{-3})$	4.27	1.65	1.38	0.748
500 nm	k_1 (%)	7.97 (88)	5.29 (74)	4.82 (36)	16.68 (38)
	k_2 (%)	0.87 (12)	0.24 (26)	0.07 (64)	0.06 (62)
	$\Delta A(*10^{-3})$	5.87	2.15	2.50	1.93

Table 2-7. Electron injection dynamics for electron transfer from the N3, $[Ru(L_1^{OH})_2(NCS)_2]$ (N3_1), $[Ru(L_2^{OH})_2(NCS)_2]$ (N3_2) and $[Ru(L_3^{OH})_2(NCS)_2]$ (N3_3) dyes to TiO_2 on TiO_2 films sensitized with the dyes fit with the equation $y = A_1(1-e^{-k1x}) + A_2(1-e^{-k2x})$. The k values are in units of $(ps)^{-1}$ and $\Delta A = \Delta$ Absorbance. Films were pumped at 400 or 500 nm and probed in the mid-IR region. The FWHM was set at 0.2 ps. The percentage of each component was calculated using the formula $\%(k_1) = A_1/(A_1+A_2)$ and $\%(k_2) = A_2/(A_1+A_2)$.

VI. Conclusions

The complexes $[Ru(L_1^{OMe})_2(NCS)_2]$, $[Ru(L_2^{OMe})_2(NCS)_2]$, $[Ru(L_1^{OH})_2(NCS)_2]$, $[Ru(L_2^{OH})_2(NCS)_2]$ and $[Ru(L_3^{OH})_2(NCS)_2]$ were synthesized and characterized to study the effects of methylene spacers on the spectral, electrochemical, structural, and photophysical properties and electron injection dynamics. The complexes exhibit very similar electronic absorption spectra that are blue shifted with respect to the N3 dye. $[Ru(L_1^{OMe})_2(NCS)_2]$ and $[Ru(L_2^{OMe})_2(NCS)_2]$ displayed quasi-reversible, one-electron oxidation events (Ru(II/III)) and several ligand-based reduction events. For the complexes $[Ru(L_n^{OH})_2(NCS)_2]$, the reversibility of the Ru(II/III) couple increased with increasing linker length, with the couple being most reversible for $[Ru(L_3^{OH})_2(NCS)_2]$ and least reversible for the N3 dye. The complexes with

one methylene spacer, $[Ru(L_1^{OMe})_2(NCS)_2]$ and $[Ru(L_1^{OH})_2(NCS)_2]$, are significantly less stable under reducing conditions than the complexes with two or three methylene spacers.

VII. Experimental Section and Supplementary Material

Ligand and Dye Synthesis

The ligands and their precursors were synthesized following a literature procedure[24] with the following modifications:

2,2'-Bipyridine-4,4'-di(2-ethanoic Acid) (L_1^{OH}). This product was synthesized following the literature procedure.[24] If any monosubstituted product was present, it was found to be easier to remove it by chromatography after converting it to an ester in the next step.

$\delta_H(D_2O, 300\ MHz)/ppm$: 8.47 (d, J = 5.1 Hz, 2H), 7.79 (s, 2H), 7.34 (d, J = 5.1 Hz, 2H), 3.60 (s, 4H)

2,2'-Bipyridine-4,4'-di(methyl ethanoate), (L_1^{OMe}). L^1OH (662 mg, 2.47 mmol) and 10.7 equivalents of $SOCl_2$ were refluxed in 26 mL MeOH under N2 for 16 h. The reaction was then cooled to room temperature and the solvent removed under reduced pressure. The resulting residue was extracted into dichloromethane (200 mL) and washed three times with aqueous saturated $NaHCO_3$ (100 mL each). The organic layer was then dried over Na_2SO_4, filtered and the solvent removed under reduced pressure to yield a cream colored solid. The product was purified by column chromatography using Silica-60, eluting with 66.25% Et_2O, 33.25% pentane and 0.5% Et_3N, by volume. The product eluted at $R_f = 0.14$. Yield = 79%.

IR (KBr) ν_{max}/cm^{-1} 3005.1 w (sp^2 CH), 2953.9 (sp^3 CH), 1742.2 s (CO), 1602.0 m, 1461.0 m, 1430.0 (pyridyl CN, CC).

λ_{max}/nm (DMSO) ($\varepsilon/cm^{-1}\ M^{-1}$): 230.0 (2570); 284.9 (1570).

δ_H($CDCl_3$, 300 MHz)/ppm: 8.64 (d, *J* = 5.1 Hz, 2 H), 8.33 (s, 2 H), 7.27 (dd, *J* = 5.1 Hz, 1.5 Hz, 2 H), 3.74 (s, 4 H), 3.71 (s, 6 H).

δ_C($CDCl_3$, 400 MHz)/ppm: 170.92, 156.50, 149.71, 144.19, 125.01, 122.49, 52.68, 40.91. HRMS-EI *m/z*: M^+ calculated for $C_{16}H_{16}N_2O_4$ 300.1188; found 300.1185.

Dimethyl 2,2"-Bipyridine-4,4'-di(3-propanoate) (L_2^{OMe}). Beginning with 1.9 g of the olefin precursor, the literature procedure was followed until the purification step. The crude product was chromatographed on Si-60 with 0.5% triethylamine in Et_2O. The product eluted at R_f = 0.38. Yield 1.2 g, 51%.

δ_H($CDCl_3$, 300 MHz)/ppm: 8.59 (d, J = 4.8 Hz, 2H), 8.30 (d, 2H), 7.20 (dd, 4.8 Hz, 1.2 Hz, 2H), 3.69 (s, 6H), 3.06 (t, J = 7.8 Hz, 4H), 2.74 (t, J = 7.8 Hz, 4H) ppm

2,2'-Bipyridine-4,4'-di(3-propanoic Acid) (L_2^{OH}). Following hydrolysis and an ethyl acetate wash, as described in the literature, [24] the reaction was neutralized, at which time the product precipitated as a white solid. The product was washed with additional water and ethyl acetate, and the dried under vacuum overnight, giving the pure product. Yield = 80%.

δ_H(D_2O, 300 MHz)/ppm: 8.46 (d, J = 5.4 Hz, 2H), 7.86 (s, 2H), 7.35 (d, J = 4.8 Hz, 2H), 2.97 (t, J = 7.5 Hz), 2.53 (t, J = 7.5 Hz)

Dimethyl 2,2"-Bipyridine-4,4'-di(4-butanoate) (L_3^{OMe}). The literature procedure[24] was followed until the chromatography step; since chromatography on alumina resulted in low yields, the crude product was chromatographed on Si-60 with 0.5% triethylamine in Et_2O. The product eluted at R_f = 0.40, along with a small amount of impurity, so two slower columns were run with 25% pentane in Et_2O to elute the pure product at R_f = 0.19. Yield

= 28%.

δ_H($CDCl_3$, 300 MHz)/ppm: 8.57 (d, J = 4.8 Hz, 2H), 8.24 (d, 2H), 7.15 (dd, J = 5.1 Hz, 1.5 Hz, 2H), 3.67 (s, 6H), 2.75 (t, J = 8.4 Hz, 4H), 2.37 (t, J = 7.5 Hz, 4H), 2.04 (t, J = 7.8 Hz, 4H)

2,2'-Bipyridine-4,4'-di(4-propanoic Acid) (L_3^{OH}). L_3^{OMe} (1.0 g) and aqueous 1 M HCl (50 mL) were heated to 70 °C for 3 hours. The reaction was then cooled to room temperature and washed with ethyl acetate (100 mL x 2). The reaction was neutralized with 10% aqueous NaOH, precipitating the product as a white solid. The product was collected on a frit, washed with additional water and ethyl acetate, and dried under vacuum overnight. Yield = 856.4 mg (93%).

δ_H(D_2O with 1 M NaOH, 300 MHz)/ppm: δ (ppm) = 8.49 (d, J = 5.4 Hz, 2H), 7.88 (s, 2H), 7.38 (d, J = 5.4 Hz, 2H), 2.74 (t, J = 7.5 Hz, 4H), 2.19 (tt, 2H), 1.93 (t, J =7.5 Hz, 2H)

$[Ru(L_1^{OMe})_2(NCS)_2]$. LiCl (1.47 g, 34.96 mmol) was transferred to a 3 neck flask, flame dried under N2, and cooled under vacuum. Under a constant flow of N_2, L_1^{OMe} (700.0mg, 2.33 mmol), $RuCl_3 \cdot xH_2O$ (304.7 mg, 1.166 mmol), hydroquinone (2.57 g, 23.3 mmol), and a 2:1 DME–MeOH solution (69 mL) were added to the flask. The reaction was sparged gently with N_2 and then refluxed for 5 h. The reaction was then cooled to room temperature and the solvent was removed under reduced pressure. The reaction was then extracted into 580 mL dichloromethane and washed (5 x 116 mL) with deionized H_2O. The organic layer was dried over $MgSO_4$, and concentrated using a rotary evaporator. The resulting purple liquid was then added dropwise to Et_2O (~250 mL), giving a purple precipitate that was collected on a fritted glass filter. The solid was further washed with Et_2O and then dried overnight

under vacuum to yield a purple solid. In a 3-necked flask, KNCS (24.84 mmol, 2.417 g) was added to dry MeOH (~250 mL) and the solution sparged with argon for 15 min. The purple solid was then added and the reaction brought to reflux under N_2 for 15 h. The reaction was then cooled to room temperature and the MeOH removed under reduced pressure. The resulting red solid was collected on a fritted glass funnel and washed with deionized H_2O and Et_2O. The dark red solid was then extracted into dichloromethane and filtered through a fritted glass funnel. The dichloromethane was removed using a rotary evaporator, leaving a dark fuchsia solid (759 mg, 79.6% yield).

IR (KBr) ν_{max}/cm^{-1} 2103.2 s (isothiocyanate CN), 1735.7 s (CO), 1617.7 m, 1477.4 m, 1433.7 m (pyridyl CN and CC), 804.5 w (isothiocyanate CS).

UV-vis (DMSO) λ_{max} /nm ($\varepsilon/cm^{-1}\ M^{-1}$): 520.1 (9600); 364.9 (10 500); 299.9 (52 300).

UV-vis (CH_3CN) λ_{max} /nm ($\varepsilon/cm^{-1}\ M^{-1}$): 515 (10 000); 365 (11 000); 295 (54 000).

δH($CDCl_3$, 400 MHz)/ppm: 9.48 (d, J = 5.6 Hz, 2 H), 8.16 (s, 2 H), 8.00 (s, 2 H), 7.56 (d, J = 6.0 Hz, 2 H), 7.44 (d, J = 5.6 Hz, 2 H), 6.97(d, J = 6.0 Hz, 2 H), 3.93 (s, 4 H), 3.85 (s, 6 H), 3.72 (s, 6 H), 3.69 (s, 4 H).

δ_C($CDCl_3$, 400 MHz)/ppm: 170.24, 169.89, 158.81, 157.10, 153.63, 151.63, 143.31, 142.55, 133.81, 127.80, 126.85,123.68, 123.58, 52.94, 52.82, 40.24.

MS (positive ESI): m/z (%) = 818.075 (70, M^+), 787.112 (51, M^+ - OCH_3).

Elemental analysis: calculated for $C_{34}H_{32}N_6O_8RuS_2$: C 49.93, H 3.94, N 10.28. Found C 49.40, H 3.87, N 10.15.

CV (DMF, 298 K *vs.* Fc/Fc+, 0.2 M $TBAPF_6$, glassy carbon w.e.): $E_{1/2}$(Ru(II/III)) = 0.23 V.

$[Ru(L_1^{OMe})_2(NCS)_2]$ is photochemically unstable. Exposure of a solution sample of the complex to direct sunlight for 5 h resulted in ~3% decomposition of the complex (monitored by UV-vis absorption spectroscopy).

$[Ru(L_2^{OMe})_2(NCS)_2]$. LiCl (650.0 mg, 15.3 mmol) was transferred to a 3 neck flask, flame dried under N_2, and cooled under vacuum. Under a constant flow of N_2, L_2^{OMe} (337.9 mg, 1.03 mmol), $RuCl_3 \cdot x$H2O (134.8 mg, 0.51 mmol), and hydroquinone (1.14 g, 10.3 mmol), and a 2:1 DME–MeOH solution (38 mL) were added. The reaction was sparged gently with N_2 and then brought to reflux for 5 h. After cooling to room temperature the solvent was removed under reduced pressure. The reaction was then extracted into 265 mL dichloromethane and washed with (5 x 53 mL) deionized H_2O. The organic layer was dried over $MgSO_4$, and concentrated under reduced pressure. The purple liquid was then dropped into Et_2O (~110 mL), yielding a purple precipitate that was collected on a fritted glass filter and washed with ether and water. The purple solid was further washed with Et_2O and then dried overnight. In a three-necked flask, KNCS (821.5 mg, 8.44 mmol) was dissolved in dry MeOH (~240 mL) and the solution was sparged with argon for 15 min. The purple solid was added to the solution and the reaction brought to reflux under N_2 for 15 h. The reaction was then cooled to room temperature and the MeOH removed under reduced pressure. The red solid that remained was collected on a fritted glass funnel and washed with deionized H_2O and Et_2O. The dark-red solid was then extracted into dichloromethane and filtered through a fritted glass funnel The dichloromethane was removed using a rotary evaporator, leaving a dark fuchsia solid (306.7 mg, 69% yield). X-ray quality crystals were obtained by the slow diffusion of ether into an acetonitrile solution of product.

IR (KBr) ν_{max}/cm^{-1} 2103.4 s (isothiocyanate CN), 1732.6 s (CO), 1616.4 m, 1478.0 m, 1434.8 m (pyridyl CN and CC), 804.2 w (isothiocyanate CS).

UV-vis (DMSO): λ_{max}/nm ($\varepsilon/cm^{-1}\ M^{-1}$): 515 (9300); 365 (10,000); 300 (52,000).

UV-vis (CH_3CN): λ_{max}/nm ($\varepsilon/cm^{-1}\ M^{-1}$): 515 (8800); 360 (9600); 295 (52,000).

δ_H ($CDCl_3$, 400 MHz)/ppm: 9.41 (d, *J* = 5.6 Hz, 2 H), 8.03 (s, 2 H), 7.89 (s, 2 H), 7.46 (d, *J* = 5.6 Hz, 2 H), 7.32 (d, *J* = 5.6 Hz, 2 H), 6.85 (d, *J* = 5.6 Hz, 2 H), 3.78 (s, 6 H), 3.65 (s, 6 H), 3.20 (t, 7.2 Hz, 4 H), 2.95 (t, 7.2 Hz, 4 H), 2.87(t, 7.2 Hz, 4 H), 2.67 (t, 7.2 Hz, 4 H).

δ_C ($CDCl_3$, 400 MHz)/ppm: 172.7, 172.6, 158.8, 157.2, 153.5, 151.4, 150.1, 149.5, 133.6, 126.8,126.0, 123.0, 122.8, 52.3, 52.2, 34.2, 33.9, 30.3, 30.0.

MS (positive ESI): *m*/*z* (%)=874.1397 (100,M^+).

Elemental analysis calculated for $C_{38}H_{40}N_6O_8RuS_2$: C 52.22, H 4.61, N 9.62%. Found C 52.46, H 4.58, N 10.00%.

CV (DMF, 298 K *vs.* Fc/Fc+, 0.2M $TBAPF_6$, glassy carbon w.e.): $E_{1/2}$(Ru(II/III)) = 0.18 V.

Crystal data: $C_{38}H_{40}N_6O_8RuS_2$, M = 873.95 g mol^{-1}, monoclinic, a = 29.507(3), b = 15.487(2), c = 17.678(2) Å, β = 106.297°, V = 7753(6) $Å^3$, T = 173(2) K, space group *C*2/c, Z = 8, m(Cu Kα) = 4.783 mm^{-1}, 15,363 reflections measured, 5353 unique (R_{int} = 0.0459) which were used in all calculations. The final wR (F^2) was 0.1600 (all data). [23]

$[Ru(L_1^{OH})_2(NCS)_2]$. $[Ru(L_1^{OMe})_2(NCS)_2]$ (350 mg, 0.43 mmol), triethylamine (12.4 mL, 125.6 mmol), and KNCS (4.20 g, 43 mmol) were combined in 105 mL deionized H_2O and refluxed under argon in the dark for 14 hours. 1M HCl was added until a red precipitate formed, at ~ pH =3. This precipitate was collected on a frit, washed well with aqueous HCl (pH = 3) and ether, and dried under vacuum overnight, giving a red solid, mass = 278 mg. ^{1}H NMR revealed that the product contained ~10 – 20% impurity (depending on whether or not the impurity contains a second set of pyridyl peaks that overlap with the product peaks and thus cannot be seen. I was unable to remove this impurity either by recrystallization or by reverse phase chromatography. Total yield = 85%.

IR (KBr) ν_{max}/cm^{-1}: 2102.1 s (isothiocyanate CN), 1725.3 s (CO)

UV-vis (DMSO): λ_{max}/nm (ε/cm^{-1} M^{-1}): 504.9 nm ($8.98*10^3$ $M^{-1}cm^{-1}$), 355.0 nm ($1.03*10^4$ M^{-1} cm^{-1}), 300.0 nm ($4.78*10^4$ M^{-1} cm^{-1})

δ_H (DMSO-d_6, 400 MHz)/ppm: Main product: δ (ppm) = 9.17 (d, J = 6.4 Hz, 2H), 8.66 (s, 2H), 8.52 (s, 2H), 7.87 (d, J = 4.8 Hz, 2H), 7.47 (d, J = 6.0 Hz, 2H), 7.19 (J = 4.4 Hz 2H)

δ_C (DMSO-d_6, 400 MHz)/ppm: 171.32, 171.18, 157.96, 156.71, 151.82, 150.97, 144.78, 144.18, 133.32, 128.15, 127.61, 124.60 (seems to be two peaks with the same chemical shift), 39.51 (solvent)

MS (negative ESI): m/z (%) = 761.007 (100, M - 1), 717.018 (17.7, M – 1 – CO_2H), 673.028 (14, M - 1 – $2CO_2H$), 629.038 (40, M - 1 – $3CO_2H$), 585.047 (36, M - 1 – $4CO_2H$)

CV (DMF, 298 K vs. Fc/Fc^+, 0.2 M $TBAPF_6$, glassy carbon w.e.) : $E_{1/2}$ (Ru(II/III)) = 0.23 V

C, H, & N: Elemental analysis calculated for $C_{32}H_{28}N_6O_8RuS_2$: C, 47.30%; H, 3.18%; N, 11.03%. Found: C, 47.66%; H, 2.71%; N, 10.73%.

$[Ru(L_n^{OH})_2(NCS)_2]$. (L_n^{OH}) (4.2 equivalents) and di-μ-chlorobis[(*p*-cymene)chloro-ruthenium(II)] (1.0 equivalents) were heated to 140 °C in dry and argon-degassed DMF for 4h. The reaction was performed under argon and covered in aluminum foil to keep out light. After 4h, NH_4NCS (63.0 equivalents) was added and the reaction was heated at 140 °C for 4 addition hours under argon and in darkness. The next morning, most of the DMF was removed on a rotary evaporator at 50-60 °C. The dark red residue was then suspended in deionized water (1160 mL) and sonicated for 5 minutes. The pH was adjusted to 3 with 0.2 M HNO_3 and the suspension was let stand in the refrigerator overnight. The solid was then collected on a fritted funnel, washed with aqueous HNO_3 (pH = 3) and diethyl ether, and dried overnight, giving a dark red powder.

^{1}H NMR spectroscopy indicated that the powders contained a mixture of bis- and tris-substituted complexes, so purification was performed on LH20 Sephadex. The sample was loaded in methanolic NaOH and the column eluted with MeOH. The tris-substituted complex appeared first as a dark yellow band and the bis-substituted complex appeared second as a dark pink band. Multiple columns were run to completely remove residual tris-substituted complex. The methanol was then removed on a rotary evaporator, and the dark red residue was redissolved in deionized H_2O. The pH was lowered to 3 with 0.05 M HNO_3, precipitating the complex as a very fine red solid. The solid was collected on a fritted funnel, washed with aqueous HNO_3 (pH = 3) and diethyl ether, and dried under vacuum overnight, giving a dark red powder.

$[Ru(L_2^{OH})_2(NCS)_2]$

% Yield: 50.0%

IR (KBr) ν_{max}/cm^{-1}: 2107.3 (isocyanate CN), 1712.4 (CO)

UV-vis (DMSO): λ_{max}/nm ($\varepsilon(* 10^4\ cm^{-1}M^{-1})/cm^{-1}\ M^{-1}$): 514.9, 0.92; 360.0, 1.1; 300.0, 5.3.

δ_H (DMSO-d_6, 300 MHz)/ppm: 12.33 (broad s), 9.09 (d, J = 5.7 Hz, 2H), 8.69 (s, 2H), 8.55 (s, 2H), 7.83 (d, J = 5.4 Hz, 2H), 7.34 (d, J = 5.4 Hz, 2H), 7.14 (d, J = 4.5 Hz, 2H), 3.15 (t, J = 7.8 Hz, 4H), 2.85 (two superimposed triplets, 8H total), 2.65 (t, J = 7.2 Hz, 4H)

δ_C (DMSO-d_6, 400 MHz)/ppm: 173.67, 173.51, 158.20, 156.95 (appears to be two peaks with close chemical shifts), 151.74, 150.93, 150.34, 133.15, 127.08, 126.39, 123.50, 123.40 ppm

MS ((negative ESI): m/z (%) = 817.07 (100, M – 1)

C, H, & N: Analysis calculated for $C_{34}H_{32}N_6O_8RuS_2$: C, 49.93; H, 3.94; N, 10.28. Analysis found (Trial 1): C, 48.34, H, 4.18, N, 10.28. Analysis found (Trial 2): C, 48.54; H, 3.89; N,

10.71.

CV (DMF, 298 K vs. Fc/Fc^+, 0.2 M $TBAPF_6$, glassy carbon w.e.): $E_{1/2}$ (Ru(II/III)) = 0.17 V

$[Ru(L_3^{OH})_2(NCS)_2]$

% Yield = 60.6%.

IR (KBr) ν_{max}/cm^{-1}: 2107.8 (isocyanate CN), 1707.2 (CO)

UV-vis (DMSO): λ_{max}/nm (ε(* 10^4 $cm^{-1}M^{-1}$)/cm^{-1} M^{-1}): 510.1-515.1, 1.03; 359.9, 1.21; 300.1, 5.67.

δ_H (DMSO-d_6, 300 MHz)/ppm: 12. 11 (broad singlet), 9.11 (d, J = 5.7 Hz, 2H), 8.66 (s, 2H), 8.52 (s, 2H), 7.80 (d, J = 6.3 Hz, 2H), 7.39 (d, J = 5.7 Hz, 2H), 7.11 (d, J = 6.3 Hz, 2H), 2.94 (t, J = 7.5 Hz, 4H), 2.68 (t, J = 7.5 Hz, 4H), 2.41 (t, J = 7.5 Hz, 4H), 2.23 (t, J = 7.5 Hz, 4H), 2.06 (tt, J = 7.5 Hz, J = 7.5 H, 4H), 1.83 (tt, J = 7.5 Hz, J = 7.5 Hz, 4H)

MS ((negative ESI): m/z (%) = 873.13 (62, M-1), 688.02 (45), 661.95 (90), 631.97 (100)

CV (DMF, 298 K vs. Fc/Fc^+, 0.2 M $TBAPF_6$, glassy carbon w.e.): $E_{1/2}$ (Ru(II/III)) = 0.15 V

C, H, & N: Analysis calculated for $C_{36}H_{36}N_6O_8RuS_2$: C, 52.22, H, 4.61, N, 9.62. (Trial 1): C, 50.55; H, 4.66; N, 9.66. (Trial 2): C, 51.05; H, 4.49; N, 10.03.

X-Ray Crystallography

A suitable crystal was coated with Paratone N oil, suspended on a small fiber loop and placed in a cooled nitrogen gas stream at 173 K on a Bruker D8 APEX II CCD sealed tube diffractometer with graphite monochromated Cu Kα (λ = 1.54178 Å) radiation. Data were measured using a series of combinations of phi and omega scans with 10 s frame exposures and 0.5° frame widths. Data collection, indexing and initial cell refinements were all carried out using APEX II software.[54] Frame integration and final cell refinements were done using

SAINT software.[55] The final cell parameters were determined from least-squares refinement on 2159 reflections. The structure was solved using direct methods and difference Fourier techniques (SHELXTL, v6.12).[56] Hydrogen atoms were placed their expected chemical positions using the HFIX command and were included in the final cycles of least squares with isotropic U_{ij} values related to the atom ridden upon. All non-hydrogen atoms were refined anisotropically. Scattering factors and anomalous dispersion corrections are taken from the International Tables for X-Ray Crystallography.[57] Structure solution, refinement, graphics and generation of publication materials were performed by using SHELXTL, v6.12 software. [56]

Synthesis and Sensitization of TiO_2 Nanocrystalline Thin Films

The TiO_2 nanocrystalline films were prepared using procedures similar to that described by Zaban *et al.* and Anderson and Lian.[21,58] To sensitize the films, ~ 3 mg of the N3 dye, $[Ru(L_1^{OH})_2(NCS)_2]$, $[Ru(L_2^{OH})_2(NCS)_2]$ or $[Ru(L_3^{OH})_2(NCS)_2]$ were placed in a 20 mL beaker with 3 mL 200 proof EtOH. (The dyes were not able to fully dissolve in the EtOH.) UV-visible absorption spectra were taken of the naked TiO_2 films prior to sensitization. The films were then placed in the beakers overnight, and the beakers covered with parafilm and aluminum foil. After soaking overnight, the films were washed with additional EtOH and blotted gently with a KimWipe™. The UV-visible absorption spectra of the sensitized films were then recorded. The O.D. of a sensitized film at a given wavelength was calculate by subtracting the O.D. of the naked film at that wavelength from that of the sensitized film.

Transient absorptions spectroscopy was utilized to probe the electron transfer dynamics and quantum yields to TiO_2, using the set-up and procedure described in the literature.[59] The samples were pumped with pulses of 400 nm or 500 nm radiation and

probed in the mid-IR region.

Supporting spectral and electrochemical data

L_1^{OMe}

^1H NMR ($CDCl_3$, 300 MHz):

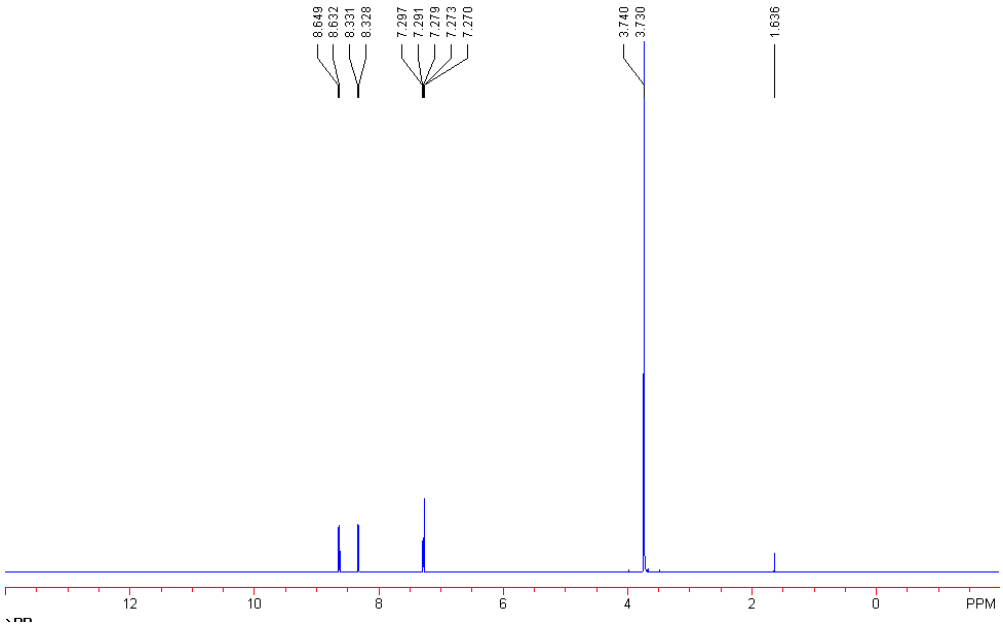

^{13}C NMR ($CDCl_3$, 400 MHz):

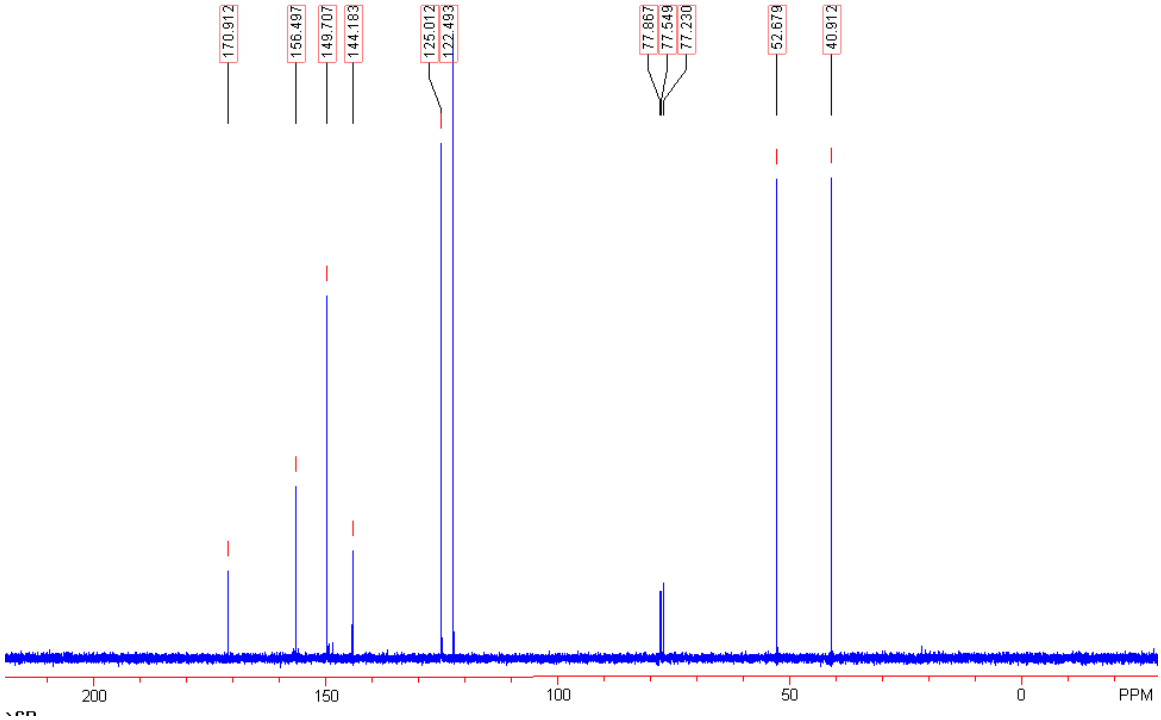

IR (KBr):

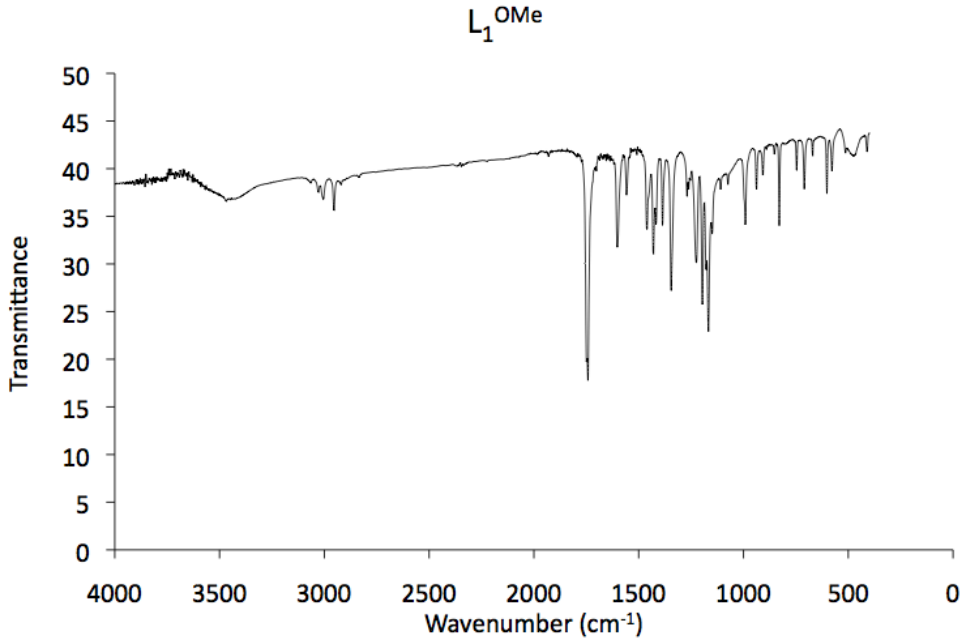

UV-vis (DMSO):

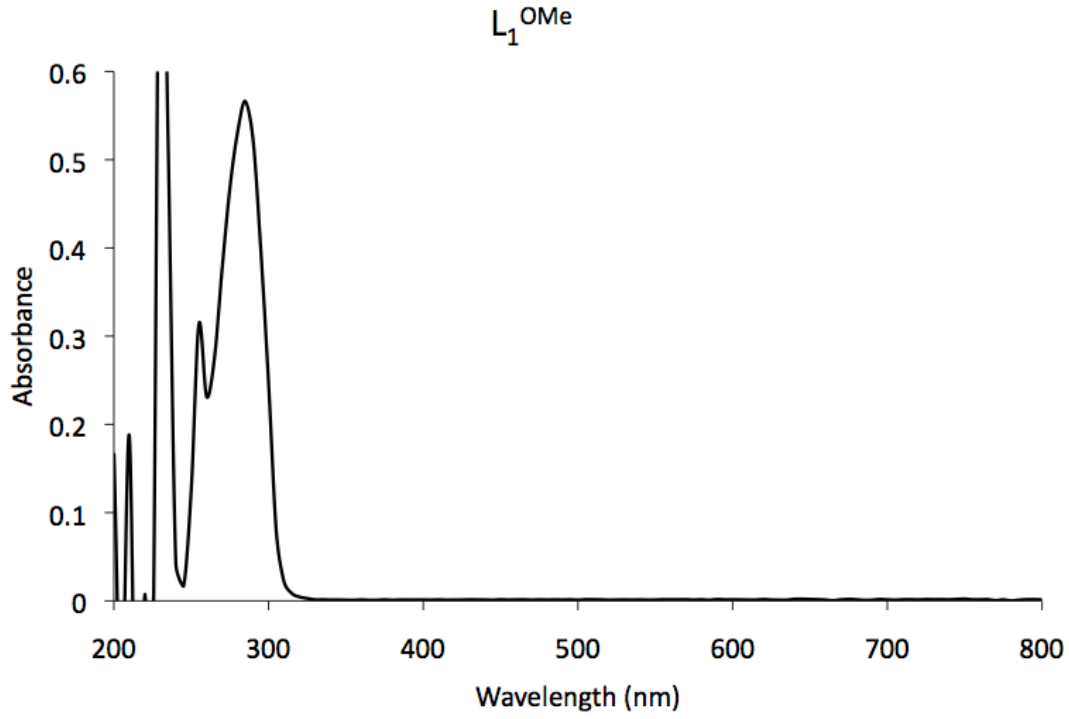

L_2^{OMe}
^1H NMR ($CDCl_3$, 300 MHz):

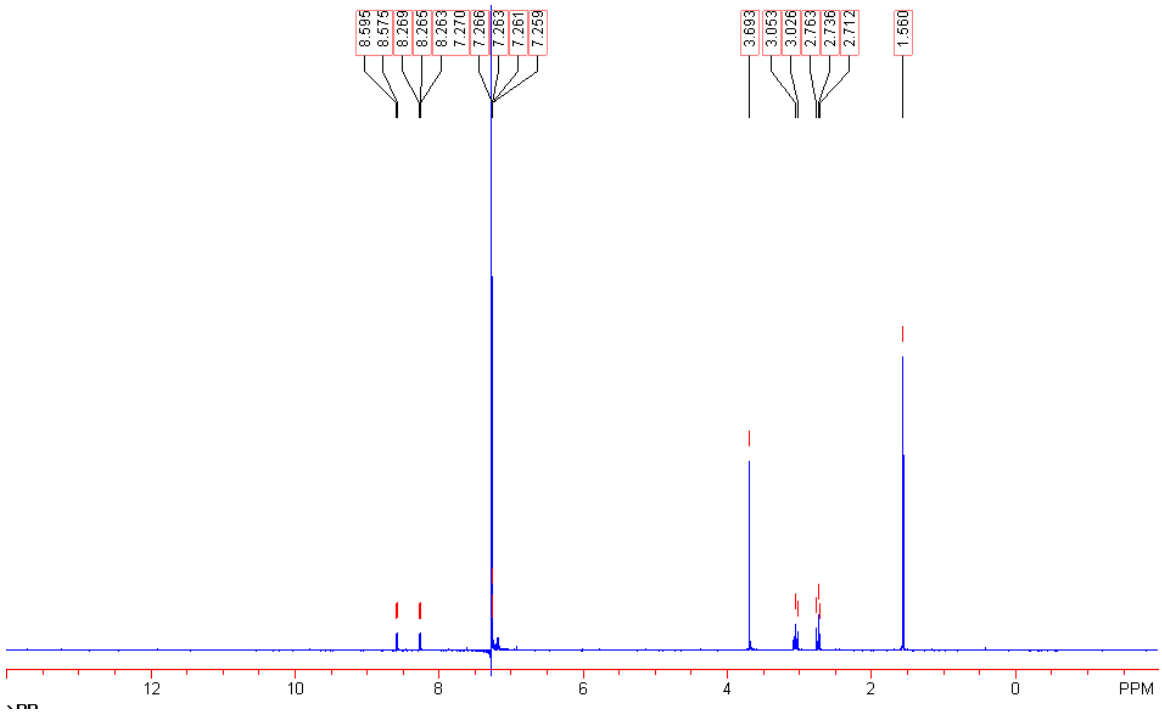

L_3^{OMe}
^1H NMR ($CDCl_3$, 300 MHz):

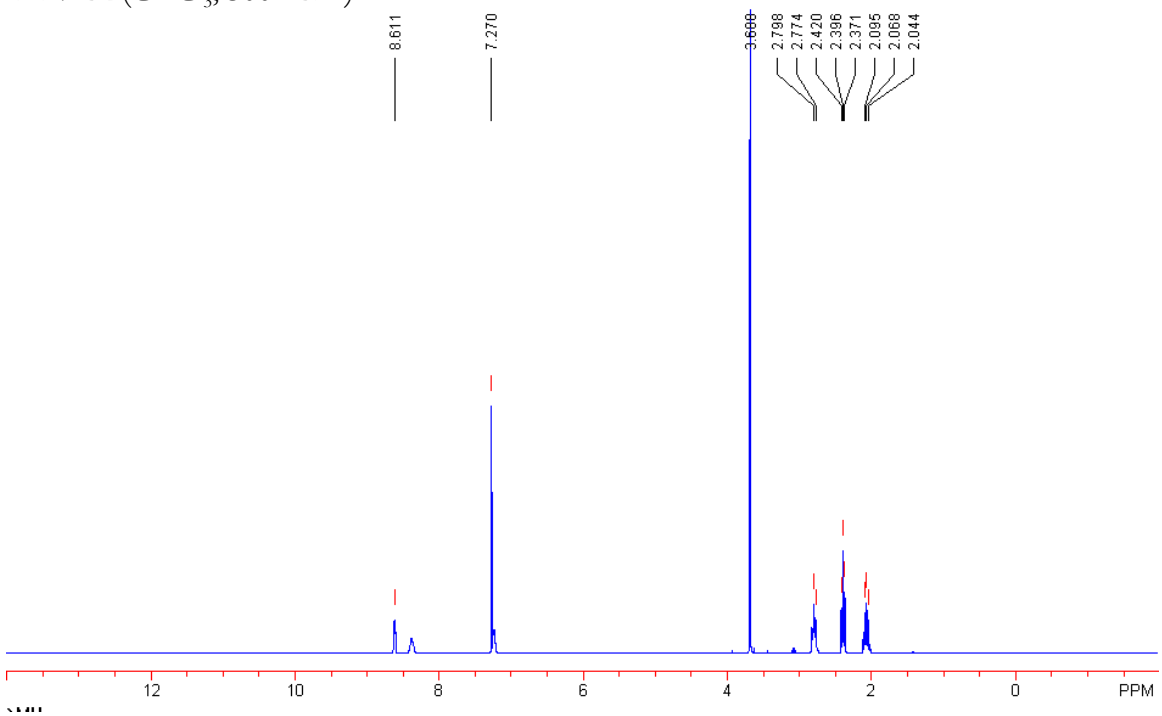

L_3^{OH}

^1H NMR (D_2O with 1 M NaOH, 300 MHz):

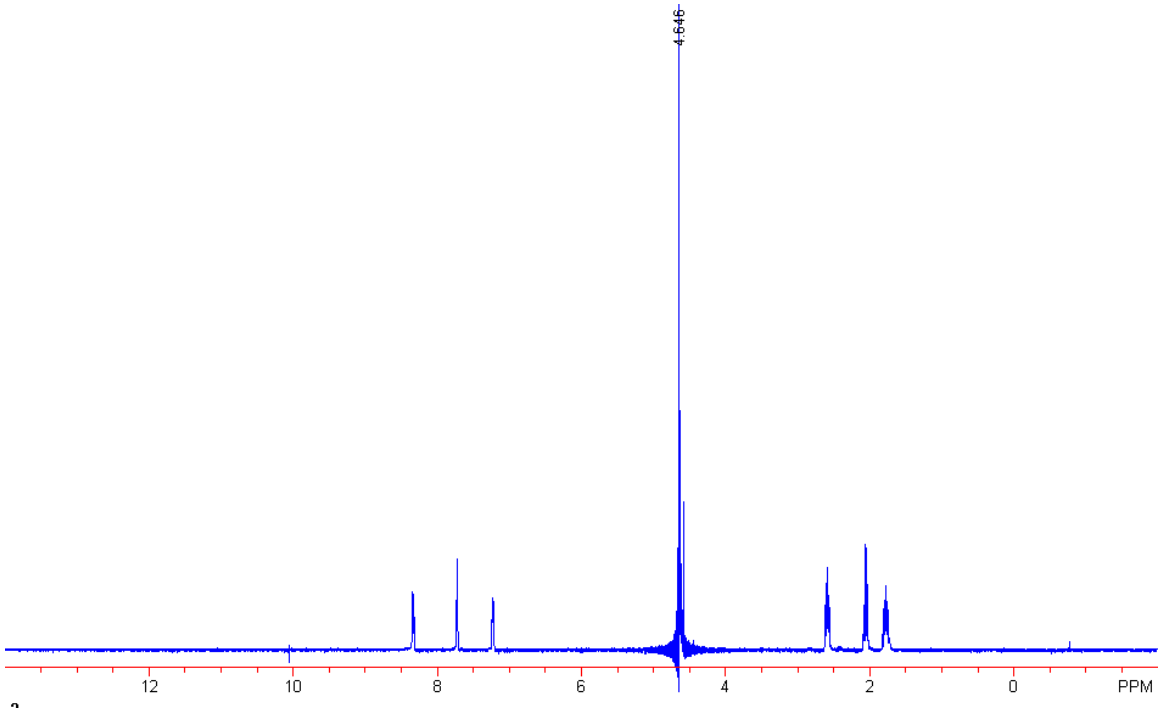

$[Ru(L_1^{OMe})_2(NCS)_2]$

^1H NMR ($CDCl_3$, 400 MHz)

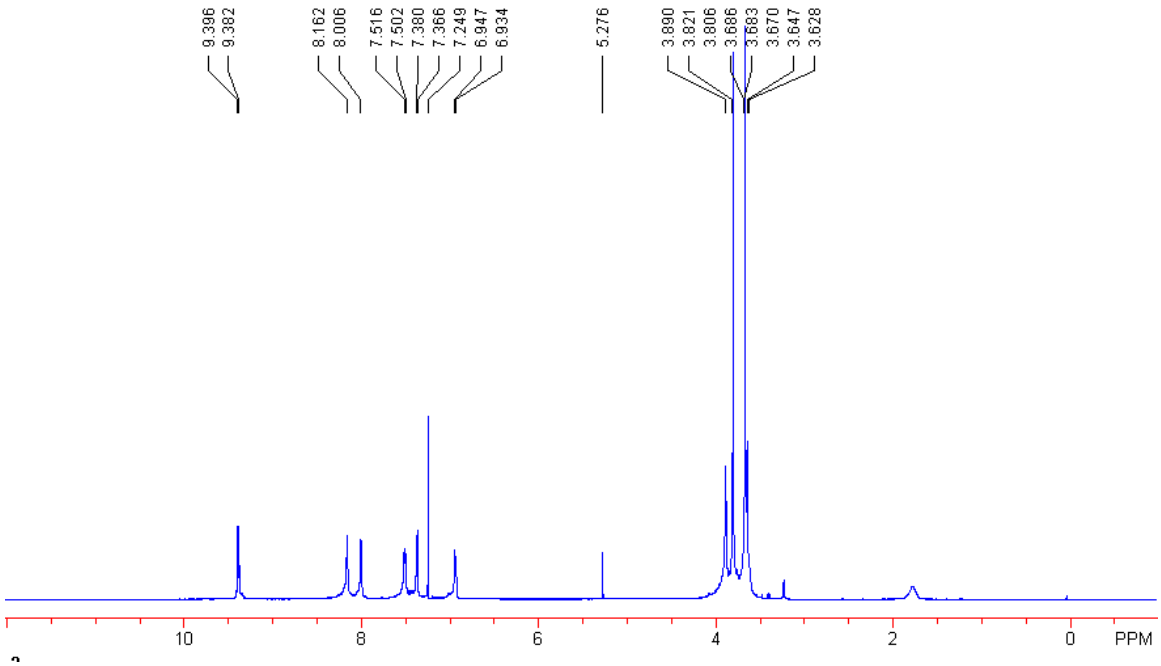

^{13}C NMR ($CDCl_3$, 400 MHz):

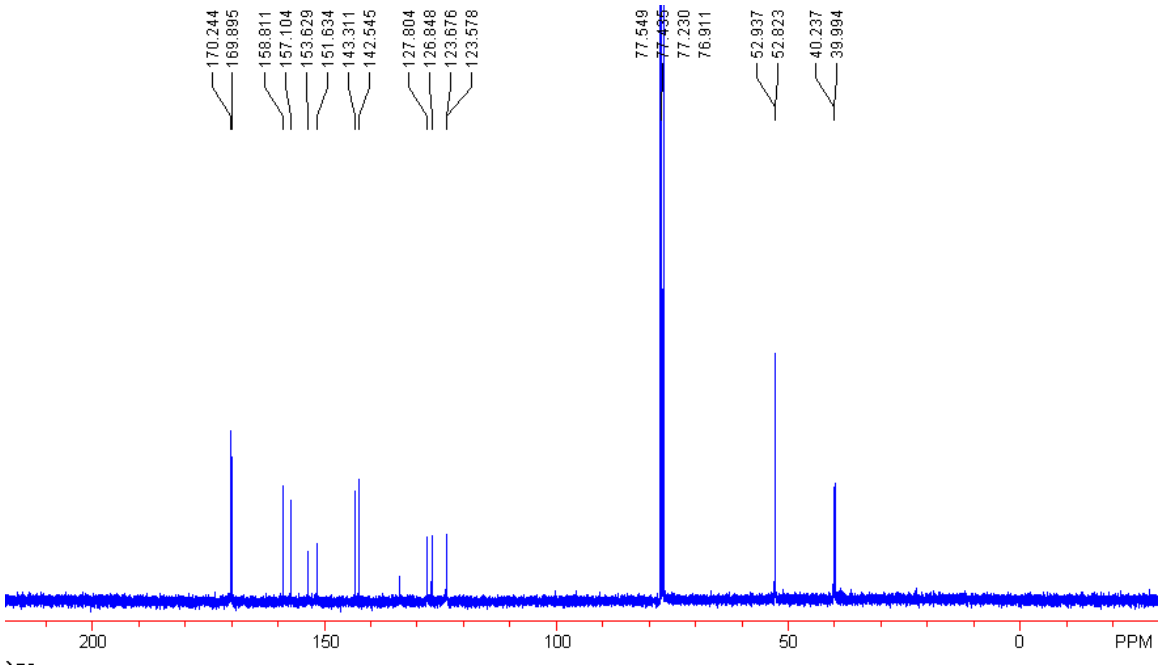

IR (KBr):

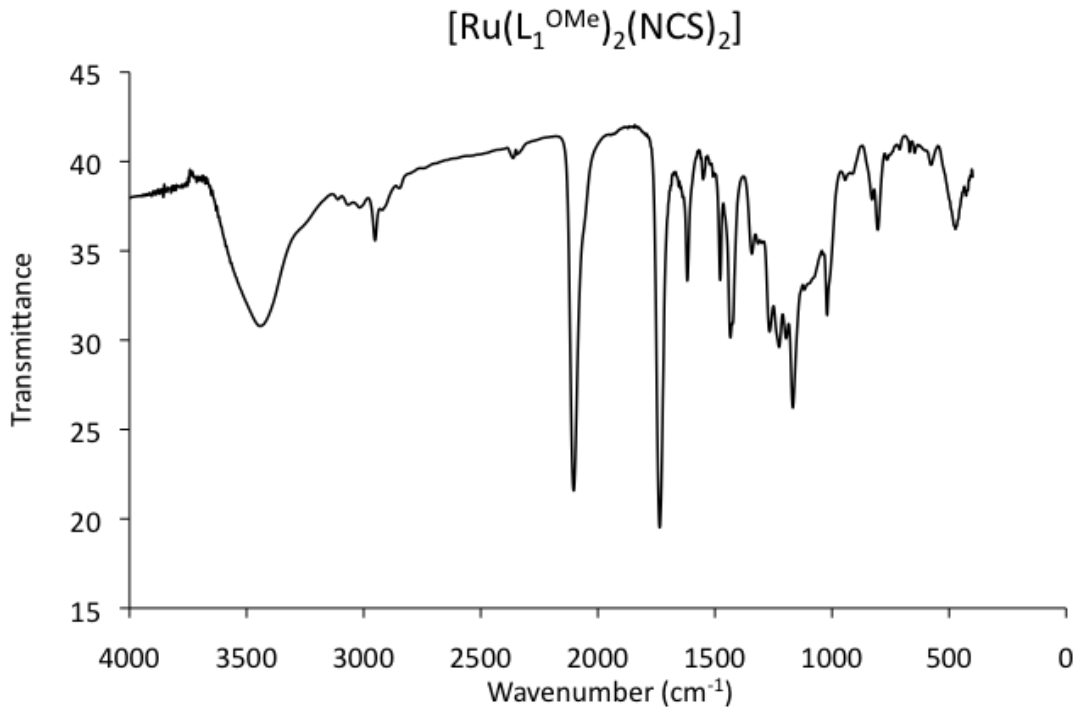

UV-vis (DMSO):

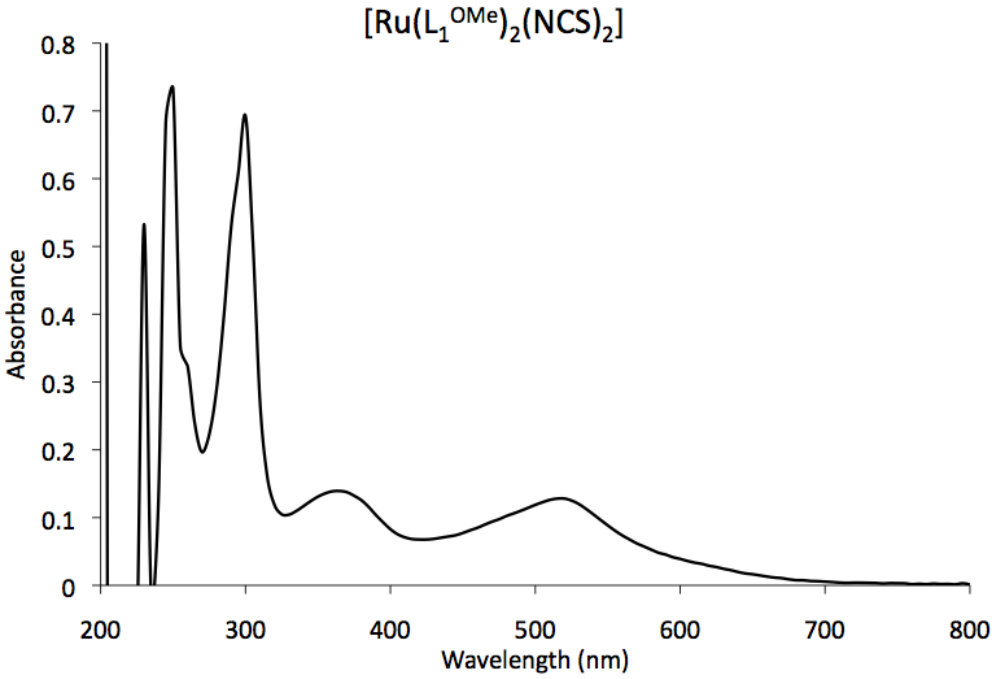

CV (DMF, 298 K *vs.* Fc/Fc+, 0.2 M $TBAPF_6$, glassy carbon w.e.):
Ru(II/III) couple

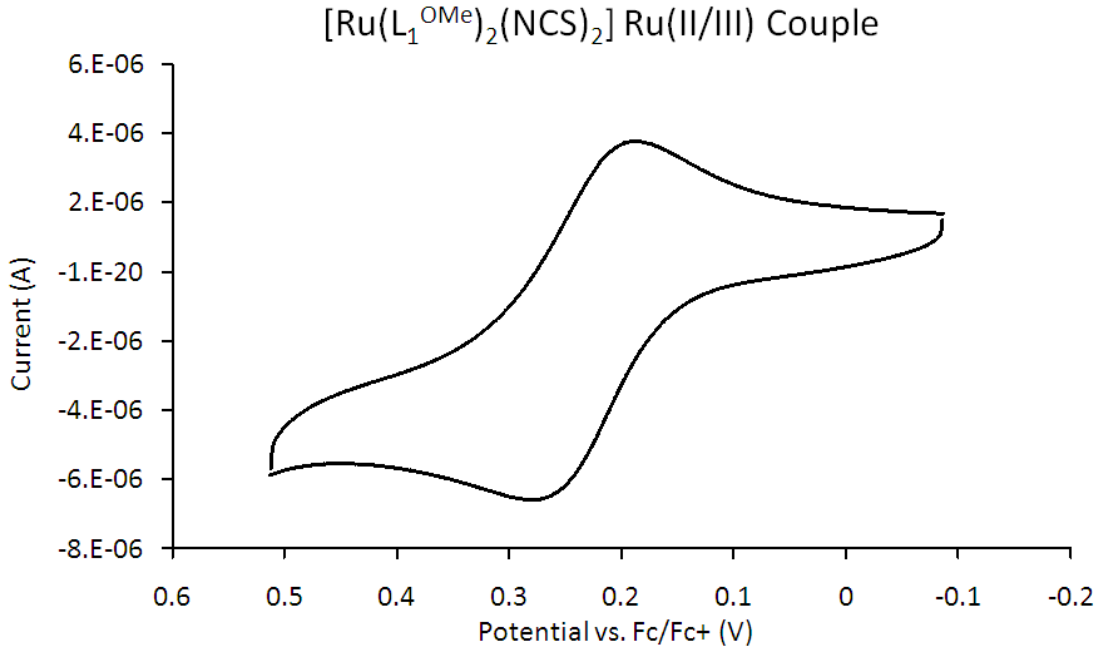

Ligand Reduction

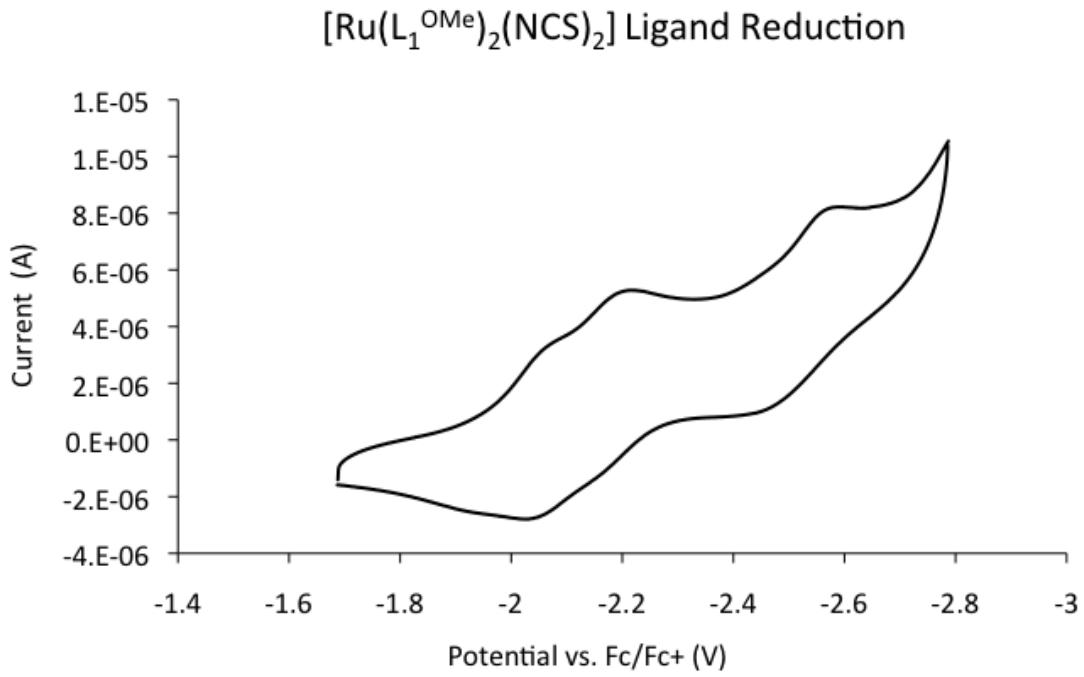

Whole scan

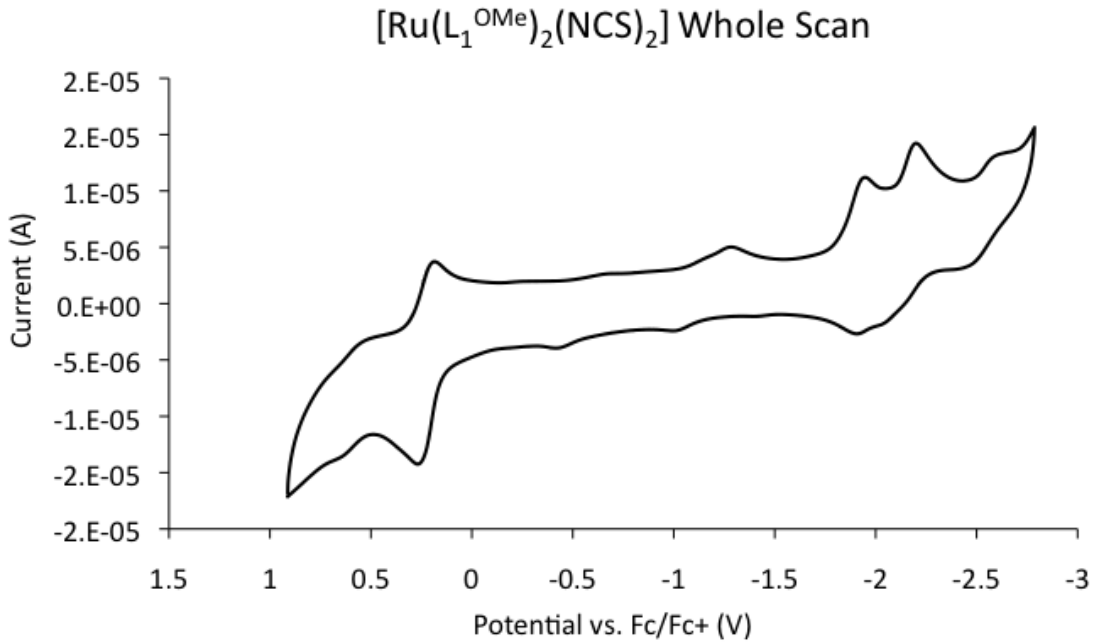

$[Ru(L_2^{OMe})_2(NCS)_2]$

^{1}H NMR ($CDCl_3$, 400 MHz):

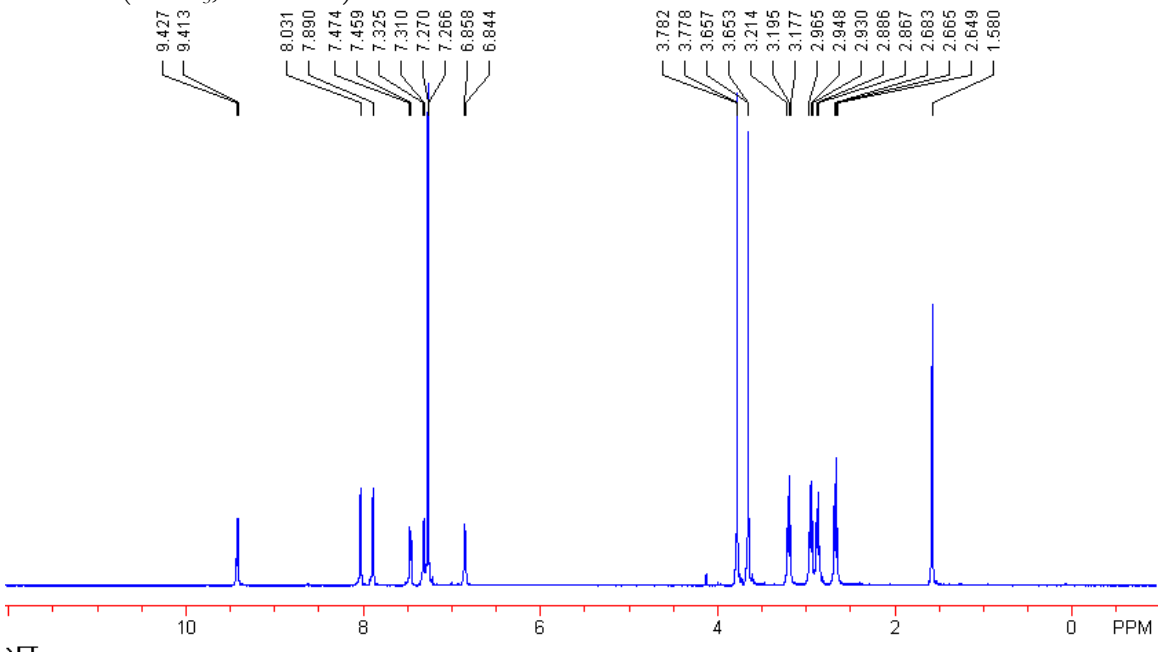

^{13}C NMR ($CDCl_3$, 400 MHz):

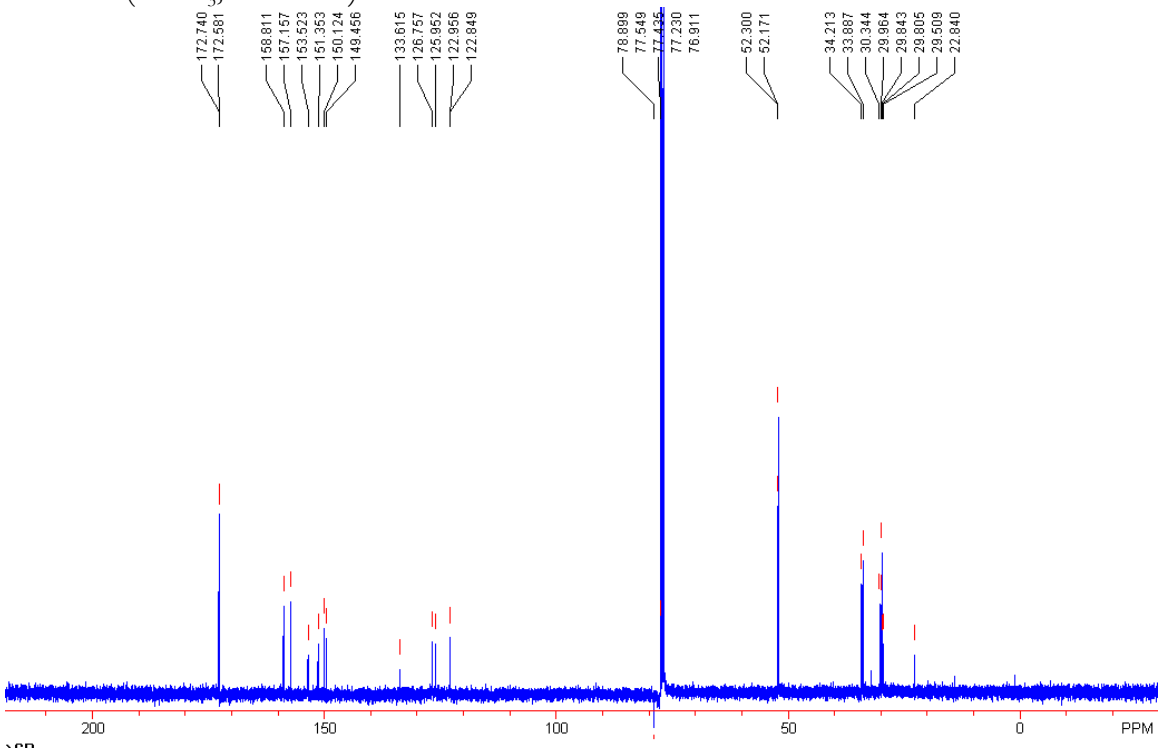

IR (KBr):

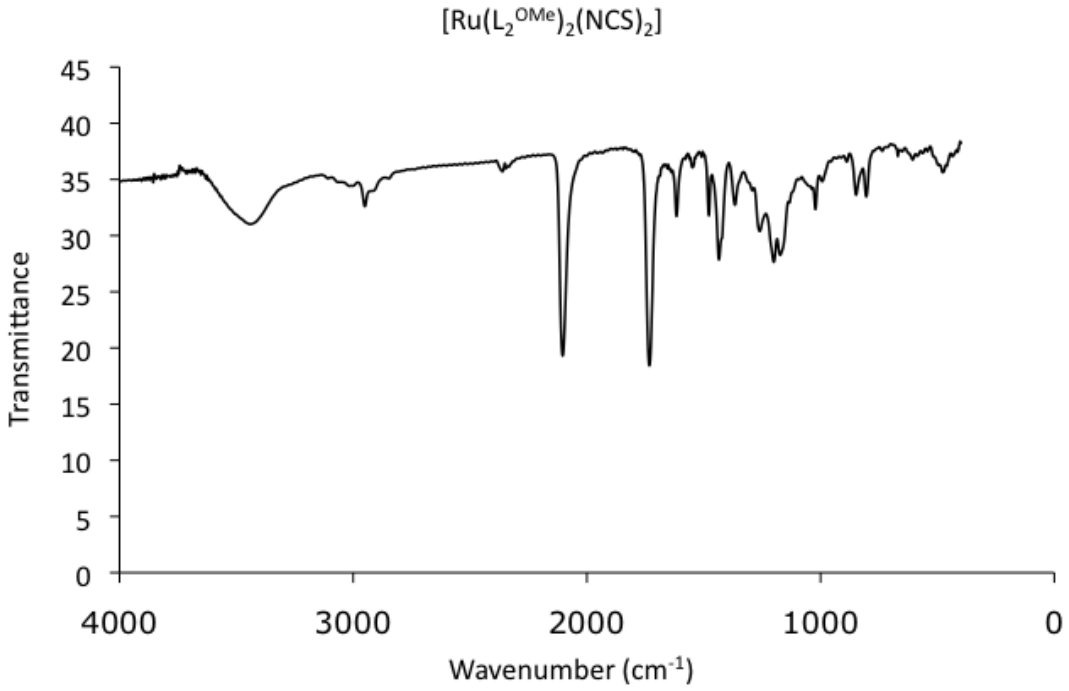

UV-vis (DMSO):

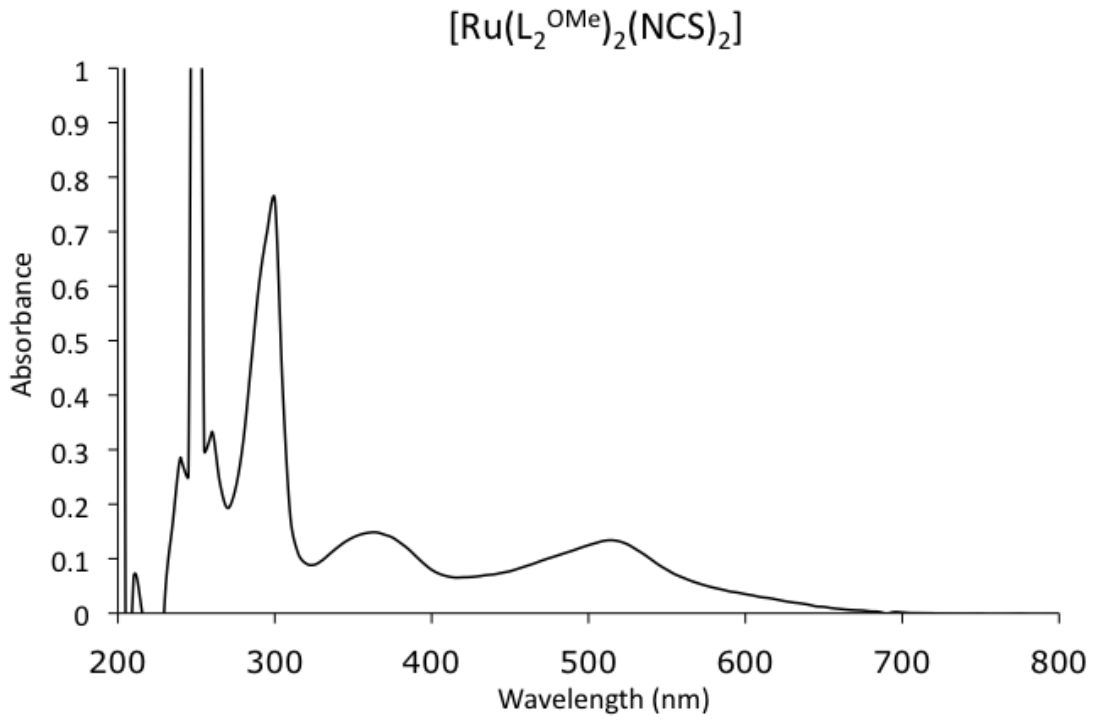

CV (DMF, 298 K *vs.* Fc/Fc+, 0.2 M $TBAPF_6$, glassy carbon w.e.):

Ru(II/III) Couple

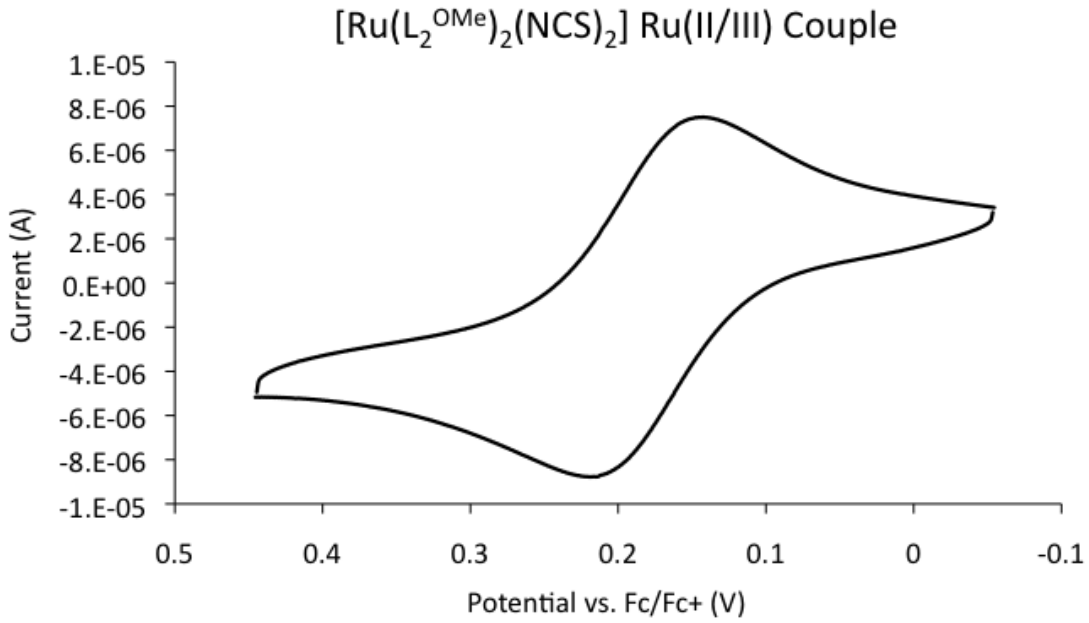

Ligand Reduction

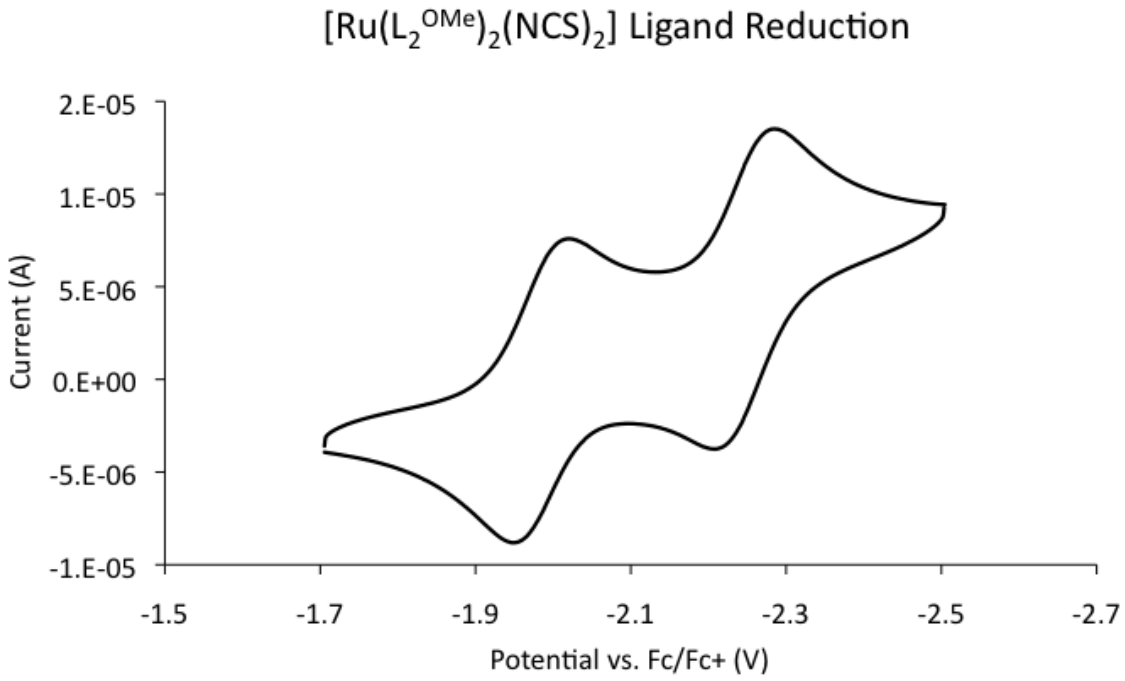

Whole Scan

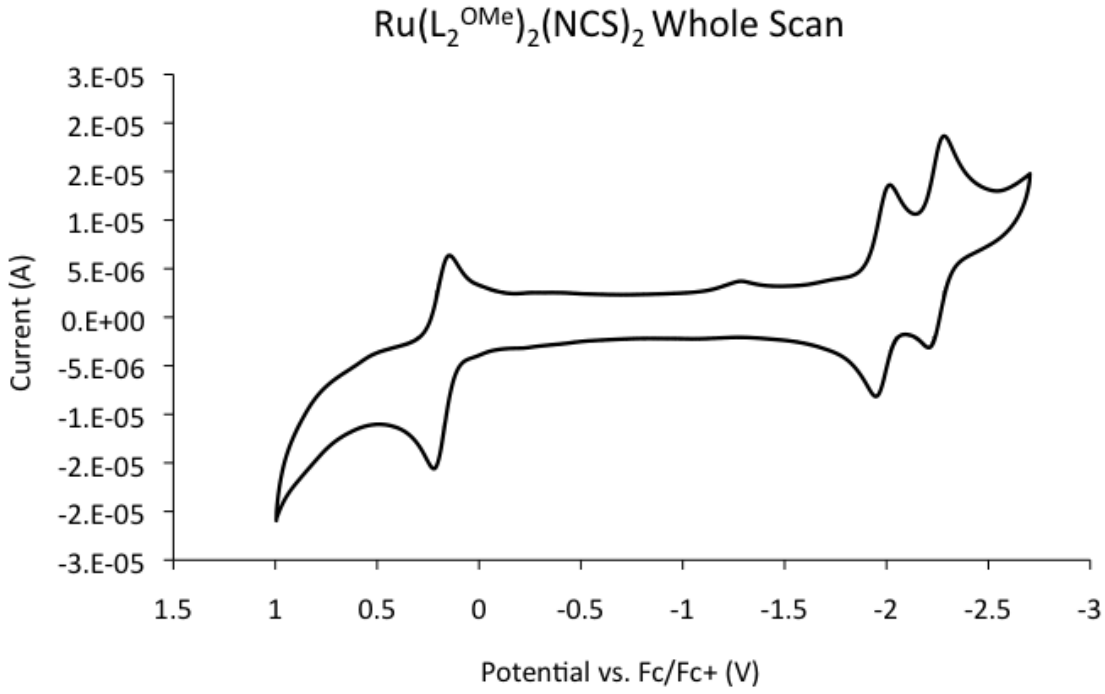

$[Ru(L_1^{OH})_2(NCS)_2]$

^{1}H NMR (DMSO-d_6, 400 MHz):

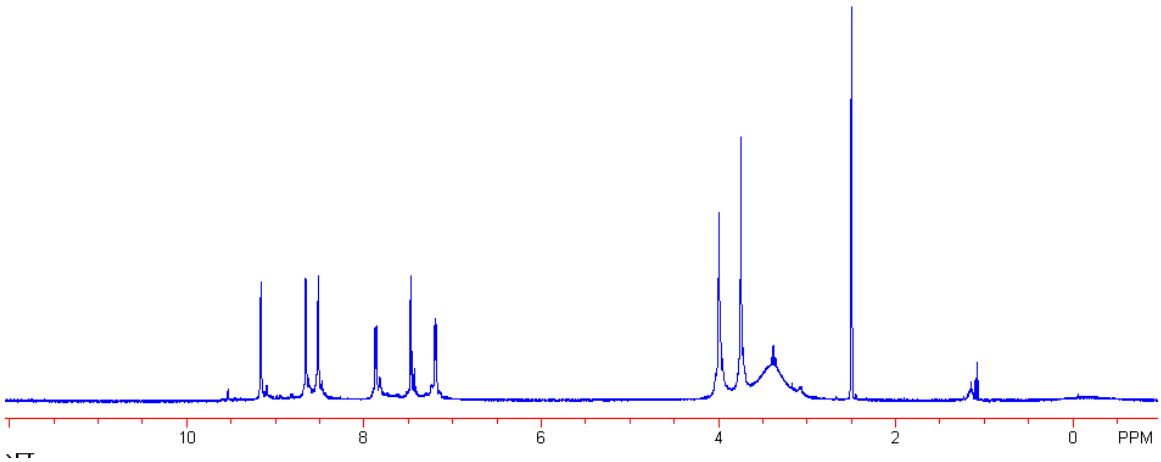

^{13}C NMR (DMSO-d_6, 400 MHz):

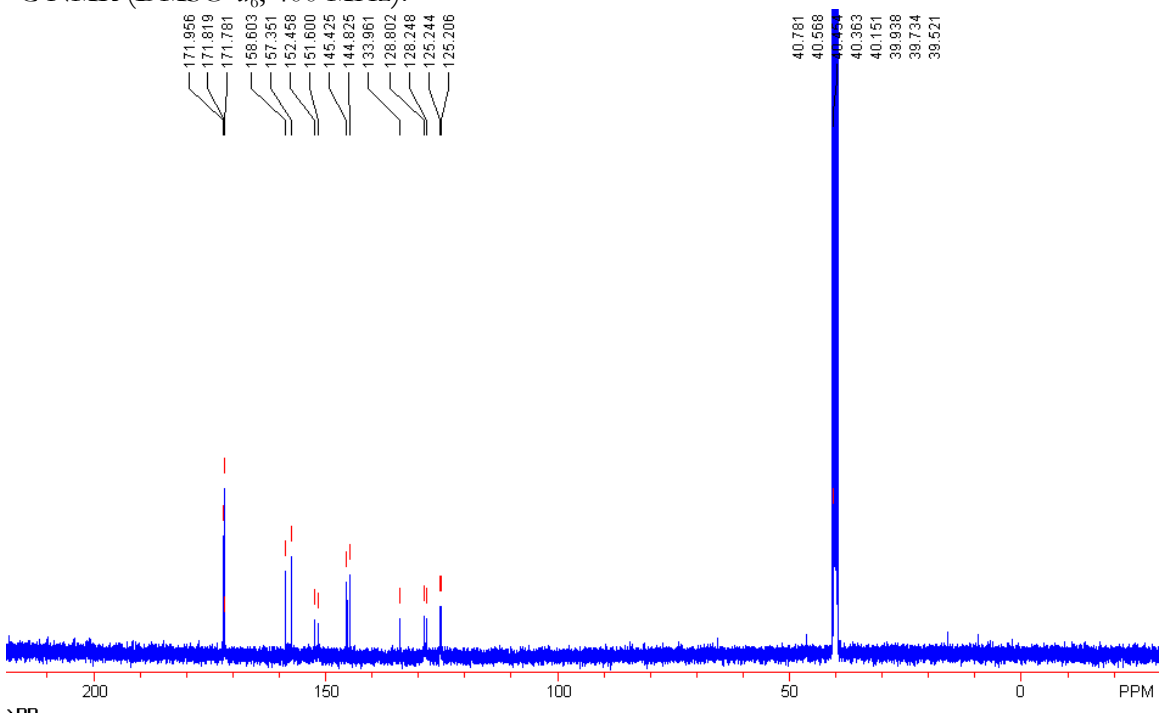

IR (KBr):

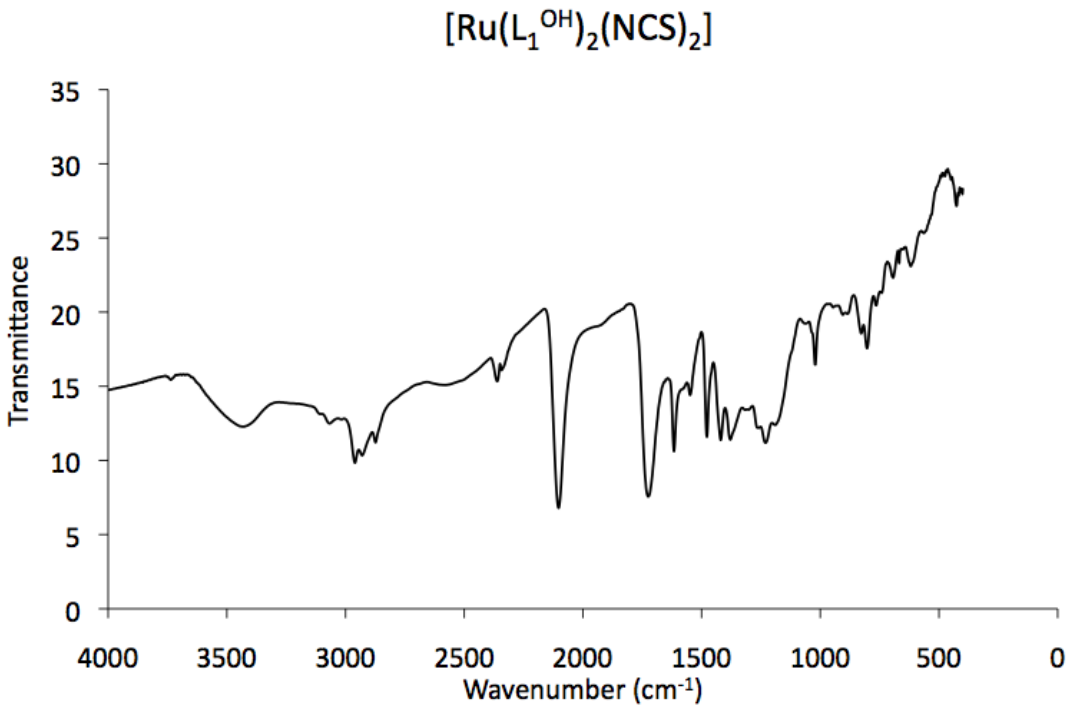

UV-vis (DMSO):

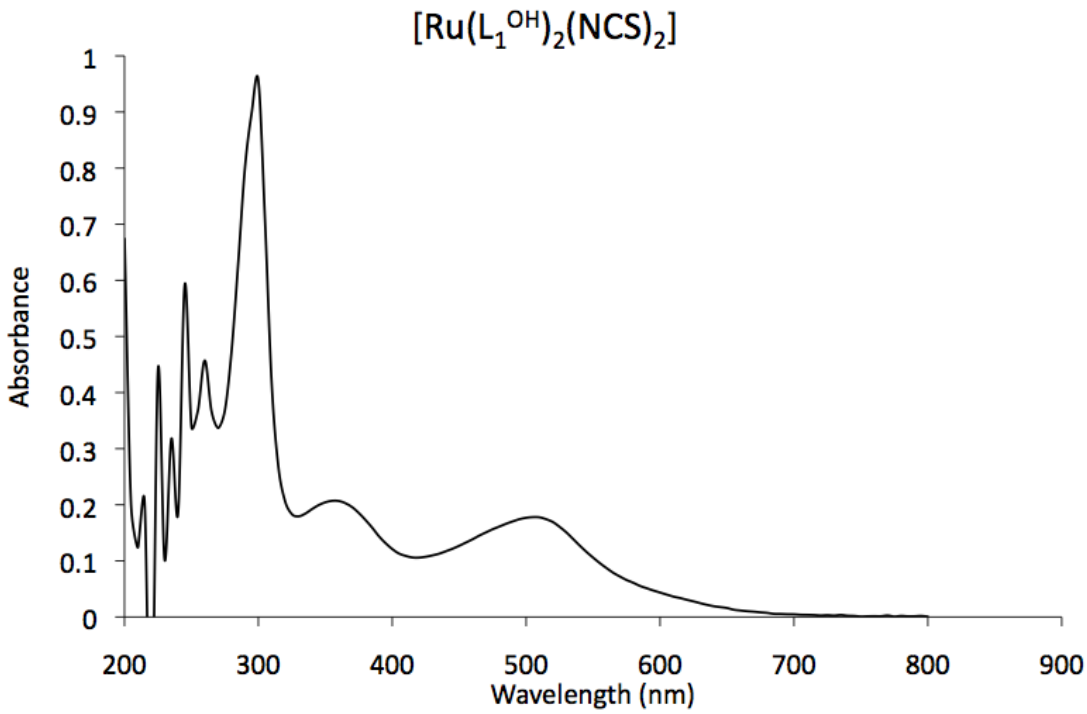

CV (DMF, 298 K *vs.* Fc/Fc+, 0.2 M $TBAPF_6$, glassy carbon w.e.):

Ru(II/III)

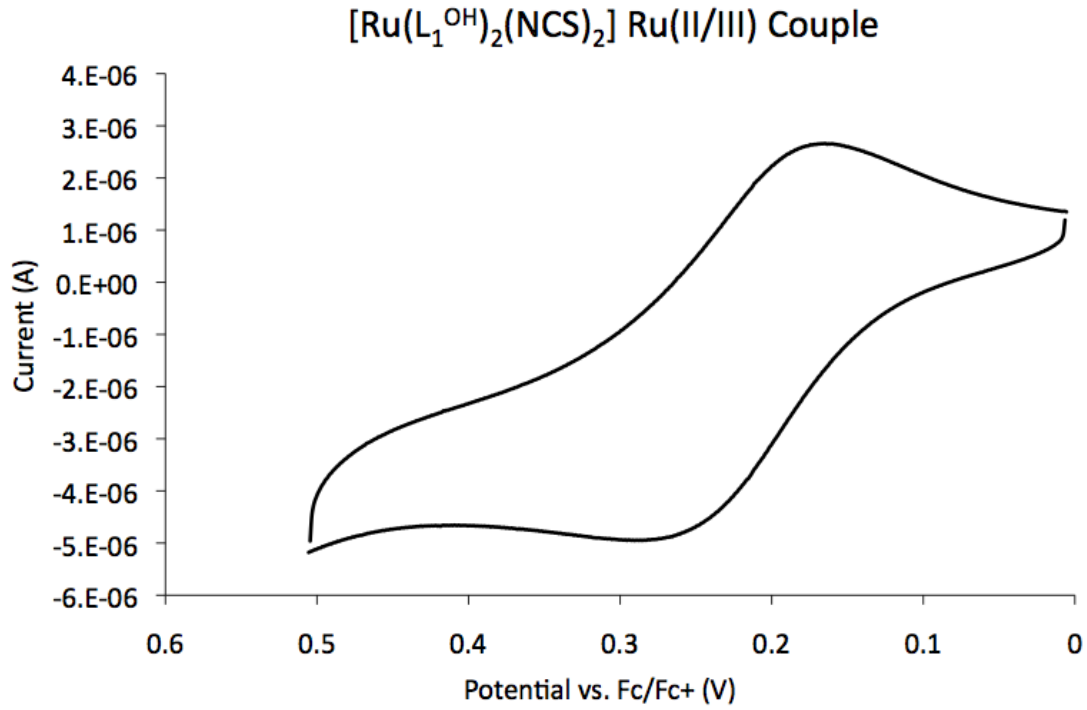

Ligand Reduction

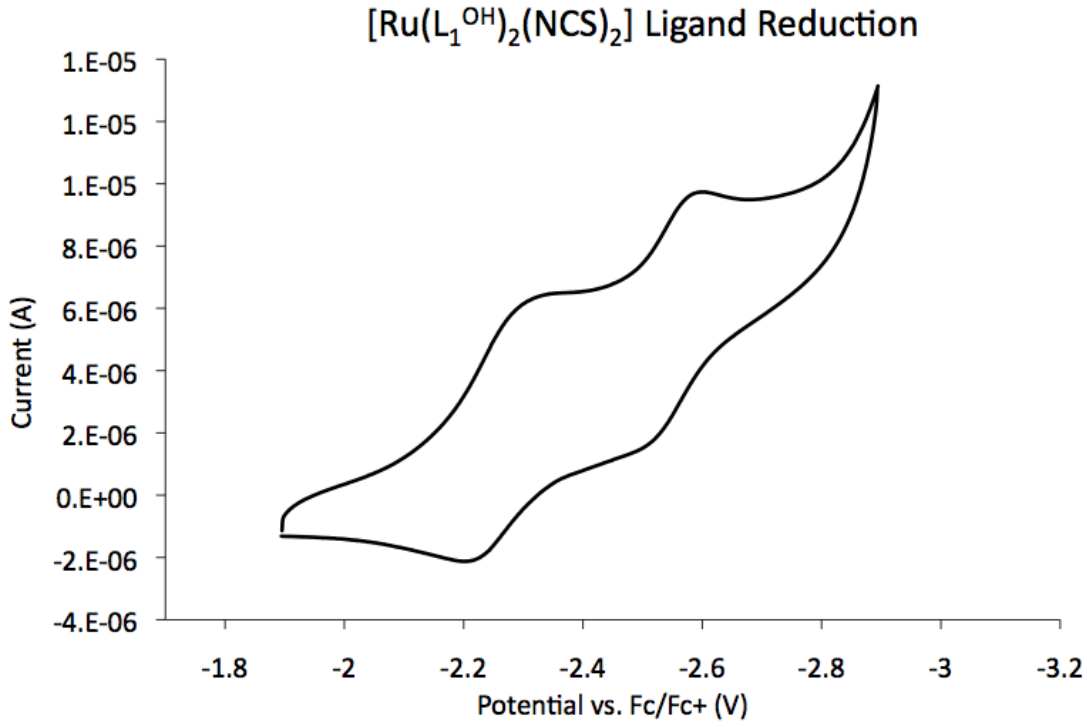

Whole Scan

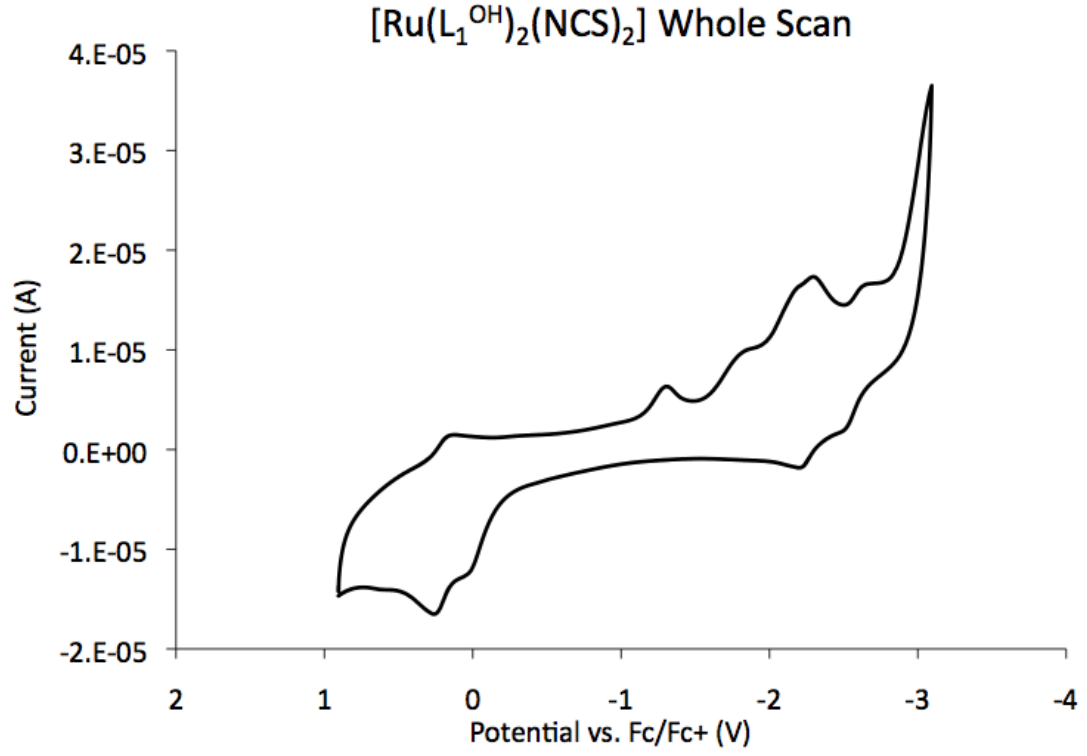

$[Ru(L_2^{OH})_2(NCS)_2]$

^{1}H NMR (DMSO-d_6, 300 MHz):

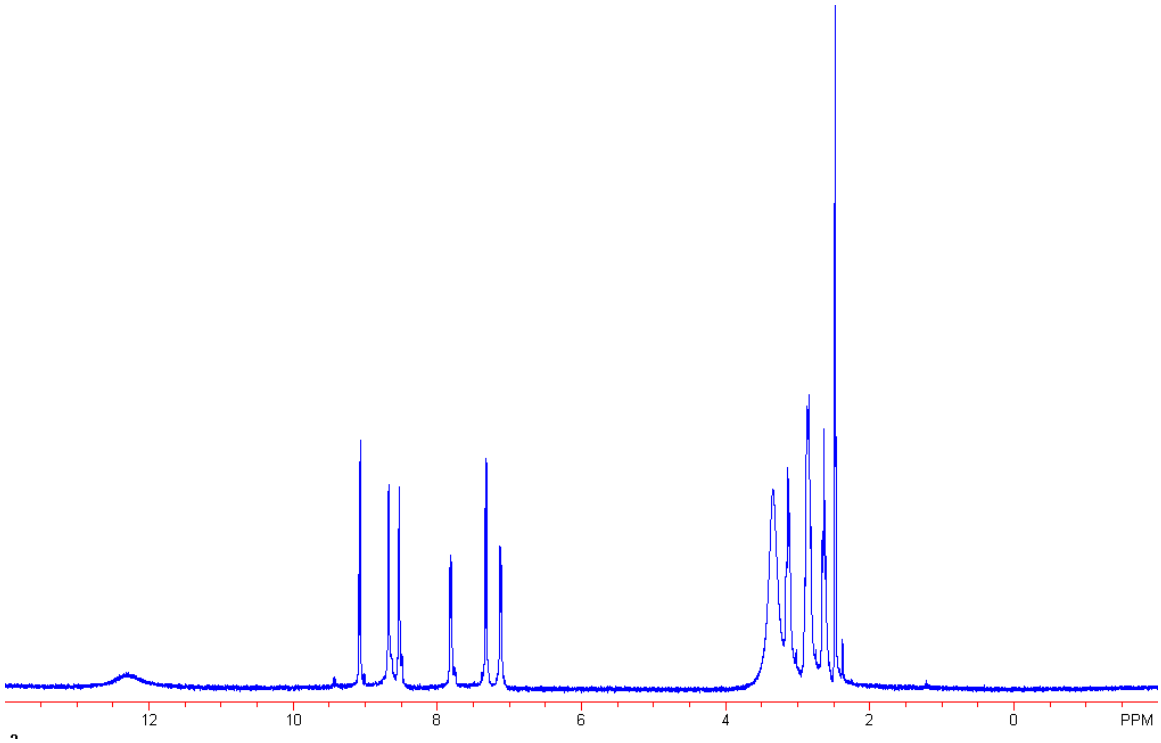

^{13}C NMR (DMSO-d_6, 400 MHz):

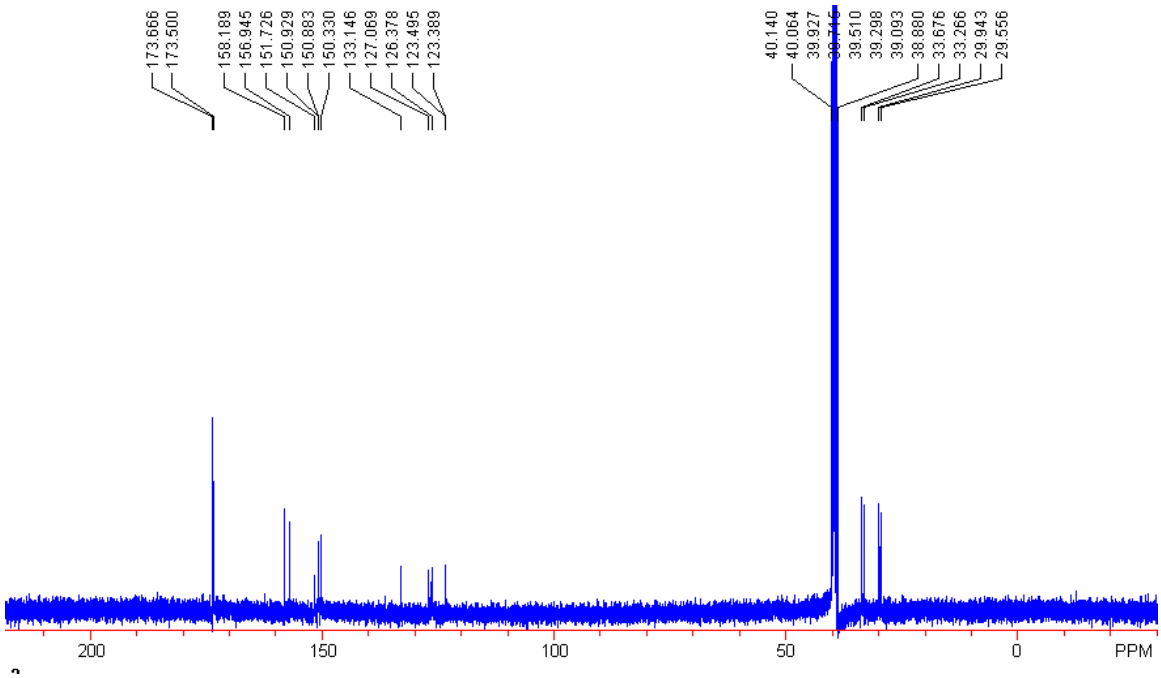

IR (KBr):

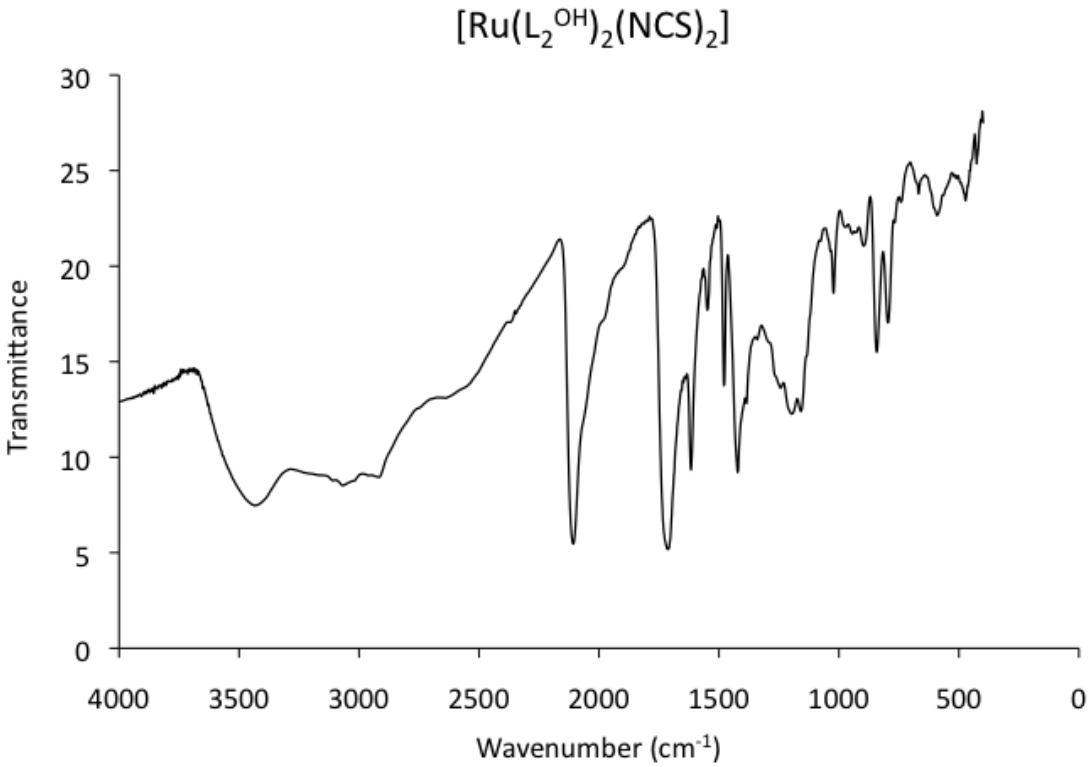

UV-vis (DMSO):

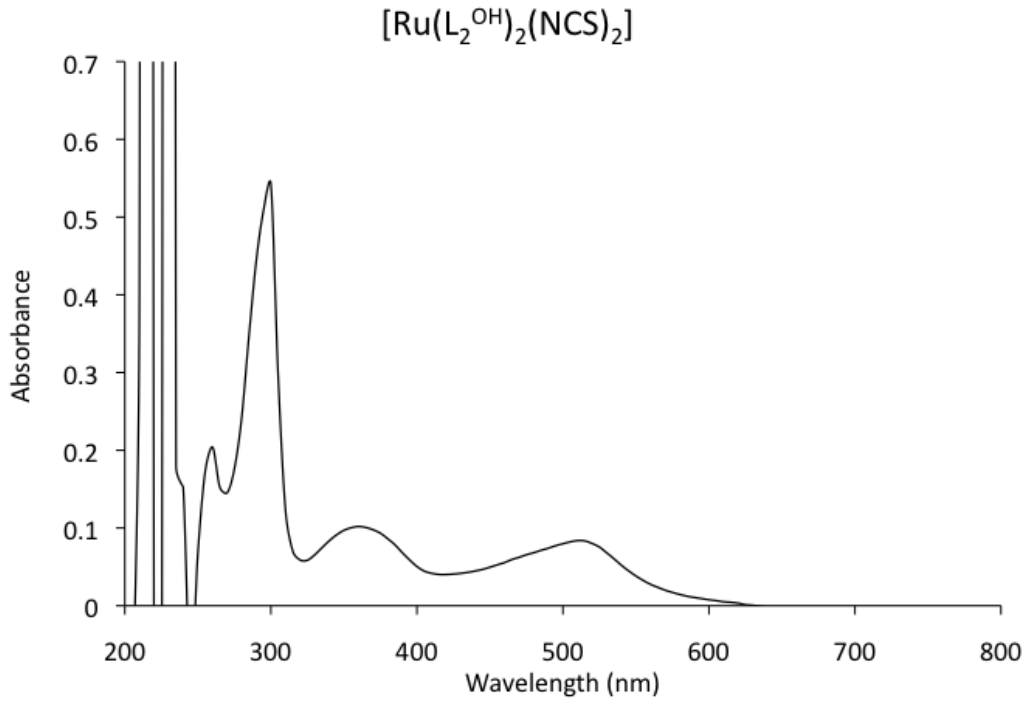

CV (DMF, 298 K *vs.* Fc/Fc+, 0.2 M $TBAPF_6$, glassy carbon w.e.):

Ru(II/III)

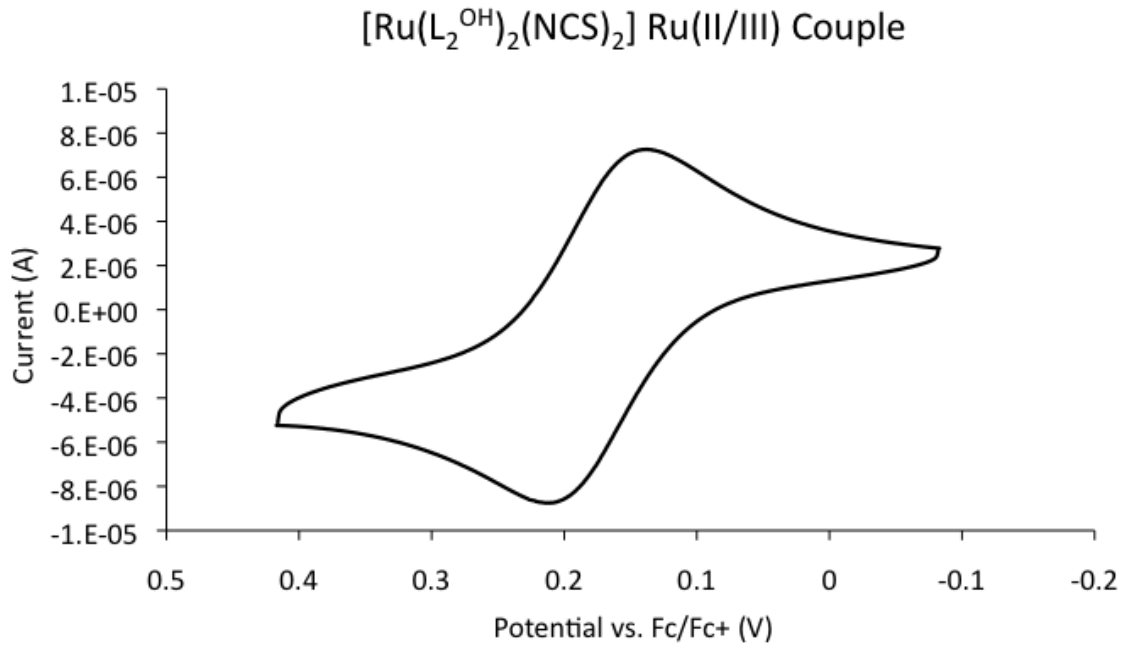

Ligand Reduction:

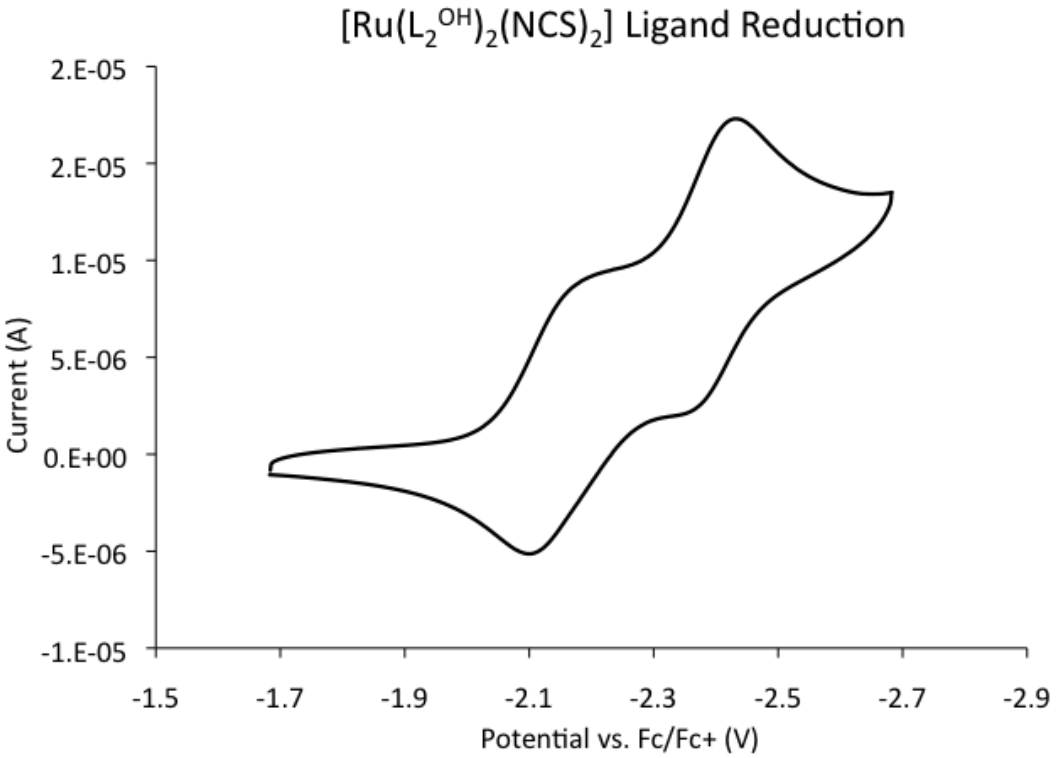

Whole Scan:

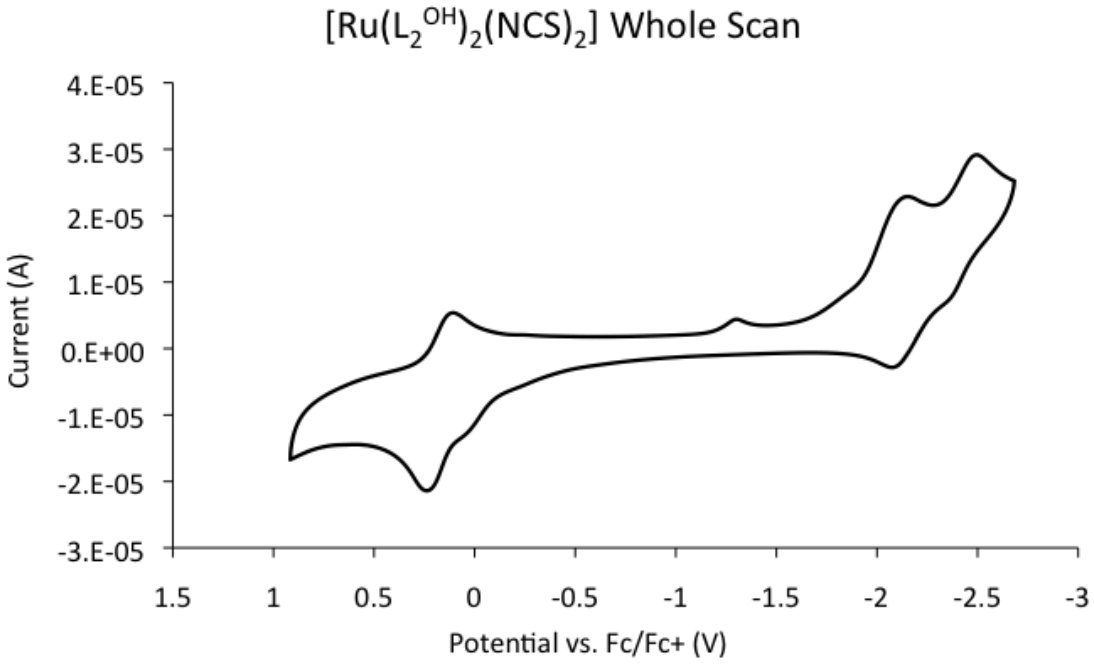

$[Ru(L_3^{OH})_2(NCS)_2]$

^{1}H NMR (DMSO-d_6, 300 MHz):

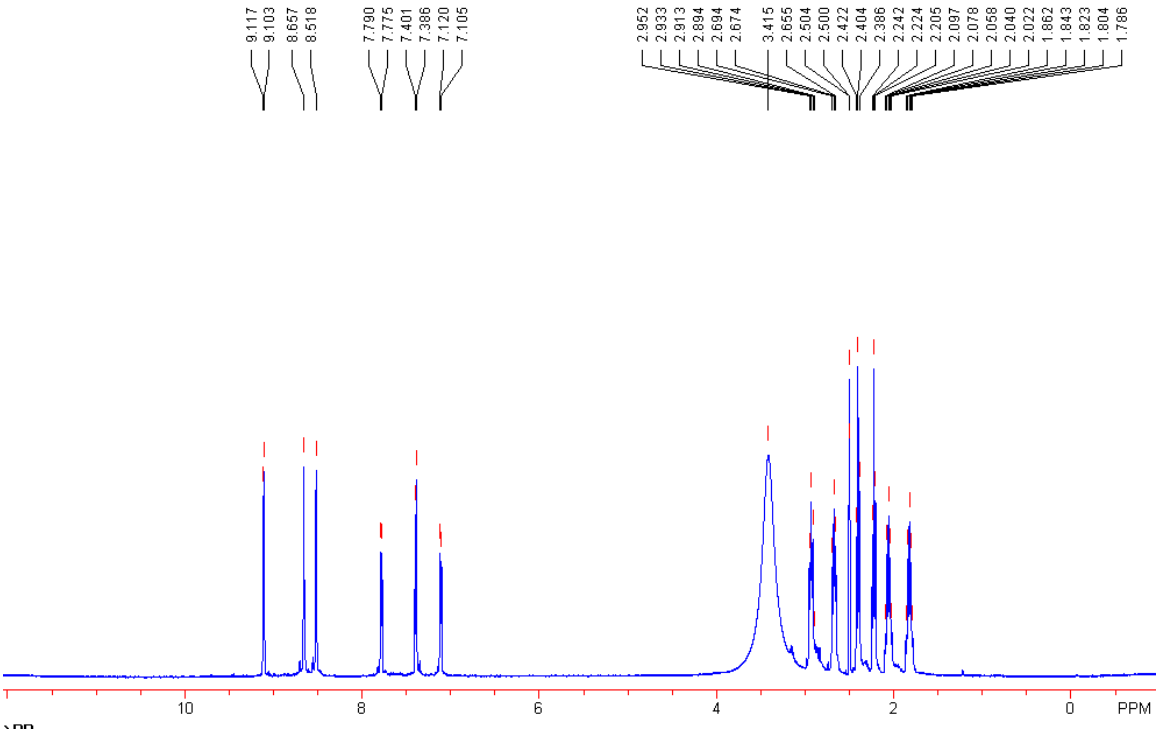

^{13}C NMR (DMSO-d_6, 400 MHz):

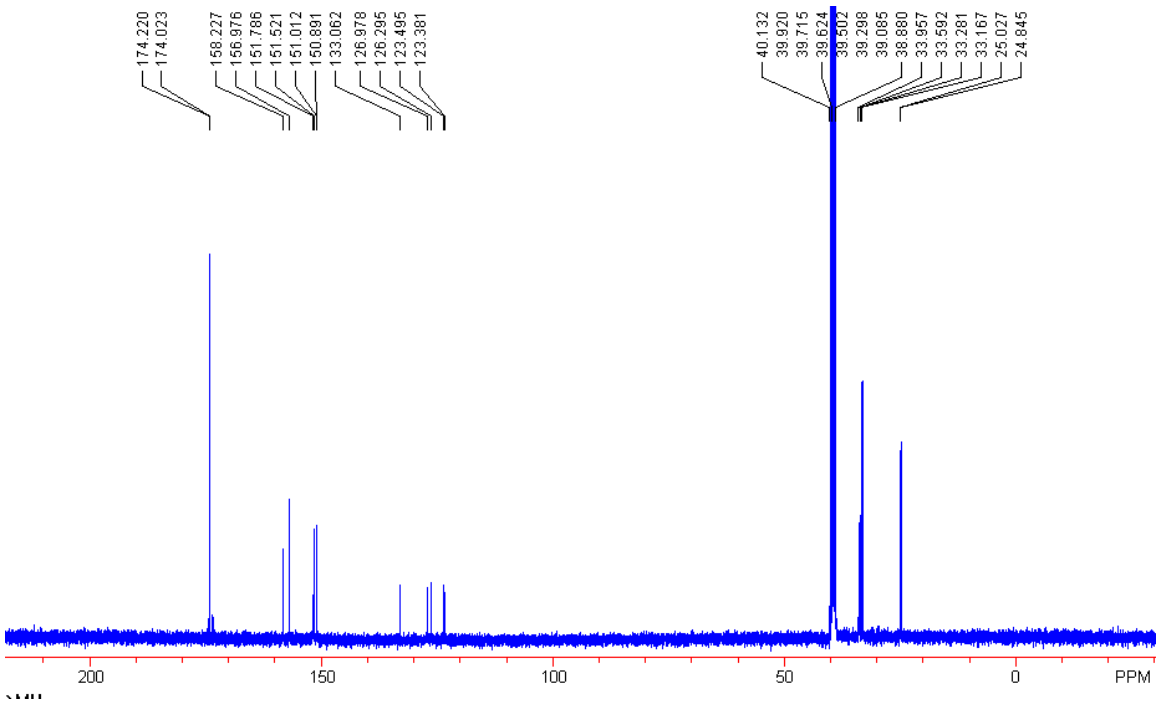

IR (KBr):

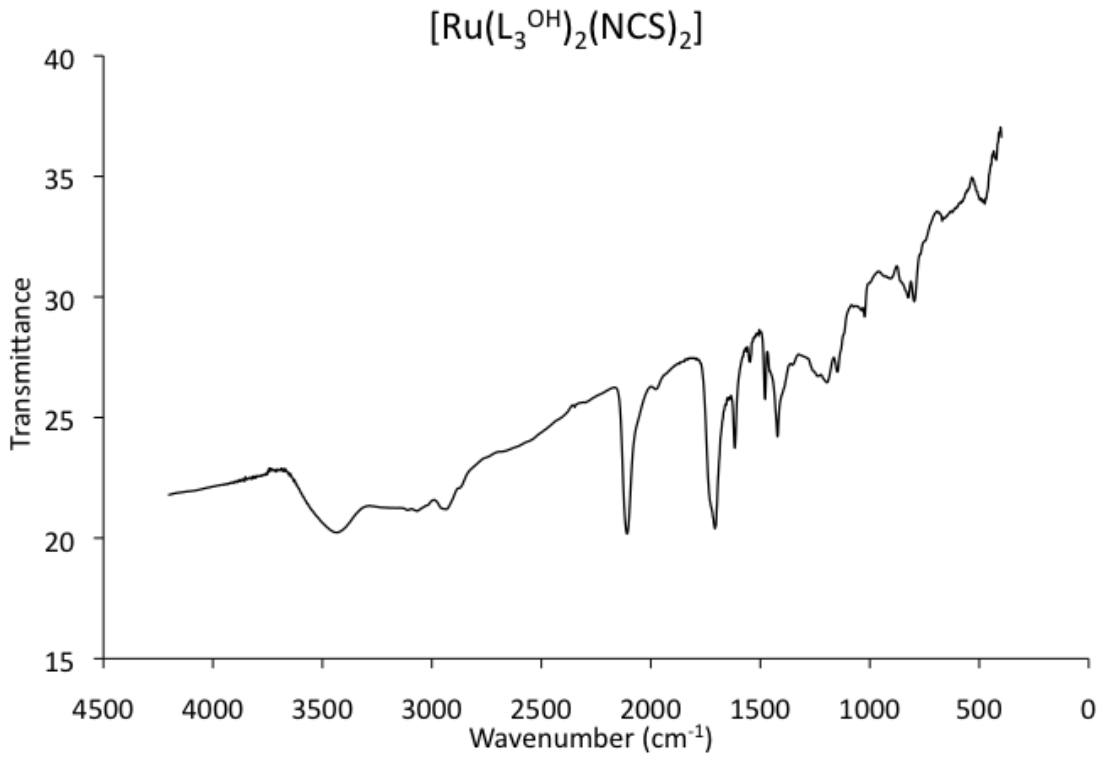

UV-vis (DMSO):

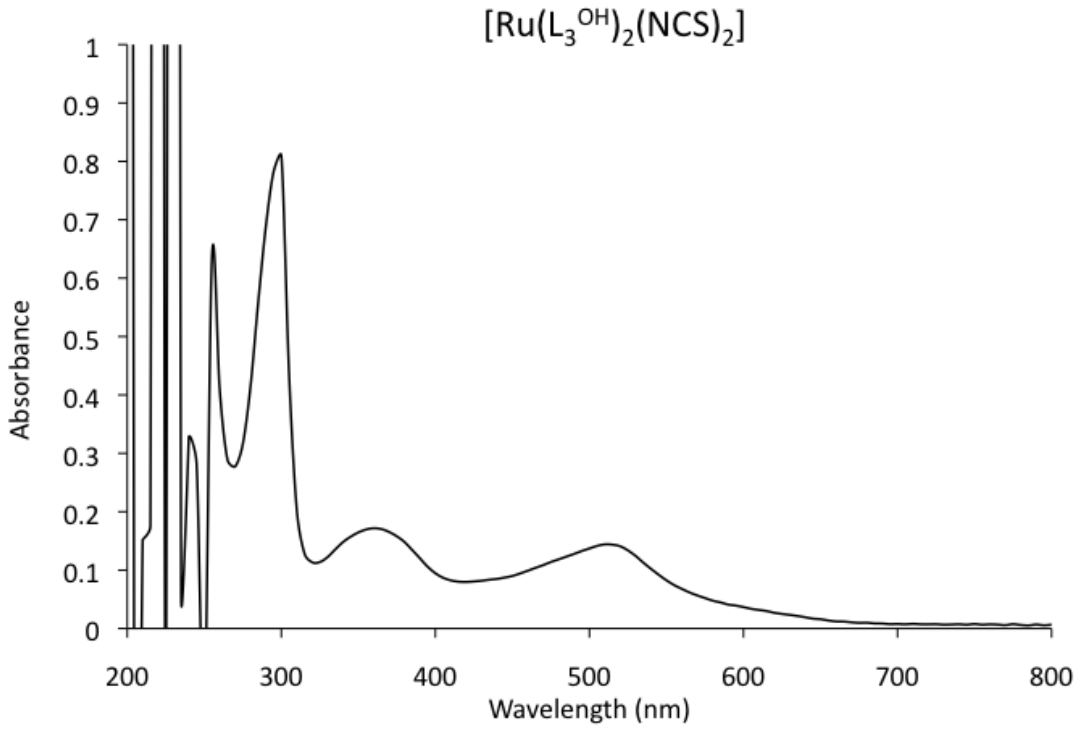

CV (DMF, 298 K *vs.* Fc/Fc+, 0.2 M $TBAPF_6$, glassy carbon w.e.):

Ru (II/III)

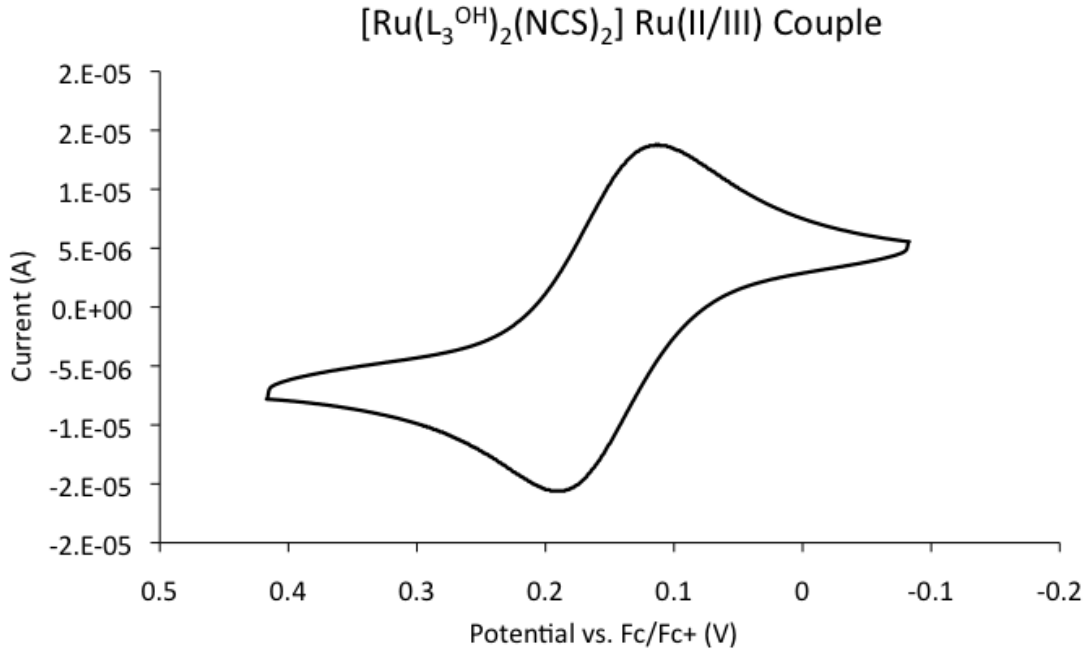

Ligand Reduction

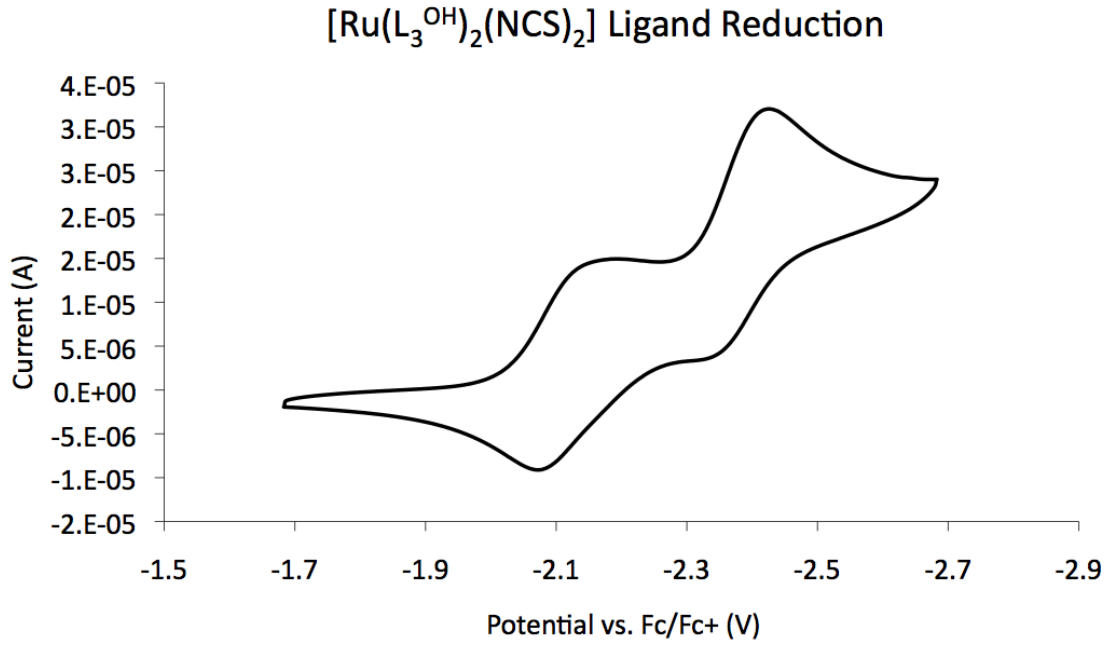

Whole scan

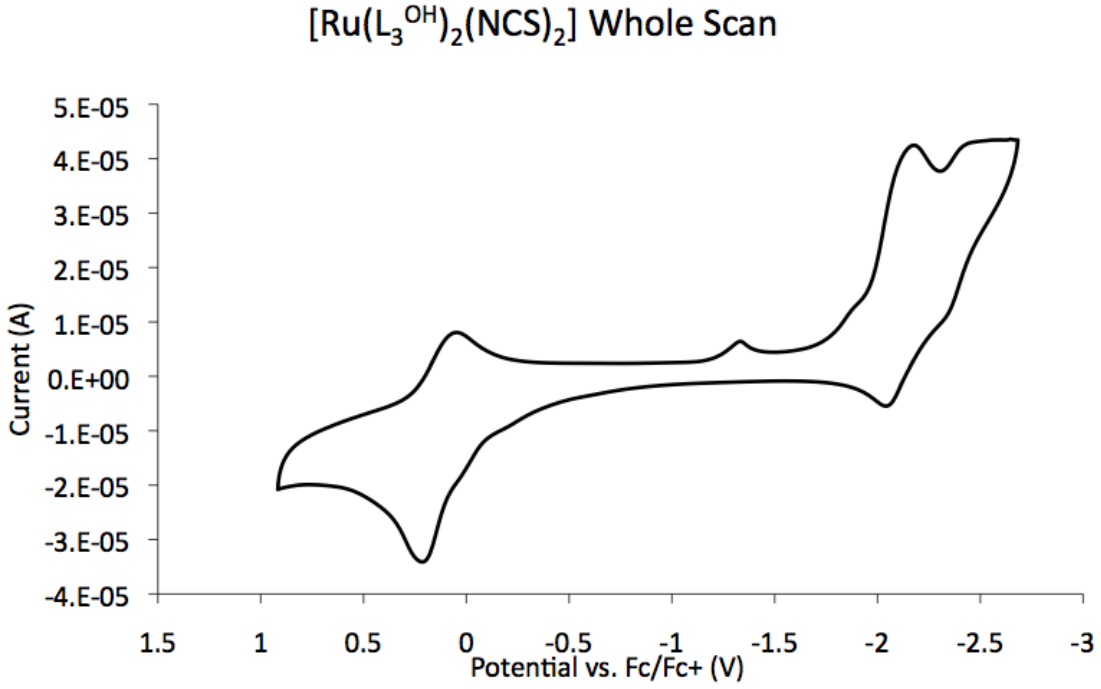

Part II. The Effect of Alkali Metal Ions on the Structure and Spectroscopy of a Tripodal Co(II) Complex

Chapter III. Introduction

Organometallic complexes that incorporate a transition metal ion and alkali or alkaline earth (alkali(ne earth)) metal ion in close proximity are of interest due to the possible structural, electronic and catalytic effects that an alkali or alkaline earth metal ion may have on a transition metal ion. There are several examples in biology, industry and small-scale synthetic chemistry where an alkali or alkaline earth (alkali(ne earth)) metal ion is integral to the function of a transition metal catalyst, most notably the oxygen evolving complex (OEC) of Photosystem II (PSII), which contains a Ca^{2+} ion near the tetramanganese cluster,[60] and the Haber Bosch catalyst, in which K^+ is added to the iron oxide catalyst to increase the catalytic conversion of N_2 to NH_3.[61] Additionally, alkali and alkaline earth metal ions can be useful in organometallic crystal engineering and self-assembly. Coordination of Group I and II metal ions to donor atoms with unused or underused donor atoms on the ligands, as well as to solvent molecules, can dictate the extended solid-state structure of the organometallic complex.

Synthetic heterodinuclear ligands for transition and alkali(ne earth) metal ions can be challenging to design because they must contain sets of donor atoms that can coordinate both a transition metal ion and a Group I or II metal ion in a geometry that minimizes the Coulombic repulsion between the positively-charged centers. However, principles of dinuclear ligand design, transition metal ion ligand design and alkali(ne earth) ion ligand design have been combined to create several synthetic ligands that can coordinate both types of metal ions at close distances and with high binding affinities. The ligands are typically designed using the hard-soft acid base (HSAB) theory, containing soft (more polarizable)

donor atoms to coordinate to the relatively soft transition metal ions and hard (less polarizable) donor atoms to coordinate to the relatively hard alkali(ne earth) metal cations.

This chapter will first provide a brief overview of the coordination environment and function of alkali(ne earth) metal cations in biological systems, with a focus on Mg^{2+} and Ca^{2+}, the two most common alkali(ne earth) metal ions in metalloproteins. The OEC of PSII, which is not as well structurally characterized as the Ca^{2+} binding site in many other Ca^{2+}-containing proteins, will then be discussed. It will then look at synthetic ligands for alkali(ne earth) metal ion coordination, which mimic many features of the first coordination sphere for these cations in proteins using much simpler and smaller molecules. Next, it will look at how these synthetic alkali(ne earth) ligands have been incorporated into ligands with high affinities for transition metals ions to create heterodinuclear transition metal ion-alkali(ne earth) metal ion ligands. These heterodinuclear ligands have been used to synthesize complexes containing many combinations of transition and alkali(ne earth) metal cations. The alkali(ne earth metal) cation in many cases influences the electrochemistry and electronic absorption of the complexes, with implications for reactivity and alkali(ne earth) metal ion sensing, which will also be discussed. Lastly, it will discuss the use of alkali(ne earth) metal ions in crystal engineering and self-assembly, which entails a different set of ligand design principles.

I. Alkali(ne earth) Metal Cations in Biology

The most abundant alkali(ne earth) metal cations in metalloproteins are Mg^{2+} and Ca^{2+} ions.[62] These are discussed here to gain insight into the coordination environment and function of alkali(ne earth) metals in proteins. Both metals play intra- and extracellular roles in biology. The magnesium cation stabilizes a variety of protein structures. For example, Mg^{2+} ions bind at the interface of ribonucleotide reductase subunits, stabilizing the

interfacial domain, and stabilize nucleic acids and the carboxylated and phosphorylated headgroups of lipids by providing charge balance for negatively charged phosphate groups. Ca^{2+} ion concentrations play an important regulatory role for a wide variety of biological processes such as muscle contraction, glycolysis and cell division and growth.

Oxygen is the most common donor atom for Ca^{2+} and Mg^{2+}cations, as would be expected given their hard character. For Mg^{2+} ions, nitrogen is the second most common donor atom. All Mg^{2+} ion-binding sites in Protein Data Bank structures contain at least one carboxylate ligand, which coordinates predominantly in a monodentate manner. Next most common are side chains of asparagine and glutamine, followed by backbone carbonyl groups, then serine and threonine side chains, and histidine and tyrosine side chains. Most Mg^{2+} ions are octahedrally coordinated, with the remaining ligands being water molecules. Mg^{2+}-O distances generally range from 2.0-2.2 Å. Carboxylate groups are also the most common ligands for Ca^{2+} ions, with carbonyl, water and hydroxyl oxygen atoms being the next most common. The coordination number of Ca^{2+} ions tends to vary from 6-8.[62]

Since Ca^{2+} ion concentrations play a regulatory role, the Ca^{2+} ion concentration is maintained using Ca^{2+} pumps. Most Ca^{2+} ion binding proteins, such as calmodulins, contain a highly conserved motif, the EF-hand, which binds Ca^{2+} even in the presence of 10^5-fold higher concentrations of Na^+, K^+ and Mg^{2+}. An illustration of an EF hand Ca^{2+} binding site is shown in Figure 3-1. The physiological cellular concentrations of Ca^{2+} (10^{-7} – 10^{-8} M) is 10^4 times lower than that of Mg^{2+}, so Mg^{2+} does at least partially populate the EF-hand binding sites in the resting state.[62] However, while Ca^{2+} binds to a glutamic acid (Glu) residue in a bidentate manner, inducing large conformational changes in the protein, Mg^{2+} coordinates to this residue in a monodentate manner, which does not produce large conformational changes and hence does not initiate signaling response.[60]

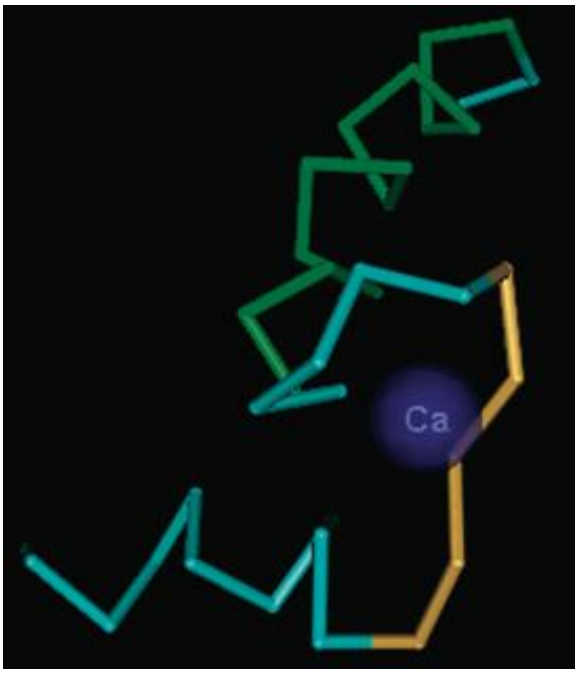

Figure 3-1. The EF-hand motif found in many Ca^{2+}-binding proteins, such as calmodulin. This figure was taken from a review by Jason Kuchar and Robert P. Hausinger.[63]

The specificity of the EF-hand binding site for Ca^{2+} is due to several factors. When the Glu residue mentioned above is bound in a bidentate manner, the geometry at the site is pentagonal bipyramidal (seven-coordinate), which favors Ca^{2+} binding over the smaller Mg^{2+}. The metal ligand side chain interactions constrain the cavity size, preventing ions larger than Ca^{2+} from binding, and the site has a charge of negative three, making it unfavorable for monovalent ions to bind.[62]

II. Ca^{2+} in Photosystem II

The OEC of PSII consists of four manganese ions, one calcium ion and one chloride ion, all of which are essential for oxidation of H_2O to O_2.[60] Ca^{2+} plays both a structural and a functional role. When Mn-depleted PSII is incubated with Mn^{2+} under weak illumination, a functional OEC complex will only be reconstituted if Ca^{2+} is also present.[64] Conversely, Ca^{2+} will not bind Mn-deplete PSII.[65] The OEC will assemble in vivo in

cyanobacteria if Sr^{2+} replaces Ca^{2+} in the growth medium, but the resultant complex has ~1/2 the catalytic function of the native protein.[60]

Structural information about the OEC is difficult to obtain because most crystals do not diffract to high resolution and samples are prone to radiation damage, which can cause structural changes. In addition to X-ray diffraction, the structure of the OEC has been investigated by EXAFS and XANES experiments, solid state magic angle spinning NMR experiments on samples where ^{113}Cd replaced Ca, FTIR and EPR. These results indicate that Ca^{2+} is ~ 3.4 Å from the Mn cluster, and probably is octahedrally coordinated. The predicted ligands for Ca^{2+} are Ala, Asp, Glu and His (imidazole side chain) (Figure 3-2).[60]

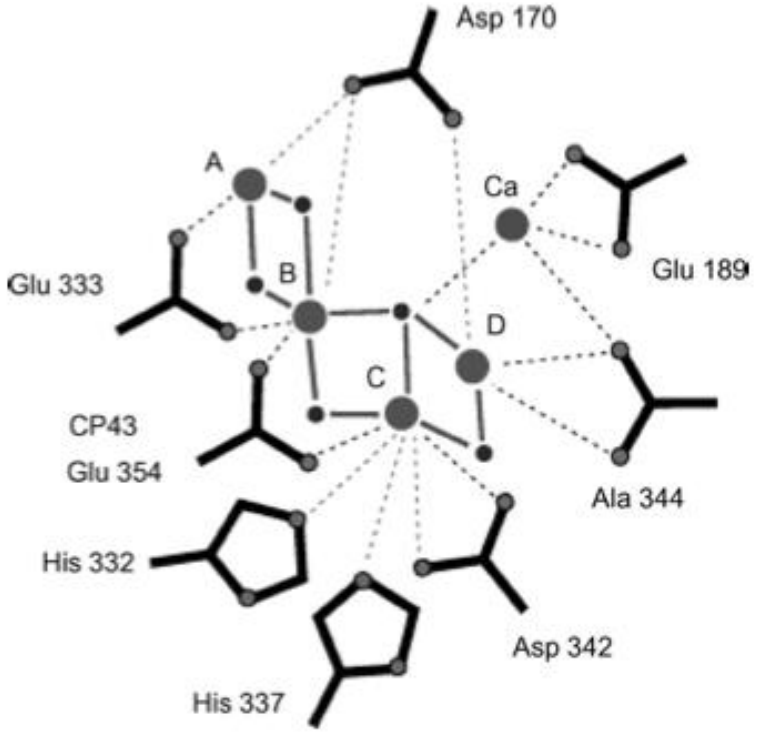

Figure 3-2. A model of the OEC Mn_4Ca group of PSII from *Thermosynechococcus elongates*. A, B, C and D are the four Mn ions. Image from a review by Charles F. Yocum.[60]

Trivalent lanthanide ions (Ln^{3+}), such as Tb^{3+}, are often used to probe Ca^{2+} binding sites. In proteins where Ca^{2+} plays only a structural role, such as thermolysin, subtilisin and

elastase, the proteins retain their function after replacement of Ca^{2+} by Ln^{3+}. In proteins where Ca^{2+} plays a functional role, the enzyme's function is inhibited by replacement of Ca^{2+} by Ln^{3+}. PS II falls into the latter category, indicating that Ca^{2+} has an additional function beyond its structural role.[60]

The functional role of Ca^{2+} in PSII may be tied to S-state advancement.[60] The four electron oxidation of two water molecules to O_2 is accomplished by the OEC cycling through five intermediate states called S states. The states are termed S_i, where i=0-4 and denotes the number of positive charges accumulated at the OEC.[66] The Ca^{2+}-depleted samples or samples in which Ca^{2+} is replaced by Cd^{2+} or Dy^{3+} do not appear to be able to advance beyond the S_2 state.[60] Many models predict that H_2O or OH^- bound to Ca^{2+} carries out a nucleophilic attack on a Mn^{5+}=O species in the S_4 state to form the initial O-O bond. Additionally, Ca^{2+} may also bind the Cl^- also necessary for water oxidation.[60] More experimental data is needed to fully understand the reaction mechanism and the role of Ca^{2+}. Biomimetic complexes containing Mn ions with proximal Ca^{2+} or other alkali(ne earth) cations will also be helpful in understanding the role of Ca in PSII, as discussed in a subsequent section.

III. Synthetic Ligands for Alkali(ne Earth) Ions: Crown Ethers

In 1967, Charles Pedersen discovered that crown ethers form stable complexes with alkali(ne) earth metal ions.[67,68] Crown ethers are neutral macrocyclic polyethers. Like binding sites for alkali(ne earth) metals in proteins, they have sets of hard oxygen donors in a preorganized geometry. An example of a crown ether is shown in Figure 3-3. The oxygen donors are separated by $-CH_2CH_2-$ spacers, so that they form energetically favorable 5-membered chelate rings upon coordinating to transition metals. A multitude of variations have been synthesized to accommodate a wide variety of guests of varying sizes,

polarizabilities, and cationic, neutral or anionic charge.[69,70] The size of the ligand cavity can be adjusted to accommodate the size of the guest and the oxygen atoms can be replaced by nitrogen, sulfur or phosphorous atoms according to the polarizability of the guest. The ethylene spacers can be replaced by less flexible linkers such as benzene groups to decrease the conformational flexibility.[69,70] Crown ethers have a multitude of applications, including ion separation, phase transfer processes, the dissolution of hard cations in low polarity organic solvents, ion sensing, preparation of ion-selective electrodes, isotope separations, membrane transport and biomimetic chemistry.[69,70] Additionally, benzo- and aza-crown ethers are often used to incorporate crown ethers into other ligands, since substituents can easily be added.[69,70]

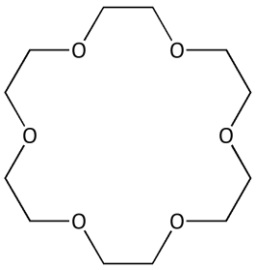

Figure 3-3. 18-crown-6, an example of a crown ether.

The most stable cation-crown complexes form when the cation/crown ether cavity ratio is ~ 1 (Figure 3-4).[71] When the relative cation and cavity size are the same, all donor atoms of the macrocycle interact with the guest cation. However, all crown ethers have some conformational flexibility, and often can twist to accommodate a cation with a radius smaller than the cavity. Additionally, crown ethers can accommodate different sizes of cations through different binding modes and stoichiometries. For example, while cations the same size as the cavity bind within the cavity in a 1:1 manner, larger cations can be sandwiched between two or more macrocycles.[69]

The cation-crown binding constant is also influenced by the temperature,

counteranion, ionic stength and choice of solvent. Figure 3-5, from [69], shows a Born-Haber-type cycle for crown-cation binding (M^+ = alkali(ne earth ion), L = macrocycle and X^- = counteranion). When the solvent is weakly coordinating, K_1 predominates, whereas when a strongly coordinating solvent is used, K_3 predominates.[69]

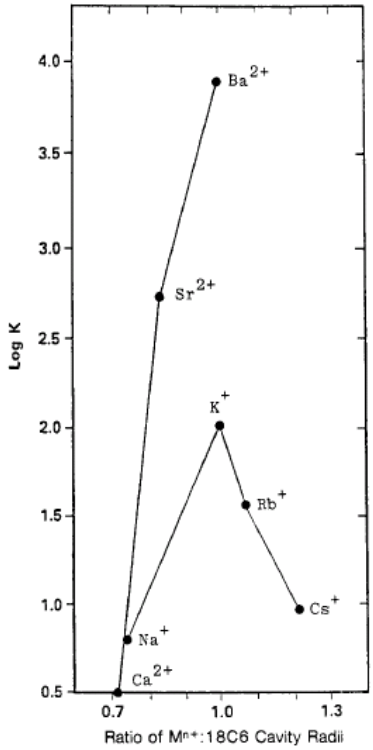

Figure 3-4. This graph was taken from a review by Izatt *et al.*[72] It shows the selectivity of 18-crown-6 with metal cations of varying radii at 25 ºC.

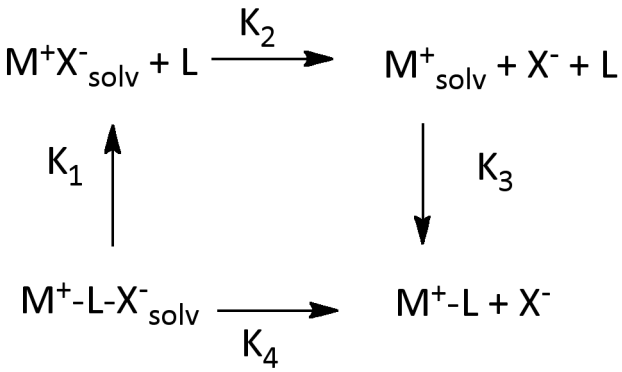

Figure 3-5. Born-Haber-type cycle for cation-crown binding.[69]

IV. Transition Metal Ion Coordination

There are an extraordinary number of synthetic ligands for transition metals, containing nitrogen, oxygen, phosphorous, sulfur and carbon (carbene) donor atoms.[73] Multidentate ligands coordinate to transition metals with high binding affinities, especially if the donor atoms are configured so as to coordinate to the ligand with 5-membered chelate rings (D-M-D chelate bite angle ~ 86°), with 6-membered chelate rings being somewhat less stable (D-M-D chelate bite angle ~ 90°).[73] One class of ligands that fits this criteria are derivatives of the tripodal tetraamine ligand tris(2-aminoethylamine) (tren) (Figure 3-6),[74] which are used in the complexes in this thesis.

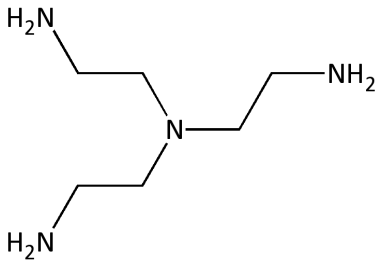

Figure 3-6. Tris(2-aminoethylamine) (tren), which has been functionalized to create many different ligands.[74]

V. Binucleating Ligands

Binucleating ligands contain two sets of donor atoms in order to coordinate two metal ions in close proximity. Fenton *et al.* place binucleating ligands in two main categories, those in which metals share at least one donor atom and those in which the metals do not share a common ion.[75] The latter group can be further divided into ligands with an aromatic or other bridging group, which can assist in communication between the metal centers, stacked planar macrocycles, in which each metal coordinates to a macrocycle, and ligands with isolated donor sets in extended macrocycles.[75]

VI. Heterodinuclear Transition Metal Ion-Alkali(ne Earth) Ion Ligands

As mentioned earlier, heterodinuclear ligands designed to coordinate a transition metal cation and an alkali metal cation in close proximity require the two sets of donor atoms to have differing characters – one to accommodate the more polarizable (softer) character of the transition metal ion, and the other to accommodate the less polarizable (harder) character of the alkali metal ion. The ligands can also be classified according to the presence or absence of a shared donor atom,[76] and there are examples of transition metal ion-alkali(ne earth) metal ion heterodinuclear complexes in each group, with the former being more common for complexes involved in catalysis and the latter more common for complexes involved in alkali(ne earth) metal ion sensing.

Alkali(ne earth) and transition metal ions sharing a donor atom can be spaced less than 4 Å from each other.[76] Reinhoudt *et al.* synthesized a series of salen and salophen-based ligands (where salen = 1,3-bis(salicylideneamino)ethane and salophen = 1,3-bis(salicylideneamino)benzene) with polyether bridges appended to form macrocycles (Figure 3-7),[76] which can be metallated with transition and alkali(ne earth) metal ions.[77] Crystal structures show the transition metal ion (M_a = Ni(II) or Cu(II)) is coordinated to the salen or salophen moiety in a square planar geometry and the alkali(ne earth) metal ion (M_b = Ba^{2+}, K^+, Na^+ or Li^+) is coordinated to the polyether. The anion X^- is ClO_4^- or $CF_3SO_3^-$. The M_a-M_b distance varies between 3.69 and 3.73 Å.[77] The molecular structure for [Ni(salophen)·$Ba(ClO_4)_2$)] is shown in Figure 3-8. The association constant for Na^+, K^+ and Ba^{2+} for these complexes is large (> 10^6 L mol^{-1} in DMSO).[76,78] Li^+ does not bind as strongly.[76,78]

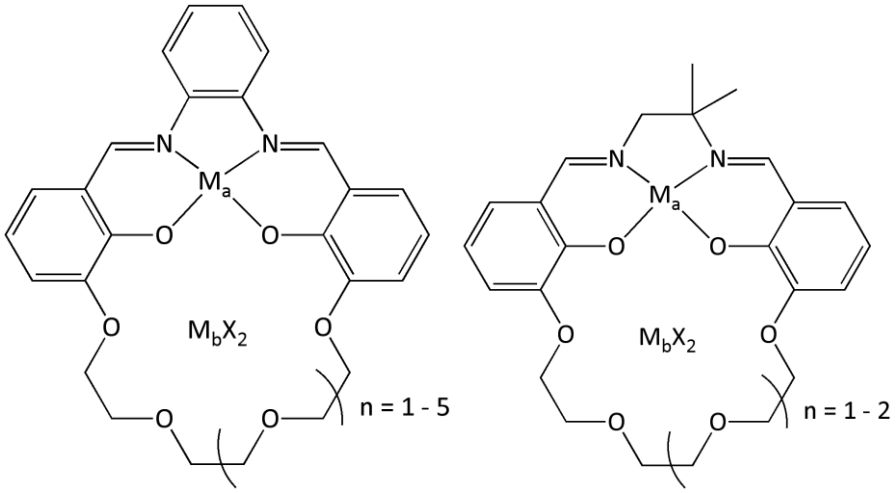

Figure 3-7. Salophen (left, 1-1) and salen (right, 1-2) -type crown ether macrocycles synthesized by Reinhoudt *et al.*[77] M_a = Ni(II), Cu(II) or Zn(II) and M_b = Li(I), Na(I), K(I) or Ba(II) and X = ClO_4^- or $CF_3SO_3^-$.

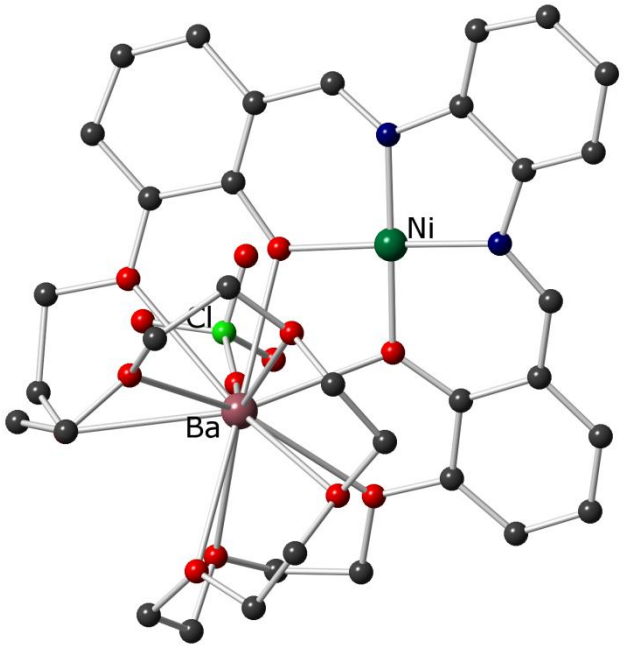

Figure 3-8. [Ni(salophen)·Ba$(ClO_4)_2$)] synthesized by Reinhoudt *et al.*[77] Carbon is shown in grey, nitrogen in blue and oxygen in red.

VII. Implications of Alkali(ne Earth) Cations for the Reactivity of Transition Metal Ion Complexes

Upon binding Ba^{2+} Reinhoudt *et al.*'s Ni(II) complexes show anodic shifts of up to 300 mV, with smaller anodic shifts (~ 50 mV) observed upon coordination of the smaller alkali metals.[76,78] This anodic shift has important implications for catalysis: [Ni(1-2)·$Ba(CF_3SO_3)_2$)] converts benzyl bromide to phenylacetone in the presence of acetic anhydride, while [Ni(1-2)] produces only toluene and bibenzyl under the same conditions. Presumably, the electron-withdrawing Ba^{2+} helps stabilize a N-C bond.[76]

Horwitz *et al.* used similar ligands to investigate the effect of alkali(ne earth) metal ions on Mn centers in order to probe the role of Ca^{2+} in PSII and the influence of Ca^{2+} on the spectroscopy of the Mn centers. The [Mn(II)(3,3'-17-crown-6-sal-3-CH,-ophen)] monomer [Mn(1-3)] (Figure 3-9), readily coordinates alkali(ne earth) cations (M^{n+} = Li^+, Na^+, K^+, Ca^{2+}, Ba^{2+}) in CH_3CN in a 1:1 manner. Electronic absorption and electrochemical studies indicate that the addition of greater than 1 equivalent M^{n+} does not produce any additional changes.[79]

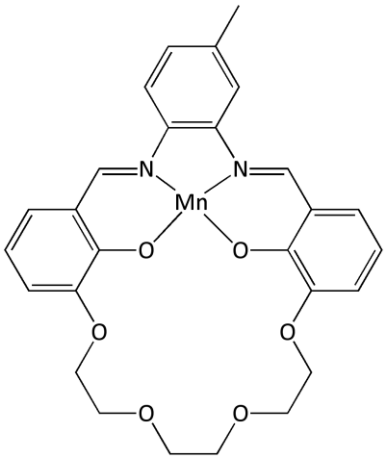

Figure 3-9. [Mn(II)(3,3'-17-crown-6-sal-3-CH,-ophen)] monomer [Mn(1-3)].

There are small shifts in both the ligand-based and charge transfer electronic

absorption bands upon coordination of the alkali(ne earth) metal ions, but some ions cause a red shifting and others a blue shifting.[79] The authors postulate this discrepancy is due to differences in the polyether geometry, ion pairing phenomena and solvation.[79] Different anions may also play a role. The Mn(II) monomer can be oxidized to the Mn(III) complex [Mn(1-3)·PF_6] with O_2 in MeOH or [Cp_2Fe][PF_6] in CH_3CN under N_2.[79] The electronic absorption spectroscopy of [Mn(1-3)·PF_6] shows a small blue-shifting upon alkali(ne earth) metal coordination. However, there is a large anodic shift in Mn(II/III) couple upon coordination of an M^{n+} ion.[79] For example, E° = -45 mV vs. SCCE for [Mn(1-3)·PF_6] and 200 mV for [Mn(1-3)·PF_6]·$CaTF_2$. Interestingly, ΔE_p varies greatly (90 mV for the parent complex, 180 mV for the $LiClO_4$ complex, 85 mV for the KPF_6 complex, 115 mV for the $CaTf_2$ complex and 105 mV for the $BaTf_2$ complex),[79] perhaps due to increased reorganization of the crown for Li^+ and, to an extent, Ca^{2+}. Exposure of [Mn(1-3)] to O_2 in CH_3CN gives the oxo-bridged dimer [$Mn(III)_2$(1-3)]$_2$(μ-O), which reacts with 2 molar equivalents of KPf_6 or $BaTf_2$.[79]

Paramagnetic ^{1}H NMR spectroscopy of the related complex [(3,3'-17-crown-6-salophen)Mn(III)]PF_6 shows a downfield shift of the crown ether resonances upon cation coordination. It also shows that the M^{n+}-bound complexes have a propensity to bind H_2O (or OH^-) at the Mn(III) center, suggesting M^{n+} increases the Lewis acidity of the Mn(III) center and enhances its water/hydroxide binding affinity. Ca^{2+} may have a similar role in PS(II).[80]

Horwitz *et al.* also synthesized μ-O_2 Mn dimers using the ligand 3,3'-17-crown-6-1,3-bis(salicylideneamino)propane in order the further probe possible intermediates during O_2 production by the OEC.[81] Both the Mn(III)Mn(IV) dimer and $Mn(IV)_2$ dimer readily incorporate alkali(ne earth cations) in a 1 Mn/1M^{n+} stoichiometry (M^{n+} = Na^+, K^+, Ca^{2+} and

Ba^{2+} for the (III/IV) dimer and Ba^{2+} for the $(IV)_2$ dimer).[81] EXAFS data for the Mn(III)Mn(IV) dimer indicate that Na^+, K^+, and Ca^{2+} are all ~ 3.6 Å from the Mn ion, similar to that reported for the Mn-metal interaction in PSII, while the Ba^{2+} is ~ 4 Å from the Mn center. The M^{n+} cation has little effect on the position of the X-ray absorption edge, but its presence is important in fitting the data.[81] The EXAFS data indicate a Mn-Mn distance 0.1 Å greater in the complexes with M^{n+} cations than in the complex without.[81] The $Mn(IV)_2$ dimer with two Ba^{2+} ions shows two rather than six atoms at 2.3 Å distance, perhaps because Ba^{2+} binds multiple water molecules and brings them close to the Mn center.[81]

Alkali(ne earth) metals also influence CO activation by *cis*-$M(CO)_4(PR_3)_2$-type complexes. The transition metal ion coordinates to CO through the carbon atom and the alkali metal (Li^+ in most cases) coordinates through the oxygen atom, activating CO for nucleophilic attack.[79,80] There are no reports of *cis*-$M(CO)_4(PR_3)_2$ (M = Cr, Mo, W) complexes reacting with RLi reagents, but similar complexes with crown ether-type substituents on the phosphinite ligands react with RLi reagents (Figure 3-10), giving heterodinuclear complexes with acyl or benxoyl ligands bridging the molybdenum and lithium ions.[76,82,83] X-ray structures show the Li^+ is also bound to the crown ether, an example of which is shown in Figure 11.[76,82,83]

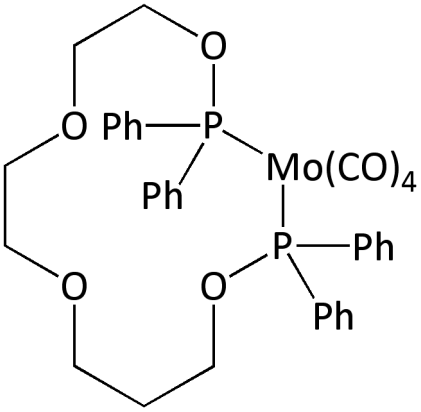

Figure 3-10. *cis*-($Mo(CO)_4[Ph_2(OCH_2CH_2)_3OPPh_2]$).[82]

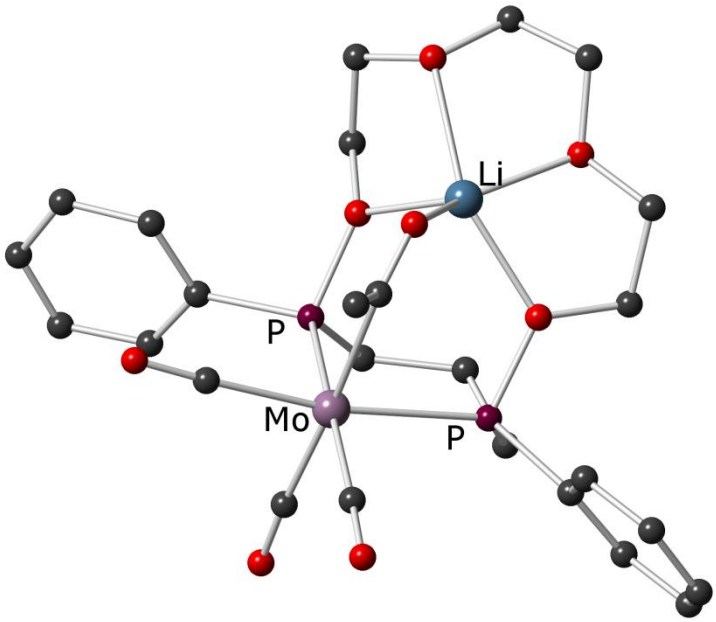

Figure 3-11. Molecular structure of fac-$Mo(CO)_3$(MeCOLi){[15]P_2O_4}, where [15] = meso-11,15-diphenyl-1,4,7,lO-tetraoxa-l1,15-diphoaphacyclopentadecane.[83] Carbon is shown in grey and oxygen in red.

There are also several examples of synthetic N_2-activation complexes that contain alkali metal ions coordinated to the π system of the bound activated N_2.[84,85,86-88] These ligands contain electron-rich aromatic rings rather than hard polyethers, and appear to exhibit π-cation interactions between the coordinated Na^+ or K^+ and both the electron rich aromatic

rings and the π system of the bound N_2.

Chirik *et al.* synthesized a bis(indenyl)zirconium complex, (η^5-C_9H_5-1-^{i}Pr-3-Me)$_2ZrCl_2$ ((1-4)$ZrCl_2$) which forms the bis(indenyl)zirconium end-on dinitrogen compound [(1-4)Zr-NaCl]$_2N_2$ (Figure 3-12) when reduced with a Na(Hg) amalgam under N_2.[86] The reaction could be repeated using ((1-4)$ZrBr_2$) and ((1-4)ZrI_2). When benzene-d_6 solutions of [(1-4)Zr-NaX]$_2N_2$ (X = Cl^-, Br^-, I^-) were exposed to 1 atm H_2 hydrogenation of N_2 occurred, forming the hydrido zirconocene hydrazido complex [(1-4)ZrH]$_2$(N_2H_2) and eliminating NaCl.[86] When one Na^+ ion is sequestered from Chirik's complex, the N_2 is only modestly activated, and upon exposure to an H_2 atmosphere N-H bond formation does not occur. It was not possible to isolate a product in which both Na^+ ions were sequestered, and no N_2H_2 formed upon hydrolysis, again suggesting weak N_2 activation.[86]

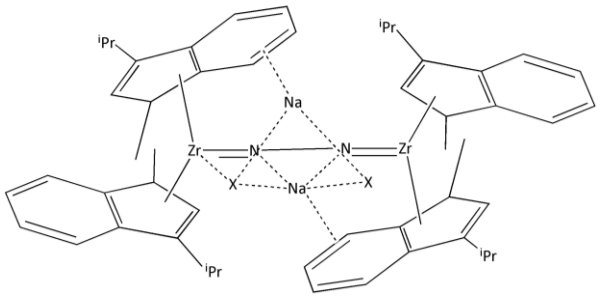

Figure 3-12. [(1-4)Zr-NaX]$_2N_2$ (X = Cl^-, Br^-, I^-).[86]

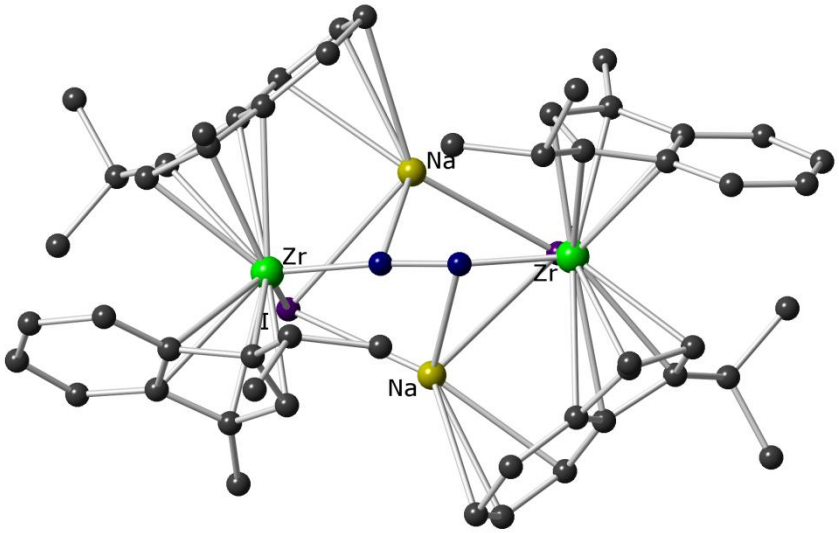

Figure 3-13. Molecular structure of $[(1\text{-}4)Zr\text{-}NaI]_2N_2$ synthesized by Pun and Chirik.[86] Carbon is shown in grey.

Holland *et al.* utilized a bulky β-diketiminate ligand, 2,2,6,6-tetramethyl-3,5- bis(2,4-diisopropylphenylimido)hept-4-yl (1-5), to isolate three-coordinate Co and Fe complexes, including a dimeric three-coordinate Co(I) hydride complex.[84,85,87,88] The halves of the dimer are held together by K^+ ions interacting with the ligand's aryl rings through π-cation interactions. The K^+ ions are also close (2.60(2) and 2.67(2) Å) to the hydride ligands. Upon exposure to N_2 the hydride ligands are replaced by an end-on bridging N_2 ligand (Figure 3-14), in which there are also K^+-aryl interactions, as we as interactions between K^+ and the N_2 π bond.[84,85] Similar complexes with Fe instead of Co also exhibit these π-K^+ interactions (Figure 3-15).[87,88]

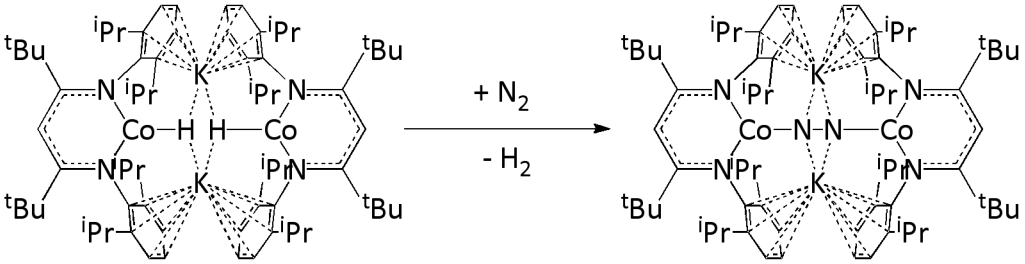

Figure 3-14. Conversion of $K_2[(1\text{-}5)Co(\mu\text{-}H)]_2$ to $K_2[(1\text{-}5)CoNNCo(1\text{-}5)]$.[87]

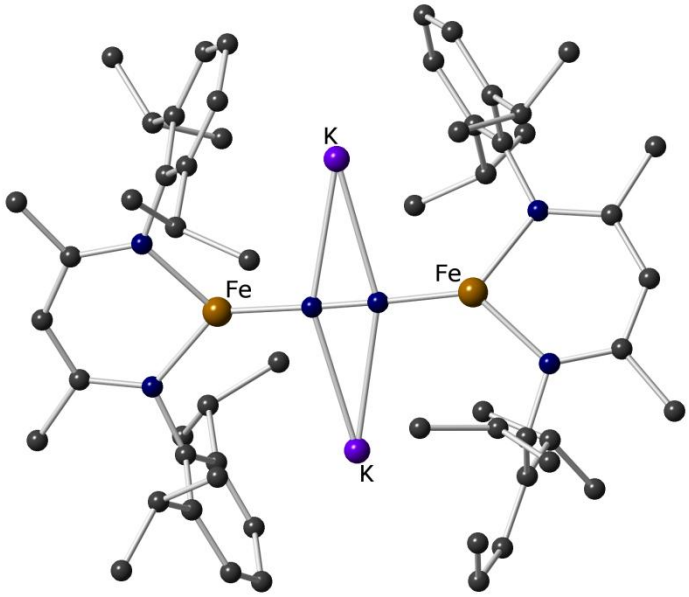

Figure 3-15. Molecular structure of $K_2[(1\text{-}5)FeNNFe(1\text{-}5)]$ synthesized by Holland *et al.*[87] Carbon is shown in grey and nitrogen in blue.

VIII. Alkali(ne Earth) Cation Sensors and Molecular Switches

Complexes in which alkali(ne earth) metal ion binding perturbs the electronic absorbance spectroscopy or electrochemistry can be used as visible sensors or redox sensors for these metals. They can also serve as molecular switches. Since most transition metals absorb visible light and are redox active, transition metal complexes with a coordination site for alkali(ne earth) cations are promising targets for cation sensors. However, in order to be

useful the sensor must have both great affinity and selectivity for a specific cation, which has proven to be a significant challenge.

One promising Mg^{2+} sensor or molecular switch is an azacrown receptor based Ir(III) complex.[89] This complex is a member of a class of complexes known as ionophore-luminophores, so named because they have an affinity for a certain cation, and upon binding, the cation induces luminescence. The crown-less cyclometallated Ir(III) complex [Ir(III)(2-phenylpyridine)$_2$(5,5'-dimethylbipyridine)]ClO_4 (1-6, Figure 3-16) luminescences (ϕ = 0.20, λ_{em} = 558 nm, λ_{em} = 400 nm).[89] The luminescence is extinguished in a similar complex containing 15-azacrown-5 substituents (1-7, Figure 3-16), due to photoinduced electron transfer (PET) from the nitrogen atom of the azacrown ether to the Ir(III) center.[89] Complex 1-7 binds Na^+ (log K_1 = 3.93(4), log K_2 = 2.8(1)), Mg^{2+} (log K_1 = 4.58(4), log K_2 = 2.8(1)) and Ca^{2+} (log K_1 = 6.1(1), log K_2 = 3.2(2)), and K^+ with a low binding affinity. However, luminescence is switched on again only by Mg^{2+} (ϕ = 0.15, λ_{em} = 475 and 507 nm , λ_{em} = 380 nm), which the authors attribute to stronger interaction between Mg^{2+} and the aza-crown nitrogen due to the higher charge density of the Mg^{2+}.[89]

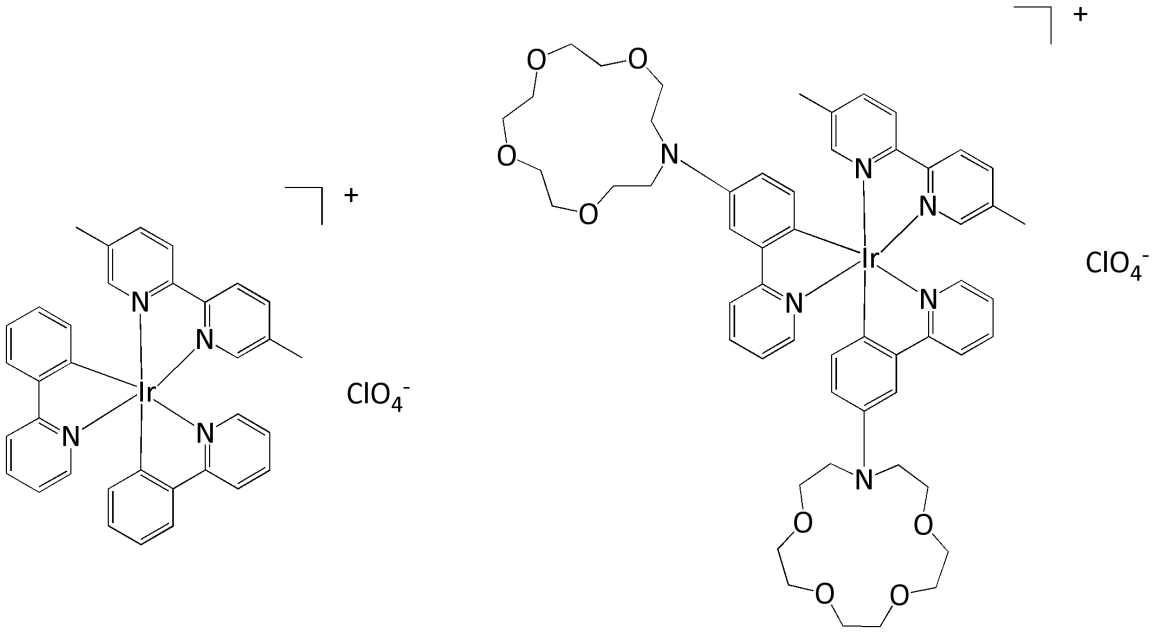

Figure 3-16. [Ir(III)(2-phenylpyridine)$_2$(5,5'-dimethylbipyridine)]ClO_4 (1-6, left) and [Ir(III)(13-(4-(pyridin-2-yl)phenyl)-1,4,7,10-tetraoxa-13-azacyclopentadecane)$_2$(5,5'-dimethylbipyridine)]ClO_4 (1-7, right).[89]

Another approach to cation sensors are ferrocenophane complexes with crown ether substituents. The polyoxaferrocenophanes 1-7_n, n = 0 – 4, shown in Figure 3-17, can extract a percentage of alkali metal picrate salts from the aqueous to organic phase. For example, 1-7_4 extracts 29.1% of Rb^+ from 1:1 CH_2Cl_2/H_2O containing $7*10^{-4}$ M of the polyether, $7*10^{-4}$ M picric acid and 0.1 M KNO_3. 1-7_4 extracts metal ions in the order $Tl^+>Rb^+>K^+>Cs^+>Na^+$.[90] ^1H NMR and Mossbauer spectroscopy suggests possible interaction between the Fe center and complexed cation.[90] However, in a crystal structure of the NaNCS complex, the Fe-Na distance is 4.129 Å, suggesting the Fe is not directly involved in complex formation and Fe-N(CS) distance is 2.541 Å.[91]

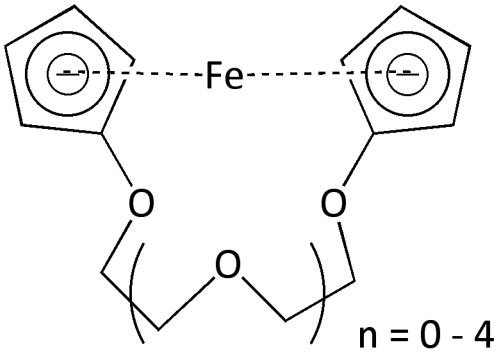

Figure 3-17. Polyoxaferrocenophanes 1-7_n.[90]

Bernhardt and Hays synthesized a series of cyclam ligands with benzo crown ether substitents of varying sizes (1-8_n, n=1-3) (Figure 3-18) and synthesized and characterized the Co(III) complexes of these ligands.[92] Coordination of the alkali metal ions resulted in an anodic shift in the Co(III/II) couple, enabling determination of their binding constants for alkali metals ions (M^+) electrochemically using the equation

$$\Delta E = \frac{RT}{F} \ln[\frac{1+K_{red}(M^+)}{1+K_{ox}(M^+)}].$$

However, the complexes do not show selectivity for a specific cation, which is surprising given that benzo crown ethers have been shown to have differing affinities for cations depending on their size.[69,70] Sample binding data for the $[Co(III)(1\text{-}8\_2)(OH)]^{2+}$ complex is listed in Table 3-1.

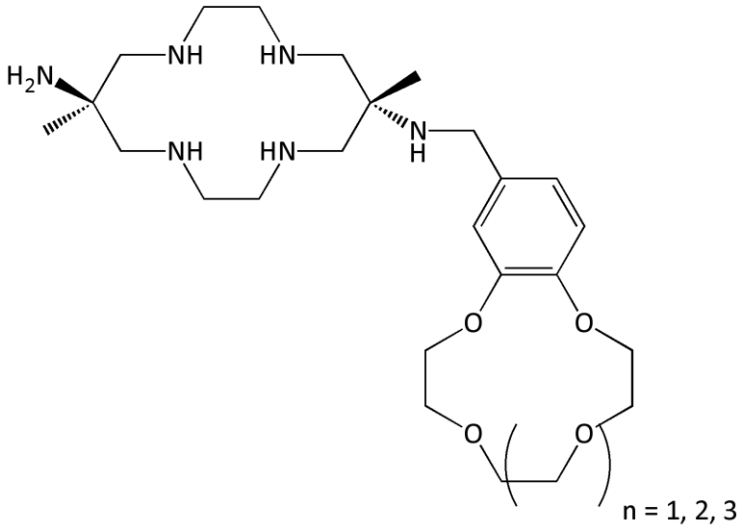

Figure 3-18. Cyclam ligands with benzo crown ether substituents of varying sizes (1-8_n, n=1-3).[92]

	Li^+	Na^+	K^+
log K_{red}	2.4(1)	2.4(1)	2.3(1)
log K_{ox}	Small	1.1(6)	Small
$\Delta E_{1/2}$ (mV)	41	42	30.5

Table 3-1. Sample binding data for the $[Co(III)(1\text{-}8\_2)(OH)]^{2+}$ complex for alkali metal cations M^{n+} [92]

Other ligands that have been combined with crown ethers are bipyridine and phenanthroline ligands, which exhibit changes in fluorescence spectroscopy upon alkali metal complexations and phthalocyanines and porphyrins, which exhibit changes in EPR, UV-visible absorption spectroscopy and electrical conductivities upon cation binding.[76] The change in electrical conductivity is due to the formation of supramolecular stacks upon complexation of large alkali metal cations.[76]

IX. Applications to Crystal Engineering

Another area where transition metal ion-alkali(ne earth) metal ion interactions are of interest is crystal engineering and self-assembling. There has been a great deal of work in organometallic crystal engineering, much of which utilizes hydrogen-bonding.[93,94] This includes tradition hydrogen-bonding between nitrogen, oxygen and fluorine atoms,[95,96,97,98] as well as charge-assisted hydrogen bonding, in which hydrogen-bonding interactions are combined with Coulombic attractions.[99] Other types of hydrogen-bonding investigated include coordination-assisted hydrogen bonding, in which metal coordinated methylidyne and methylene ligands participate in intermolecular C-H-O bonding networks,[100] and relatively strong hydrogen-bonding between C-H groups and C-C triple bonds.[101,102] Other interactions utilized include halogen bonding,[103] and other Lewis acid-base interactions, most notably those between a coordination complex with ligands bearing Lewis basic groups capable of coordinating to a second Lewis acid metal center.[104,105]

The interactions described in this thesis fall into this last category, with the second Lewis acid metal center being an alkali metal. Previous work has utilized alkali ion coordination to influence the three-dimensional framework of Cu(III) bis-1,2-dichalcogenene complexes, in which pyrazine ligands were used allowing alkali metal coordination to the N atoms of the pyrazine rings.[106] It was found that when Na^+ or Li^+ were used as cations, the alkali metal-coordinated Cu(III) monoanionic complexes formed one-dimensional stacks, whereas when the bulky tetrabutylammonium cation was used, there were no short contacts or hydrogen bonds detected between the monoanionic Cu(III) complexes.

Alkali metal ions have also been found to influence the self-assembly of transition metal clusters. Zhang *et al.* investigated Ni(II) complexes with the ligand (pyridine-2-

yl)methanol (1-9).[107,108] They found that when 10 equivalents NaH were added to the dinuclear complex $[Ni(\mu\text{-}Cl)(1\text{-}9)]_2Cl_2$, an unprecedented mixed Na-Ni complex formed in small yield (Figure 3-19).[105] Alternatively, the Na-Ni complex could be synthesized by mixing the ligand, NaH and $[NiCl_2(DME)]$ (DME = 1,2-dimethoxyethane) in a 3.2:5:1 ratio.[105] When the ligand/Ni ratio is decreased to 2.2:1 a different cluster, $[Ni_7(1\text{-}9)_{12}]Cl_2$ is formed, whereas decreasing the ligand/Ni more slightly, to 2.8/1, gives a different, wagon wheel-type complex, $[Ni_6Na(1\text{-}9)_{12}]Cl$.[105] The ability to synthesize unique transition metal clusters of differing structures and compositions using self-assembly may prove valuable in fields ranging from magnetism to catalysis. As shown by the Na-Ni clusters, alkali metals can play important roles in dictating cluster self-assembly.

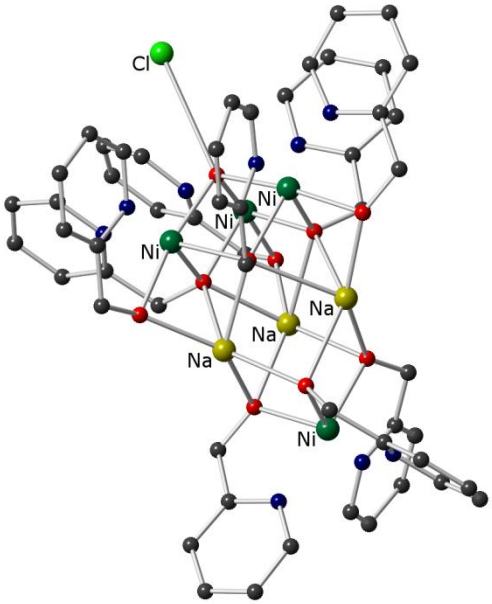

Figure 3-19. $[\{Ni(1\text{-}9)\}_3(\mu_2\text{-}(1\text{-}9))_3(\mu_3\text{-}OH)(\mu_5\text{-}Na)_3\{Ni(1\text{-}9)_3\}]Cl$.[107]

X. Outline for Part II of Thesis

The examples given in this chapter are but a few examples of the influence alkali(ne earth) metal ions can have on transition metal complexes, and visa versa. Part II of this thesis describes efforts to design heterodinuclear hard-soft ligands, and the effect of alkali metal ions on the local and extended structure of a Co(II) complex. The following is an outline for Part II of this thesis.

Chapter 4

I. Ligand Design

II. Synthesis and Characterization of LM and $[CoLM(NO_3)]BPh_4$

III. Synthesis and Characterization of LBz_1, $[Co(LBz\_1)](PF_6)_2$ and $[Zn(LBz\_1)](PF_6)_2$

IV. Experimental Section

Chapter 5

I. Overview

II. Synthesis

III. Structural Characterization

IV. NMR Spectropscopy

V. UV-Visible Absorption Spectroscopy and Calculation of Binding Constants

VI. IR Spectroscopy

VII. Electrochemistry

VIII. Ligand Design

IX. Conclusions

X. Experimental Section and Supplementary Material

Chapter IV. Initial Attempts at Heterodinuclear Ligand Design

I. Ligand Design

The first set of ligands designed contained a tetradentate, tripodal ligand, *N*,*N*-bis(R_1R_2-*N*-aminoethyl)-2-(aminomethyl)pyridine (R_1R_2pdt), (Figure 4-1) appended to a bridging aza polyethylene glycols. The ligand design is shown in Figure 4-2. The tripodal group can potentially be used as a neutral ligand, or if the pendant amines are secondary, can be deprotonated to create a dianionic amide- and amine- based ligand. There are several examples of transition metal complexes of the latter[109-114] and the former.[115-117] The ligand structure has the advantage of containing only two substitutable amines, unlike the similar tris(2-aminoethylamine) (tren) ligand, which contains three substitutable amines, which would make the addition of a polyether bridge difficult.

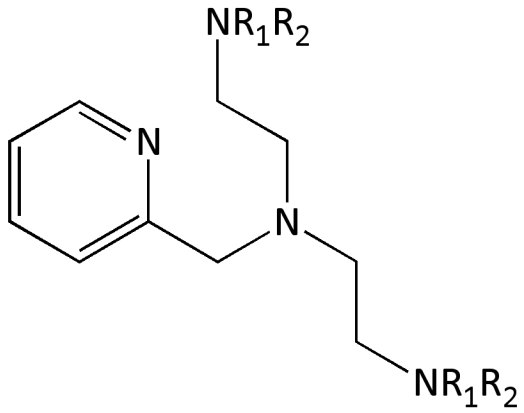

Figure 4-1. N,N-bis(aminoethyl)-2-(aminomethyl)pyridine (R_1R_2pdt).

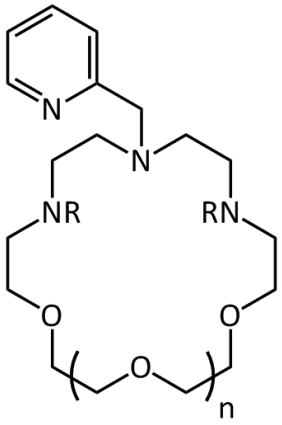

Figure 4-2. Intended ligand design, in which a bridging polyether is appended to the tripodal amine- or amide-amine- ligand.

The polyether bridge can function in a similar manner to a crown ether in coordinating alkali metals, though with a lower binding affinity since unlike a crown ether it does not possess a predisposed cavity tailored for the size and coordination preference of the alkali metal.[69,70] As mentioned in Chapter 3, salen- and salophen-based ligands that incorporate polyether bridges have been shown to coordinate transition metal ions and alkali or alkaline earth metal ions together.[73,75,79,80,81,76,77,118,119] Additionally, macrocycles with polyether bridges have been shown to facilitate coordination of neutral guest molecules containing hydrogen donors such as urea.[119] The guest molecule can coordinate to the transition metal via the carbonyl group and to the polyether oxygens via hydrogen bonding, another potentially interesting area of research.

II. Synthesis and characterization of LM and $[CoLM(NO_3)]BPh_4$

The first ligand attempted, LH_n, contained a polyether bridge appended to the tetradentate N_4 group, with R = H (Figure 4-4). The number of ether units 'n' in the bridge could potentially be varied to incorporate alkali or alkaline earth ions of varying sizes, and

the secondary amine groups could be either left protonated so that the ligand was neutral or deprotonated so that it was dianionic. The proposed synthesis of LH_n is shown in Scheme 4-1. The synthesis of the ligand LH_1 was attempted although this crown would likely be too small to coordinate an additional cation once the complex was coordinated to a transition metal, since the successful synthesis of this ligand could be applied to ligands with longer polyethylene glycol bridges, and the starting materials for this ligand were the least expensive.

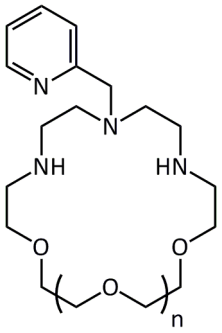

Figure 4-3. Ligand LH_n.

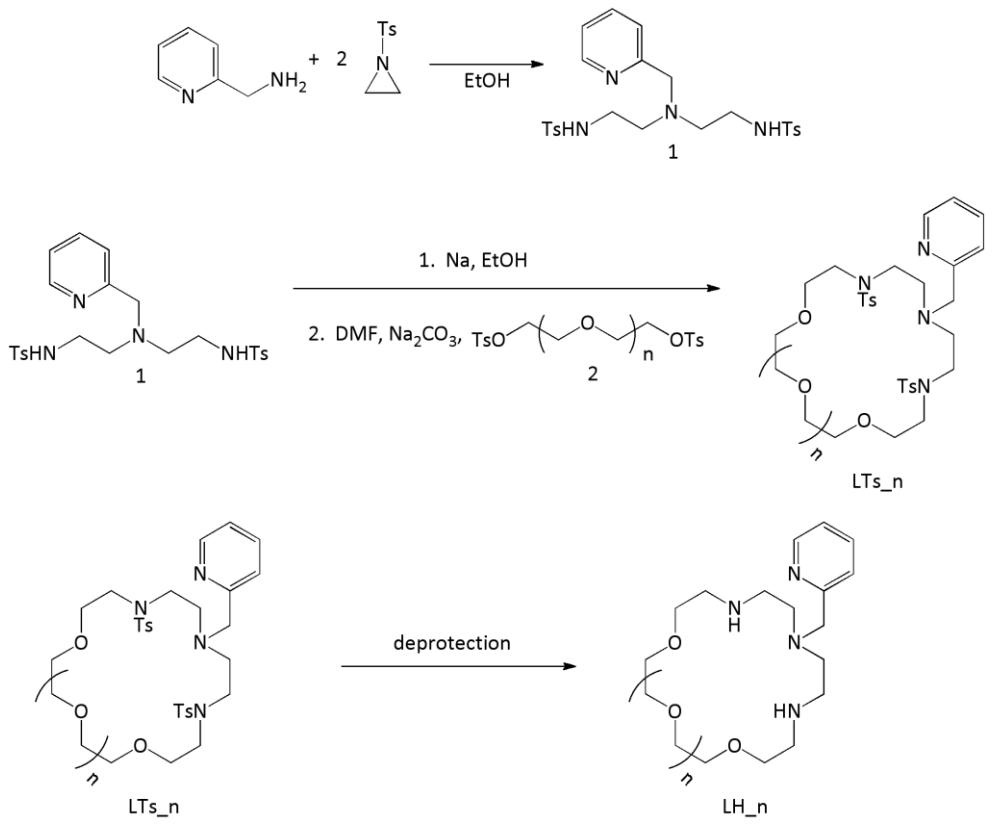

Scheme 1. Proposed synthesis for LH_n.

Precursors 1 and 2 were synthesized using literature procedures.[111,120] Precursor 1 was not deprotected at this stage in the synthesis because attempts to add tetraethylene glycol ditosylate or tetraethylene glycol diiodide to the primary amine led primarily to cyclization of the polyether on the same amine as evidenced by mass spectrometry, giving two smaller 12-membered $N(CH_2O)_3CH_2$ rings rather than the larger 18-membered ring desired. Instead, the *N*-tosylated precursor 2 was deprotonated with NaOEt, and then reacted with 2. The reaction was run in a dilute manner and 2 was added in a dropwise fashion over several hours to facilitate the intramolecular reaction. LTs_1 could be purified by column chromatography and isolated in 42% yield. A more detailed procedure can be found in the Experimental Section.

Sulfonamides are one of the most stable nitrogen protecting groups and cleavage of

an N-tosyl group, particularly when the amine involved is a basic alkyl amine, is difficult and requires harsh conditions. Most are stable to basic hydrolysis and catalytic reduction.[121] The two main means of deprotecting involve either hydrolysis or nucleophilic attack by phenol or a similar alcohol under highly acidic conditions (HBr/AcOH, H_2SO_4, HBr/AcOH + phenol),[111,120,121] or reducing conditions ($NaAlH_2(OCH_2CH_2OCH_3)_2$, sodium naphthalenide or anthacenide, Li or Na + NH_3, Na(Hg) + Na_2HPO_4).[121] Heating the sulfonamide with a solution of HBr and AcOH with an excess of phenol is one of the most common means of deprotection[122,123,124,125] so this method was attempted first.

Briefly (please see the Experimental Section for a full description of the preparation), LTs_1 was heated to 80 °C with 33% HBr/acetic acid and an excess of phenol for 30 hours. After cooling to room temperature the product was precipitated by addition of Et_2O, collected, neutralized, and purified by column chromatography to give the pure product as a colorless oil in 37% yield. However, the NMR spectroscopy and mass spectrometry did not match that expected for LH_1. Though the aromatic and alkyl protons could all be assigned in the ^1H NMR, the amine protons could not be located. The ^{13}C NMR spectra showed only five peaks in the alkyl region corresponding to five distinct carbon atoms, rather than the seven peaks expected. (However, only four aromatic peaks could be located, rather than the five expected from the 2-substituted pyridyl group.) Additionally, whereas the expected exact mass for LH_1 is 352.24744, mass spectroscopy, done by positive electrospray ionization, show peaks at m/z = 335.24380 (relative intensity = 100%), 17.00364 m/z units smaller than the expected mass and 18.01147 m/z units smaller than [LH_1 + H^+].

These discrepancies were resolved upon metallating this ligand and obtaining a crystal structure. The complex was metallated with $Co(NO_3)_2$ in MeOH, followed by the

addition of $NaBPh_4$ to precipitate the complex. Recrystallization from diffusion of Et_2O into a CH_2Cl_2 solution of the product, or by layering hexanes onto a CH_2Cl_2 solution of the complex, gave X-ray quality pale green needle crystals. The crystal structure revealed that the ligand was not the intended LH_1. Rather the ligand had undergone a dehydration reaction when it had been deprotected in the previous step, losing the central polyether oxygen and cyclizing to form two smaller morpholine rings. The reaction scheme for the actual ligand synthesized, termed LM, is shown in Scheme 4-2, and the molecular structure of the Co(II) complex, $[CoLM(NO_3)]BPh_4$, is shown in Figure 4-6.

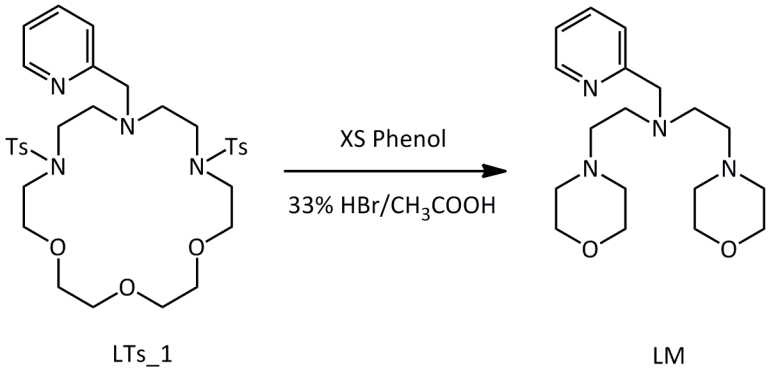

Scheme 4-2. Synthesis of the ligand LM.

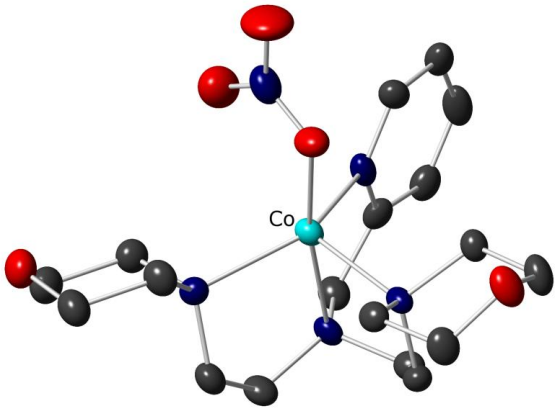

Figure 4-4. $[CoLM(NO_3)]^+$, thermal ellipsoids drawn at 50% probability. The tetraphenylborate counterion is omitted for clarity. Carbon is shown in grey, oxygen in red and nitrogen in blue.

Morpholine is synthesized by the dehydration of diethanolamine with 70% H_2SO_4 (Figure 4-7).[126] In this synthesis one oxygen acts as the nucleophile and the other as part of the leaving group. In the synthesis of LM, the nitrogen must act as the nucleophile, and the central polyether oxygen as part the leaving group. The pKa of a secondary amine nitrogen would be expected to be much higher than that of an ether oxygen (for example, the pKa of $Et_2O/Et_2(OH)^+$ is -3.5,[127] whereas the pKa of $(Et)_2NH/(Et)_2NH^+$ is 11.0[128]), so after deprotection the resulting secondary amine would be expected to be protonated over the ether oxygen, and therefore unable to act as a nucleophile. The tosyl group is electron-withdrawing,[129] making protonation of the nitrogen less favorable, which would allow it to act as the nucleophile. Therefore, a likely mechanism is that the tosylated nitrogen displaces the protonated central ether oxygen before being deprotected to form an energetically favorable six-membered ring. The phenol oxygen could then easily displace the resulting quaternary nitrogen from the sulfonamide to leave the morpholine-type ring. Due to the highly acidic reaction conditions, the deprotected nitrogen would be expected to be protonated and therefore not undergo further reaction. The proposed mechanism is shown in Figure 4-8.

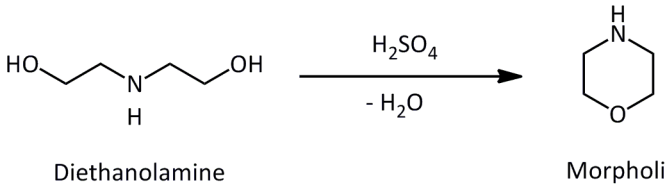

Figure 4-5. Synthesis of morphine by the dehydration of diethanolamine with H_2SO_4.[126]

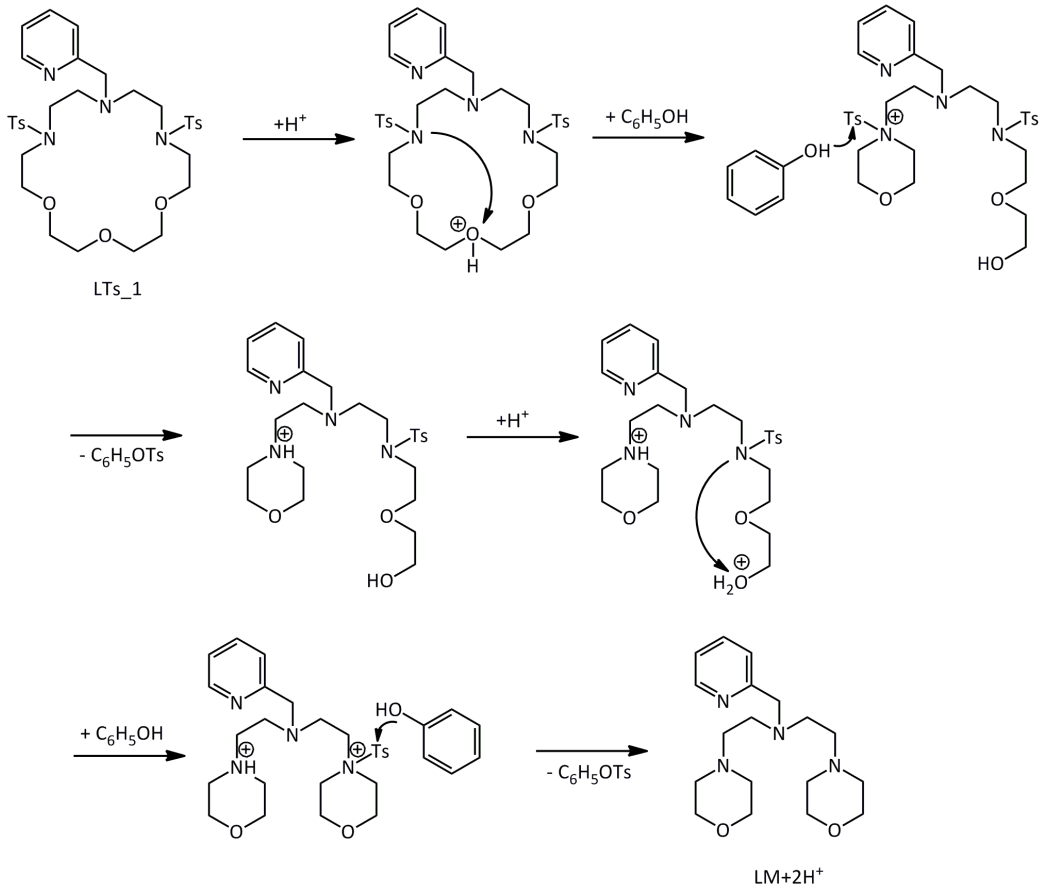

Figure 4-6. Proposed mechanism for formation of LM from LTs_1 with HBr/acetic acid and excess phenol at 80 °C.

The Co(II) complex of LM, $[CoLM(NO_3)]BPh_4$ crystallizes in the *C*c space group, with two complexes in the unit cell. The structure has an R_1 value of 5.3%. $[CoLM(NO_3)]^+$ has a very distorted trigonal bipyamidal geometry, with the Co(II) coordinated to the pyridyl and three amino groups of the ligand as well as a unidentate NO_3^- ligand. The τ_5 value is 0.66.[130] There is one reported structure of a five-coordinate complex of a neutral pdt ligand, $[Cu(H_2pdt)]Cl$ (Figure 4-9),[117] which has a τ_5 value of 0.86, closer to an ideal trigonal bipyramidal geometry. There are several reported five-coordinate structures of twice deprotonated pdt ligand derivatives, which have a range of different τ_5 values. For example, the complex $[Sc((Me_3Si)pdt)(Me_3SiCH_2)]$ has τ_5 = 0.45,[111,120,121] and the complex

$[Co(((OC)NH(^tBu))_2pdt)(O_2CCH_3)]^+$ [114] has τ_5 = 0.75 and $[Ti((Me_3Si)_2pdt)(NC_6H_3Pr^i_2\text{-}2,6)]$ has τ_5 = 0.79.[131] Thus, $[CoLM(NO_3)]^+$ has a τ_5 value within the reported range for complexes of pdt-derived ligands.

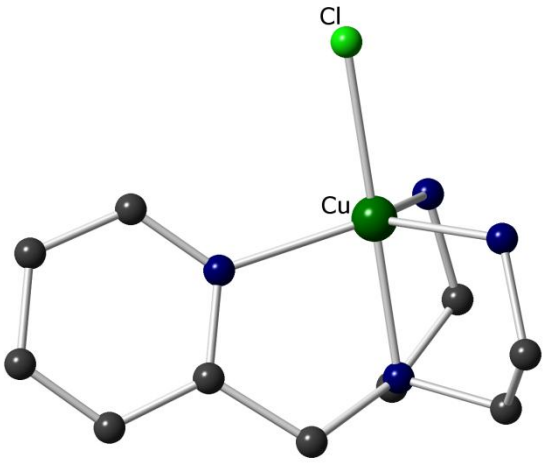

Figure 4-7. $[Cu(H_2pdt)]Cl$.[117] Carbon is shown in grey and nitrogen in blue.

The unidentate nitrato ligand gives stretching bands in the IR spectrum at 1488 (ν_5 (B_2)), due to asymmetric NO_2 stretching, 1385 (ν_1 (A_1)), due to symmetric NO_2 stretching, and 1113 cm^{-1} (ν_5 (A_1)), due to NO stretching. The separation between the two highest frequency bands is 103 cm^{-1}, which is typical for unidentate nitrato complexes; bidentate complexes tend to have larger separations.[132]

Deprotection of LTs_n precursors using a reductive rather than acidic route may produce the desired LH_n ligands rather than the LM ligand. These methods were explored briefly, but not in depth.

III. Synthesis and characterization of LBz_1, $[CoLBz\_3](PF_6)_2$ and $[ZnLBz\_3](PF_6)_2$

An alternative ligand explored was the LBz_1 ligand, in which (from Figure 1) R = Bz and n = 1. The use of an R-group other than H eliminates the need for a deprotection

step, but it does not allow the ligand to be deprotonated to create the dianionic ligand. This is a disadvantage in a ligand designed to coordinate two positively charged metals, but an external bridging anion may allow for coordination of both a transition and alkali metal.

The synthesis for LBz_1 is shown in Scheme 4-3. Briefly (a full account is in the Experimental Section), 1,11-tetraethylene glycol dichloride was heated with an excess of ethanolamine followed by addition of two equivalents NaOH to give 6,9,12-Trioxa-3,15-diazatetradodecane-l,l6-diol (3). 3 was then heated with benzyl chloride and Na_2CO_3 to give 3,15-benzyl-6,9,12-Trioxa-3,15-diazatetradodecane-l,l6-diol (4), which was then treated with an excess of thionyl chloride in benzene to give 3,15-benzyl-6,9,12-Trioxa-3,15-diazatetradodecane-l,l6-dichloride (5). 5 was then cyclized with 2-aminopyridine by refluxing with Na_2CO_3, to give the ligand LBz_1, a yellow oil, after purification.

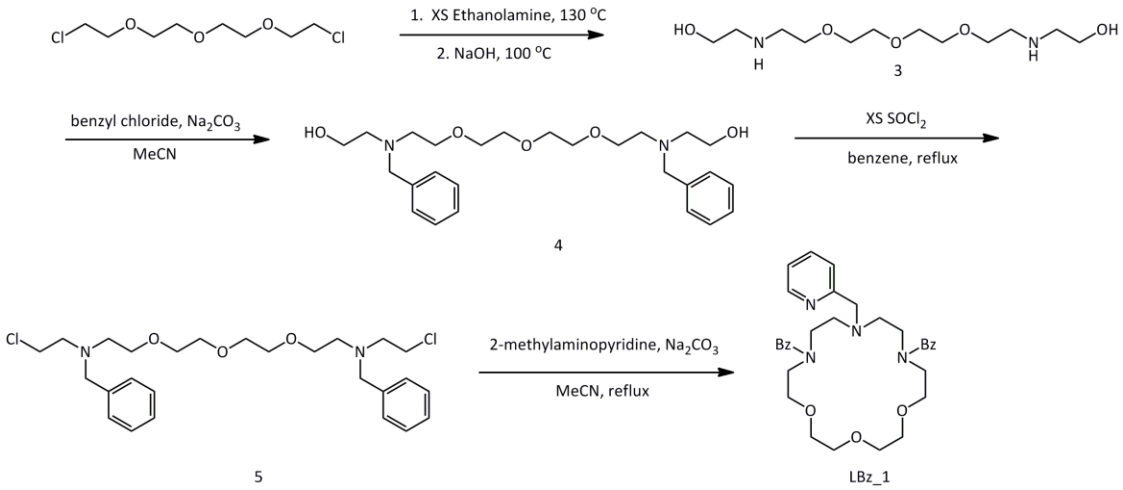

Scheme 4-3. Synthetic scheme for LBz_1.

LBz_1 was metallated using two different strategies. In the first, 1 equivalent of LBz_1 and 1.5 equivalents of $Co(NO_3)_2$ were dissolved in MeOH, followed by the addition of saturated NH_4PF_6 to precipitate $[Co(LBz\_1)](PF_6)_2$ as a pink powder that could then be recrystallized by diffusion of Et_2O into an MeCN solution of the product. The complex $[Zn(LBz\_1)](PF_6)_2$ was also desired to gain insight from its diamagnetic NMR spectrum, but

X-ray quality crystals could not be grown from the above strategy. Thus, in the glovebox, 1 equivalent each LBz_1 and $ZnCl_2$ were combined in DMF, followed by the addition of two equivalents $AgPF_6$. The DMF was removed and $[Zn(LBz\_1)](PF_6)_2$ extracted into CH_2Cl_2, leaving two equivalents of AgCl behind. X-ray quality crystals were grown by diffusion of Et_2O into an MeCN solution of $[Zn(LBz\_1)](PF_6)_2$, decanting the filtrate from a small amount of oily residue that appeared and letting the filtrate sit overnight. Detailed procedures can be found in the Experimental Section.

$Co(LBz\_1)](PF_6)_2$ and $[Zn\ (LBz\_1)](PF_6)_2$ are isostructural. The molecular structures are shown in Figure 4-10. Both crystallize in the orthorhombic $P2_12_12_1$ space group and both have distorted octahedral geometries about the transition metal, with the metal coordinating to the pyridyl and three amino nitrogens of the ligand, as well as the non-central oxygens of the crown ether. Coordination to the non-central oxygens forms energetically favorable five-membered rings composed of the transition metal, the coordinating N(Bz), the two ethylene carbons, and the oxygen. R_1 is 6.05% for the $[Co(LBz\_1)](PF_6)_2$ structure and 8.31% for the $[Zn(LBz\_1)](PF_6)_2$ structure.

A.

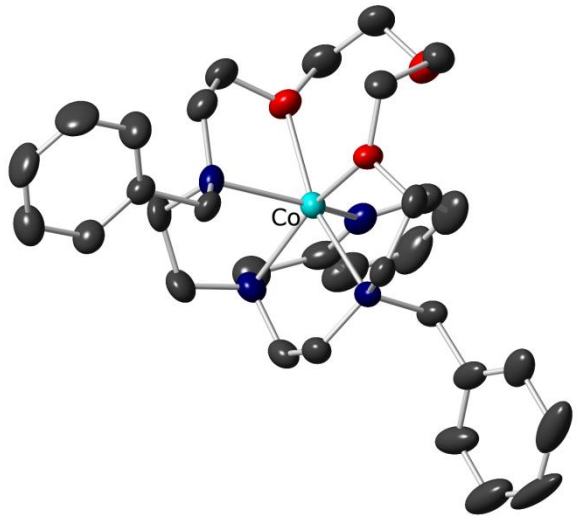

B.

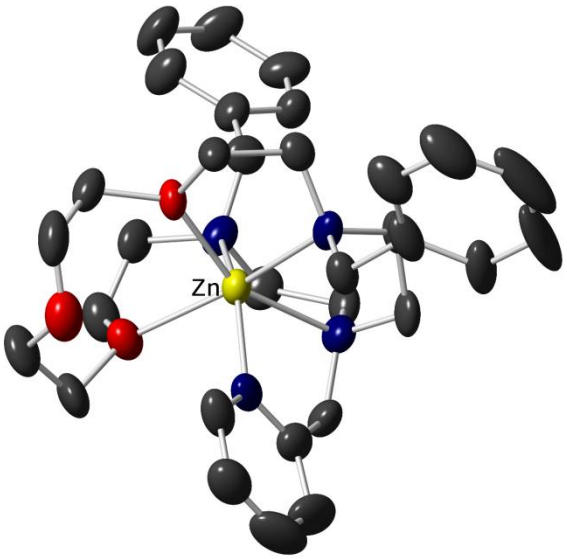

Figure 4-8. Molecular structures of $[Co(LBz\_1)]^+$ (A, top) and $[Zn(LBz\_1)]^+$ (B, bottom). Thermal ellipsoids drawn at 50% probability. Carbon is shown in grey, nitrogen in blue and oxygen in red. Counterions have been omitted for clarity.

The solution state geometry of $[Co(LBz\_1)]^{2+}$ and $[Zn(LBz\_1)]^{2+}$ was investigated through solution state ^1H NMR spectroscopy. The paramagnetic ^1H spectrum of $[Co(LBz\_1)](PF_6)_2$ shows 12 large peaks and > 13 smaller peaks, many more than the 15 peaks that would be expected if the ligand had a C_2 axis of symmetry and existed in only one form in solution. The diamagnetic ^1H NMR spectrum of $[Zn(LBz\_1)](PF_6)_2$ shows a great deal of broadening amongst the alkyl protons, which indicates that the coordination of the crown ether oxygens to the metal is fluxional on the NMR time scale (1.0 s). On the other hand, the pyridyl peaks in the aromatic region are fairly sharp, indicating there is little fluxionality in the coordination of the pyridyl ligand to the metal.

Addition of one equivalent $NaBPh_4$ to the free ligand resulted in a peak with m/z = 555.33 (ligand + Na^+, relative intensity =100%) in the mass spectrum and broadening and a change in chemical shift of the peaks in the alkyl region of the ^1H NMR spectrum, indicating coordination of the polyethylene glycol bridge oxygens to Na^+. The ^1H NMR spectra are shown in in Figure 4-10. The polyethene gycol moiety is not available for alkali metal coordination in $[Co(LBz\_1)]^{2+}$ and $[Zn(LBz\_1)]^{2+}$, but it was attempted to add an alkali metal by adding Na^+ salts with anions that have high affinities for transition metals and could displace the weakly bound ether oxygens from the transition metal center. The anions might also serve as a bridge between the transition metal and alkali metal. One equivalent NaNCS, NaCN, NaNCO, NaN_3 and NaOAc, as well as $Bu_4N(NCS)$, $Et_4N(CN)$ and $Bu_4N(NCO)$ were added to methanolic solutions of $[Co(LBz\_1)](PF_6)_2$ and $[Zn(LBz\_1)](PF_6)_2$. Mass spectrometry showed large peaks for $(LBz\_1)+Na^+$ and $[Co(LBz\_1)]^{2+}$, as well as $[Co(LBz\_1)(NCS)]^+$ when NaNCS was added, but no evidence for coordination of both Co^{2+} and Na^+. IR spectroscopy was done to compare differences in stretching frequencies when Na^+ versus a non-coordinating countercation was used, but no significant differences

were detected. Similar, while ^{1}H NMR spectroscopy of the Zn^{2+} solutions showed a sharpening of alkyl peaks and change in the chemical shifts of the pyridyl protons after adding certain anions, no differences were found when Na^{+} versus a non-coordinating countercation was used.

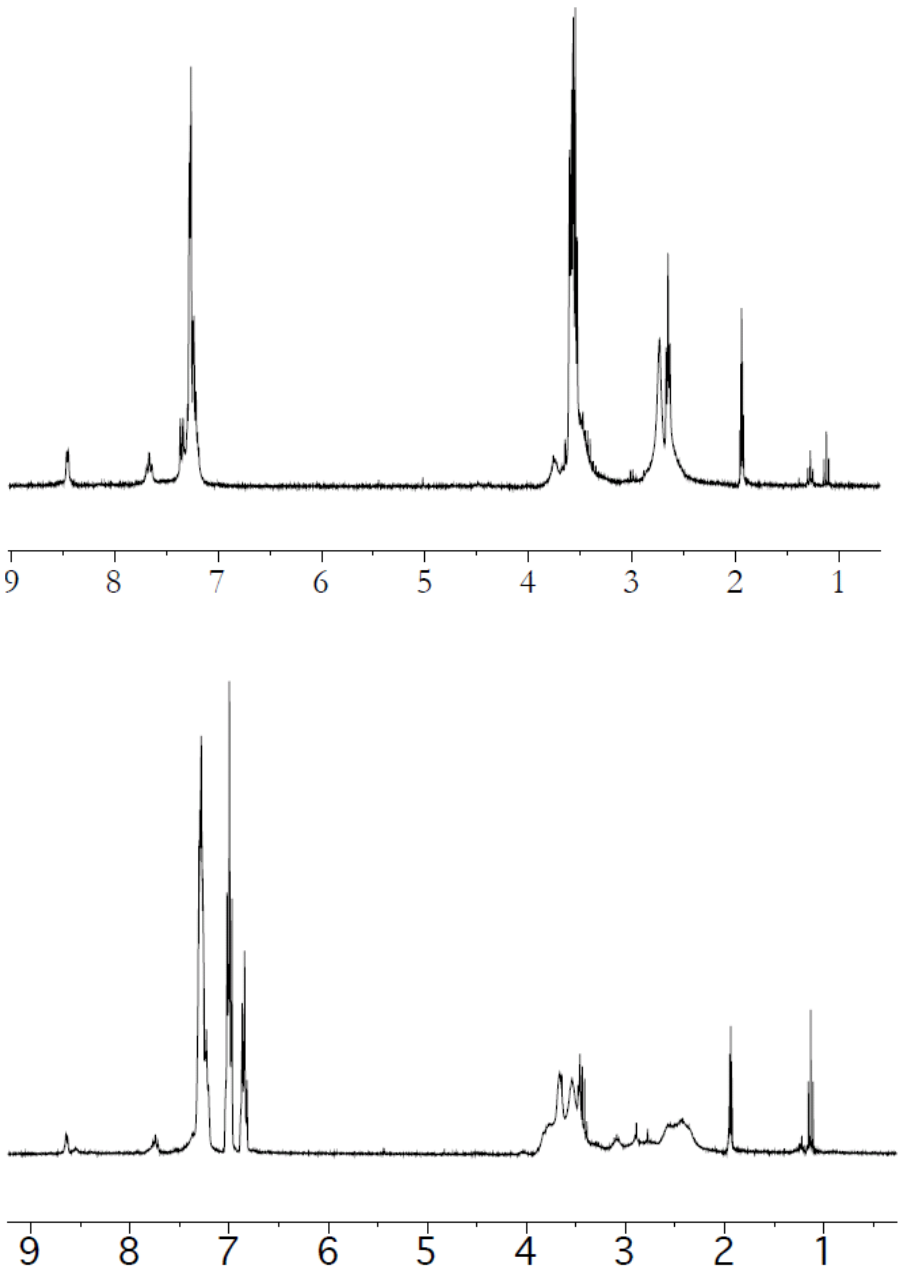

Figure 4-9. ^{1}H NMR spectra of LBz_1 in CD_3CN (top) and LBz_1 + 1 equivalent $NaBPh_4$ in CD_3CN.

The synthesis of the similar ligand (LMe_1) was also attempted in order to be able to look at the effect of the more electron-donating methyl substituent[133] on coordination. 3,15-methyl-6,9,12-Trioxa-3,15-diazatetradodecane-l,l6-diol (6) (Figure 4-11) was synthesized from N-methylethanolamine and 1,11-tetraethylene glycol dichloride in a procedure analogous to that used to synthesize 3. However, attempts to convert 6 to the dichloro derivative with both excess and stoichiometric quantities of $SOCl_2$, in the presence or absence of base (pyridine) resulted in complex product mixtures with neither ^{1}H NMR nor mass spectra resembling that expected for the desired product. Similarly, attempts to convert 6 to the ditosylate by stirring with 2.2 equivalents of tosyl chloride and 3.53 equivalents NaOH failed to produce the desired product. One explanation for the failure to produce 3,15-methyl-6,9,12-Trioxa-3,15-diazatetradodecane-l,l6-dichloride, where 4 was easily synthesized, is that the more electron-donating substituent on the amine allows it to act as a nucleophile to either the chloride or tosyl leaving groups, or with the $SOCl_2$ or tosyl chloride, forming quarternary ammonium centers.

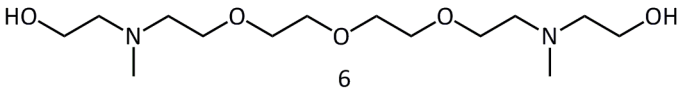

6

Figure 4-10. 3,15-methyl-6,9,12-Trioxa-3,15-diazatetradodecane-l,l6-diol (6).

IV. Experimental Section and Supplementary Material

Ethanol was dried over molecular sieves before use, and Dri-Solv DMF was purchased from Sigma Aldrich. $(2\text{-}NC_5H_4)CH_2N(CH_2CH_2NHTs)_2$ (1) was synthesized using a published procedure[111], as was $TsO(CH_2CH_2O)_2CH_2OTs$ (2).[120]

LTs_1. The reaction was conducted using Schlenk line techniques under N_2. A sodium ethanolate solution (10.7 mmol, 250 mg Na in 17.5 mL EtOH) was added to 1 (4.95 mmol,

2.5 g) in 69 mL EtOH. The reaction was refluxed for forty minutes, the cooled to room temperature and the solvent removed at reduced pressure. The resulting solid was dissolved in DMF (100 mL). Na_2CO_3 (14 mmol, 1.5g) was added, and the resulting suspension heated to 115 °C. 2 (4.95 mmol, 2.5 g) in 50 mL DMF was then added in a dropwise manner. After addition, the reaction was kept stirring at 115 °C overnight, and then cooled to room temperature and filtered. The DMF was removed on a rotary evaporator. Approximately 125 mL each CH_2Cl_2 and H_2O were added to the reaction. The CH_2Cl_2 layer was separated, washed with an additional 125 mL H_2O and dried over $MgSO_4$. The crude product was filtered to remove $MgSO_4$ and the CH_2Cl_2 removed on the rotary evaporator. The crude product was purified via chromatography on Si-60, eluting with EtOAc. The pure product eluted at R_f = 0.22, and upon removal of the solvent was a very pale yellow oil (1.4 g, 42% yield).

MS (positive ESI): M/z Expected for LTs_1 $+H^+$: 661.27297; M/z Measured: 661.27283. Also: 683.25483 (LTs_1 + Na^+)

δ_H(CDCl3, 300 MHz)/ppm: 8.55 (d, J = 6.4 Hz, 1H), 7.68 (t, J = 7.8 Hz, 1H), 7.58 (d, J = 8.4 Hz, 4H), 7.41 (d, J = 7.8 Hz, 1H), 7.21 (d, J = 8.4 Hz, 4H), 7.19 (t, 7.2 Hz, 1H), 3.77 (s, 2H), 3.60-3.54 (m, 12 H), 3.31-3.26 (m, 8H), 2.82 (t, J = 8.1 Hz, 4H), 2.40 (s, 6H)

Lm. LTs_1 (1.97 mmol, 1.3 g), phenol (43.3 mmol, 4.1 g) and 33% HBr/acetic acid (337 mL) were heated at 80 °C for 30 hours. The reaction was then cooled to room temperature, transferred to a large beaker and 700 mL Et_2O were added. The flocculent precipitate was collected on a fritted funnel with Celite to prevent the fine material from washing through the pores of the frit. The oily purple precipitate collected on the Celite was washed with additional Et_2O (1700 mL), and then extracted into deionized H_2O (350 mL) and washed

through the Celite, giving a yellow filtrate. The aqueous filtrate was basified to ~ pH 14 with 10 % aqueous NaOH, and the neutralized crude product then extracted into CH_2Cl_2 (2*~500 mL). The CH_2Cl_2 was removed on a rotary evaporator. The crude product was purified by column chromatography on neutral alumina, eluting with 2% MeOH/CH_2Cl_2. The pure product eluted at R_f = 0.1, and was a colorless oil upon removal of the solvent. (260 mg, 37% yield.)

MS (positive ESI): m/z (%) = 335.24448 (100.00, M + H^+), 357.22641 (6.87, M + Na^+)

δ_H(CDCl3, 300 MHz)/ppm: 8.52 (ddd, J = 4.8 Hz, 1.5 Hz, 1H), 7.66 (td, J = 7.5 Hz, 1.8 Hz, 1H), 7.48 (d, J = 8.1 Hz, 1H), 7.16 (td, J = 6.0 Hz, 1.2 Hz, 1H), 3.84 (s, 2H), 3.70 (t, J = 4.8 Hz, 8H), 2.76 (t, J = 6.6 Hz, 4H), 2.56-2.47 (m, 12H)

δ_C($CDCl_3$, 300 MHz)/ppm: 149.02, 136.42, 123.00, 122.05, 66.77, 60.98, 56.70, 53.99, 51.58

[CoLM(NO_3)]BPh_4. This reaction was conducted in a glovebox under an N_2 atmosphere. LM (0.108 mmol, 36.2 mg) and $Co(NO_3)_2$ (0.102 mmol, 18.7 mg) were stirred for one hour in ~ five mL MeOH. A solution of $NaBPh_4$ (0.197 mmol, 67.3 mg) in ~1 mL THF was then injected into the reaction solution. A pale green precipitate formed almost immediately. The reaction was further stirred 1.5 days, and then collected on fritted funnel, washed with additional MeOH and Et_2O, and dried under vacuum. (56.6 mg, 35.8 % yield) Recrystallization from slow diffusion of Et_2O into a CH_2Cl_2 solution of the product, or layering a CH_2Cl_2 solution of the product with hexanes gave X-ray quality pale green needle crystals.

MS (positive ESI): m/z (%) = 196.58 (83.96, LM+Co^{2+}), 233.11 (100.00, LM+Co^{2+}+DMF), 335.24 (19.43, LM+H^+), 438.17 (32.14, ?), 455.16 (46.12, LM+Co^{2+}+NO_3^-)

1,11-tetraethylene glycol dichloride was synthesized using a literature procedure [134] and ethanolamine was purchased commercially.

6,9,12-Trioxa-3,15-diazatetradodecane-l,l6-diol (3). 3 was synthesized using an a literature procedure for 6,9-Diioxa-3,12-diazatetradodecane-l,l4-diol. [135] Ethanolamine (16.5 g, 0.56 moles) and 1,11-tetraethylene glycol dichloride (7.9 g, 0.03 moles) were stirred and heated at 130 °C for 24 hours. NaOH (2.4 g, 0.06 moles) was then added and the reacted stirred and heated at 100 °C for 50 minutes. The excess ethanolamine was then distilled off, leaving an opaque orange oil. THF was added and the reaction filtered, leaving behind a dark orange liquid. The THF was removed on a rotary evaporator leaving behind a dark orange oil. 15 mL THF was added and the product placed in the freezer overnight, resulting in a thick orange oil on the bottom of the flask and a liquid on top. The liquid was decanted off, leaving the thick oil, which was further dried under vacuum. (5.67 g, 67.5% yield)

δ_H($CDCl_3$, 400 MHz)/ppm: 3.71-3.61 (m, 20 H), 2.80 (t, J = 4.8 Hz, 4H), 2.73 (m, 4H)

HRMS-EI m/z: M^+ calculated for $C_{12}H_{28}N_2O_5+H^+$: 281.20765; found 281.20750 (relative intensity = 100)

3,15-benzyl-6,9,12-Trioxa-3,15-diazatetradodecane-l,l6-diol (4). 3 (1.00 g, 3.57 mmol), benzyl chloride (0.95 g, 7.50 mmol) and Na_2CO_3 (0.91 g, 8.57 mmol) were refluxed in dry CH_3CN (25 mL) under N_2 for 48 hours. The solvent was removed on a rotary evaporator, leaving a yellow residue which was extracted into CH_2Cl_2, washed twice with water and dried over $MgSO_4$. Removal of the solvent gave the pure product. (1.431 g, 87.2% yield)

δ_H($CDCl_3$, 300 MHz)/ppm: 7.33 (m, 10 H), 3.71 (s, 4 H), 3.68-3.51 (m, 20 H), 3.19 (broad, 2H), 2.76-2.70 (m, 8 H)

HRMS-EI m/z: M^+ calculated for $C_{26}H_{40}N_2O_5+H^+$: 461.30155; found 461.30080

3,15-benzyl-6,9,12-Trioxa-3,15-diazatetradodecane-l,l6-dichloride (5). 4 (861 mg, 1.87 mmol) was dissolved in dry benzene (~50 mL), and $SOCl_2$ (5 mL) was added dropwise at room temperature. The reaction was then refluxed overnight under dry N_2. The solvent was removed on a rotary evaporator and the remaining orange residue extracted into CH_2Cl_2 and H_2O. The CH_2Cl_2 layer was separated. The pH of the aqueous layer was adjusted from 1 to 12 with LiOH, and then extracted with CH_2Cl_2. The CH_2Cl_2 layers were combined, washed once with water and dried over Na_2SO_4. The solvent was removed to give the product, 5. (580 mg, 62.3% yield)

δ_H($CDCl_3$, 300 MHz)/ppm: 7.31-7.24 (m, 10 H), 3.66 (s, 4 H), 3.57-3.42 (m, 16 H), 2.85 (t, J = 6.9 Hz, 4H), 2.71 (t, J = 6.0 Hz, 4H)

δ_C($CDCl_3$, 400 MHz)/ppm: 139.53, 128.87, 128.48, 127.27, 70.87, 70.67, 70.23, 59.78, 56.63, 53.83, 42.46

LBz_1. 5 (331.0 mg, 0.665 mmol) in 30 mL dry MeCN was added to 2-aminomethylpyridine (68.4 mg, 0.633 mmol) and Na_2CO_3 in 250 mL dry MeCN and the reaction brought to reflux for 1.5 days. The solvent was removed on the rotary evaporator and the resulting orange-brown residue extracted into CH_2Cl_2 (~ 50 mL), washed twice with H_2O (50 mL x 2) and dried over $MgSO_4$. Removal of the solvent on the rotavap left an orange oil, the crude product. This was purified by column chromatography on silica-60 gel, eluting with CH_2Cl_2, 2% MeOH and 0.5% Et_3N by volume. The product (LBz_1) eluted at R_f = 0.09. (223.4 mg, 66% yield) Upon scaling the reaction, the product was not completely purified after this step, so an additional column was run using Et_2O and alumina.

δ_H($CDCl_3$, 300 MHz)/ppm: 8.49 (d, J = 3.3 Hz, 1 H), 7.57 (t, J = 8.7 Hz, 1 H), 7.40 (d, J = 7.8 Hz, 1H), 7.26 – 7.20 (m, 10 H), 7.12 (t, J = 6.6 Hz, 1 H), 3.72 – 3.58 Hz (m, 15 H), 2.72-2.70 (m, 8 H)

HRMS-EI m/z: M^+ calculated for $C_{32}H_{44}N_4O_3+H^+$: 533.34862; found 533.34783

[Co(LBz_1)]$(PF_6)_2$. $Co(NO_3)_2 \cdot 6H_2O$ (135.5 mg, 0.465 mmol) in 1.55 mL MeOH was added to (165.4 mg, 0.311 mmol) LBz_1 in 1.55 mL MeOH and the reaction stirred 1 hour. Saturated aqueous NH_4PF_6 was then added dropwise to the solution until it looked as though no additional precipitated was forming. The precipitate was collected, dried under vacuum, then redissolved in MeCN and recrystallized by slow diffusion of Et_2O into the solution. This gave pale pink needle crystals of X-ray quality. (151.0 mg, 54.0% yield)

δ_H($CDCl_3$, 300 MHz)/ppm: (Main peaks) 48.74, 46.89, 16.41, 13.87, 12.40, 10.48, 9.21, 7.38, 6.45, 5.21, 3.56, 2.25

IR (KBr) ν_{max}/cm^{-1}: 2934.4 (w, sp^3 C-H stretching), 1611.48 (w, pyridyl C-N or pyridyl or aryl C-C stretching), 1457.78 (w/m, pyridyl C-N or pyridyl or aryl C-C stretching), 838.72 (vs, P-F stretching), 557.69 (s, P-F bending)

MS (positive ESI): m/z (%) =295.63 (15.54, $[Co(LBz\_1)]^{2+}$), 650.29 (100.00, ?)

UV-vis (MeCN): λ_{max}/nm ($\varepsilon/cm^{-1}\ M^{-1}$): 265.0 (4575.4), 510.0 (20.8)

C, H & N: Elemental analysis calculated for $C_{32}H_{44}CoF_{12}N_4O_3P_2$: C, 43.60%; H, 5.03%; N, 6.68%. Found: C, 43.45%; H, 5.13%; N, 6.52%.

[Zn(LBz_1)]$(PF_6)_2$. This reaction was done in a glove box under an N_2 atmosphere and the reaction vessels light-proofed with aluminum foil. LBz_1 (38.3 mg, 0.07 mmol) and $ZnCl_2$ (9.8 mg, 0.07 mmol), each dissolved in DMF, were combined (total volume of DMF ~ 2

mL) and stirred seven hours. $AgPF_6$ (35.4 mg, 0.14 mmol) in ~ 3 mL DMF was added and the reaction stirred overnight. The DMF was then removed under vacuum and the residue extracted into CH_2Cl_2 and filtered first through a fritted funnel and celite and then through glass fiber filter paper to completely remove insoluble material. The solvent was removed and the product redissolved in MeCN. Et_2O was diffused into this solution to attempt to recrystallize but the material appeared to oil out. However, the filtrate was decanted from the oil and set aside, and colorless needle crystals of X-ray quality grew from this filtrate. A yield was not calculated due to confusion and lost material during recrystallization.

$\delta_H(CDCl_3$, 300 MHz)/ppm: (Main peaks, coupling constants and integration could not be calculated due because the peaks were extremely broadened) 9.039, 8.14 (t), 7.61, 7.45 (phenyl protons), 7.20, 4.43, 4.26, 4.14, 3.89, 3.66, 3.50, 3.12, 2.92, 2.80, 2.65, 2.54, 1.95

C, H & N: Elemental analysis calculated for $C_{32}H_{44}CoF_{12}N_4O_3Zn_2$: C, 43.28%; H, 4.99%; N, 6.31%. Found: C, 42.99%; H, 5.01%; N, 6.42%.

Spectral data

$[CoLM(NO_3)]BPh_4$

IR (KBr)

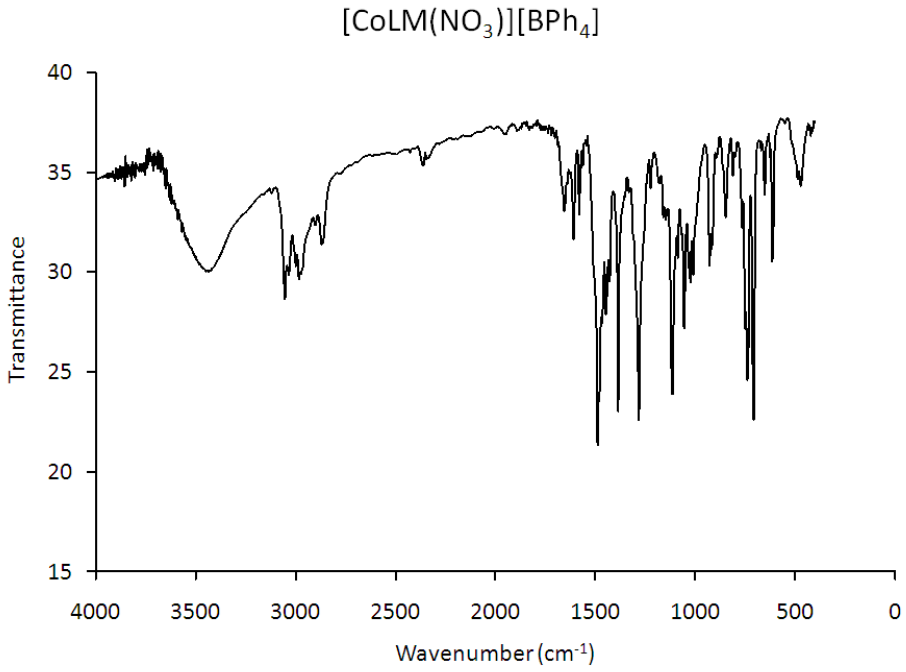

LBz_1

^1H NMR:

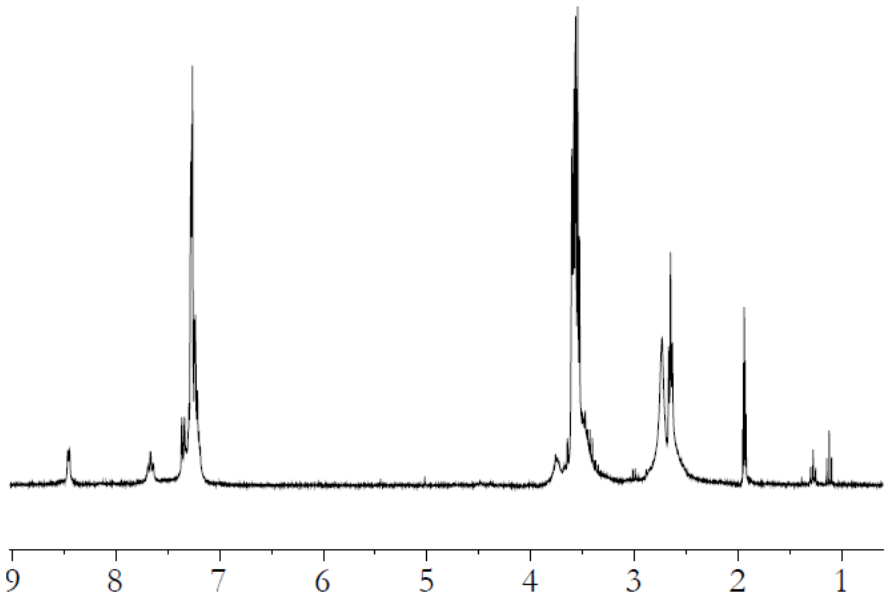

Chapter V. The Influence of Alkali Metals on the Local and Extended Structure of a Tripodal Transition Metal Complex

I. Overview

The ligand utilized in this chapter features a tripodal amine- and amidate-based ligand, in which all three arms possess 2, 3-dimethoxybenzoate substituents (Figure 5-1). The tripodal amidate/amine motif has been shown to coordinate to transition metals in trigonal bipyramidal and trigonal monopyramidal geometries.[136-139] Amidate and amine groups are good ligands for transition metals and the ligand geometry is well-suited for coordination of all four nitrogen donor atoms to the transition metal, since it involves formation of energetically favorable five-membered rings. The ligand also contains 2,3-dimethoxybenzate substituents. These provide a sort of deconstructed crown ether composed of carbonyl and methoxy-ether oxygens for alkali metal coordination.

The cobalt (II) complexes of these ligands have been characterized in solution and in the solid state with a variety of alkali metal and non-coordinating cations. Coordinating alkali metal cations were found to influence both the primary coordination sphere of the ligand about the metal and the extended solid-state structure. Upon alkali metal coordination the ligand geometry around the metal changed from trigonal monopyramidal to trigonal bipyramidal and the solid state structure took on an extended form, with the transition metal complexes linked through shared alkali metals to form one-dimensional chains. The Zn(II) complex of this ligand was also synthesized and characterized in order to further understand the electrochemistry of these complexes.

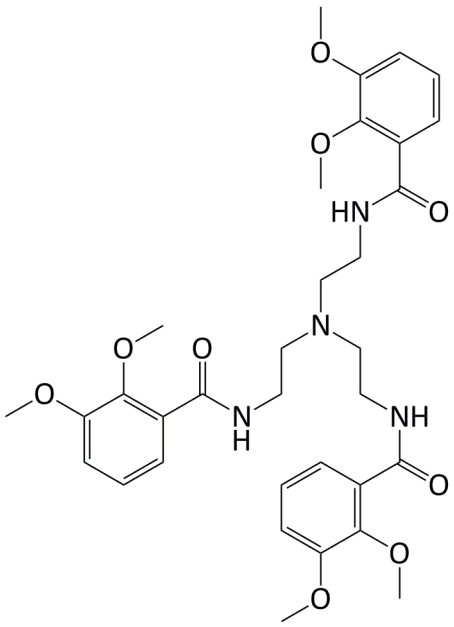

H_3L

Figure 5-1. Ligand 'H_3L', containing a tripodal amide-based site, well-suited for transition metal coordination upon deprotonation to create the amidate form, and methoxy-benzoate substituents, which can facilitate coordination of an alkali metal.

II. Synthesis

The Co(II) complex was synthesized with a non-coordinating cation, bis*(*triphenylphosphoranyl-idene)ammonium (PNP^+), by deprotonating the three amide nitrogens with three equivalents KH in DMF, followed by addition of $Co(OAc)_2$, at which time the reaction was royal blue solution with a small amount of white precipitate, presumably KOAc. A salt metathesis was then performed using PNPCl. The DMF was removed under vacuum and the residue extracted into MeCN and filtered to remove KOAc and KCl. PNP[CoL] could be recrystallized from either DMF/Et_2O or MeCN/Et_2O in good yield to produce turquoise plates. The synthesis is shown in Scheme 5-1 and a detailed procedure is given in the Experimental Section.

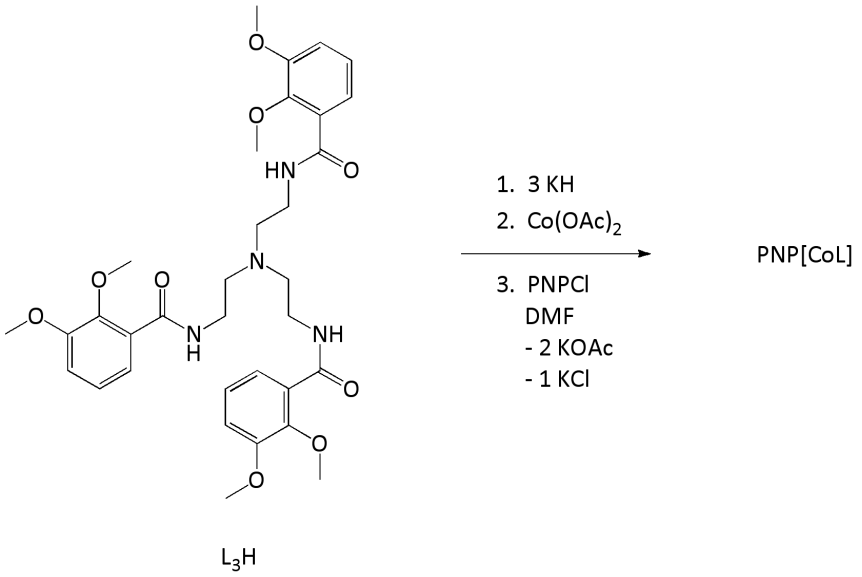

Scheme 5-1. Synthesis of PNP[CoL].

$[CoL]^-$ complexes with coordinating cations (K^+, Na^+ and Li^+) were also synthesized. K[CoL] and Na[CoL] were synthesized be deprotonation with KH and NaH respectively, followed by metallation with $Co(OAc)_2$ (Scheme 5-2). The two equivalents of KOAc or NaOAc could then be filtered from the DMF leaving a DMF solution of K[CoL] or Na[CoL]. X-ray quality crystals were grown by diffusion of Et_2O into DMSO solutions of the complexes, producing pink block-like crystals. The yields were only 49.4% and 38.9% for K[CoL] and Na[CoL], respectively. These lower yields can be explained by the limited solubility of K[CoL] and Na[CoL] in DMF, which leads to some loss of product during filtration of the DMF solution to remove KOAc or NaOAc, and difficulty in collecting all the crystals from the DMSO/Et_2O solution.

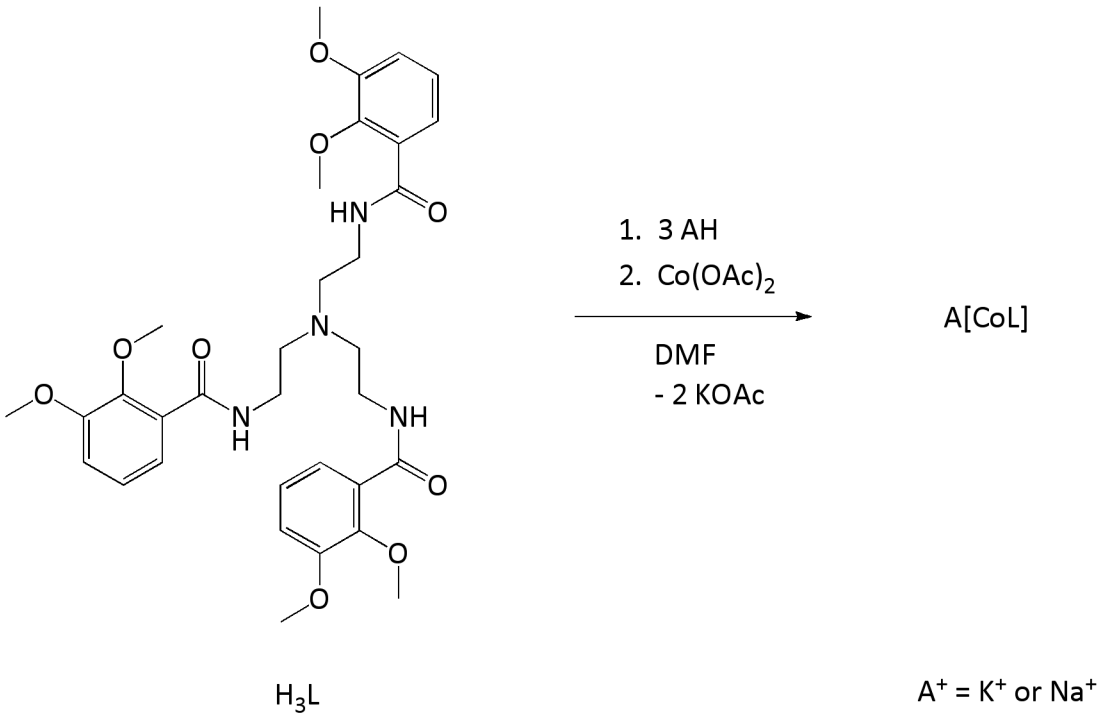

Scheme 5-2. Synthesis of A[CoL], where $A^+ = K^+$ or Na^+.

Li[CoL] was synthesized by deprotonation of the three amide protons with lithium bis(trimethylsilyl)amide (LiHMDS) in THF, as complete deprotonation of the ligand amide protons with LiH was not possible. The solvent was then removed under vacuum, leaving an off-white solid. The product was then washed thoroughly with hexanes to remove unreacted base and hexamethyldisilazane. DMF was then added to the deprotonated ligand, followed by $Co(OAc)_2$. The reaction turned dark blue and then dark purple. The DMF was removed under vacuum, leaving a dark purple solid that could be extracted into CH_2Cl_2. The product was recrystallized from CH_2Cl_2 and hexanes in 59% yield. The synthesis is shown in Scheme 5-3.

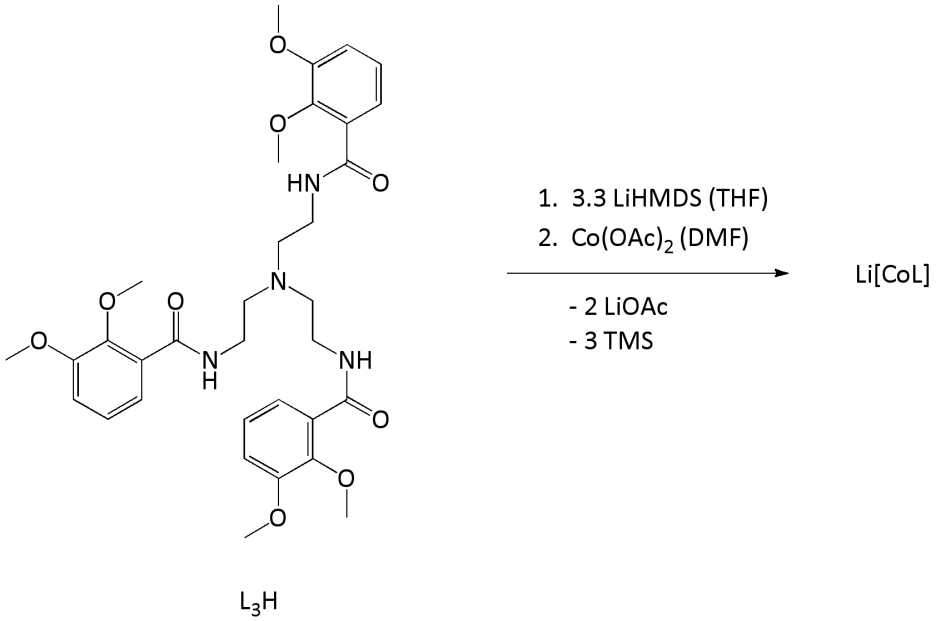

Scheme 5-3. Synthesis of Li[CoL].

III. Structural Characterization

With the non-coordinating PNP^+ cation, the ligand adopts a trigonal monopyramidal geometry about the Co(II) center in the solid state, with a Co-N(apical) distance = 2.140(2) Å and average Co-N(equatorial) distance = 1.983(1) Å (Figure 5-2). The geometry can be characterized using the four-coordinate geometry index, $\tau_4 = [360° - (\alpha + \beta)]/141°]$, where α and β are the two largest ligand-metal-ligand angles in the four-coordinate species. $\tau_4 = 1.00$ for a perfect tetrahedral geometry, 0.85 for a perfect trigonal monopyramidal geometry, smaller values for C_{2v} seesaw structures, and 0.00 for a perfect square planar geometry.[140] For PNP[CoL], τ_4 = [360° - (122.08(9)° + 118.34(8)°)]/141°] = 0.84(1), nearly a perfect trigonal monopyramidal geometry. The solid state structure is discrete rather than extended, with no bonding interactions between the $[CoL]^+$ units or the PNP^+ cations. The Zn^{2+} analogue, which was synthesized using analogous condition with $Zn(OAc)_2$ rather than

$Co(OAc)_2$ in order to determine the electrochemical behavior of the ligand (*vide infra*), has a similar geometry, with an Zn-N(apical) distance = 2.163(2) Å, average Zn-N(equatorial) distance = 1.980(1) Å and τ_4 = [360° - (122.04(8)° + 118.13(8)°)]/141°] = 0.85(1). The molecular structure of PNP[ZnL] is shown in Figure 5-3.

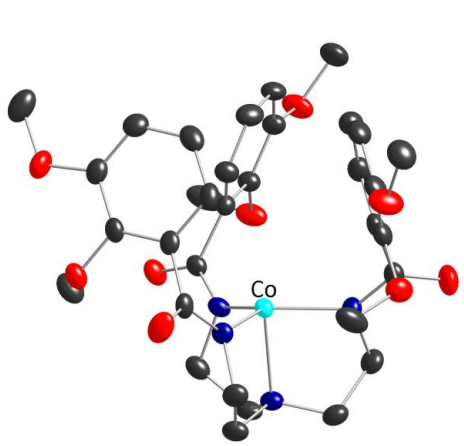

Figure 5-2. Molecular structure of $[CoL]^-$ from PNP[CoL]. Thermal ellipsoids are drawn at 50% probability. Carbon is shown in grey, oxygen in red and nitrogen in blue.

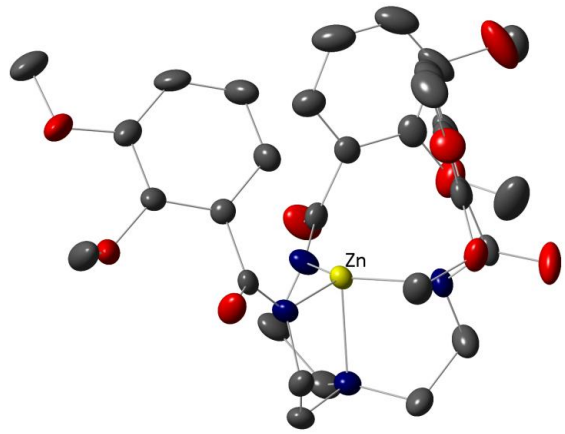

Figure 5-3. Molecular structure of $[ZnL]^-$ from PNP[ZnL]. Thermal ellipsoids are drawn at 50% probability. Carbon is shown in grey, oxygen in red and nitrogen in blue.

While neither PNP[CoL] nor PNP[ZnL] possess a second apical ligand, both complexes appear to exhibit intramolecular edge-to-face π interactions among the 2,3-dimethoxy benzyl substituents. Edge-to-face π interactions occur when there is an attraction between the proton on one aromatic group and the electron rich π system on the next aromatic ring. An example of an edge-to-face π interaction in a simple benzene dimer T-structure is shown in Figure 5-4. There are several examples of edge-to-face π interactions in flexible organic molecules.[141] While these interactions tend to be energetically favorable they tend to be disfavored entropically. When a tripodal ligand like L^{3-} is coordinated to a metal, the aryl groups are preorganized into a geometry favorable for edge-to-face interactions, making the interactions less entropically disfavorable and the overall free energy difference more favorable. A similar example is seen in the Ag(I) complex {tris[2-(benzylamino)-ethyl]amine-κ^4N}Ag(I) ClO_4^-.[142]

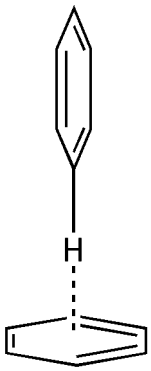

Figure 5-4. Example of an edge-to-face interaction in a benzene dimer T-structure.

Edge-to-face π interactions in the solid state can be quantified by the centroid-centroid distance of the two rings, the distance between the proton on the first ring and the centroid of the second ring (H-centroid), the perpendicular distance between the proton on

the first ring and the plane of the second aryl ring (H-plane), the offset from the center of the second ring when the proton is projected perpendicularly onto the plane of that second ring (offset), and the angle between the planes of the two rings (inter-ring angle). Ab initio molecular orbital calculations on the benzene dimer T-structure give a centroid-centroid distance of ~ 5.0 – 5.2 Å and H-centroid distance of 2.5 – 2.7 Å. Gas phase spectroscopy indicates a centroid-centroid distance of 4.96 Å and H-centroid distance of 2.48 Å.[141] In an ideal edge-to-face π interaction one would expect there to be no offset and the inter-ring angle to be 90°.

The values of these metrics for PNP[CoL] and PNP[ZnL] are listed in Tables 5-1 and 5-2. The protons involved in the edge-to-face π interactions are *ortho* to the amidate substituent. As can be seen from the tables, there are two sets of the edge-to-face interactions amongst the ligand aryl rings (R_1-H_{16} and R_3-H_5 in PNP[CoL] and R_2-H_5 and R_3-H_{16} in PNP[ZnL]), with values that fall well within the range reported in the literature.[141] The third proton and ring set do not exhibit an edge-to-face π interaction, with significantly greater centroid-centroid, H-centroid and offset distances, as well as inter-ring angles that differ much more from 90°. Edge-to-face π interactions appear to constrain the lengths of two sides of the triangle of aryl rings around the cavity, whereas the third side is longer allowing the size of the cavity to be larger as well.

Evidence of edge-to-face π interactions can also be seen in the solution state in the diamagnetic ^{1}H NMR spectrum of PNP[ZnL]. The chemical shifts of the ligand aryl protons in CD_3CN are δ (ppm) = 6.871, 6.630 and 5.197. The *ortho* proton is likely the most upfield, due to shielding from both electron donation from the amidate group and from the

ring current opposing the applied magnetic field inside of the adjacent aromatic ring.

Ring-H_O	Centroid-centroid distance (Å)	H-centroid distance (Å)	H-plane distance (Å)	Offset (Å)	Inter-ring angle (°)
R_1-H_{16}	4.88	2.66	2.63	0.41	97.34
R_2-H_{27}	5.55	3.48	2.82	2.02	41.08
R_3-H_5	4.87	2.77	2.77	0.11	114.70

Table 5-1. Intramolecular edge-to-face π interactions in PNP[CoL].

Ring-H_O	Centroid-centroid distance (Å)	H-centroid distance (Å)	H-plane distance (Å)	Offset (Å)	Inter-ring angle (°)
R_2-H_5	4.89	2.72	2.67	0.52	96.96
R_3-H_{16}	4.81	2.73	2.70	0.40	108.23
R_1-H_{27}	5.42	3.59	3.04	1.91	36.40

Table 5-2. Intramolecular edge-to-face π interactions in PNP[ZnL].

In the solid state structures of K[CoL], Na[CoL] and Li[CoL] the ligand adopts a five-coordinate geometry rather than a four-coordinate geometry about the Co(II). Whereas in PNP[CoL] all three ligand arms are positioned upright around the cavity, in K[CoL], Na[CoL] and Li[CoL] two of the arms splay outwards and the third folds up over the cavity, with the proximal methoxy ether oxygen coordinating to the Co(II) (Figure 5-5). This change in geometry is likely due to two factors: The coordinating cation decreases the electron density of the ligand, making it more favorable for the Co(II) center to coordinate to a fifth ligand, and when the alkali ion binds, it causes two of the ligand arms to splay outwards and the third to fold up over the Co(II) center, creating a cavity composed of

carbonyl and methoxy ether oxygens in which it binds. This places the methoxy ether oxygen in a favorable position in which to coordinate to Co(II).

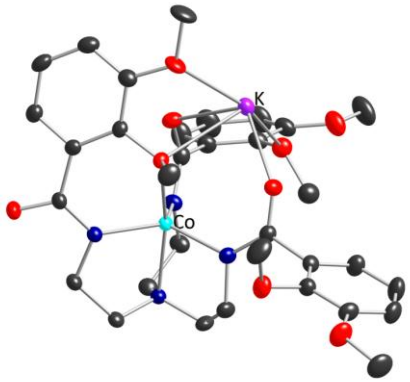

A.

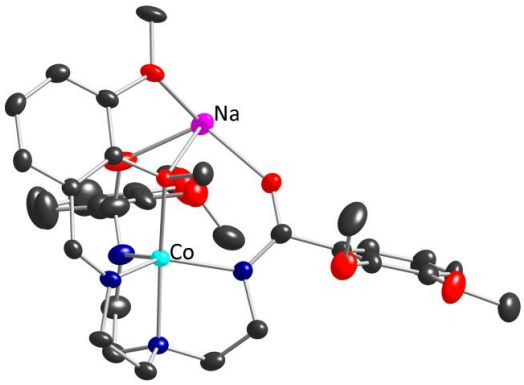

B.

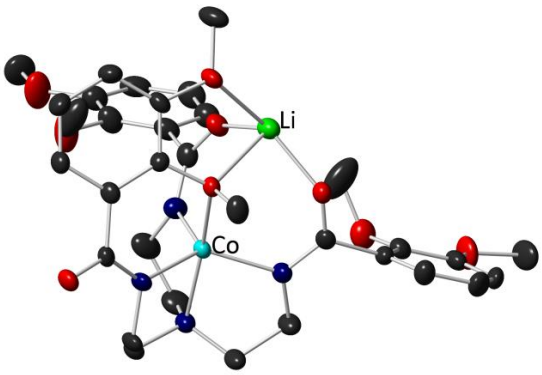

C.

Figure 5-5. Molecular structures of K[CoL] (top, A), Na[CoL] (middle, B) and Li[CoL] (bottom, C) showing a single unit. Thermal ellipsoids are drawn at 50% probability. Carbon is shown in grey, oxygen in red and nitrogen in blue.

The bond distances and angles for all complexes are summarized in Table 5-3. The ligand bends to form a cavity in which the alkali metal ions are bound to two (Na^+ and Li^+) or three (K^+) methoxyether oxygens and two carbonyl oxygens from that ligand, as well as a carbonyl oxygen from an adjacent complex. As expected, the ligand-alkali metal ion bond lengths increase with the size of the alkali metal ion: The average distances to the carbonyl oxygens on the same ligand are 2.594(1) (K^+), 2.292(3) (Na^+) and 1.953(7) (Li^+) Å and the distances to the carbonyl oxygen on the adjacent ligand are 2.570(2) (K^+), 2.289(3) (Na^+) and 1.907(10) (Li^+) Å. The average distances to the methoxy ether oxygens are 2.887(1) (K^+), 2.614(1) (Na^+) and 2.310(4) (Li^+) Å. The Co-N(apical) bond distances decrease from K[CoL] (2.175(2) Å) to Na[CoL] (2.158(3) Å) to Li[CoL] (1.991(3) Å), whereas the average Co-N(equatorial) bond distances increase (2.007(1) Å for K[CoL], 2.012(2) Å for Na[CoL] and 2.139(4) Å for Li[CoL]). The decrease in Co-N(apical) bond distance and increase in Co-N(equatorial) bond distance with decreasing ionic radii may be explained by the decrease in alkali ion-oxygen bond lengths with decreasing alkali ion size: To form a smaller cavity to accommodate the smaller cations, the amide carbonyls fold more sharply into the cavity. This causes an increase in the Co-N(equatorial) distance and, consequently, a decrease in the Co-N(axial) distance. This Co(II) centers are all fairly close to the equatorial plane of the amidate donors: 0.192 (PNP^+), 0.271 (K^+), 0.273 (Na^+) and 0.241 (Li^+) Å.

The τ_5 values can be calculated using Addison and Reedijk's method to give an index of the degree of trigonality: $\tau_5 = (b-a)/60$, where a and b are the two largest angles. $\tau_5 = 0$ for an ideal square pyramidal complex and 1 for an ideal trigonal bipyramidal complex.[130] For K[CoL] τ_5 = (162.74(8)-129.11(9))/60 = 0.56(1), for Na[CoL] τ_5 = (163.17(10)-128.26(13))/60 = 0.58(1) and for Li[CoL] τ_5 = (165.09(15)-130.46(18))/60 = 0.58(2). Thus, all complexes deviate significantly from an ideal trigonal bipyramidal geometry; They are

almost halfway between trigonal bipyramidal and square monopyramidal.

Bond	**PNP[CoL]**	**K[CoL]**	**Na[CoL]**	**Li[CoL]**
Co-N (av. equ.) (Å)	1.983(1)	2.007(1)	2.012(2)	2.139(4)
Co-N (apical) (Å)	2.140(2)	2.175 (2)	2.158(3)	1.991(3)
A–O (Å) carbonyl		2.577(2) 2.570(2) 2.611(2)	2.273(4) 2.288(4) 2.311(3)	1.924(11) 1.981(10) 1.907(10)
A–O (Å) ether		2.997(2) 2.791(4) 2.872(2)	2.483(4) 2.745(2)	2.290(1) 2.329(9)
Co-O		2.2214(19)	2.199(2)	2.234(3)
Space Group	*P*1	*P*2(1)/c	*P*2(1)/n	*P*2(1)/n
R	4.63%	5.83%	6.94%	7.69%

Table 5-3. Bond distances and angles for PNP[CoL], K[CoL], Na[CoL] and Li[CoL]. A^+ = K^+, Na^+ or Li^+.

The coordinating cations also influence the extended structure. Because the alkali metal coordinates to a third carbonyl oxygen from an adjacent complex, it drives the molecular assembly of the complex into one dimensional chains rather than the discrete molecular structure of the PNP[CoL] structures. This has important implications for crystal engineering, as discussed in Chapter 3. The extended structures are shown in Figure 5-6.

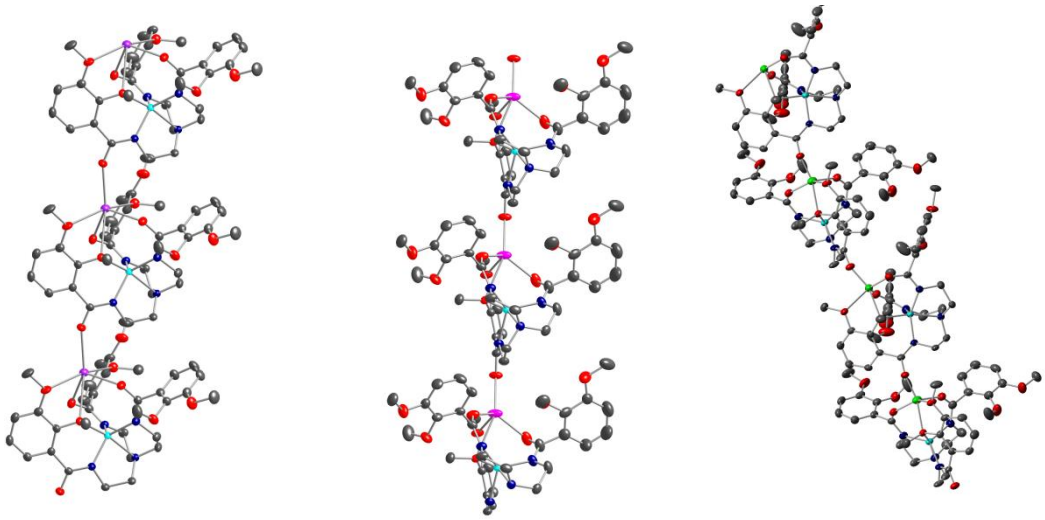

Figure 5-6. Extended structures of K[CoL] (left), Na[CoL] (middle) and Li[CoL]. Thermal ellipsoids are drawn at 50% probability. Cobalt is shown in turquoise, carbon in grey, oxygen in red, nitrogen in blue, potassium in purple, sodium in pink and lithium in green.

While K[CoL] and Na[CoL] are only soluble in DMSO when recrystallized, Li[CoL] is soluble in much less polar solvents including dichloromethane, toluene and diethyl ether. The increased solubility of the Li[CoL] complex may be due to a decrease in the bond strength between Li^+ and the carbonyl oxygen from the adjacent complex compared to that of Na^+ and K^+, making it easier to solvate the extended structure.

IV. NMR Spectroscopy

In order to investigate the solution state structures of the complexes, ^{1}H NMR and UV-visible absorption spectroscopy of the complexes was performed. The ^{1}H NMR spectrum of PNP[CoL] in DMSO-d_6 shows paramagnetic broadening and shifting as would be expected from a Co(II) d^7 complex. In addition to peaks at 7.73 and 7.58 ppm from PNP^+ and 7.94, 2.89 and 2.71 from DMF, the spectrum contains seven main peaks (71 ppm

(very broad), 20.46 ppm (broad), 3.34 ppm (sharp), 1.40 ppm (sharp), 1.06 ppm (sharp), −6.46 ppm (slightly broad) and -10.48 ppm (broad). The seven peaks can be assigned to the seven inequivalent protons of the ligand, indicating the complex has C_3 symmetry in solution, congruent with the pseudo C_3 symmetry in the trigonal monopyramidal solid state structure. There are also several smaller peaks that indicate the presence of a second isomer in solution, perhaps the five-coordinate form.

The ^{1}H NMR spectrum of K[CoL] in DMSO-d_6 shows the same peaks as that of PNP[CoL] with the exception of those belonging to PNP^+, indicating the same solution-state geometry. The ^{1}H NMR spectrum of Na[CoL] in DMSO shows the seven main peaks found in the spectra of PNP[CoL] and K[CoL], but the secondary peaks become larger, indicating increased concentration of a second phase in solution. The ^{1}H NMR spectrum of Li[CoL], taken in both DMSO-d_6 and CD_2Cl_2, differs greatly from those of the other complexes, indicating that either there are not significant amounts of the trigonal monopyramidal complex in solution or that it interconverts with another isomer on a timescale faster than the ^{1}H NMR relaxation time. In CH_2Cl_2, there are fourteen distinct peaks as well as broad, indistinct peaks indicating both a high degree of fluxionality in solution and a decrease in symmetry of the complex. All NMR spectra are shown in the Supporting Information.

Solution state magnetic susceptibility measurements, performed using the Evans method,[143] indicate that all the cobalt complexes are Co(II) high spin. The μ_{eff} values measured in DMSO-d_6 are 4.48 (PNP[CoL]), 4.33 (K[CoL]), 4.43 (Na[CoL]) and 4.36 (Li[CoL]), all of which fall within the range of 4.3-5.2 measured for Co(II) high spin complexes.[144]

V. UV-Visible Absorption Spectroscopy and Calculation of Binding Constants

The solution state geometry was also investigated by UV-visible absorption spectroscopy. In DMF, PNP[CoL] has absorbances at 434.9 nm (ε = 23.75 $M^{-1}cm^{-1}$), an asymmetrical band with a maximum at 590.0 nm (ε = 63.1 $M^{-1}cm^{-1}$), centered at 593.0 nm, and broad band around 740 nm. This spectrum is similar to that reported for other Co(II) trigonal monopyramidal complexes, notably those reported by Ray *et al.* [139] and Banci *et al.*[145] The most similar complex was synthesized by Ray *et al.*, Co(II) ligated with the tris((N-*tert*-butylcarbamoyl)methyl)amidate ligand, $[Co(Bu^tNC(O)CH_2)_3N]^-$. This complex has a symmetrical band at 414 nm, an unsymmetrical band centered at 590 nm, and a broad shoulder at 700 nm. Using the assignments of Banci *et al.*, they assign these as a $^4A_2 \rightarrow {}^4A_2$ transition (414 nm) and $^4A_2 \rightarrow {}^4E$ transitions (590 and 700 nm). Interestingly, these bands all have higher extinction coefficients than PNP[CoL], and a lower baseline, indicating that whereas $[Co(Bu^tNC(O)CH_2)_3N]^-$ is rigidly trigonal monopyramidal in solution, PNP[CoL] exhibits some fluxionality in solution, which is expected given the availability of methoxy ether oxygens from the benzoate substituents as ligands for the Co(II).

The electronic absorbance spectrum of K[CoL] in DMF has some commonality with that of PNP[CoL] but differs in that the asymmetric band becomes more asymmetrical and slightly blue-shifted. Whereas the maxima for the asymmetric band of PNP[CoL] have extinction coefficients of 63.1 $M^{-1}cm^{-1}$ (590.0 nm) and 60.3 $M^{-1}cm^{-1}$ (615.0.0 nm), the maxima for the asymmetric band of K[CoL] have extinction coefficients of 72.7 $M^{-1}cm^{-1}$ (584.9 nm) and 51.7 $M^{-1}cm^{-1}$ (610.0 nm). Additionally, the absorbance at wavelengths below 584.9 nm increases. For example, the extinction coefficient of the broad peak at 434.9 nm changes from 23.41 $M^{-1}cm^{-1}$ for PNP[CoL] to 26.44 $M^{-1}cm^{-1}$ for K[CoL]. A shoulder at 545.0 nm also begins to appear. These changes can be explained by a complex that exists

mainly in the trigonal monopyramidal form seen in the PNP[CoL] complex in solution, indicating the K^+ remains largely uncoordinated. However, a small amount of the complex exists in a different coordination geometry, likely the trigonal bipyramidal geometry seen in the crystal structure of the K[CoL] complex, in which K^+ is coordinated.

The electronic absorbance spectrum of Na[CoL] differs further from that of PNP[CoL], with the asymmetrical band becoming even more asymmetrical. The band has a maximum at 583.0 nm with an extinction coefficient of 69.3 $M^{-1}cm^{-1}$, and what now appears to be a shoulder with no clear maximum; an approximate extinction coefficient for this broad shoulder is 44.7 $M^{-1}cm^{-1}$. The absorbance at wavelengths below the asymmetric band is greatly increased over that of PNP[CoL] and K[CoL]. The electronic absorbance spectrum of Li[CoL] differs even more greatly, with a great decrease in the absorbance of the asymmetrical band and appearance of a band at 535.0 nm (ε = 47.9 $M^{-1}cm^{-1}$). The electronic absorption spectra of all complexes is shown in Figure 5-7. Solid state electronic absorbance data on all complexes will be collected in the near future and compared with the solution state data in order to further investigate the geometry of the complexes in solution.

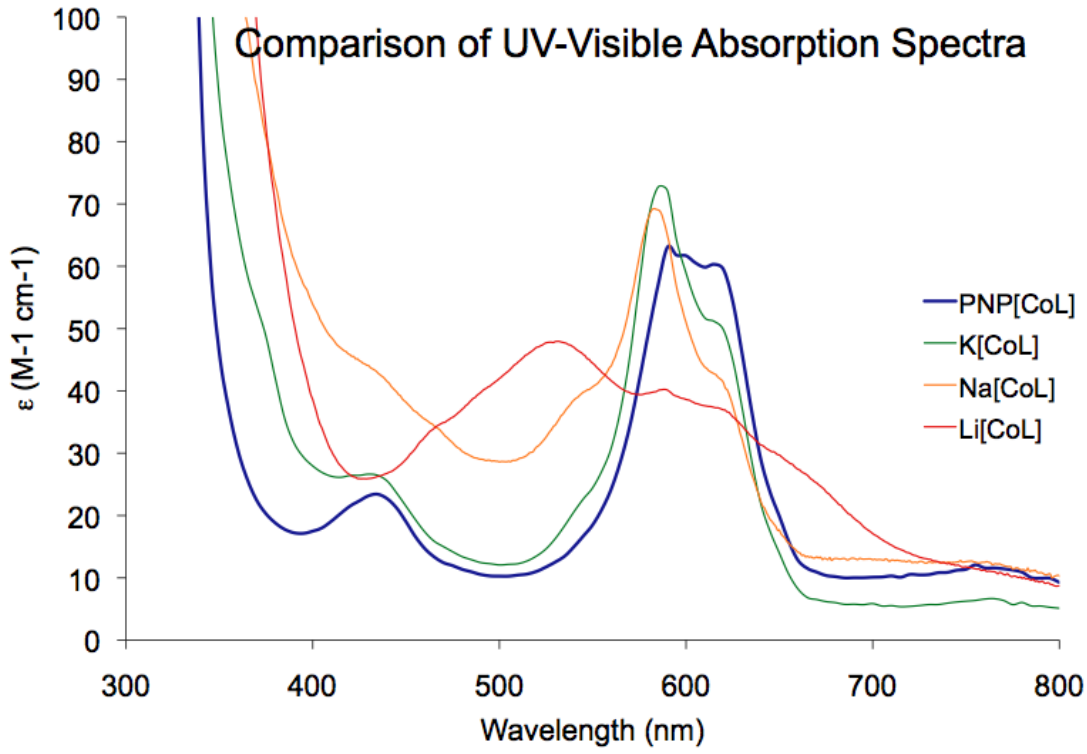

Figure 5-7. UV-visible absorption spectra of PNP[CoL], K[CoL], Na[CoL] and Li[CoL], taken in DMF.

The decreasing concentration of the trigonal monopyramidal geometry in the solution state upon changing from PNP^+ to K^+ to Na^+ to Li^+ can be explained by an increase in binding affinity of the $[CoL]^-$ complex for the alkali metal ion as the ionic radius of the alkali metal ion decreases. To investigate this further, titration experiments were performed in which solutions of PNP[CoL] in DMF were titrated with KPF_6, $NaPF_6$ or $LiPF_6$. The solutions were made 0.1 M in tetrabutylammonium hexafluorophosphate ($TBAPF_6$) in order to control for the effects of varying ionic strengths as concentrations of the alkali metal salts were increased. A full account of the experimental procedure is given in the Supporting Information.

Up to 75 equivalents KPF_6, the complex appeared to bind K^+ in a 1:1 manner, with solutions changing from pale turquoise to pale purple to pale pink in color. The spectra resulting from the titration are shown in Figure 5-8. The absorbance spectra maintains an isosbestic point at approximately 577 nm. The data was plotted using a 1:1 binding isotherm

$$\Delta A/b = S_t K_{11} \Delta\varepsilon_{11}[L]/(1+ K_{11}[L])$$

where $\Delta A = A - A_o$, and A and A_o = the absorbance in the presence and absence of substrate, respectively, $K_{11} = [SL]/[S][L]$ is the binding constant, b is the cuvette path length, S_t is the total concentration of substrate, $\Delta\varepsilon_{11} = \varepsilon_{11} - \varepsilon_S - \Delta\varepsilon_L$ is the change in extinction coefficient upon substrate binding and [L] is the concentration of ligand.[146] Fitting the data at 620 nm gave a binding constant of 32(1) M^{-1}, whereas fitting the data at 540 nm gave a binding constant of 26(2) M^{-1}. The fits are shown in the Supporting Information. When 100 equivalents KPF_6 are added the spectrum bleaches, perhaps because the K^+ displaces Co(II). In the near future, another trial will be run to confirm these binding constants and a Job's plot experiment will be run to determine the binding stoichiometry.

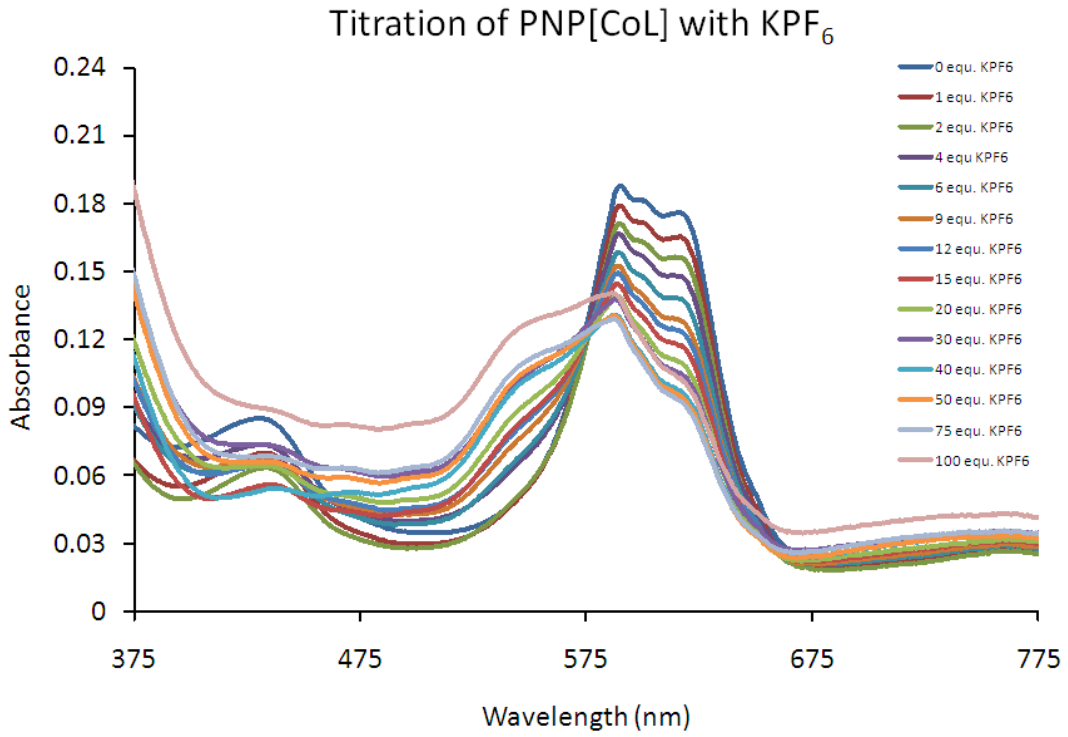

Figure 5-8. Titration of PNP[CoL] with KPF_6. Experimental details are given in text.

The binding data for Na^+ and Li^+ is more complex. When the titration is performed with $NaPF_6$ the isosbestic point only lasts until 9 equivalents of $NaPF_6$ are added; Upon addition of more equivalents the absorbance at this point begins to increase (Figure 5-9). Plotting of the absorbance data indicates a second binding event occurs involving Na^+. (Supporting Information) Upon addition of 60 equivalents of $NaPF_6$ the spectrum becomes bleached, as occurred with 100 equivalents KPF_6. Attempts were made to fit this data using a multiple equilibria binding equation:

$$\Delta A/b = S_t(\beta_{11}\Delta\varepsilon_{11}[L] + \beta_{12}\Delta\varepsilon_{12}[L]^2) / (1 + \beta_{11}[L] + \beta_{12}[L]^2),$$

but this equation is extremely parameter-dependent, and it was not possible to obtain a meaningful fit of the data. However, the increased spectral changes upon addition of small

(0-8 equivalents) amounts of Na^+ compared to low amounts of K^+ indicate greater binding affinity for Na^+ than K^+.

This system does not strictly meet all the criteria for Job's method to be applicable since there appears to be more than one product formed.[147] However, because the second product does not appear to form until > 8 equivalents $NaPF_6$ are added, the first product likely predominates at the concentrations used for Job's method and the technique can be used to gain insight into the molecular formula of the first product.[148] The Job's plot data, shown in the Supporting Information, peaks at a 1 Na^+/1 $[CoL]^-$ molar ratio, indicating the chemical formula of the first product is Na[CoL]. The second product may be due to coordination of a second Na^+ and the bleaching upon addition of 75 equivalents to displacement of Co(II) by Na^+. In the mass spectrum of Na[CoL], done by electrospray ionization, there is a small m/z peak = +740.18, the mass/charge ratio of $Na_2[CoL]^+$. Electrospray ionization (ESI) mass spectrometry was done on samples of PNP[CoL] with 1, 5, 12, 20 and 40 equivalents $NaPF_6$ in an effort to detect the $Na_2[CoL]^+$ species, but here the corresponding m/z peak was not found. Rather, the samples tended to show a decrease in the intensity of the $[CoL]^-$ peak in the negative electrospray ionization mass spectrometry (ESI MS) and an increase in the $L+Na^+$ peak in the positive ESI MS. A crystal structure of the complex with multiple Na^+ ions could not be obtained.

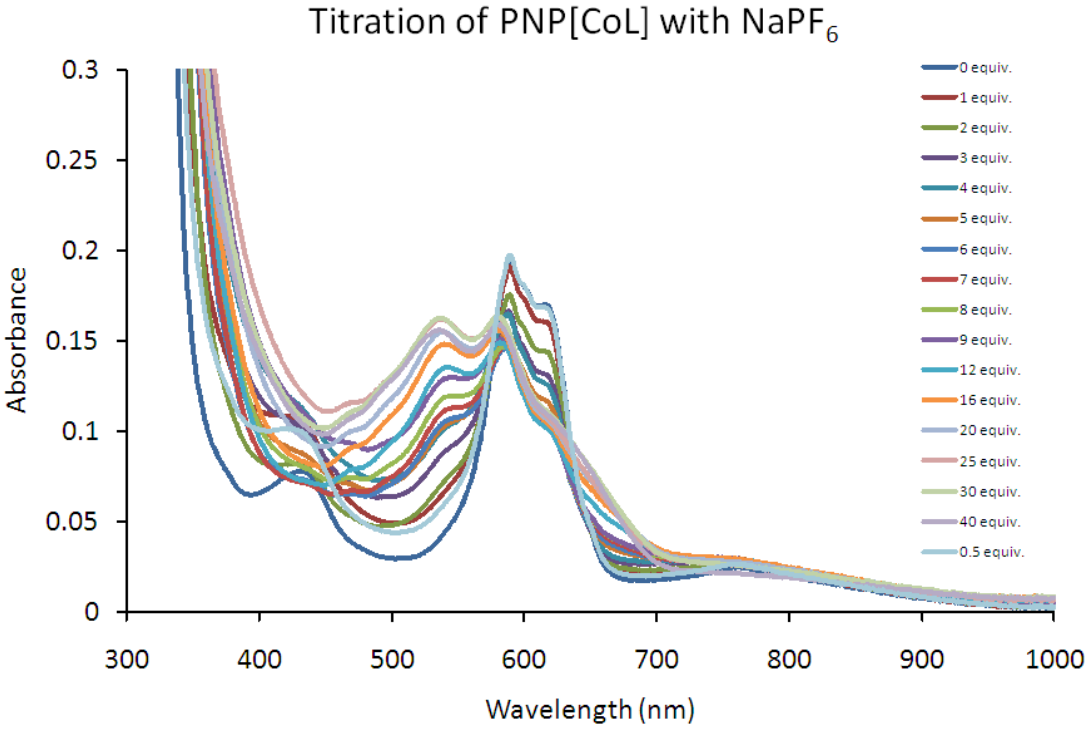

Figure 5-9. Titration of PNP[CoL] with $NaPF_6$. Experimental details are given in text.

The titration experiments with $LiPF_6$ differed even more drastically, as shown in Figure 5-10. At low concentrations of Li^+, the solutions showed greater sensitivity to Li^+ than to comparable amounts of Na^+ and K^+, indicating greater binding affinity. However, by the addition of 5 equivalents $LiPF_6$, the solution had turned a deep purple color. This deep purple color persisted upon addition of up to 15 equivalents $LiPF_6$. Upon addition of 25 equivalents $LiPF_6$ the spectrum became bleached, as was the case with large concentrations of $NaPF_6$ and KPF_6. A Job's method experiment was also run for this system but since significant concentrations of both products exist under the experimental conditions, no information was obtained about the chemical formula of the products. (However, it may be possible to simulate the data expected for the products and compare these to the experimental data to figure out the product compositions.[148]) One possible

explanation for the observed titration results is formation of three different products: Li[CoL], which has a structure similar to the solid state structure, $Li_2[CoL]^+ + PF_6^-$, in which perhaps the second Li^+ displaces one or two of the nitrogen donors from Co(II), decreasing the symmetry of the complex and hence causing the increase in the extinction coefficient, and a third product seen upon addition of 25 equivalents $LiPF_6$, in which the Li^+ completely displaces Co(II) from the ligand. The electronic absorbance spectroscopy between 5-15 equivalents $LiPF_6$ strongly resembles that of $Co(OAc)_2$ in DMF, so it is possible that when a second Li^+ coordinates one or more of the nitrogen donors to Co(II) is replaced by an oxygen donor, either from the ligand or DMF. In the mass spectrometry of Li[CoL], done by electrospray ionization, there is a small m/z peak = +708.24, the mass/charge ratio of $Li_2[CoL]^+$.

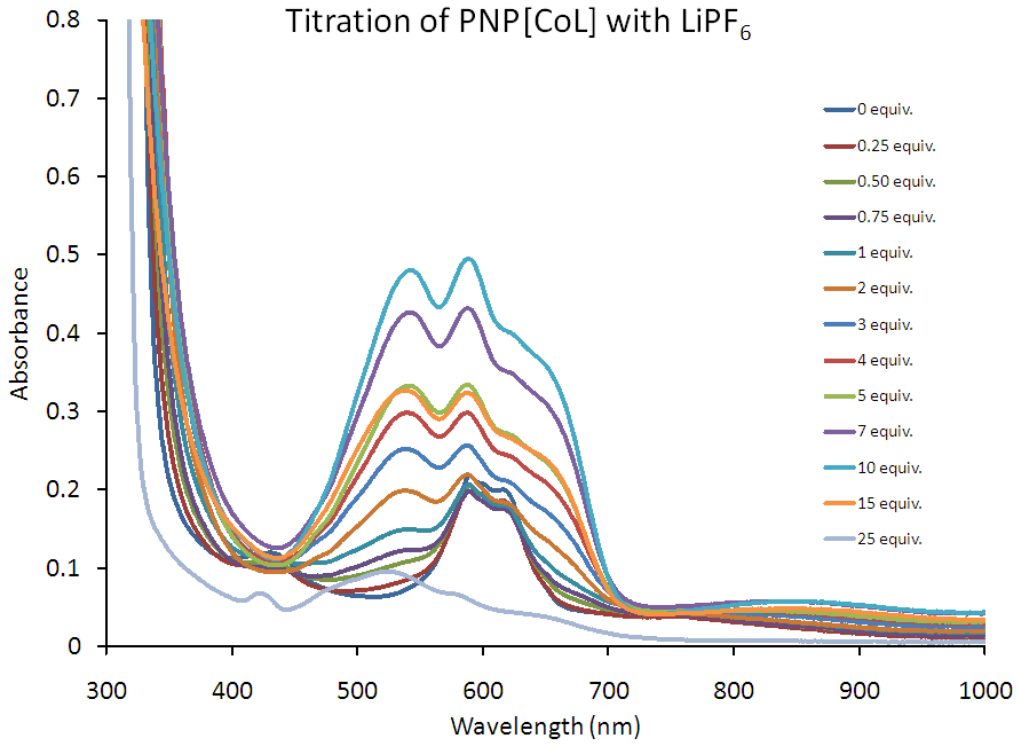

Figure 5-10. Titration of PNP[CoL] with $LiPF_6$. Experimental details are given in text.

VI. IR Spectroscopy

The ligand and complexes were also investigated by infrared absorption (IR) spectroscopy. The ligand shows an intense N-H stretch at 3367.8 cm^{-1}, several bands corresponding to sp^2 and sp^3 C-H stretching, an intense carbonyl stretch at 1647.3 cm^{-1}, medium intensity bands due to aryl C-C stretching at 1578.1 and 1527.6 cm^{-1}, and a complex fingerprint region due to absorption from asymmetrical and symmetrical C-H bending vibrations in the methyl groups, C-H bending vibrations of the methylene C-H bonds, C-O-C stretching, N-H bending vibrations and C-N bending vibrations. In the metallated complexes, the N-H amide stretch is no longer present, indicating the ligand is completely deprotonated. The carbonyl stretching band is split into multiple bands, indicating carbonyl groups in differing chemical environments. This makes sense for K[CoL], Na[CoL] and Li[CoL], where the C_3 symmetry has been broken, and the arms are coordinated differently to the Co(II) complex and the alkali metal. In the solid state structure of PNP[CoL], the complex also deviates from C_3 symmetry, as discussed regarding the crystal structure, which may explain the splitting of the carbonyl stretching frequency. The C=O stretching frequencies in PNP[CoL] are at a higher frequency compared to that of the free ligand, indicating that the decrease in carbonyl bond strength anticipated from deprotonation of the amide group is compensated for by coordination of the lone pair to Co(II). The ν(C=O) stretching frequencies in the A[CoL] complexes (where A^+ = alkali metal ion) are at frequencies lower than in PNP[CoL] and similar to that in the free ligand, indicating a decrease in C=O bond strength due to coordination of the carbonyl groups to the alkali metal ions. The IR spectra of all complexes are in the Supporting Information.

VII. Electrochemistry

The electrochemistry of these complexes was investigated by cyclic voltammetry in DMF containing 0.2 M $TBAPF_6$ with the complexes at 1.5 mM concentration. All complexes show irreversible oxidation events. PNP[CoL], K[CoL] and Na[CoL] show a very similar electrochemistry, with three irreversible oxidation events at approximately 0.10 V, 0.32 V and 0.53 V versus Fc/Fc^+, with a small variation in the potential of oxidation events between the complexes. Given that the UV-visible absorbance spectroscopy indicate that in solution K[CoL] and Na[CoL] are largely in the trigonal monopyramidal coordination, this similarity makes sense. Li[CoL]'s cyclic voltammogram differs from those of the other complexes, with four irreversible oxidation events at approximately -0.02 V, 0.10 V, 0.32 V and 0.53 V vs. Fc/Fc^+. The cyclic voltammograms of the Co(II) complexes are shown in Figure 5-11.

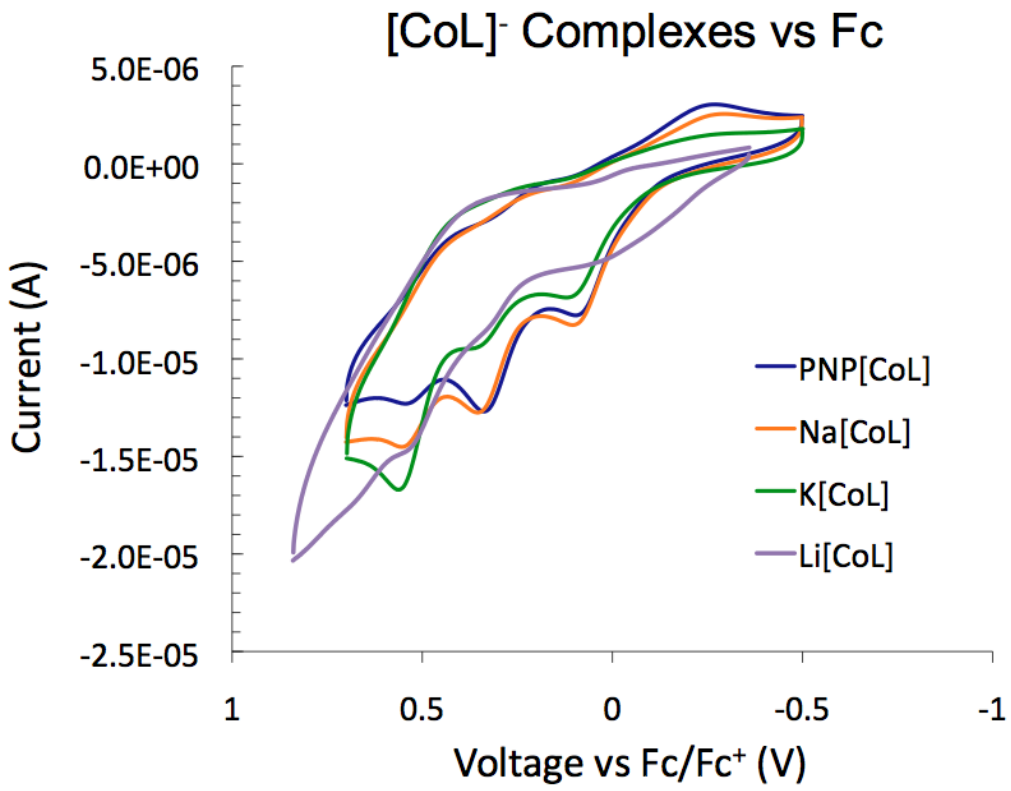

Figure 5-11. Cyclic voltammograms of PNP[CoL], K[CoL], Na[CoL] and Li[CoL]. Electrochemistry was done in DMF containing 0.2 M $TBAPF_6$, using a 0.1 mM glassy carbon working electrode, $Ag/AgNO_3$ reference electrode and Pt counter electrode at 298 K, and referenced vs. Fc/Fc^+.

To investigate whether any of the electrochemical events could be attributed to ligand oxidation, the complex PNP[ZnL] was synthesized and characterized. Its cyclic voltammogram is shown in Figure 5-12. The voltammogram shows two irreversible oxidation events at approximately 0.58 and 0.68 V vs. Fc/Fc^+, indicating two of the electrochemical events shown by the $[CoL]^-$ complexes can be attributed to irreversible ligand oxidation events, and the third can likely be ascribed to an irreversible Co(II/II) couple.

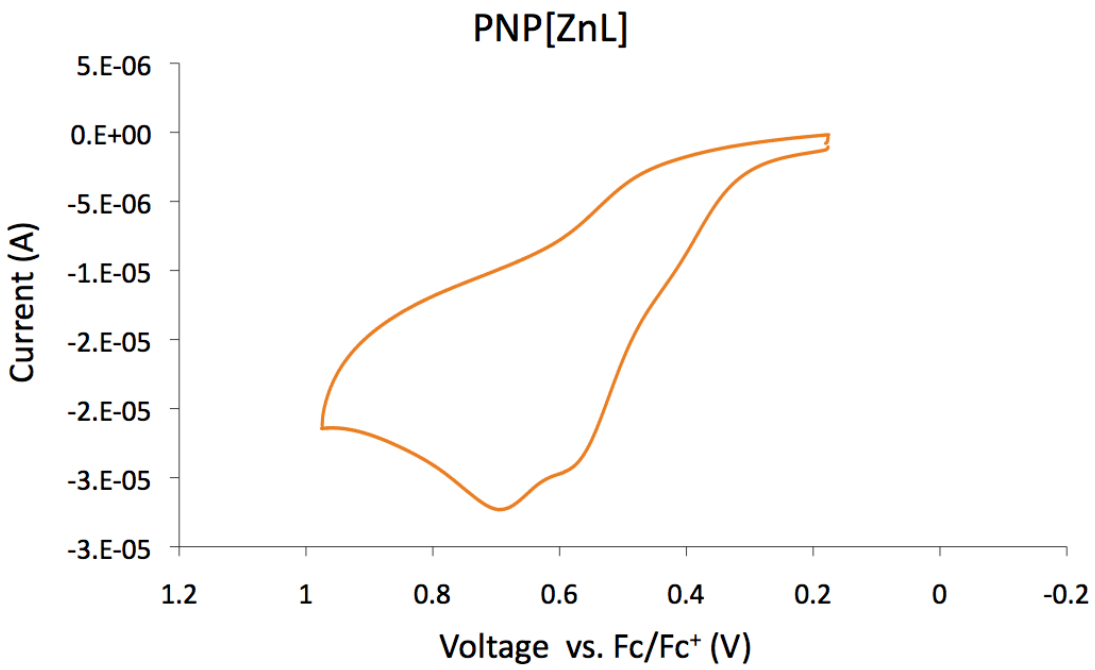

Figure 5-12. Cyclic voltammograms of PNP[ZnL]. Electrochemistry was done in DMF containing 0.2 M $TBAPF_6$, using a 0.1 mM glassy carbon working electrode, $Ag/AgNO_3$ reference electrode and Pt counter electrode at 298 K, and referenced vs. Fc/Fc^+.

To observe the effects of greater concentrations of alkali metals on the electrochemistry, cyclic voltammograms were run of 3.06 mM PNP[CoL] with 0, 4, 9, 20, 40 and 75 equivalents KPF_6 in 0.1 M $TBAPF_6$/DMF. The cyclic voltammograms are shown in Figure 5-13, and potentials vs. Fc/Fc^+ for the three irreversible oxidation events listed in Table 5-4. As can be seen in the table, there is little change in the oxidation potentials upon addition of many equivalents KPF_6, which is unsurprising considering the low binding affinity of $[CoL]^-$ for K^+.

However, the relative magnitudes of the anodic peaks for the three oxidation events changes as K^+ added. The second oxidation event has the largest anodic peak and the third oxidation event the smallest when no K^+ is present. As more K^+ is added the peak for the

third oxidation event becomes the largest and the second event the smallest. Differences in the overall current drops of the voltammograms prevent a direct comparison of the three anodic peaks for the different samples, so the changes were quantified by drawing a best fit line through each voltammogram and calculating the vertical distance between the peak current and the line, which is listed in Table 5-4. The distances for the three oxidation events for a sample were summed and the distance for each event divided by the sum to give the relative current change for each event as a percentage. The results, which are also listed in Table 5-4, indicate that K^+ suppresses the second oxidation event and increases the magnitude of the third event. The magnitude of the overall current drop also decreases as more K^+ is added, though this is also difficult to quantify since the magnitude of the current drops also decrease with additional scans due to the irreversibility of the processes. Nevertheless the overall current drop for the first scan for each sample measured at $3.06*10^{-3}$ M is also reported in Table 5-4. It appears the overall effect of adding K^+ is to suppress oxidation, although this may be due to interactions of K^+ with the electrode suppressing current transfer as well as to interaction of K^+ with the $[CoL]^-$ complex.

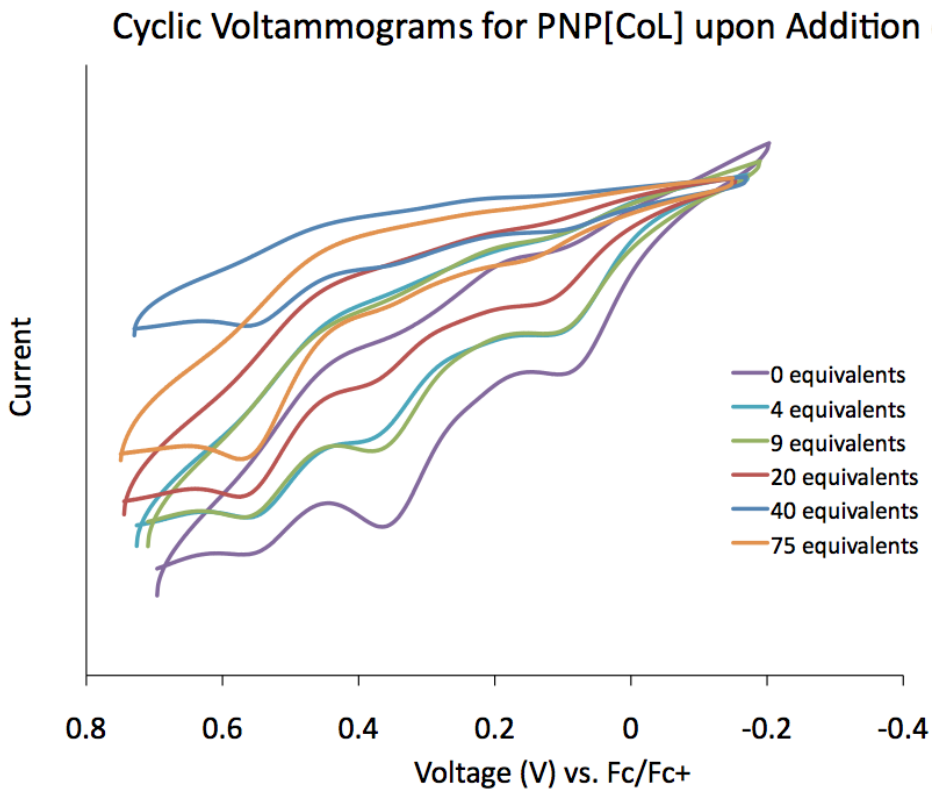

Figure 5-13. Cyclic voltammograms of $3.06*10^{-3}$ M PNP[CoL] with the addition of 0, 9, 20, and 75 equivalents KPF_6. The samples with 4 and 40 equivalents were recorded at lower concentrations. Samples were stirred two days before conducting the measurements. Electrochemistry was done in DMF containing 0.1 M $TBAPF_6$, using a 0.1 mM glassy carbon working electrode, $Ag/AgNO_3$ reference electrode and Pt counter electrode at 298 K, and referenced vs. Fc/Fc^+.

Equivalents KPF_6	E_{ox}^1 (V) Distance ($*10^{-6}$ A)	E_{ox}^2 (V) Distance ($*10^{-6}$ A)	E_{ox}^3 (V) Distance ($*10^{-6}$ A)	Overall current drop (A)
0	0.09	0.35	0.54	$-3.49*10^{-5}$
4*	0.10	0.37	0.54	n/a
9	0.10	0.36	0.55	$-2.99*10^{-5}$
20	0.10	0.36	0.56	$-2.69*10^{-5}$
40*	0.10	0.36	0.56	n/a
75	0.14	0.36	0.56	$-2.30*10^{-5}$

Table 5-4. E_{ox} potentials vs. Fc/Fc^+ for $3.06*10^{-3}$ M PNP[CoL] with the addition of 0, 9, 20 and 75 equivalents KPF_6. *4 and 40 equivalents were run more dilutely.

Equivalents KPF_6	E_{ox}^1 (V) Distance ($*10^{-6}$ A)	E_{ox}^2 (V) Distance ($*10^{-6}$ A)	E_{ox}^3 (V) Distance ($*10^{-6}$ A)
0	32.6%	46.1%	21.3%
4*	32.4%	31.6%	36.0%
9	29.8%	37.3%	32.9%
20	27.9%	23.0%	49.0%
40*	25.0%	21.2%	53.8%
75	18.3%	5.91%	75.8%

Table 5-5. The relative percentages for the three oxidation events of $3.06*10^{-3}$ M PNP[CoL] with the addition of 0, 9, 20 and 75 equivalents KPF_6. *4 and 40 equivalents were run more dilutely. The calculations are explained in the text.

Equivalents KPF_6	E_{ox}^1 (V) Distance ($*10^{-6}$ A)	E_{ox}^2 (V) Distance ($*10^{-6}$ A)	E_{ox}^3 (V) Distance ($*10^{-6}$ A)
0	6.77	9.57	4.43
4*	5.31	5.19	5.90
9	5.07	6.35	5.59
20	3.85	3.17	6.75
40*	1.57	1.34	3.39
75	1.88	0.61	7.78

Table 5-6. The distance of the anodic peak from the best fit line for the voltammogram for the three oxidation events of $3.06*10^{-3}$ M PNP[CoL] with the addition of 0, 9, 20 and 75 equivalents KPF_6. *4 and 40 equivalents were run more dilutely. The calculations are explained in the text.

VIII. Ligand Design

$[CoL]^-$ does not contain a preorganized cavity for alkali metal ion binding, which is reflected in the complex's low binding affinity for alkali metal ions. As discussed earlier, in order to form a binding site for the alkali metal the ligand must distort from a trigonal monopyramidal geometry into a trigonal bipyramidal geometry in which two arms splay outwards and the third folds up over the metal. The ability of the $[CoL]^-$ to form the binding site for alkali metals can be explained by the geometry of the ligand: When one arm folds up over the Co(II) center, it forms an energetically favorable 6-membered ring. For example, in K[CoL] the ring is composed of Co1, N4, C25, C26, C31 and O9. Energetically favorable five-membered rings also form from two methoxyether oxygen atoms from the

same arm coordinating to the alkali metal ion and, for K^+, from coordination of a carbonyl oxygen and proximal methoxyether oxygen from the same arm. Additionally, the position of the proximal methyoxyether substituents four atoms from the carbonyl places one (in the case of $Na^+$and Li^+) or two (in the case of K^+) of these oxygen atoms in a location where they can participate in coordination to the alkali metal ion.

To further investigate the effect of the ligand geometry on the ability of the complex to form a cavity for alkali metal binding, two ligands with the methoxyether substituents positioned one atom further from the carboxyl groups, L2 and L3 (Figure 5-14), were synthesized and metallated using NaH and Co(II) acetate in a procedure analogous to that used to synthesize Na[CoL]. Both Na[CoL2] and Na[CoL3] crystallized as turquoise plates when Et_2O was slowly diffused into DMF solutions of the complexes. Na[CoL2] and Na[CoL3] crystallized in the *P*1bar and *P*2(1)/c space groups respectively. The molecular structures are shown in Figure 5-16. Unlike Na[CoL], in Na[CoL2] and Na[CoL3] the geometry around the Co(II) centers is trigonal monopyramidal, with τ_4 values of 0.86[140] for both complexes. The Na^+ ions are coordinated in a tetrahedral geometry to carboxyl oxygen atoms from four different ligands (a DMF molecule also makes up one of the four ligands for one the two types of Na^+ in Na[CoL2]). Thus, the methoxyether oxygens are not involved in coordination to the alkali metal ion and the geometry around the Co(II) center in the solid state does not change to trigonal bipyramidal in the presence of an alkali metal ion.

The UV-visible absorption spectroscopy of these complexes was also investigated. Both complexes have asymmetrical bands centered at ~ 600 nm, with λ_{max} ~ 588 nm. The extinction coefficients for this band for both complexes are greater than for PNP[CoL], with Na[CoL2] significantly higher, and the baseline past 750 nm lower, which can be explained

by these complexes being less fluxional than the PNP[CoL] complex in solution.

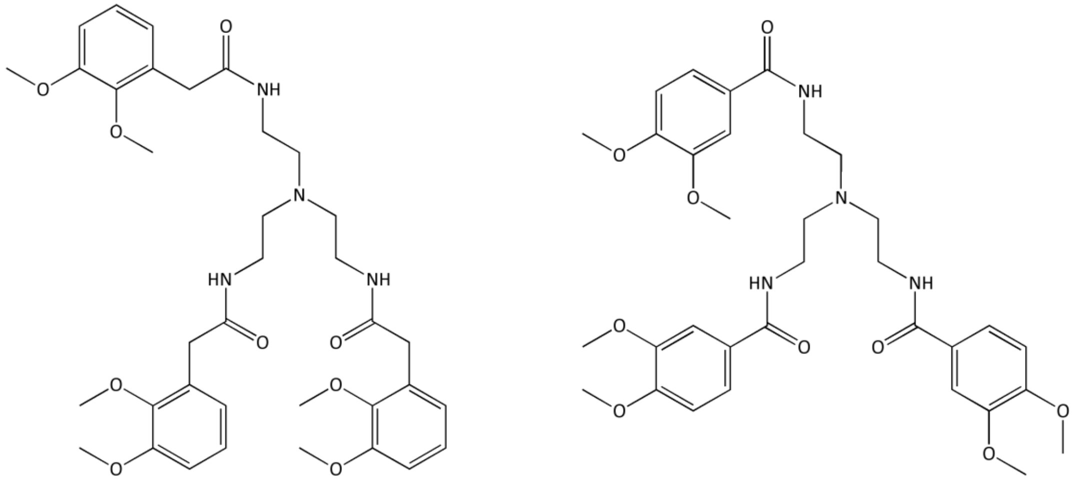

Figure 5-14. Ligands L2 (left) and L2 (right).

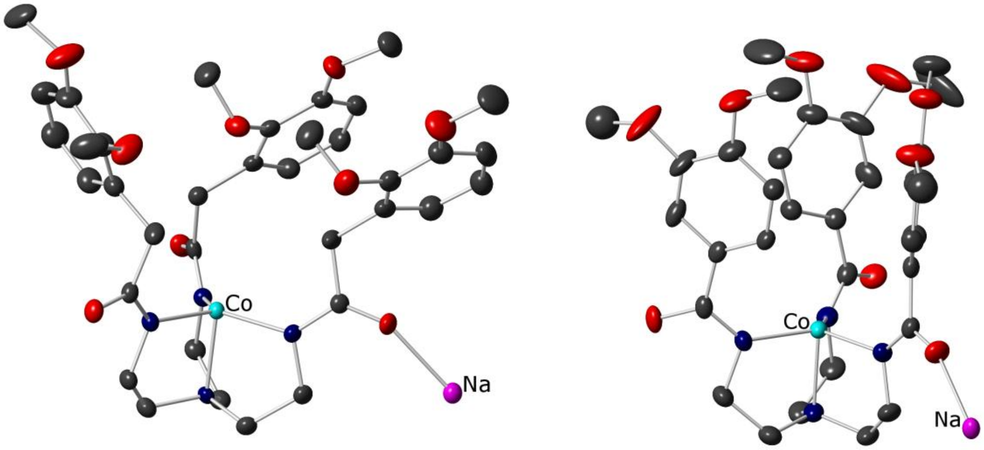

Figure 5-15. Molecular structures of Na[CoL2] (left) and Na[CoL3] (right). Thermal ellipsoids are drawn at 50% probability. Carbon is shown in grey, oxygen in red and nitrogen in blue.

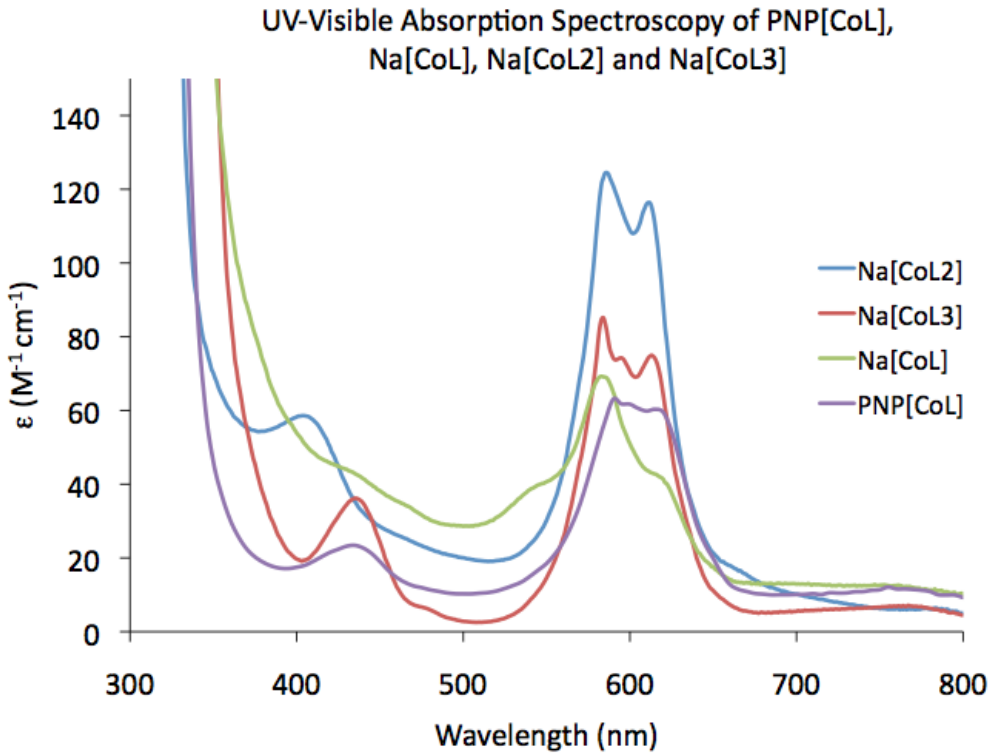

Figure 5-16. UV-visible absorption spectra for PNP[CoL], Na[CoL], Na[CoL2] and Na[CoL3] recorded in DMF.

It was also attempted to synthesize other tripodal ligands that could potentially coordinate both transition and alkali metal ions, aided by the formation of favorable chelate rings. Some of these are shown below in Figure 5-17. However, crystal structures of the metallated complexes could not be obtained in the time available.

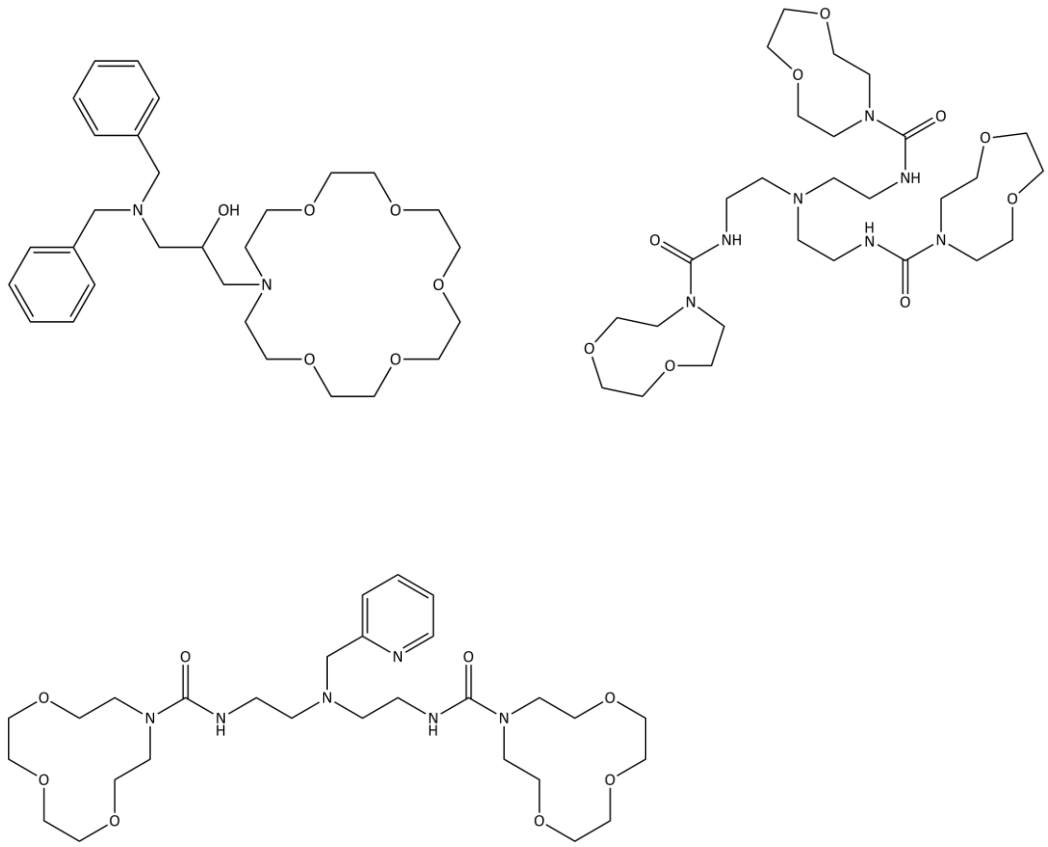

Figure 5-17. Other ligands that were synthesized, but for which crystal structures of the metallated products could not be obtained in the available time.

IX. Conclusions

Coordination of alkali metals by $[CoL]^-$ influences both the local and extended geometry of these complexes. The change in ligand coordination about the Co(II) center upon alkali metal coordination may provide useful insight into the role of alkali and alkaline earth metals in influencing structure in metalloproteins. Additionally, concepts from these complexes may be utilized in crystal engineering and the design of heterogeneous versus homogeneous catalysts. For example, the complexes K[CoL] and Na[CoL] form extended

solids insoluble in solvents less polar than DMSO and, to a limited extent, DMF, whereas PNP[CoL] is soluble in MeCN and CH_2Cl_2, and Li[CoL] is also soluble in toluene, benzene and ether. Additionally, the addition of groups that can coordinate an alkali metal can cause an organometallic complex to organize in a preferred extended structure, which may be useful for organometallic crystal engineering and topochemical reactions.

X. Experimental Section and Supplementary Material

General Considerations

All reactions and manipulations were carried out using Schlenk line techniques or conducted in an MBraun Labmaster 130 glovebox under a nitrogen atmosphere. All reagents used were purchased from commercial vendors and used as received unless otherwise noted. Anhydrous solvents were purchased from Sigma-Aldrich, and acetonitrile, tetrahydrofuran, dichloromethane and ether were further purified by sparging with Ar gas followed by passage through activated alumina columns. Deuterated acetonitrile and dichloromethane were purchased from Cambridge Isotopes and used as received. Deuterated dimethyl sulfoxide (DMSO-d_6) was purchased from SigmaAldrich and dried using either standard procedures,[149] or by drying with 300 Å molecular sieves. Elemental analyses were performed by Atlantic Microlab, Norcross, GA. ^{1}H and ^{13}C NMR spectra were recorded on a Varian Mercury 300 MHz or Varian Innova 400 MHz spectrometer at ambient temperature. Chemical shifts were referenced to residual solvent peaks. Infrared spectra were recorded as KBr pellets on a Varian Scimitar 800 Series FT-IR spectrophotometer. UV-visible absorption spectra were recorded on a Cary 50 spectrophotometer using 1.0 cm quartz cuvettes. Solution state magnetic moments were measured using the Evans method.[143] Mass spectra were recorded in the Mass Spectrometry Center at Emory University on a JEOL JMSSX102/SX102A/E mass spectrometer. X-ray

diffraction studies were carried out in the X-ray Crystallography Laboratory at Emory University on a Bruker Smart 1000 CCD Diffractometer containing a molybdenum tube.

Synthesis

H_3L. H_3L has been previously reported in the literature using a different procedure. [150] Here, 2,3-dimethoxybenzoic acid (10 g, 0.055 mols) was stirred with 36 mL $SOCl_2$ for two hours at room temperature on a flask fitted with a drying tube. The $SOCl_2$ was then removed on a rotary evaporator and ~ 36 mL benzene added and then removed on the rotary evaporator, two times. The residue was then dissolved in CH_2Cl_2 (~ 150 mL) and added dropwise to a solution of tris-2-aminoethylamine (2.56 mL, 0.017 mmol) and triethylamine (7.8 mL, 0.056 mmol) in ~ 100 mL CH_2Cl_2 under N_2 at room temperature. The reaction was stirred under N_2 overnight. H_2O (~200 mL) was then added, the mixture shaken in a separatory funnel, and the organic layer collected. The reaction was then further extracted with saturated aqueous $NaHCO_3$ (~200 mL) and brine (~200 mL), dried over $MgSO_4$, and the solvent then removed on the rotovap. The crude product was recrystallized from hot ethyl acetate, which was then cooled to room temperature and placed in the freezer overnight. (Mass of recrystallized product = 7.4 g, 68% yield)

PNP[CoL]. KH (75.2 mg, 1.88 mmol) was added to L (400.0 mg, 0.624 mmol) dissolved in ~5 mL DMF. The pale yellow solution was stirred for six hours. $Co(OAc)_2$ (110.4 mg, 0.624 mmol) was added as a solid, and the reaction was further stirred overnight. PNPCl (358.4 mg, 0.624 mmol) was then added and the reaction stirred 2 hours further. DMF was then removed under vacuum and the residue extracted into MeCN. Insoluble material (161.0 mg) was filtered off. The solvent was removed from the filtrate under vacuum, leaving a

turquoise oil that was recrystallized from slow diffusion of Et_2O into DMF. This resulted in turquoise plate-like crystals (650 mg, 79.7% yield).

K[CoL]. KH (75.2 mg, 1.88 mmol) was added to L (400.0 mg, 0.624 mmol) dissolved in ~5 mL DMF. The pale yellow solution was stirred for six hours. $Co(OAc)_2$ (110.4 mg, 0.624 mmol) was added as a solid, and the reaction was further stirred overnight. The pale blue-grey precipitate (160.2 mg) was then filtered off. Ether was diffused into the filtrate, resulting in precipitation of a pale blue powder (292.7 mg). This pale blue powder was dissolved in DMSO and recrystallized by slow diffusion of either, resulting in pink block-like crystals (226.3 mg, 49.4% yield).

Na[CoL]. NaH (11.6 mg, 0.47 mmol) was added to L (100.0 mg, 0.156 mmol) dissolved in ~ 1.5 mL DMF. The white mixture was stirred 24 h. $Co(OAc)_2$ (27.6 mg, 0.156 mmol) was then added as a solid, and the reaction stirred further overnight. Insoluble material (20.8 mg) was then filtered off. The DMF was removed from the filtrate under vacuum and the resulting purple solid redissolved in DMSO. Pink block-like crystals were grown via slow diffusion of Et_2O into this solution (48.2 mg, 38.9%).

Li[CoL]. LiHMDS (1.0 M in THF) (0.52 mL, 0.515 mmol) was added to L (100 mg, 0.156 mmol) in ~ 5 mL THF and the resulting white mixture stirred 24 h. The solvent was then removed under vacuum and the resulting off-white solid washed thoroughly with hexanes. DMF (~ 2 mL) was added to the solid, followed by $Co(OAc)_2$ (27.6 mg, 0.156 mmol) as a solid. The reaction was further stirred overnight. DMF was then removed under vacuum, leaving a dark purple solid. This solid was dissolved in dichloromethane, insoluble material

filtered off, and recrystallized by layering with hexanes, resulting in pink block-like crystals (64.8 mg, 59.0% yield).

PNP[ZnL]. KH (18.8 mg, 0.47 mmol) was added to L (100.0 mg, 0.156 mmol) dissolved in ~1.5 mL DMF. The pale yellow solution was stirred for six hours. $Zn(OAc)_2$ (28.6 mg, 0.156 mmol) was added as a solid, and the reaction was further stirred overnight. PNPCl (89.6 mg, 0.156 mmol) was then added and the reaction stirred 2 hours further. DMF was then removed under vacuum and the residue extracted into MeCN. Insoluble material (43.5.0 mg) was filtered off. The filtrate was recrystallized by slow diffusion of Et_2O into the MeCN solution. This resulted in colorless plate-like crystals (101.7 mg, 51.7% yield). Crystals could also be grown by diffusion of Et_2O into a DMF solution of the complex.

Titration Experiments

Stock solutions of PNP[CoL] and APF_6 ($A^+ = K^+$, Na^+, or Li^+) were made up in DMF containing 0.1 M tetrabutylammonium hexafluorophosphate. A set volume of the PNP[CoL] solution was then pipetted into each vial to give an end concentration of $3.06 * 10^{-3}$ M PNP[CoL] once the remaining solutions were added. Varying amounts of the APF_6 solutions were then added (up to 35 equivalents $NaPF_6$/PNP[CoL], up to 40 equivalents $NaPF_6$/PNP[CoL], and up to 100 equivalents $NaPF_6$/PNP[CoL]). Enough 0.1 M $TBAPF_6$ in DMF solution was then added to bring the total volume of each volume up to 3 mL. The solutions were then stirred at room temperature for two days, and then transferred to 1 cm quartz cuvettes so that their UV-visible absorption spectra could be recorded. The UV-visible absorption spectra were recorded from 1000 nm to 275 nm at 22 °C.

Job's method experiments with $NaPF_6$ and $LiPF_6$ were conducted with $6.12*10^{-3}$ M solutions of PNP[CoL] and $NaPF_6$ or $LiPF_6$ in DMF. Nine solutions ($NaPF_6$) or seven

solutions ($LiPF_6$) were made up with mole fractions ranging from 0.917 MPF_6 (M = Na^+ or Li^+)/0.083 PNP[CoL] to 0.083 MPF_6/0.917 PNP[CoL]. The solutions were stirred for two days and their UV-visible absorption spectra then recorded at room temperature. The data were plotted with mole fraction on the x-axis and A' = A-$C_1\varepsilon_1 l$ on the y-axis, where A' = the corrected absorbance, A = the actual absorbance, C_1 = the molar concentration of PNP[CoL], ε_1 = molar extinction coefficient of PNP[CoL] and l = the path length of the cuvette. The absorbance of MPF_6 in the region of interest was negligible, so it was not included in the formula.

Data

H_3L

^{1}H NMR (300 MHz, CD_2Cl_2) (ppm): 8.13 (broadened triplet, 3H), 7.52 (dd, J = 8.1 Hz, 1.8 Hz, 3H), 7.09 (t, J = 8.1 Hz, 3H), 7.01 (dd, J = 8.1 Hz, 1.8 Hz, 3H), 3.84(s, 18H), 3.56 (q, J = 5.7 Hz, 6H), 2.85 (t, J = 6.6 Hz, 6H)

PNP[CoL]

1. ^{1}H NMR (300 MHz, DMSO-d_6) (ppm): 72, 21.56, 9.04 (PNP^+), 8.83 (PNP^+), 8.68 (PNP^+), 4.45, 3.99, 3.82, 3.60, 2.16, -5.35, -9.37

2. IR (KBr) (cm^{-1}): 3051.8 (aryl C-H), 2987.4, 2938,7, 2900.1, 2844.5 (sp^3 C-H), 1672.0, 1649.3 (carbonyl C=O), 1557.2 (aryl C-C), 1468.5, 1438.8, 1389.3, 1263.8, 1115.4, 1072.9, 754.2, 724.5, 694.2

3. UV-visible (DMF) {A ($\varepsilon(M^{-1}\,cm^{-1})$)}: 434.9 (23.75), 590.0 (64.2) + shoulder

4. C,H,N (Theory, Found): C (66.20, 66.35); H (5.86, 5.73); N (6.43, 6.39)

5. Cyclic Voltammetry (0.2 M $TBAPF_6$/DMF, glassy carbon w.e., Pt counter electrode, $Ag/AgNO_3$ reference electrode, vs. Fc/Fc^+): Irreversible oxidation events at 0.1 V, 0.35 V, 0.55 V

6. Magnetic Susceptibility: μ_{eff} = 4.48 (DMSO-d_6); μ_{eff} = 4.66 (CD_2Cl_2)

7. Mass Spec (m/z, relative %): Positive ESI 538.33, 100% (PNP^+), Negative 694.203, 100% (L^{3-} + Co^{2+})

K[CoL]

1. ^{1}H NMR (300 MHz, DMSO-d_6) (ppm): 72, 21.63, 9.05, 4.01, 3.82, 3.61, -5.37, -9.42

2. IR (KBr) (cm^{-1}): 3074.4 (aryl C-H), 2939.7, 2900.5, 2854.2 (sp^3 C-H), 1642.5 (C=O), 1565.4, 1540.9 (aryl C-C), 1473.6, 1415.9, 1265.0, 1059.0

3. UV-visible (DMF) {A ($\varepsilon(M^{-1}\,cm^{-1})$)}: 430.0 (24.2), 585.0 (66.07) + shoulder

4. C,H,N for K[CoL] + 1.5 DMSO (Theory, Found for 3 different trials): C (50.81, 50.58, 50.47, 50.29); H: (5.69, 5.75, 5.63, 5.46); N (6.58, 6.54, 6.56, 6.60)

5. Cyclic Voltammetry (0.2 M $TBAPF_6$/DMF, glassy carbon w.e., Pt counter electrode, $Ag/AgNO_3$ reference electrode, vs. Fc/Fc^+): Irreversible oxidation events at 0.1 V, 0.35 V, 0.55 V

6. Magnetic Susceptibility: μ_{eff} = 4.33 (DMSO-d_6)

7. Mass Spec (m/z): Positive ESI 677.258, 100% (L_3H + K^+), 772.13, 10.33% (L^{3-} + Co^{2+} + $2K^+$) and 1315.562, 33.2% (2 L_3H + K^+), Negative 694.203 (L^{3-} + Co^{2+}) and 1427.367 (2 L^{3-} + 2 Co^{2+} + K^+)

Na[CoL]

1. ^{1}H NMR (300 MHz, DMSO-d_6) (ppm): 72, 21.48, 9.40, 9.08, 8.26, 8.24, 7.18, 6.91, 6.60, 4.96, 4.87, 4.49, 4.05, 3.86, 3.77, 3.66, 2.19, -5.33, -9.36

2. IR (KBr): 2937.59 (sp^3 C-H), 2848.04 (sp^3 C-H), 1672.09 (C=O), 1552.12 (aryl C-C), 1467.42, 1423.64, 1264.17, 1065.59, 755.41

3. UV-visible (DMF) {A ($\varepsilon(M^{-1}\,cm^{-1})$)}: 580.1 (61.1)

5. C,H,N for Na[CoL] (Theory, Found): C (52.83, 52.69); H (5.70, 5.65); N (7.04, 7.08)

5. Cyclic Voltammetry (0.2 M $TBAPF_6$/DMF, glassy carbon w.e., Pt counter electrode, $Ag/AgNO_3$ reference electrode, vs. Fc/Fc^+): Irreversible oxidation events at 0.1 V, 0.35 V, 0.55 V

6. Magnetic Susceptibility: μ_{eff} = 4.43 (DMSO-d_6)

7. Mass Spec (m/z, relative %): Positive ESI: 661.28, 100% ($L_3H + Na^+$), 677.26, 70.27% ($L_3H + K^+$), 740.18, 15.46% ($L^{3-} + Co^{2+} + 2Na^+$), Negative ESI: 694.20, 100% ($L^{3-} + Co^{2+}$)

Li[CoL]

1. ^1H NMR (300 MHz, DMSO-d_6) (ppm): Numerous peaks

2. IR (KBr): 2936.84 (sp^3 C-H), 2851.08 (sp^3 C-H), 1646.88 (C=O), 1637.15 (C=O), 1553.60 (aryl C-H), 1473.88, 1424.67, 1263.74, 1060.86, 795.71

3. UV-visible (DMF) {A ($\varepsilon(M^{-1}\,cm^{-1})$)}: Broad absorbance 530.0 nm (63.9)

4. C,H,N (Theory, Found for 2 different trials) for Li[CoL] + 4/3 CH_2Cl_2: C (50.61, 50.32, 50.20), H (5.15, 5.43, 5.41), N (6.88, 7.00, 6.92)

5. Cyclic Voltammetry (0.2 M $TBAPF_6$/DMF, glassy carbon w.e., Pt counter electrode, $Ag/AgNO_3$ reference electrode, vs. Fc/Fc^+) - Broad irreversible oxidation events at -0.1 V, 0.4 V, 0.5 V, 0.7 V

6. Magnetic Susceptibility: μ_{eff} = 4.36 (DMSO-d_6)

7. Mass Spec (m/z, relative %): Positive ESI: 645.31, 100% ($L_3H + Li^+$), 708.24, 5.5% ($L^{3-} + Co^{2+} + 2Li^+$) and Negative ESI: 694.20, 100% ($L^{3-} + Co^{2+}$)

PNP[ZnL]

1. ^1H NMR (300 MHz, CD_3CN) (ppm) (multiplicity, J (Hz), number of H, assignment): 7.689 – 7.443 (multiplet, 30 H, PNP aryl protons,), 6.871 (d, J=8.1 Hz, 3H), 6.630 (dd, J

(avg.)=7.8 Hz, 3H), 5.197 (d, J=7.2 Hz, 3H), 3.787 (s, 9H), 3.686 (s, 9H), 3.362 (t, J=5.1 Hz, 6H), 2.556 (J=5.1 Hz, 6H)

2. ^{13}C NMR (400 MHz, CD_3CN) (ppm) 172.49 ($[ZnL]^+$ carbonyl C), 153.60 ($[ZnL]^+$ aryl C), 146.70 ($[ZnL]^+$ aryl C), 140.12 ($[ZnL]^+$ aryl C), 134.88 ($[PNP]^-$), 133.52 (J=22.8 Hz) ($[PNP]^-$), 130.65 (J=27.6 Hz) ($[PNP]^-$), 129.03 (d, J=7.6 Hz) ($[PNP]^-$), 127.96 (d, J=7.6 Hz) ($[PNP]^-$), 125.82 ($[ZnL]^+$ aryl C), 120.23 ($[ZnL]^+$ aryl C), 118.60 (CD_3CN), 112.45 ($[ZnL]^+$ aryl C), 61.14 ($[ZnL]^+$ methoxy C), 56.74 ($[ZnL]^+$ methoxy C), 55.56 ($[ZnL]^+$ methylene C), 42.25 ($[ZnL]^+$ methoxy C)

3. IR (KBr): 3051.93 (aryl C-H), 2988.70 (sp^3 C-H), 2940.60 (sp^3 C-H), 2843.78 (sp^3 C-H), 1647.94 (C=O), 1561.31 (aryl C-C), 1468.55, 1438.76, 1397.79, 1263.50, 1115.40, 723.81

4. C,H,N (Theory, Found for PNP[ZnL] + 2/3 DMF: C (65.53, 65.40), H (5.47, 5.60), N (6.37, 6.31)

5. Cyclic Voltammetry (0.2 M $TBAPF_6$/DMF, glassy carbon w.e., Pt counter electrode, $Ag/AgNO_3$ reference electrode, vs. Fc/Fc^+): Broad irreversible oxidation events at 0.57 V and 0.67 V

6. Mass Spec (m/z, relative %): Positive ESI: 538.18 (PNP^+), 639.30 ($L_3H + H^+$), Negative ESI: 699.20, 100% ($L + Zn^{2+}$)

Supporting Information

NMR Spectra

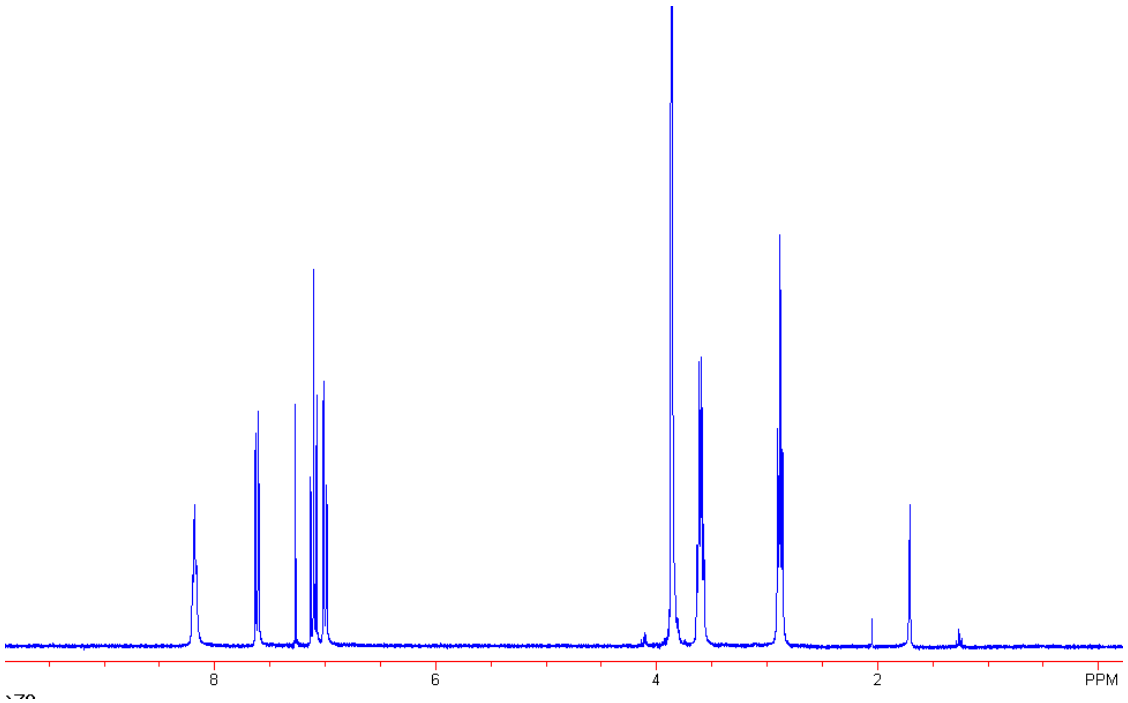

^{1}H NMR spectra of H_3L in $CDCl_3$

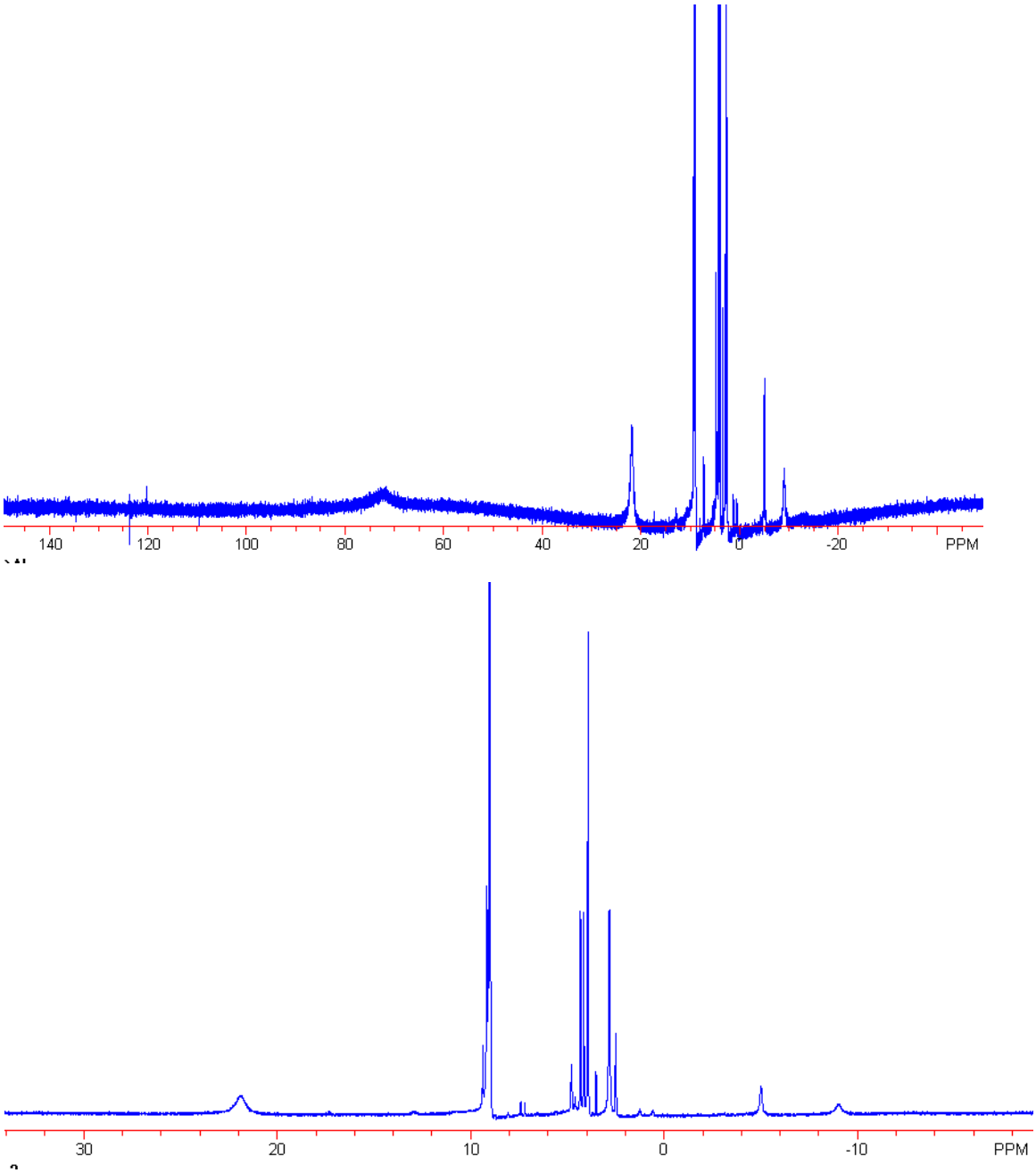

^{1}H NMR of PNP[CoL] in DMSO-d_6

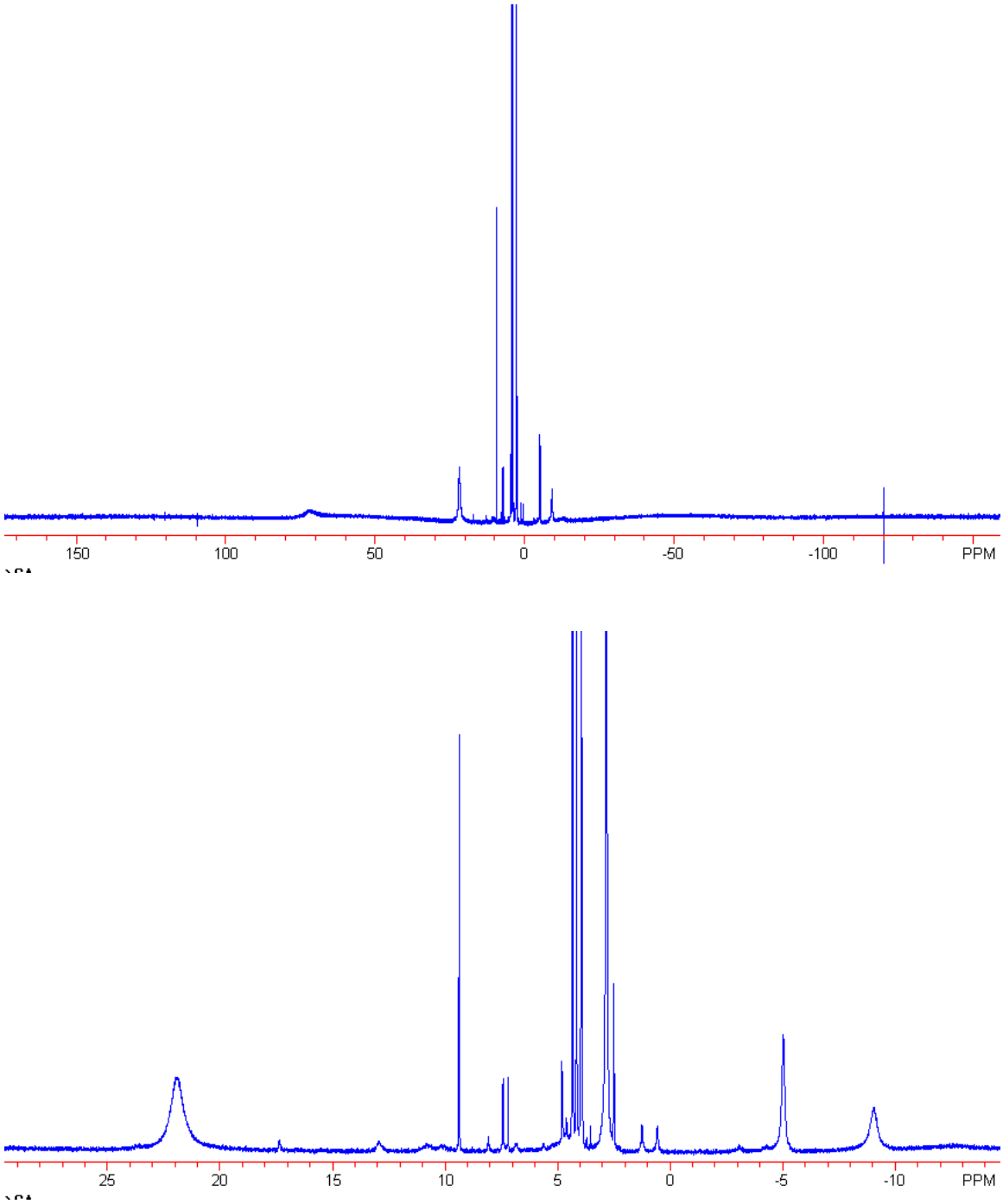

1H NMR of K[CoL] in DMSO-d_6

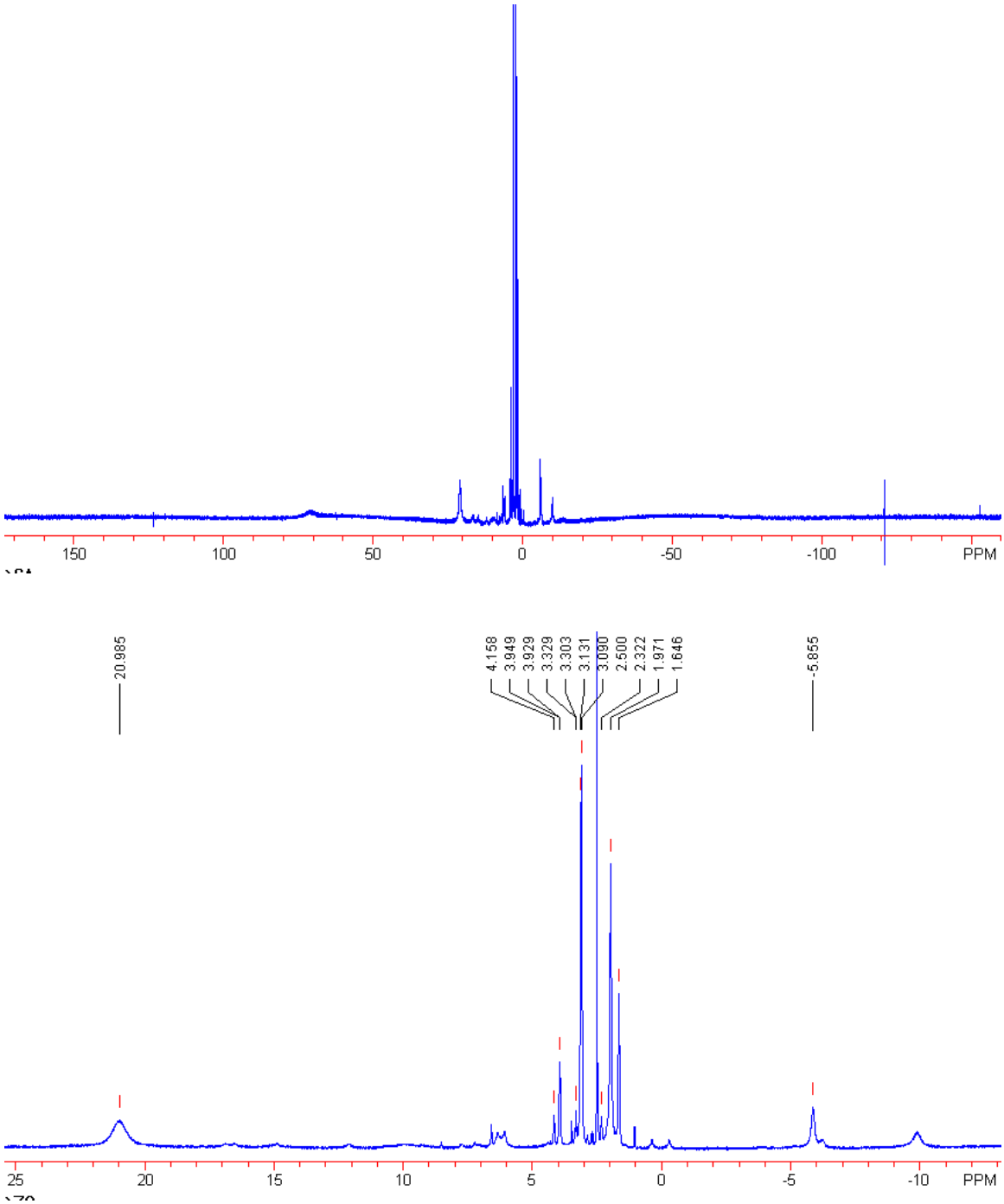

^{1}H NMR of Na[CoL] in DMSO-d_6. This spectrum was taken from the Evans Method experiments, and hence have residual solvent peaks at both the normal frequency and at a frequency shifted due to the paramagnetism of the sample.

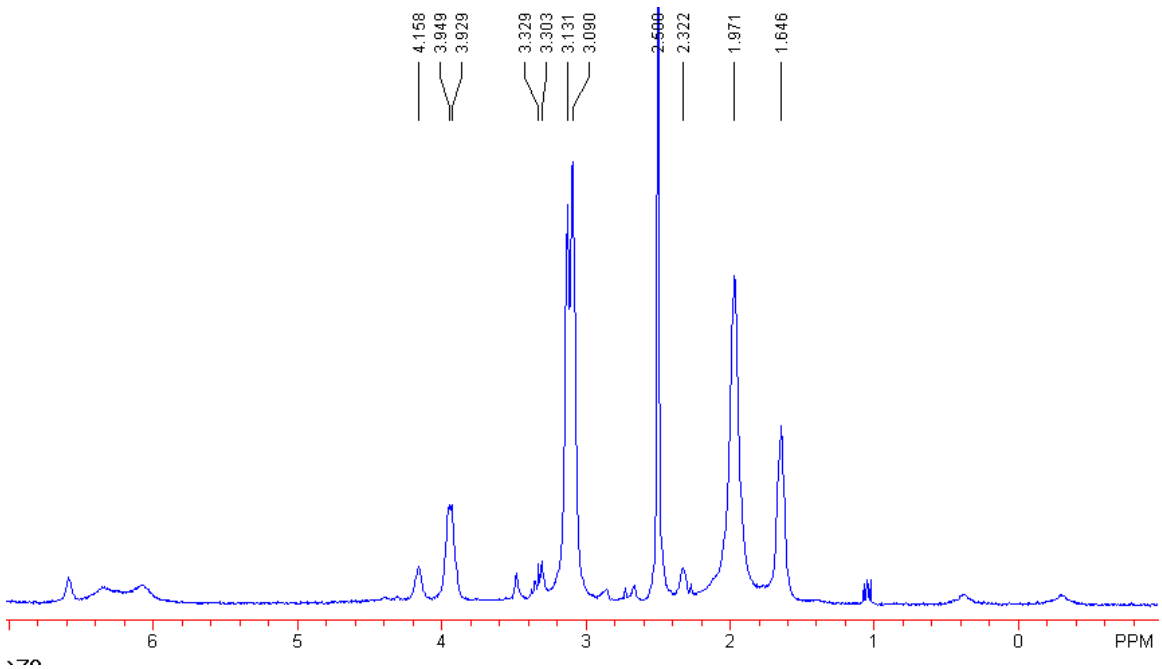

^{1}H NMR of Na[CoL] in DMSO-d_6. These spectra were taken from the Evans Method experiments, and hence have residual solvent peaks at both the normal frequency and at a frequency shifted due to the paramagnetism of the sample.

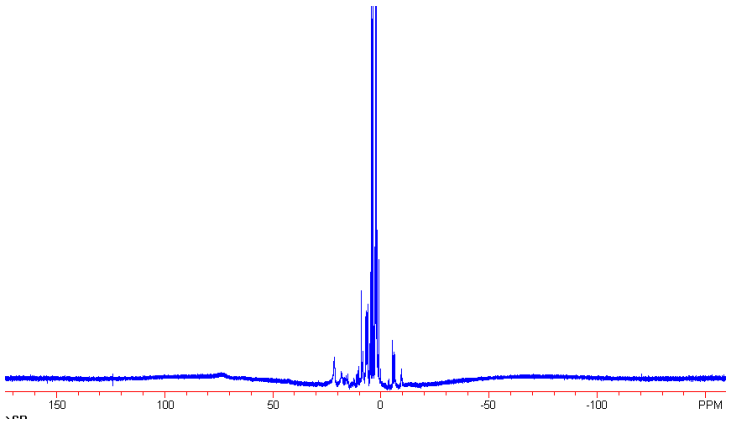

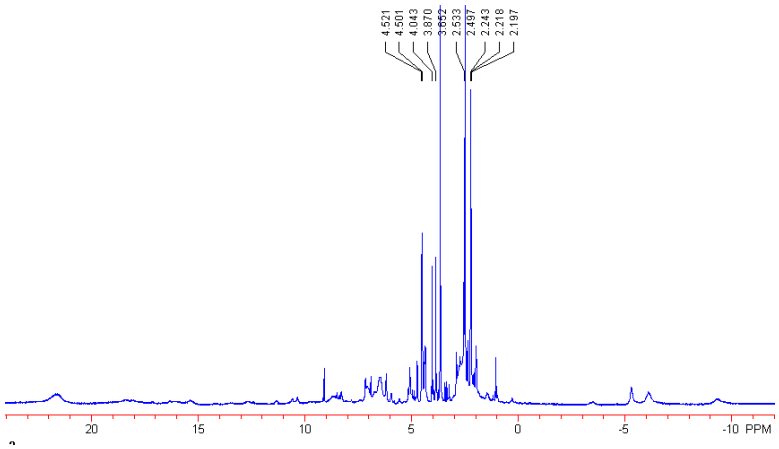

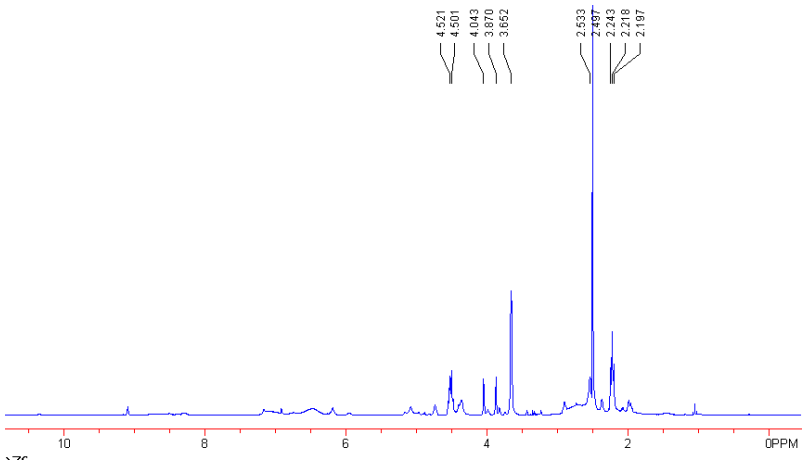

1H NMR of Li[CoL] in DMSO-d_6. These spectra were taken from the Evans Method experiments, and hence have residual solvent peaks at both the normal frequency and at a frequency shifted due to the paramagnetism of the sample.

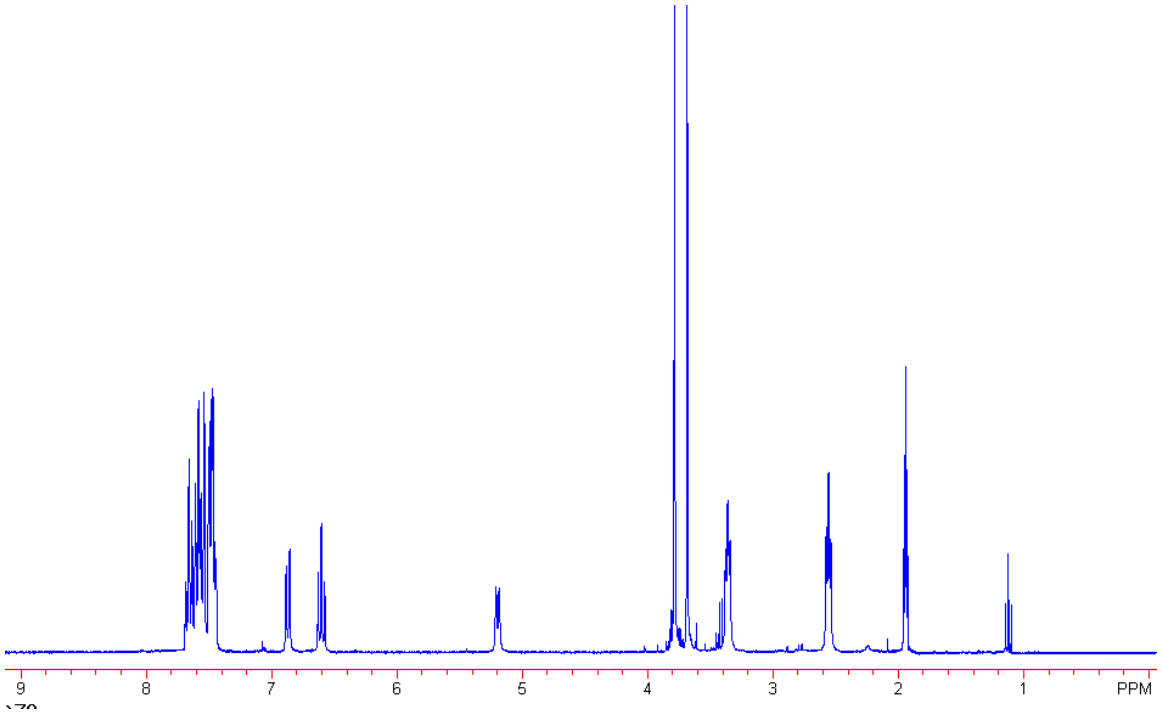

^{1}H NMR of PNP[ZnL] in CD_3CN

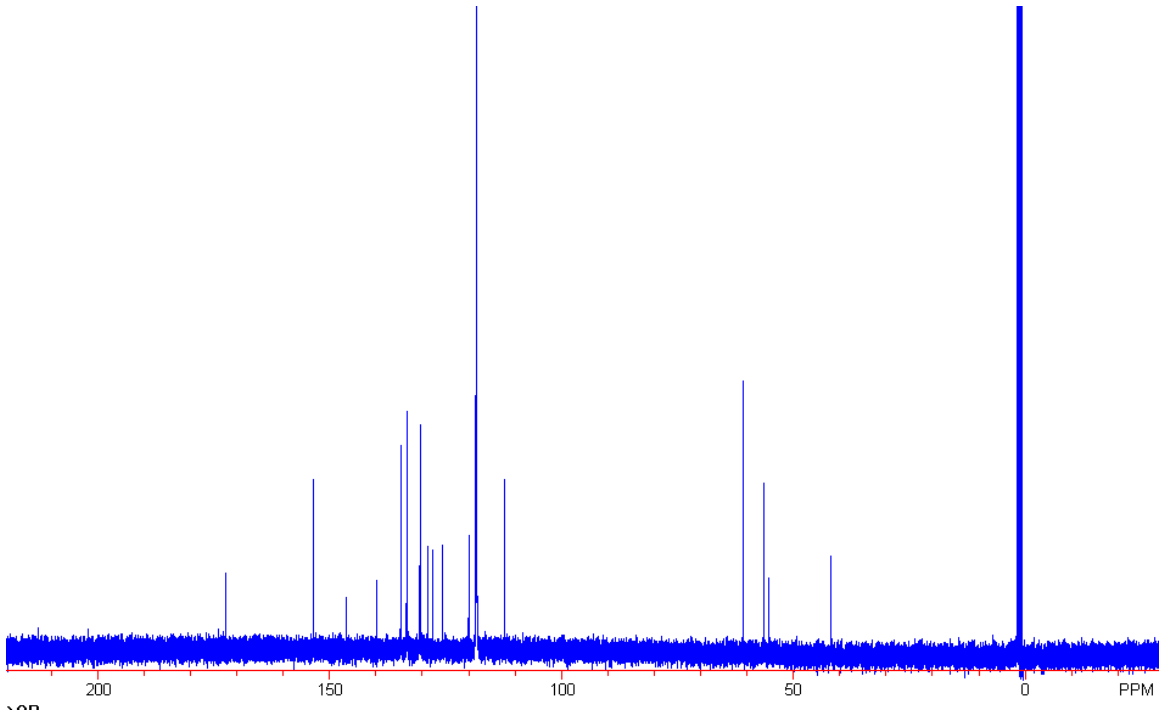

^{13}C NMR of Zn[CoL] in CD_3CN

Titration Data

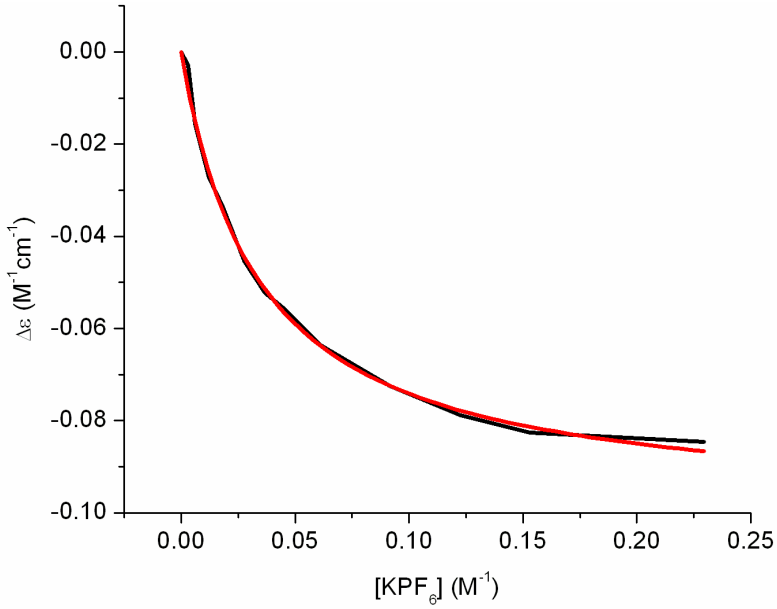

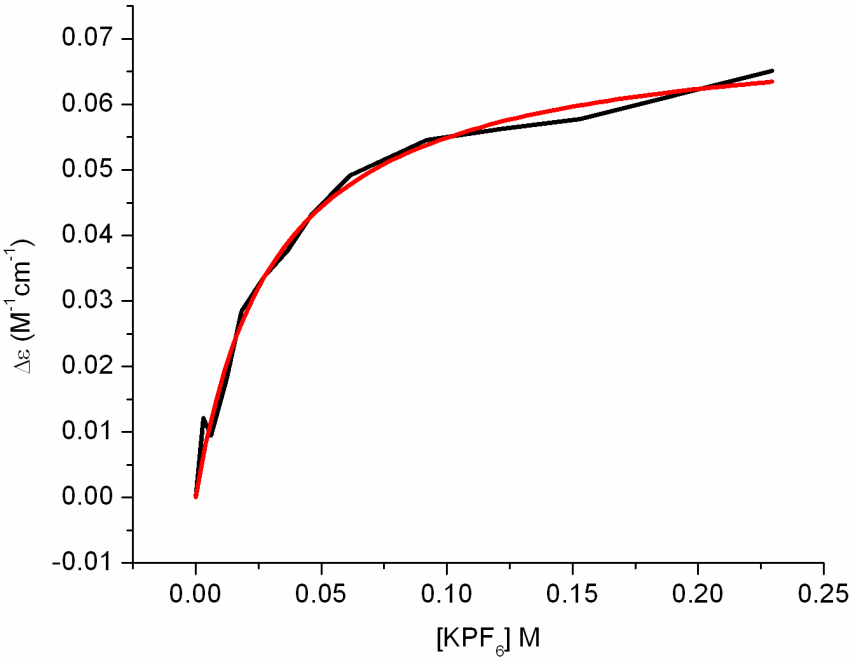

Sample titration data of PNP[CoL] with KPF_6 plotted and fitted at 620 nm (top) and 540 nm (bottom).

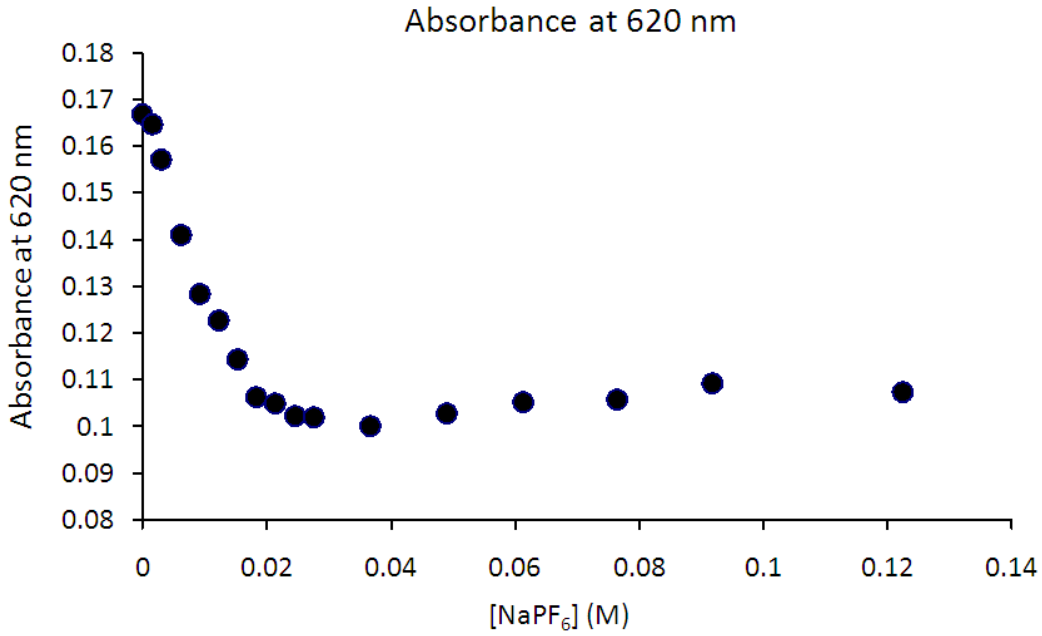

Sample titration data of PNP[CoL] with $NaPF_6$ plotted and fitted at 620 nm

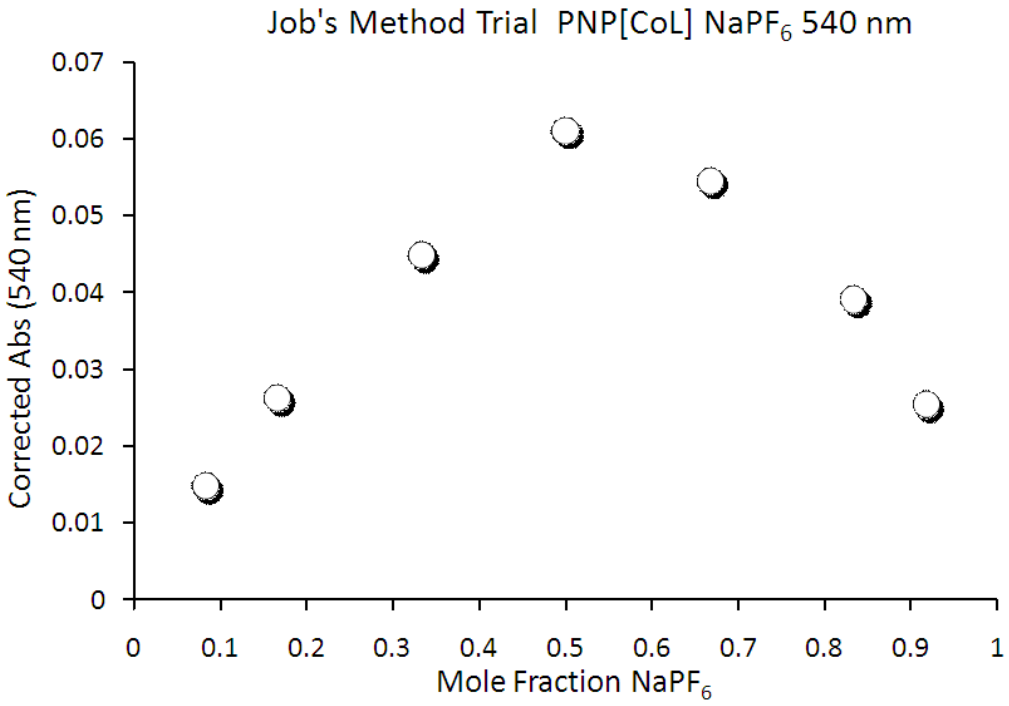

Job's method plot for $NaPF_6$ and PNP[CoL]

IR Spectra:

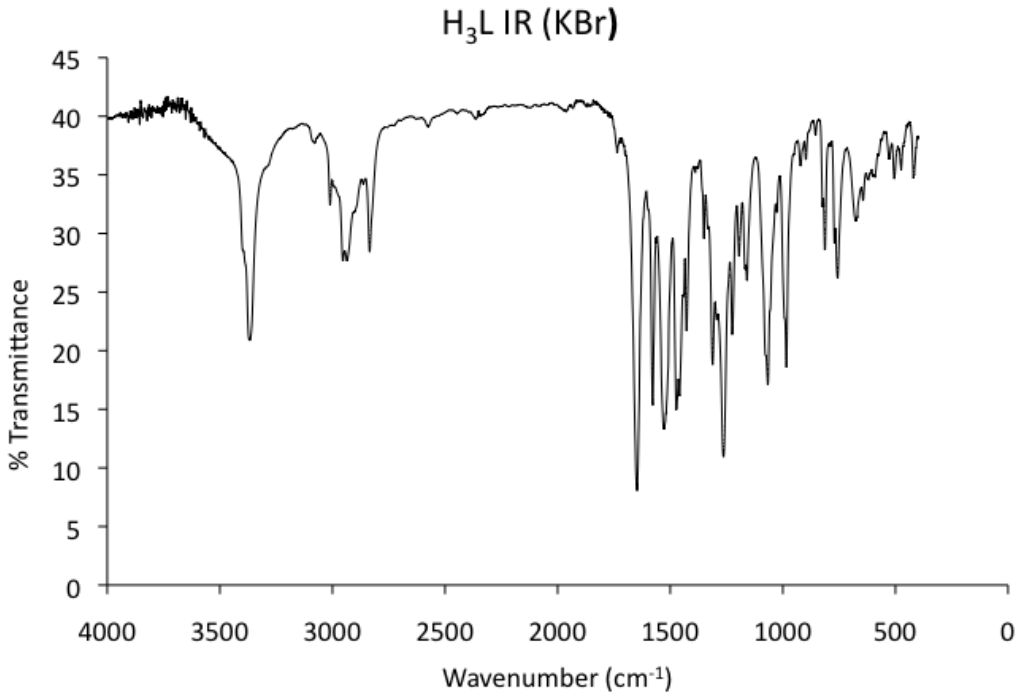
H3L IR (KBr)
% Transmittance
Wavenumber (cm-1)
45
40
35
30
25
20
15
10
5
0
4000
3500
3000
2500
2000
1500
1000
500
0

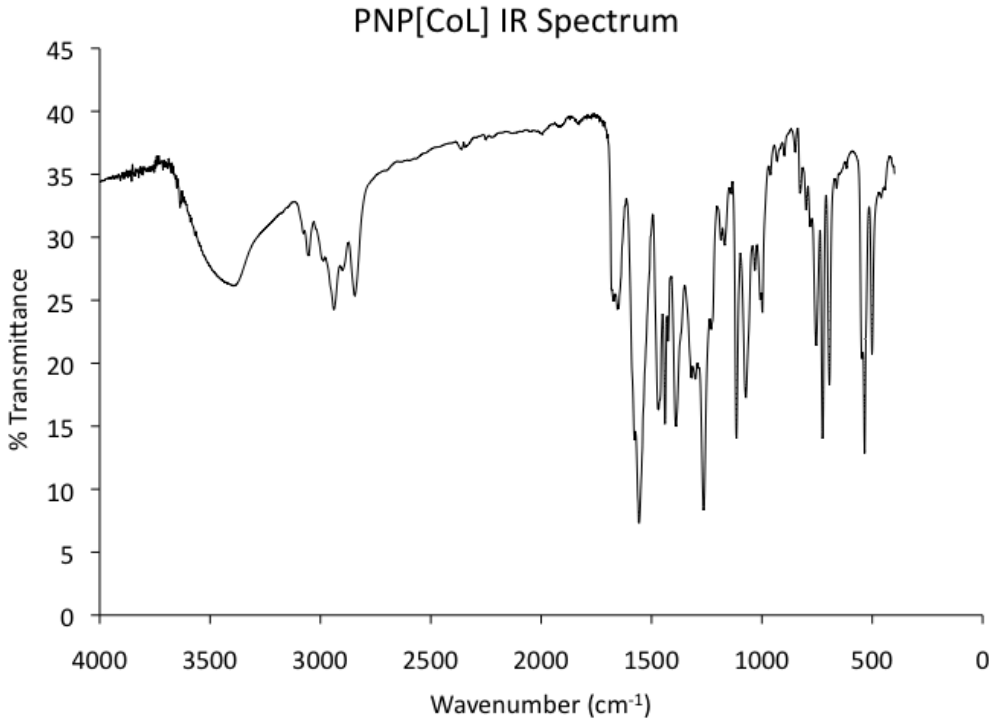
PNP[CoL] IR Spectrum
% Transmittance
Wavenumber (cm-1)
45
40
35
30
25
20
15
10
5
0
4000
3500
3000
2500
2000
1500
1000
500
0

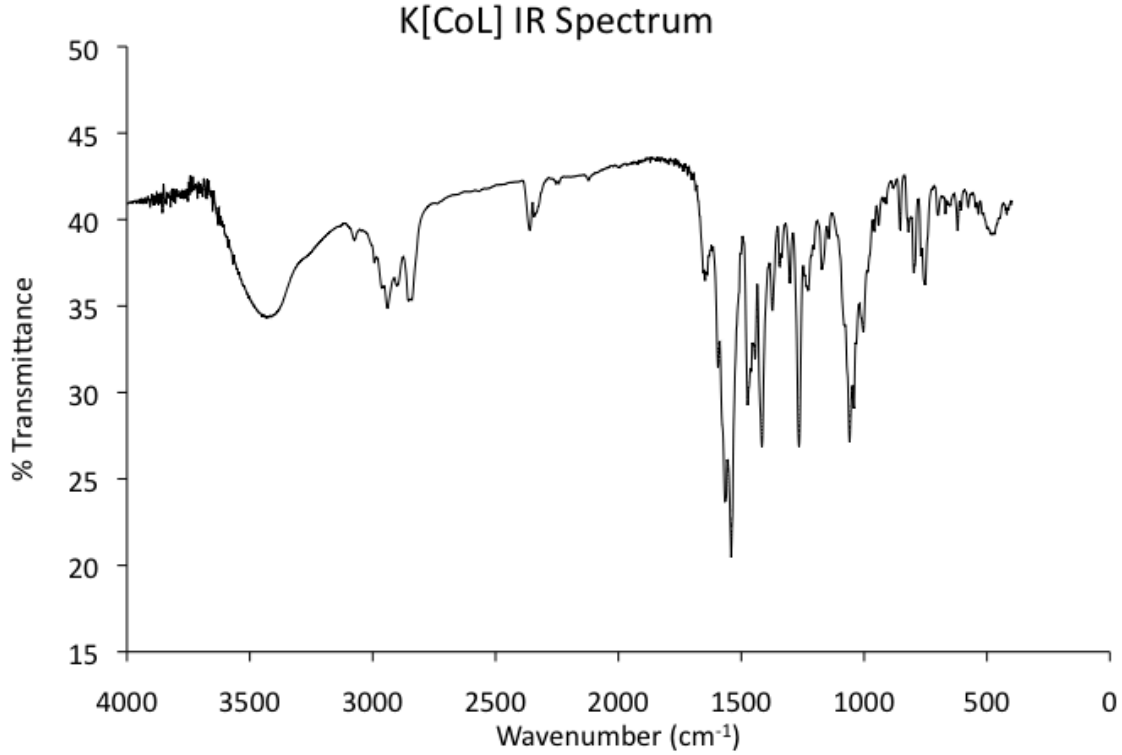
K[CoL] IR Spectrum
% Transmittance
50
45
40
35
30
25
20
15
4000
3500
3000
2500
2000
1500
1000
500
0
Wavenumber (cm-1)

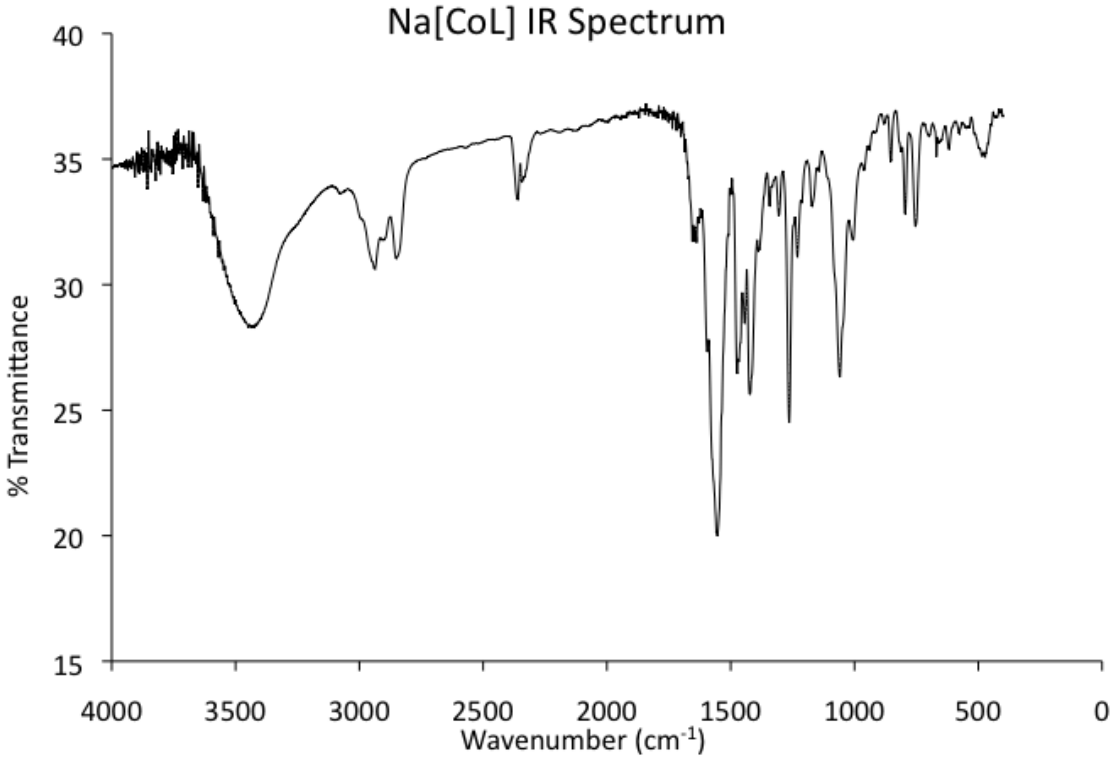
Na[CoL] IR Spectrum
% Transmittance
40
35
30
25
20
15
4000
3500
3000
2500
2000
1500
1000
500
0
Wavenumber (cm-1)

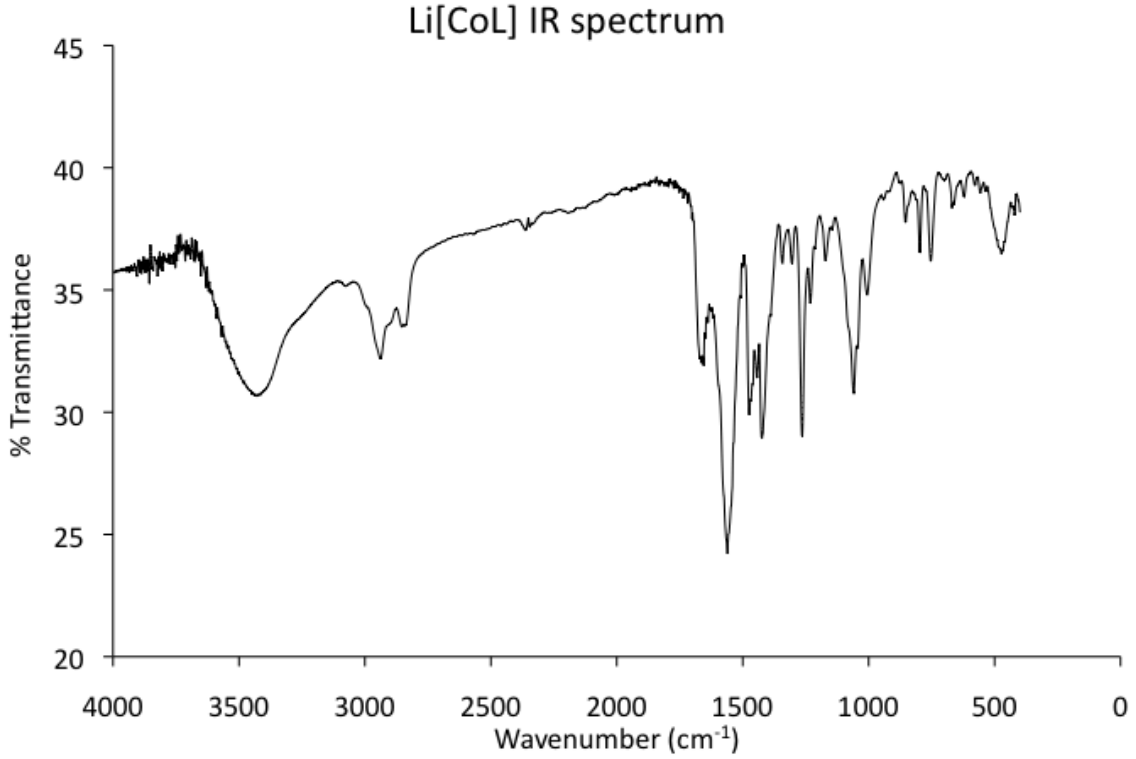
Li[CoL] IR spectrum
% Transmittance
45
40
35
30
25
20
4000
3500
3000
2500
2000
1500
1000
500
0
Wavenumber (cm-1)

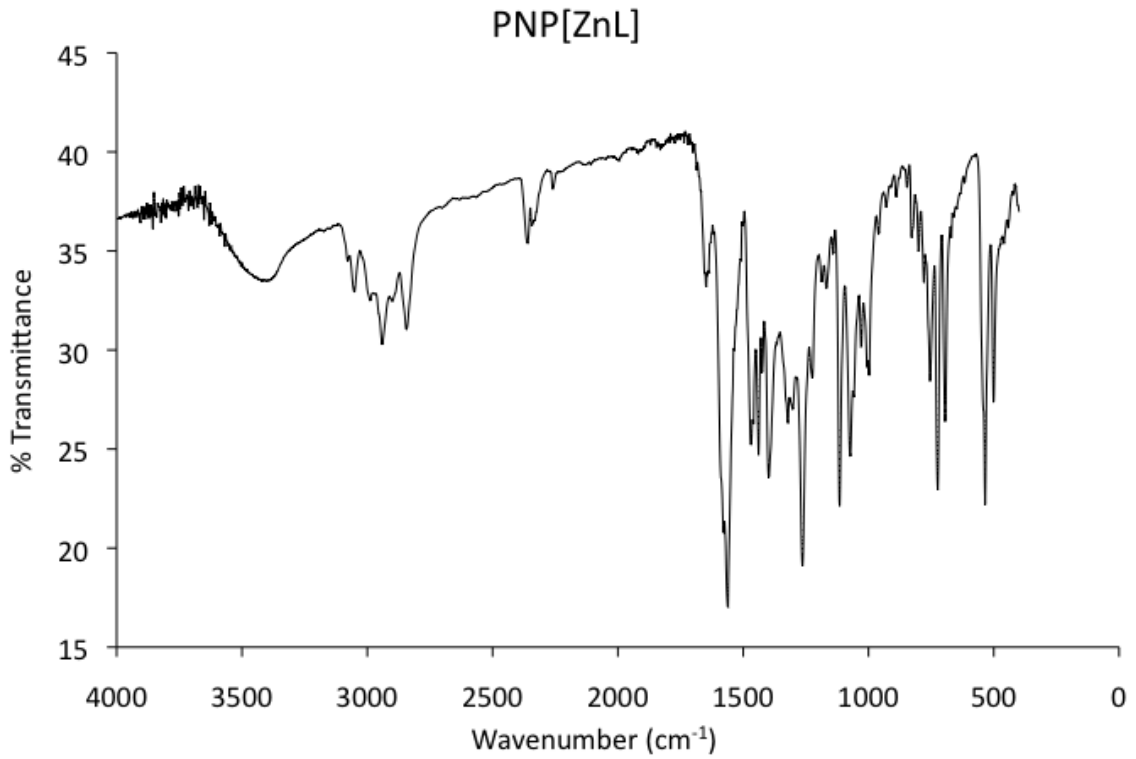
PNP[ZnL]
% Transmittance
45
40
35
30
25
20
15
4000
3500
3000
2500
2000
1500
1000
500
0
Wavenumber (cm-1)

References

(1) Ribeiro, H. A.; Sommeling, P. M.; Kroon, J. M.; Mendes, A.; Costa, C. A. V. *Intl. J. of Green Energy* **2009**, *6*, 245.

(2) Green, M. A.; Emery, K.; Hishikawa, Y.; Warta, W. *Prog. in Photovoltaics: Res. and Appl.* **2010**, *18*, 144.

(3) Green, M. A. *J. Mater. Sci.: Mater. Electron.* **2007**, *18*, S15.

(4) Hains, A. W.; Liang, Z.; Woodhouse, M. A.; Gregg, B. A. *Chem. Rev.* **2010**.

(5) Yu, H.; Irie, H.; Hashimoto, K. *J. Am. Chem. Soc.* **2010**, *132*, 6898.

(6) O'Regan, B.; Graetzel, M. *Nature* **1991**, *353*, 737.

(7) Jones, M. R. Dye-sensitized solar cell. http://en.wikipedia.org/wiki/Dye-sensitized_solar_cell (accessed July 2010).

(8) Liska, P.; Vlachopoulos, N.; Nazeeruddin, M. K.; Comte, P.; Graetzel, M. J. *J. Am. Chem. Soc.* **1988**, *110*, 3686.

(9) Nazeeruddin, M. K.; Kay, A.; Rodicio, I.; Humphrey-Baker, R.; Muller, E.; Liska, P.; Vlachopoulos, N.; Graetzel, M. *J. Am. Chem. Soc.* **1993**, *115*, 6382.

(10) Nazeeruddin, M. K.; Humphry-Baker, R.; Liska, P.; Graetzel, M. *J. Phys. Chem. B.* **2003**, *107*, 8981.

(11) Nazeeruddin, M. K.; Klein, C.; Liska, P.; Graetzel, M. *Coord. Chem. Rev.* **2005**, *249*, 1460.

(12) Klein, C.; Nazeeruddin, M. K.; Liska, P.; Censo, D. D.; Hirata, N.; Palomares, E.; Durrant, J. R.; Gratzel, M. *Inorg. Chem.* **2005**, *44*, 178.

(13) Nazeeruddin, M. K.; Pechy, P.; Renouard, T.; Zakeeruddin, S. M.; Humphrey-Baker,

R.; Comte, P.; Liska, P.; Cevey, L.; Costa, E.; Shklover, V.; Spiccia, L.; Deacon, G. B.; Bignozzi, C. A.; Graetzel, M. *J. Am. Chem. Soc.* **2001**, *123*, 1613.

(14) Graetzel, M. *Acc. Chem. Res.* **2009**, *42*, 1788.

(15) Ooyama, Y.; Harima, Y. *Eur. J. Org. Chem* **2009**, 2903.

(16) Mishra, A.; Pootrakulchote, N.; Fischer, M. K. R.; Klein, C.; Nazeeruddin, M. K.; Zakeeruddin, S. M.; Bäuerle, P.; Grät, M. *Chem. Comm.* **2009**, 7146.

(17) Robertson, N. *ChemSusChem* **2008**, *1*, 977.

(18) Koops, S. E.; O'Regan, B. C.; Barnes, P. R. F.; Durrant, J. R. *J. Am. Chem. Soc.* **2009**, *131*, 4808.

(19) Haque, S. A.; Palomares, E.; Cho, B. M.; Green, A. N. M.; Hirata, N.; Klug, D. R.; Durrant, J. R. *J. Am. Chem. Soc.* **2005**, *127*, 3455.

(20) Asbury, J. B.; Hao, E.; Wang, Y.; Ghosh, H. N.; Lian, T. *J. Phys. Chem. B.* **2001**, *105*, 4545.

(21) Anderson, N. A. L., T. *Coord. Chem. Rev.* **2004**, *248*, 1231.

(22) Anderson, N. A.; Ai, X.; Chen, D.; Mohler, D. L.; Lian, T. *J. Phys. Chem. B.* **2003**, *107*, 14231.

(23) Lense, S.; Hardcastle, K. I.; MacBeth, C. E. *Dalton Trans.* **2009**, 7396.

(24) Mohler, D. L.; Chen, D.; Reddy, V. B. *Synthesis* **2002**, *6*, 745.

(25) Aranyos, V.; Hagfeldt, A.; Grennberg, H.; Figgemeier, E. *Polyhedron* **2004**, *23*, 589.

(26) Sullivan, B. P.; Salmon, D. J.; Meyer, T. J. *Inorg. Chem.* **1978**, *17*, 3334.

(27) Silverstein, R. M.; Webster, F. X.; Kiemle, D. J. *Spectroscopic Identification of Organic Compounds*; seventh ed.; John Wiley & Sons: Hoboken, NJ, 2005.

(28) Rau, S.; Schäfer, B.; Grüßing, A.; Schebesta, S.; Lamm, K.; Vieth, J.; Görls, H.; Walther, D.; Rudolph, M.; Grummt, U. W.; Birkner, E. *Inorg. Chim. Acta* **2004**, *15*,

4496.

(29) Anderson, T. J.; Scott, J. R.; Millett, F.; Durham, B. *Inorg. Chem.* **2006**, *45*, 3843.

(30) Amirnasr, M.; Nazeeruddin, M. K.; Graetzel, M. *Thermochimica Acta* **2000**, *348*, 105.

(31) Xie, P.-H.; Hou, Y.-J.; Wei, T.-X.; Zhang, B.-W.; Cao, Y.; Huang, C.-H. *Inorg. Chim. Acta* **2000**, *308*, 73.

(32) Leasure, R. M.; Ou, W.; Moss, J. A.; Linton, R. W.; Meyer, T. J. *Chem. Mater.* **1996**, *8*, 264.

(33) Shklover, V.; Nazeeruddin, M. K.; Zakeeruddin, S. M.; Barbe, C.; A. Kay; Haibach, T.; Steurer, W.; Hermann, R.; Nissen, H. U.; M. Graetzel *Chem. Mater.* **1997**, *9*, 430.

(34) Chen, C.-Y.; Pootrakulchote, N.; Wu, S.-J.; Wang, M.; Li, J.-Y.; Tsai, J.-H.; Wu, C.-G.; Zakeeruddin, S. M.; Graetzel, M. *J. Phys. Chem. C.* **2009**, *113*, 20752.

(35) Abbotto, A.; Barolo, C.; Bellotto, L.; Angelis, F. D.; Graetzel, M.; Manfredi, N.; Marinzi, C.; Fantacci, S.; Yum, J.-H.; Nazeeruddin, M. K. *Chem. Comm.* **2008**, 5318.

(36) Nazeeruddin, M. K.; Graetzel, M. *Struct. Bonding* **2007**, *123*, 113.

(37) Hermann, R.; Graetzel, M.; Nissen, H.-U. S.; Nazeeruddin, V. M.-K.; Zakeeruddin, S. M.; Barbe, C.; Kay, A.; Haibach, T.; Steurer, W. *Chem. Mater.* **1997**, *10*, 2533.

(38) Kohle, O.; Ruile, S.; Graetzel, M. *Inorg. Chem.* **1996**, *35*, 4779.

(39) Zanello, P. *Molecular Electrochemistry in Inorganic Chemistry: Theory, Practice and Applications*, 2003.

(40) Wolfbauer, G.; Bond, A. M.; MacFarlane, D. R. *Inorg. Chem.* **1999**, *38*, 3836.

(41) Wolfbauer, G.; Bond, A. M.; MacFarlane, D. R. *J. Chem. Soc., Dalton Trans.* **1999**, *24*, 4363.

(42) Bond, A. M.; Deacon, G. B.; Howitt, J.; MacFarlane, D. R.; Spiccia, L.; Wolfbauer, G. *J. Electrochem. Soc.* **1999**, *146*, 648.

(43) Wolfbauer, G.; Bond, A. M.; Deacon, G. B.; MacFarlane, D. R.; Spiccia, L. *J. Am. Chem. Soc.* **2000**, *122*, 130.

(44) Kobayashi, A.; Fujihara, T.; Iwai, M.; Nagasawa, A. *Acta Crystallogr., Sect. E: Struct. Rep. Online* **2004**, *60*, m1172.

(45) Schwalbe, M.; Schaefer, B.; Goerls, H.; Rau, S.; Tschierlei, S.; Schmitt, M.; Popp, J.; Vaughan, G.; Henry, W.; Vos, J. G. *Eur. J. Inorg. Chem.* **2008**, 3310.

(46) Black, S. I.; Skapski, A. C.; Young, G. B. *J. Chem. Soc., Chem. Comm.* **1989**, 911.

(47) Eskelinen, E.; Luukkanen, S.; Haukka, M.; Ahlgren, M.; Pakkanen, T. A. *J. Chem. Soc., Dalton Trans.* **2000**, 2745.

(48) Shklover, V.; Ovchinnikov, Y. E.; Braginsky, L. S.; Zakeeruddin, S. M.; Graetzel, M. *Chem. Mater.* **1998**, *10*, 2533.

(49) Herber, R. H.; Nan, G.; Potenza, J. A.; Schugar, H. J.; Bino, A. *Inorg. Chem.* **1989**, *28*, 938.

(50) Zakeeruddin, S. M.; Nazeeruddin, M. K.; Humphry-Baker, R.; Péchy, P. P.; Quagliotto, P.; Barolo, C.; Viscardi, Graetzel, M. G. *Langmuir* **2002**, *18*, 952.

(51) León, C. P.; Kador, L.; Peng, B.; Thelakkat, M. *J. Phys. Chem. B.* **2006**, *110*, 8723.

(52) Graetzel, M. *Inorg. Chem.* **2005**, *44*, 6841.

(53) *Global 1.0 ed.,* **1997**.

(54) *Apex II***,** Bruker AXS Inc., Analytical X-Ray Systems: 5465 East Cheryl Parkway, Madison, WI 53711–5373, USA, 2005.

(55) *SAINT v 6.45A* , Bruker AXS Inc., Analytical X-Ray Systems: 5465 East Cheryl Parkway, Madison, WI 53711–5373, USA, 2003.

(56) Sheldrick, G. M. *Acta Crystallogr., Sect. A: Fundam. Crystallogr.*, 2008; Vol. 64.

(57) *Internation Tables for X-Ray Crystallography*; Academic Publishers: Dordrecht, The

Netherlands, 1992; Vol. C.

(58) Zaban, A.; Ferrere, S.; Sprague, J.; Gregg, B. A. *J. Phys. Chem. B.* **1997**, *101*, 55.

(59) Asbury, J. B.; Ellingson, R. J.; Ghosh, H. N.; Ferrere, S.; Nozik, A. J.; Lian, T. *J. Phys. Chem. B.* **1999**, *103*, 3110.

(60) Yocum, C. F. *Coord. Chem. Rev.* **2008**, *252*, 296.

(61) Smil, V. *Enriching the earth: Fritz Haber, Carl Bosch, and the transformation of world food production*; MIT Press: Cambridge, Mass., 2001.

(62) Dudev, T.; Lim, C. *Chem. Rev.* **2003**, *103*, 773.

(63) Kirberger, M.; Yang, J. K. *J. Inorg. Biochem.* **2008**, *102*, 1901.

(64) Boussac, A.; Rappaport, F.; Carrier, P.; Verbavatz, J.-M.; Goin, R.; D. Kirilovsky; Rutherford, A. W.; Sugiura., M. *J. Biol. Chem.* **2004**, *279*, 22809.

(65) Shen, J. R.; Satoh, K.; Katoh, S. *Biochim. Biophys. Acta* **1988**, *936*, 386.

(66) Roelofs, T. A.; Liand, W.; J.Latimer, M.; Cinco, R. M.; Rompel, A.; Andrews, J. C.; Sauer, K.; Yachandra, V. K.; Klein, M. P. *Proc. Natl. Acad. Sci. USA* **1996**, *93*, 3335.

(67) Pedersen, C. J. *J. Am. Chem. Soc.* **1967**, *89*, 7017.

(68) Pedersen, C. J. *J. Am. Chem. Soc.* **1967**, *89*, 2495.

(69) Izatt, R. M.; Pawlak, K.; Bradshaw, J. S. *Chem. Rev.* **1995**, *95*, 2529.

(70) Izatt, R. M. P., K.; Bradshaw, J. S.; Bruening, R. L. *Chem. Rev.* **1991**, *91*, 1721.

(71) Lamb, J. D.; Izatt, R. M.; Christensen, J. J.; Eatough, D. J. *Coordination Chemistry of Macrocyclic Compounds*; Plenium Press: New York, 1979.

(72) Izatt, R. M.; Bradshaw, J. S.; Nielsen, S. A.; Lamb, J. D.; Christensen, J. J. *Chem. Rev.* **1985**, *85*, 271.

(73) Gavrilova, A. L.; Bosnich, B. *Chem. Rev.* **2004**, *104*, 349.

(74) Blackman, A. G. *Polyhedron* **2005**, *24*, 1.

(75) Fenton, D. E.; Casellato, U.; Vigato, P. A.; Vadali, M. *Inorg. Chim. Acta* **1982**, *62*, 57.

(76) van Veggel, F. C. J. M.; Verboom, W.; Reinhoudt, D. N. *Chem. Rev.* **1994**, *94*, 279.

(77) Veggel, F. C. J. M. v.; Harkema, S.; Bas, M.; Verboom, W.; Staveren, C. J. v.; Gerritsma, G. J.; Reinhoudt*, D. N. *Inorg. Chem.* **1989**, *28*, 1133.

(78) Staveren, C. J. v.; Eerden, J. v.; Veggel, F. C. J. M. v.; Harkema, S.; Reinhoud, D. N. *J. Am. Chem. Soc.* **1988**, *110*, 4994.

(79) Horwitz, C. P.; Ciringh, Y. *Inorg. Chim. Acta* **1994**, *225*, 191.

(80) Ciringh, Y.; Gordon-Wylie, S. W.; Norman, R. E.; Clark, G. R.; Weintraub, S. T.; Horwitz, C. P. *Inorg. Chem.* **1997**, *36*, 4968.

(81) Turconi, S.; Horwitz, C. P.; Ciringh, Y.; Weintraub, S. T.; Warden, J. T.; Nugent, J. H. A.; Evans, M. C. W. *J. Chem. Soc., Dalton Trans.* **1997**, 4075.

(82) Powell, J.; Kuksis, A.; May, C. J.; Nyburg, S. C.; Smith, S. J. *J. Am. Chem. Soc.* **1981**, *103*, 5941.

(83) Powell, J.; Lough, A.; Wang, F. *Organomet.* **1992**, *11*, 2289.

(84) Ding, K.; Brennessel, W. W.; Holland, P. L. *J. Am. Chem. Soc.* **2009**, *131*, 10804.

(85) Ding, K.; Pierpont, A. W.; Brennessel, W. W.; Lukat-Rodgers, G.; Rodgers, K. R.; Cundari, T. R.; Bill, E.; Holland, P. L. *J. Am. Chem. Soc.* **2009**, 9471.

(86) Pun, D.; Bradley, C. A.; Lobkovsky, E.; Keresztes, I.; Chirik, P. J. *J. Am. Chem. Soc.* **2008**, *130*, 14046.

(87) Smith, J. M.; Lachicotte, R. J.; Pittard, K. A.; Cundari, T. R.; Lukat-Rodgers, G.; Rodgers, K. R.; Holland, P. L. *J. Am. Chem. Soc.* **2001**, *123*, 9222.

(88) Smith, J. M.; Sadique, A. R.; Cundari, T. R.; Rodgers, K. R.; Lukat-Rodgers, G.; Lachicotte, R. J.; Flaschenriem, C. J.; Vela, J.; Holland, P. L. *J. Am. Chem. Soc.* **2006**, *128*, 756.

(89) Brandel, J.; Sairenji, M.; Ichikawa, K.; Nabeshima, T. *Chem. Comm.* **2010**, *46*, 3958.

(90) Ababori, S.; Habata, Y.; Sakamoto, H.; Sato, M.; Ebine, S. *Bull. Chem. Soc. Jpn.* **1983**, *56*, 537.

(91) Akabori, S.; Habata, Y.; Sato, M. *Bull. Chem. Soc. Jpn.* **1984**, *57*, 68.

(92) Bernhardt, P. V.; Hayes, E. J. *Inorg. Chem.* **2002**, *41*, 2892.

(93) Braga, D.; Grepioni, F. *Coord. Chem. Rev.* **1999**, *183*, 19.

(94) Braga, D.; Grepioni, F. *Acc. Chem. Res.* **2000**, *33*, 601.

(95) Braga, D.; Polito, M.; Giaffreda, S. L.; Grepioni, F. *Dalton Trans.* **2005**, *16*, 2766.

(96) Braga, D.; Polito, M.; Grepioni, F. *Crystal Growth and Design* **2004**, *4*, 769.

(97) Braga, D.; Polito, M.; Bracaccini, M.; D'Addario, D.; Tagliavini, E.; Sturba, L.; Grepioni, F. *Organomet.* **2003**, *22*, 2142.

(98) Burrows, A. D.; Chan, C.-W.; Chowdhry, M. M.; McGrady, J. E.; Michael, D.; Mingos, P. *Chem. Soc. Rev.* **1995**, *24*, 329.

(99) Son, S. U.; Reingold, J. A.; Carpenter, G. B.; Sweigart, D. A. *Chem. Comm.* **2006**, 708.

(100) Braga, D.; Grepioni, F.; Tedesco, E.; Gebert, S.; Wadepohl, H. *J. Chem. Soc. Dalton Trans.* **1997**, 1727.

(101) Muller, T. E.; Choi, W.-K. S.; Mingos, D. M. P.; Murphy, D.; Williams, D. J.; Yam, W. W. V. **1994**, *484*, 209.

(102) Fan, M. F.; Lin, Z.; McGrady, J. E.; Mingos, D. M. P. *J. Chem. Soc. Perkin Trans.* **1996**, *2*, 563.

(103) Bertania, R.; Sgarbossa, P.; Venzo, A.; Lelj, F.; Amati, M.; Resnati, G.; Pilatie, T.; Metrangolo, P.; Terraneo, G. *Coord. Chem. Rev.* **2010**, *254*, 677.

(104) Kitaura, R.; Onoyama, G.; Sakamoto, H.; Matsuda, R.; Noro, S.; Kitagawa, S. *Angew. Chem. Int. Ed.* **2004**, *43*, 2684.

(105) Gerrard, L. A.; Wood, P. T. *Chem. Comm.* **2000**, 2107.

(106) Ribas, X.; Dias, J. C.; Morgado, J.; Wurst, K.; Molins, E.; Ruiz, E.; Almeida, M.; Veciana, J.; Rovira, C. *Chem. Eur. J.* **2004**, *10*, 1691.

(107) Kermagoret, A.; Braunstein, P. *Dalton Trans.* **2008**, 1564.

(108) Zhang, J.; Teo, P.; Pattacini, R.; Kermagoret, A.; Welter, R.; Rogez, G.; Hor, T. S. A.; Braunstein, P. *Angew. Chem. Int. Ed.* **2010**, *49*, 1.

(109) Company, A.; Gomez, L.; Fontrodona, X.; Ribas, X.; Costas, M. *Chem.-Eur J.* **2008**, *14*, 5727.

(110) Schwarz, A. D.; Thompson, A. L.; Mountford, P. P. *Inorg. Chem.* **2009**, *48*, 10442.

(111) Skinner, M. E. G.; Li, Y.; Mountford, P. *Inorg. Chem.* **2002**, *41*, 1110.

(112) Skinner, M. E. G.; Li, Y.; Mountford, P. *Inorg. Chem.* **2002**, *41*, 1110.

(113) Skinner, M. E. G.; Mountford, P. *J. Chem. Soc., Dalton Trans.* **2002**, 1694.

(114) Zart, M. K.; Sorrell, T. N.; Powell, D.; Borovik, A. S. *Dalton Trans.* **2003**, 1986.

(115) Davies, C. J.; Hilton, S. J.; Solan, G. A.; Stannard, W.; Fawcett, J. *Polyhedron* **2005**, *24*, 2017.

(116) Salehzadeh, S.; Golbedaghi, R.; Tidmarsh, I. S.; Sorace, L.; Adams, H.; Ward, M. D. *Polyhedron* **2009**, *28*, 162.

(117) Utz, D.; Kisslinger, S.; Hampel, F.; Schindler, S. *J.Inorg.Biochem.* **2008**, *102*, 1236.

(118) Horwitz, C. P.; Warden, J. T.; Weintraub, S. T. *Inorg. Chim. Acta* **1996**, *246*, 311.

(119) Staveren, C. J. v.; Eeerden, J. v.; Veggel, F. C. J. M. v.; Harkema, S.; Reinhoudt, D. N. *J. Am. Chem. Soc.* **1988**, *110*, 4994.

(120) Ouchi, M.; Inoue, Y.; Kanzaki, T.; Hakushi, T. *J. Org. Chem.* **1984**, *49*, 1408.

(121) Greene, T. W.; Wuts, P. G. M. *Protective Groups in Organic Synthesis*; 3rd ed.; John Wiley and Sons: New York, 1999.

(122) García-España, E.; Gaviña, P.; Latorre, J.; Soriano, C.; Verdejo, B. *J. Am. Chem. Soc.* **2004**, *126*, 5082.

(123) Hosseini, M. W.; Blacker, A. J.; Lehn, J. M. *J. Am. Chem. Soc.* **1990**, *112*, 3896.

(124) Roemmele, R. C.; Rapoport, H. *J. Org. Chem.* **1988**, *53*, 2367.

(125) Compagnone, R. S.; Rapoport, H. *J. Org. Chem.* **1986**, *51*, 1713.

(126) Weissermel, K.; Arpe, H.-J. *Industrial Organic Chemistry*; 3rd ed.; VCH Verlagsgesellschaft mbH: Weinheim, 1997.

(127) Serjeant, E. P.; Dempsey, B.; Pergamon Press: Oxford, 1979.

(128) Daftary, R. D.; Haldar, B. C. *Anal. Chim. Acta* **1960**, *25*, 538.

(129) Kochi, J. K.; Hammond, G. S. *J. Am. Chem. Soc.* **1953**, *75*, 3445.

(130) Addison, A. W.; Rao, T. N.; Reedijk, J.; Rijn, J. v.; Verschoor, G. C. *J. Chem. Soc., Dalton Trans.* **1984**, 1349.

(131) Skinner, M. E. G.; Cowhig, D. A.; Mountford, P. *Chem. Comm.* **2000**, 1167.

(132) Nakamoto, K. *Infrared and Raman Spectra of Inorganic and Coordination Compounds*; 5th ed.; John Wiley and Sons, Inc.: New York, 1997.

(133) Hammett, L. P. *J. Am. Chem. Soc.* **1937**, *59*, 96.

(134) Kimura, M. *Heterocycles* **2006**, *68*, 2375.

(135) Krespan, C. G. *J. Org. Chem.* **1974**, *40*, 1205.

(136) Dey, A.; Hocking, R. K.; Larsen, P.; Borovik, A. S.; Hodgson, K. O.; B.Hedman; Solomon, E. I. *J. Am. Chem. Soc.* **2006**, *128*, 15476.

(137) Lucas, R. L.; Zart, M. K.; Murkerjee, J.; Sorrell, T. N.; Powell, D. R.; Borovik, A. S. *J. Am. Chem. Soc.* **2006**, *128*, 15476.

(138) Parsell, T. H.; Yang, M.-Y.; Borovik, A. S. *J. Am. Chem. Soc.* **2009**, *131*, 2762.

(139) Ray, M.; Hammes, B. S.; Yap, G. P. A.; Rheingold, A. L.; Borovik, A. S. *Inorg. Chem.*

1998, *37*.

(140) Yang, L.; Powell, D. R.; Houser, R. P. *Dalton Trans.* **2007**, 955.

(141) Jennings, W. B.; Farrell, B. M.; Malone, J. F. *Acc. Chem. Res.* **2001**, *34*, 885.

(142) Yoon, I.; Shin, Y. W.; Kim, J.; Park, K.-M.; Park, S. B.; Lee, S. S. *Acta Cryst. Sect. C* **2002**, *C58*, m165.

(143) Evans, D. F. *J. Chem. Soc. Faraday Trans.* **1959**, 2003.

(144) Burger, K. *Coordination Chemistry: Experimental Methods*; Butterworth: London, 1973.

(145) Banci, L.; Benelli, C.; Gatteschi, D.; Mani, F.; Chem., I. *Inorg. Chem.* **1982**, *21*.

(146) Connors, K. A. *Binding Constants: The Measurement of Molecular Complex Stability*; John Wiley and Sons: U.S.A., 1987.

(147) Hill, Z. D.; MacCarthy, P. *J. Chem. Ed.* **1986**, *63*, 162.

(148) Gil, V. M. S.; Oliveira, N. C. *J. Chem. Ed.* **1990**, *67*, 473.

(149) Armarego, W. L. F.; Chai, C. L. L. *Purification of Laboratory Chemicals*; 5th ed. ed. New York, 2003.

(150) Berezin, S. K.; Davis, J. T. *J. Am. Chem. Soc.* **2009**, *131*, 2458.